Atmospheric reaction chemistry of cloud droplets and aerosol by laser tweezers and neutron scattering

Stephanie Helen Jones

A thesis submitted for the degree of

Doctor of Philosophy at the University of London

Department of Earth Sciences

Royal Holloway, University of London

2015

Declaration of Authorship

I, Stephanie Helen Jones hereby declare that this thesis and the work presented in it is entirely my own unless otherwise stated. My contributions to the six co-authored papers that make up the body of this thesis are stated clearly on the cover page of each paper.

Signed: S.H. JONES

Date: 08/12/15

Acknowledgments

First of all I would like to thank my supervisors, Martin King and Andy Ward for their encouragement, support and guidance throughout my PhD. Having two different supervisors has given me an insight into different ways of thinking and methods of working and has also shown me that there is always more than one way to approach a problem.

I would also like to thank Adrian Rennie for his support during the various neutron and X-ray experiments undertaken throughout my PhD and for always making time to answer my questions.

I want to thank my parents for their constant support and words of motivation and encouragement when I needed them the most. I especially want to thank my sister Alison, who has helped me to get through this PhD by always being at the end of the phone or just a quick train ride away!

Special thanks also go to numerous friends from RAL, RHUL, Bristol and home who have helped to keep me sane and been there for some much needed light relief, especially during the writing up period!

Abstract

Aerosols and their indirect contribution to the Earth's climate remains a poorly understood field. The indirect effect of aerosols on the climate refers to aerosol ability to form cloud condensation nuclei (CCN) and affect cloud properties. Naturally forming, thin organic films exist on the surface of atmospheric aerosols and have the ability to influence aerosol behaviour. Given the oxidative nature of the atmosphere, thin organic films on the surface of aerosols are readily oxidised which will impact on CCN formation and the properties of cloud droplets, affecting the Earth's climate indirectly.

The purpose of this thesis was to investigate the oxidation of atmospherically relevant thin films at the air-water interface using the complementary techniques of optical trapping and neutron and X-ray reflectometry, to determine whether such reactions are important in the atmosphere.

An optical trapping technique was developed to coat individual solid silica beads with a thin film of oleic acid and characterise both the size and wavelength dependent refractive index of the core silica aerosol and the oleic acid coating using white light Mie scattering. The size of the core aerosol and coating thickness were determined to a precision of ± 0.5 nm and 1 nm respectively.

The oxidation of monolayer organic films of atmospheric proxies at the air-water interface was studied using neutron reflectometry and the common atmospheric oxidants, O_3, $^{\cdot}OH$, $NO_3^{\cdot}$, $SO_4^{\cdot -}$. These studies provided insight into the oxidation mechanism of the film as well as film persistence and thickness. Furthermore, the oxidation of monolayer films was also found to be independent of the viscosity and ionic strength of the solution that the film was present on.

X-ray reflectivity studies were carried out on the oxidation of monolayer organic films extracted from real atmospheric aerosol and sea-water samples at the air-water interface. The films were found to be inert to gaseous ozone indicating a lack of unsaturated material in atmospheric samples and that oxidation by gaseous ozone may not be important in the atmosphere.

Table of Contents

List of Figures

Introduction:

Method:

Paper 1: Determining the unique refractive index properties of solid polystyrene aerosol using broadband Mie scattering from optically trapped beads

Figure 4. Refractive index dispersion fitted to the determined values of refractive index for individual resonance positions of an optically trapped polystyrene bead in air.

Figure 5. The value of the Levenberg–Marquardt residual as a function of bead radius for an optically trapped polystyrene bead.

Figure 6. Refractive index dispersions for ten individual polystyrene beads.

Figure 7. Comparison of the refractive index dispersions from literature with the refractive index dispersion obtained in this study over the wavelength range 480–700 nm.

Paper 2: Atmospherically relevant core–shell aerosol studied using optical trapping and Mie scattering

Figure 1. Comparison of a typical experimental Mie spectrum for an optically trapped oleic acid droplet and its calculated Mie spectrum.

Figure 2. Comparison of a typical experimental Mie spectrum for an optically trapped silica bead and its calculated Mie spectrum and comparison of a typical Mie spectrum for an optically trapped silica bead coated in a thin film of oleic acid and its calculated core-shell Mie spectrum.

Figure 3. Resonance peak shift with increasing exposure time to gaseous oleic acid for an optically trapped silica bead.

Paper 3: Degradation and rearrangement of a lung surfactant lipid at the air-water interface during exposure to the pollutant gas ozone

Scheme 1. Initial reaction of POPC with gaseous ozone leading to the cleavage of the carbon−carbon double bond of the oleoyl strand.

Figure 1. Structure and deuteration schemes of Pd_{17}OPC and d_{31}POPC.

Figure 2. Surface pressure vs mean molecular area isotherms obtained by compressing a fixed amount of a 1:1 mixture of DPPC and POPC on the water surface at 21 and 31 °C.

Figure 3. Examples of the reflectivity profiles obtained when a monolayer of Pd_{17}OPC is exposed to gas-phase ozone.

Figure 4. Typical kinetic plot that shows the rapid loss of the deuterated portion of Pd_{17}OPC from the air−water interface and the simultaneous increase in surface pressure with time when a film of Pd_{17}OPC is exposed to gas-phase ozone.

Figure 5. Surface pressure and fitted ρδ when d_{31}POPC and Pd_{17}OPC are exposed to gas-phase ozone.

Figure 6. Plots showing the different results obtained when binary mixtures of (i) ^{1}H-DPPC and d_{31}POPC and (ii) d_{62}DPPC and ^{1}H-POPC are exposed to gas-phase ozone at the air−water interface with an initial surface pressure of about 17 mN m^{-1} at 31 °C.

Figure 7. Plots showing the different results obtained when binary mixtures of (i) ^{1}H-DPPC and d_{31}POPC and (ii) d_{62}DPPC and ^{1}H-POPC are exposed to gas-phase ozone at the air−water interface with an initial surface pressure of about 40 mN m^{-1} at 21 °C.

Paper 4: The atmospheric importance of aqueous radical initiated oxidation of an organic monolayer at the air-water interface studied by neutron reflectivity

Figure 1. A typical neutron reflectivity profile for a monolayer film of fully deuterated DSPC at the air-water interface on exposure to the aqueous phase hydroxyl radical.

Figure 2. Determination of the steady-state concentration of hydroxyl radicals from kinetic modelling.

Figure 3. Determination of the steady-state concentration of sulfate radicals from kinetic modelling.

Figure 4. The multi-step degradation mechanism fitted to the experimental decay in relative surface coverage of deuterated material at the air-water interface during $NO_3^{\cdot}$ radical initiated oxidation.

Figure 5. The multi-step degradation mechanism fitted to the experimental decay in relative surface coverage of deuterated material at the air-water interface during $SO_4^{\cdot -}$ radical initiated oxidation.

Figure 6. The multi-step degradation mechanism fitted to the experimental decay in relative surface coverage of deuterated material at the air-water interface during $^{\cdot}OH$ radical initiated oxidation.

Figure 7. Cartoon of multi-step degradation mechanism approximating the surface coverage of material at the air-water interface following each step in the proposed degradation mechanism for the attack of a monolayer of DSPC by an aqueous phase radical, X.

Figure 8. Stylised mechanism for the aqueous radial initiated oxidation of a DSPC molecule showing the proposed reaction products.

Figure 9. Atmospheric lifetime of the film versus proportion of the film removed by oxidation for three different $^{\cdot}OH$ radical concentrations.

Paper 5: The reaction of a monolayer of oleic acid with gas-phase ozone at the air-water interface: The effect of solution viscosity

Figure 1. Kinetic decays of deuterated oleic acid at the air-water interface in the presence of 0.13 ppm of gas-phase ozone.

Figure 2. Kinetic decays of deuterated oleic acid at the air-water interface in the presence of 0.13 ppm of gas-phase ozone for all experiments conducted.

Paper 6: Are atmospheric aerosol and sea-water film forming materials at the air-water interface inert to oxidation?

Figure 1. Slab model for an organic thin film at the air-water interface.

Figure 2. Example reflectivity profile for atmospheric film material during exposure to the aqueous phase hydroxyl radical.

Figure 3. The relative amount and thickness of atmospheric film forming material at the air-water interface during exposure to gas phase ozone.

Figure 4. Change in the reflectivity profile with time when a monolayer of atmospheric film forming material is exposed to the aqueous phase hydroxyl radical.

Figure 5. The relative amount and thickness of atmospheric film forming material at the air-water interface during exposure to the aqueous phase hydroxyl radical.

Figure 6. Reflectivity profiles for three different pure water subphases and three filter blanks at the air-water interface.

Figure 7. Change in the reflectivity profile with time when a monolayer film of sea-water material is exposed to the nitrate radical.

Figure 8. The change in relative surface coverage when a monolayer film of sea-water material is exposed to the nitrate radical and gas-phase ozone.

Figure 9. Adapted diagram from Rogge et al., 1993 showing the percentage chemical composition of material identified from a mean annual sample collected in West Los Angeles in 1982.

Appendix figures. GC-MS and ESI-MS spectra for atmospheric aerosol and sea-water samples.

Summary and critical evaluation:

Figure 1. Comparison of the Mie resonance spectrum for an optically trapped sodium chloride droplet to the subsequent Mie resonance spectrum of the same droplet following collisions with a number of oleic acid droplets.

Figure 2. The core-shell Mie resonance spectrum for a 300 nm thick oleic acid film on a 0.9559 μm radius core silica bead.

List of Tables

Introduction

Paper 1: Determining the unique refractive index properties of solid polystyrene aerosol using broadband Mie scattering from optically trapped beads

Paper 2: Atmospherically relevant core–shell aerosol studied using optical trapping and Mie scattering

Paper 3: Degradation and rearrangement of a lung surfactant lipid at the air-water interface during exposure to the pollutant gas ozone

Paper 4: The atmospheric importance of aqueous radical initiated oxidation of an organic monolayer at the air-water interface studied by neutron reflectivity

1. Introduction

The work detailed in this thesis covers the formation and characterisation of atmospherically relevant optically trapped solid aerosol and solid core-liquid shell aerosol using white light Mie scattering. Studies have also been conducted on the oxidation of monolayer organic films at the air-water interface using neutron and X-ray reflectivity as proxies for coatings found at the surface of atmospheric aerosols.

1.1. Atmospheric Aerosols

Aerosols are solid particles or liquid droplets dispersed in a gaseous phase ranging from ~0.01 to 100 μm in diameter, and they are abundant throughout the Earth's troposphere, the lowest layer of the atmosphere (ground level up to ~15 Km in height) (Seinfeld and Pandis, 1998). Primary aerosols are emitted directly into the atmosphere and secondary aerosols are emitted into the atmosphere by chemical reactions such as gas to particle conversion (Finlayson-Pitts and Pitts Jr, 1997). Atmospheric processes involving aerosols are influenced by the aerosol properties such as size, mass, number concentration, chemical composition and their optical properties. Aerosol size is the most important property as it dictates aerosol effects on visibility, human health and the Earth's climate (Finlayson-Pitts and Pitts Jr, 1997 and Boucher et al., 2013).

Reduced visibility in both urban and rural areas can result from air pollution (Malm, 1999) owing to the scattering of light by pollutant aerosols. Aerosol size is important because it directly affects the amount of light scattered. Typically, severe air pollution in large cities causes a reduction in visibility in urban areas e.g. in cities like Beijing (Chang et al., 2009). Visibility in non-urban areas can also be affected by air pollution; an example of which is the presence of haze observed in the Grand Canyon as a result of aerosol emissions from a local coal burning power station (Malm, 1999). Inhalation of aerosol particles can also cause human health problems (Finlayson-Pitts and Pitts Jr, 1997, Alexis et al., 2004). Particle size and chemical composition will both affect the nature and severity of such health problems (Finlayson-Pitts and Pitts Jr, 1997).

As well as influencing visibility and human health, atmospheric aerosols also play a major role in the Earth's climate (e.g. Dickerson et al., 1997, Andreae and Crutzen, 1997, Ramanathan et al., 2001, Lohman and Feichter, 2005, Fuzzi et al., 2006 and references therein). Aerosols influence the climate directly, by scattering and absorbing solar radiation and indirectly, by their contribution to cloud condensation nuclei (CCN) formation and their associated influence on cloud properties. These effects are known as the aerosol direct and indirect effect respectively.

Figure 1 is taken from the latest report by the Intergovernmental Panel on Climate Change (IPCC), (IPCC, 2013: Summary for Policymakers) and highlights the different atmospheric contributions to radiative forcing of the climate and their associated uncertainties. Radiative forcing is the extra energy into the earth per unit area, measured in W m^{-2}. It is not only aerosols that contribute to both direct and indirect radiative forcing as shown in Figure 1; other significant contributions also include Greenhouse gas emissions, short lived gaseous species, the change in albedo due to land use and the change in solar irradiance. Focussing on aerosol contribution to radiative forcing, Figure 1 emphasises the large amount of uncertainty associated with the aerosol indirect effect as evidenced by the large error bar present on the atmospheric driver 'cloud adjustments due to aerosols'. The uncertainty relating to the aerosol indirect effect has motivated a large number of studies (e.g. Pandis et al., 1995, Rudich, 2003, Finlayson-Pitts, 2009 and many more).

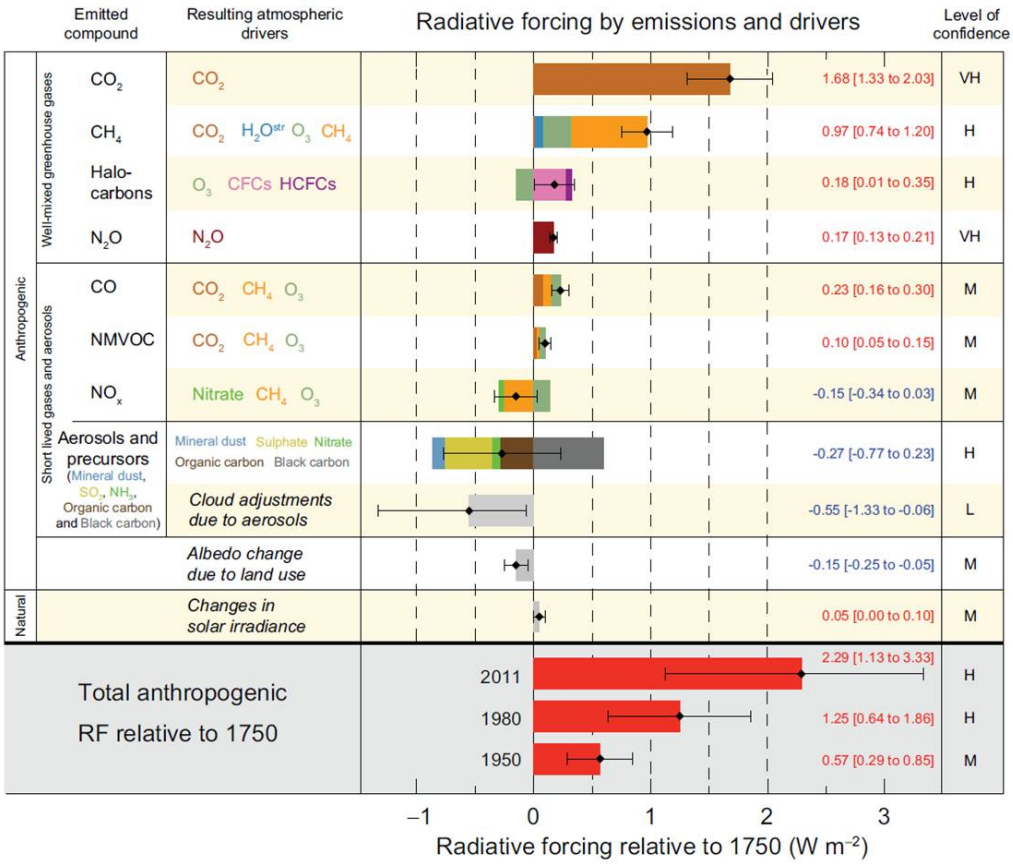

Figure 1. Natural and anthropogenic contributions to radiative forcing (IPCC, 2013: Summary for Policymakers). The left hand side of the figure represents contributions that cool the climate and the right hand side of the figure represents contributions that warm the climate. Note that the largest error bar for all contributions is present on the atmospheric driver 'Cloud adjustments due to aerosols'.

1.2. Cloud formation

Clouds form from aerosols that have the ability to act as CCN. Aerosol size, morphology and chemical composition play an important role in CCN formation and it is therefore important to be able to accurately characterise these aerosol properties.

When an air parcel rises, it expands and cools adiabatically owing to the decrease in atmospheric pressure. The decrease in pressure causes the gas to expand and do work which results in a loss in heat. The decrease in temperature results in a decrease in equilibrium vapour pressure which is exceeded by the actual vapour pressure thus the air parcel becomes supersaturated with respect to water. Water can then condense on to wettable droplets or particles (aerosols) that are present in the air parcel (Hobbs, 2000, Wallace and Hobbs, 2006). All aerosols can be thought of as condensation nuclei, CN, but not all aerosols can form clouds, only cloud condensation nuclei, CCN have the ability to form cloud droplets (Hobbs, 2000). Particle size, chemical composition and the supersaturation of the surrounding air dictate CCN formation (Seinfeld and Pandis, 1998). Aerosol morphology and the chemical reactions that an aerosol may undergo within its lifetime can influence the ability of an aerosol to uptake water (its hygroscopicity) which in turn can influence CCN formation. Aerosols that do not act as CCN can still be incorporated into a cloud and are known as cloud interstitial aerosol (CIA) (Hobbs, 2000).

The formation of cloud droplets can be described by Köhler theory which combines two important effects, the Kelvin effect and the Raoult effect. The Kelvin effect describes how the vapour pressure above a curved surface such as a liquid droplet depends on the radius of curvature and is defined by equation 1.

$$p_A = p_A^{\circ} \exp\left(\frac{2\sigma M}{RT\rho_l R_p}\right) \qquad 1$$

Where p_A is the equilibrium partial pressure over a liquid droplet A, p_A° is the vapour pressure of pure A over a flat surface, σ is the surface tension of the curved liquid-air interface, M is the molecular weight of the liquid, R is the gas constant, T is the temperature, ρ_l is the liquid phase density and R_p is the drop radius. The smaller the radius, the larger the vapour pressure will be.

Aerosols are seldom 100 % pure water droplets and often contain a solute. The Raoult effect describes the effect of the solute content on aerosol vapour pressure and is defined by equation 2 for ideal behaviour.

$$p_i = p_i^{\circ} x_i \qquad 2$$

Where p_i is the water vapour partial pressure over the solution, p_i° is the vapour pressure of the pure solution component and x_i is the aqueous mole fraction in solution. An increased solute content results in a lower vapour pressure because there are fewer pure water molecules at the air-droplet interface.

The combination of the Kelvin and Raoult effects (equations 1 and 2) results in the Köhler equation (equation 3), from which Köhler curves can be plotted as shown in Figure 2. Köhler curves can be used to predict the formation of cloud droplets given the supersaturation as a function of particle radius. The first term in the Köhler equation (equation 3) describes the contribution from the Kelvin effect and the second term describes the contribution from the Raoult effect.

$$\ln\left(\frac{p_w(D_p)}{p^{\circ}}\right) = \frac{4M_w\sigma_w}{RT\rho_w D_p} - \frac{6n_s M_w}{\pi\rho_w D_p^3} \qquad 3$$

where $p_w(D_p)$ is the water vapour pressure over a droplet of diameter D_p, p° is the water vapour pressure over a flat surface at the same temperature, M_w is the molecular weight of water, σ_w is the surface tension of water, ρ_w is the density of water and n_s is the number of moles of solute present (Seinfeld and Pandis, 1998).

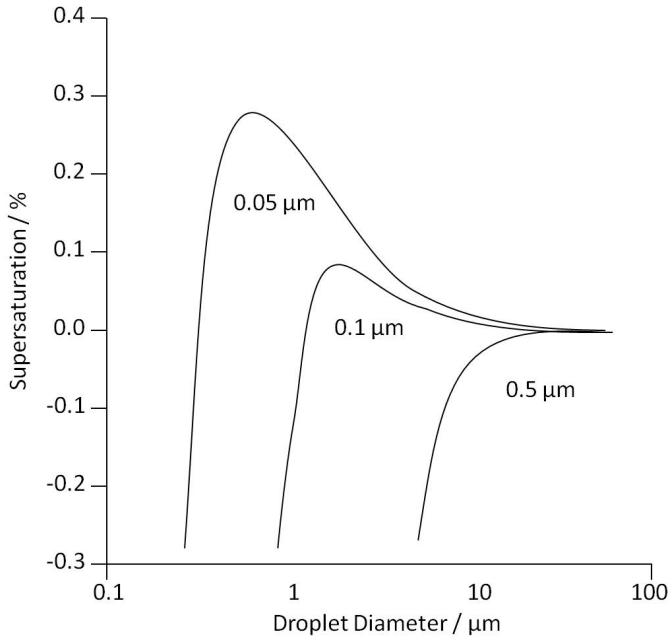

Figure 2. Example Köhler curves for three spherical NaCl particles of dry diameter, 0.05, 0.1 and 0.5 µm. Supersaturation is defined as the saturation ratio minus one.

The sketch in Figure 2 shows examples of typical Köhler curves for NaCl particles of differing dry diameters which can be used to describe cloud droplet formation as a function of droplet supersaturation and radius. The peak of each curve corresponds to the critical diameter and the supersaturation required for growth into a cloud droplet. The portion of the curve where the diameter is less than the critical diameter represents a stable equilibrium which is dominated by the Raoult effect. As the droplet increases in size, the contribution from the Raoult effect decreases and the importance of the Kelvin effect increases. Once the droplet has reached its critical diameter (the peak of the Köhler curve) and beyond, the contribution from the Raoult effect is so small that the Köhler curves approach the Kelvin equation. The portion of the Köhler curve where the droplet diameter is greater than the critical diameter represents an unstable equilibrium where cloud droplets can grow.

Example situations for a droplet on both the stable and unstable equilibrium sides of the above Köhler curves will now be considered. Small perturbations in the atmosphere mean that it is possible for a few molecules of water to either condense on to or to evaporate from a droplet at any time. Considering droplets that have a diameter less than the critical diameter that are on the stable equilibrium part of the Köhler curve in Figure 2, the condensation of a few water molecules on to an aerosol will cause an increase in aerosol size. The larger aerosol can be thought of as having a higher equilibrium vapour pressure than the ambient, and therefore will subsequently evaporate returning to its original size. The opposite case can also occur for the evaporation of a few water molecules from a droplet whose diameter is less than the critical diameter. The droplet will decrease in size and have a lower equilibrium vapour pressure than the ambient and thus water will condense on to the droplet returning it to its original size.

For droplets whose diameter is larger than the critical diameter that are on the unstable equilibrium part of the Köhler curve, a small increase in droplet size from the condensation of a few water molecules will cause a decrease in vapour pressure but the ambient vapour pressure is supersaturated so the droplet will continue to grow into a cloud droplet. However, if a droplet lost a few water molecules it would shrink in size resulting in an increase in vapour pressure which is then higher than the ambient vapour pressure and therefore the droplet would either evaporate if it was a pure water droplet or continue to evaporate until it intersected the stable equilibrium portion of the Köhler curve (Seinfeld and Pandis, 1998).

1.3. Aerosol size range

As mentioned previously aerosol size has an important influence on aerosol properties. Aerosols can generally be classified into two size ranges: fine particles that are less than 2.5 μm in diameter; and coarse particles that are greater than 2.5 μm in diameter (Seinfeld and Pandis, 1998). Figure 3 highlights the different aerosol size modes, including typical sizes, sources and formation processes associated with each mode. Fine particles can be broken down into two modes: Aitken nuclei-particles with diameters between ~0.005-0.1 μm; and accumulation mode particles-particles with diameters between 0.1-2.5 μm. The coarse mode contains aerosols with a diameter greater than 2.5 μm that are typically formed from mechanical processes such as erosion and wind action (Finlayson-Pitts and Pitts Jr, 2000).

The three different modes in Figure 3 arise because of the efficient removal mechanisms at the size extremes of each mode, resulting in the formation of a peak in each size range. All removal processes can be classified as either dry or wet deposition. Dry deposition includes impaction onto surfaces, coagulation and gravitational settling, whereas wet deposition includes incorporation into cloud droplets and precipitation (Hobbs, 2000 and Seinfeld and Pandis, 1998). The peak in the fine mode for Aitken nuclei arises from the following removal mechanisms: condensation (removal of particles smaller than ~0.005 μm); and coagulation and condensation of low volatility vapours (removal of particles ~0.1 μm in diameter). The peak in the coarse mode arises from rainout which removes particles 1-2 μm in diameter and greater, and gravitation settling which removes particles >10 μm in diameter. It follows that the peak in the accumulation mode (in between the Aitken nuclei and coarse modes in Figure 2) results from the coagulation and condensation of low volatility vapours at the smaller size range and rainout at the larger size range (Seinfeld and Pandis, 1998).

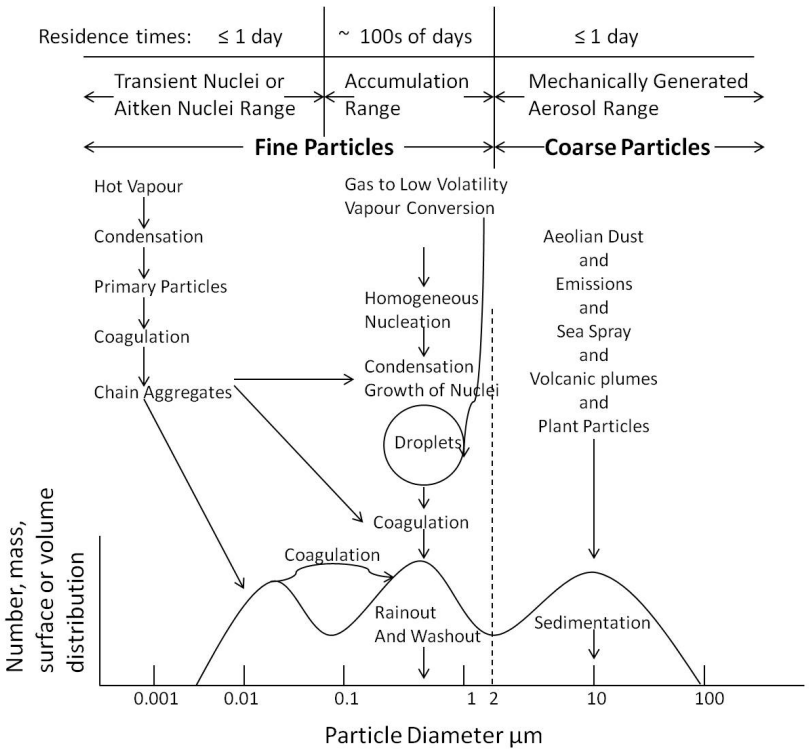

Figure 3. Aerosol size ranges, adapted from Whitby and Sverdrup, 1980. The y axis can represent either the number, mass, surface or volume distribution and the interested reader is referred to Finlayson-Pitts and Pitts Jr, 2000 and Whitby and Sverdrup, 1980 for more information.

Atmospheric residence times for each mode are shown at the top of Figure 3 (Hobbs, 2000). As described previously, removal mechanisms are efficient at the extremes of each mode and particularly at the extremes of the whole aerosol size range. Accumulation mode particles therefore tend to have the longest atmospheric residence times (Seinfeld and Pandis, 1998). Particles ranging from ~ 0.2-2 µm in diameter have residence times of the order of tens to hundreds of days depending on whether they reside in the lower/middle or upper troposphere respectively. Residence times for particles that are < 0.01 µm in diameter are on the order of ~ ≤ 1 day as they are typically removed by coagulation and phoretic diffusion to cloud particles. Coarse mode particles also have residence times on the order of ~ ≤ 1 day because they are efficiently removed by processes such as impaction, gravitational settling, precipitation and scavenging (Hobbs, 2000).

1.4. Aerosol sources and composition

Particles in the atmosphere arise from both natural and anthropogenic sources and have a varied chemical composition. Sea spray, airborne dust and volcanic eruptions are examples of natural particle sources and the combustion of fuels is an example of an anthropogenic particle source. When particles are made airborne, they have the

potential to change their composition through atmospheric chemical interactions and processes such as evaporation, the condensation of vapour species, coagulation with other particles, participation in chemical reactions and through the formation of CCN (Seinfeld and Pandis, 1998).

The main constituents of tropospheric aerosol include inorganic species (sulfates, nitrates, ammonium and sea salt), organic compounds, black carbon, mineral species (mineral dust) and primary biological aerosol particles (Boucher et al., 2013). Global emissions of both natural and anthropogenic aerosol and aerosol precursors are listed in Table 1 which is adapted from Boucher et al., 2013.

Source	Global Minimum / Tg yr^{-1}	Global Maximum / Tg yr^{-1}
Natural		
Sea spray	1400	6800
Mineral dust	1000	4000
Terrestrial PBAPs	50	1000
Dimethylsulphide (DMS)	10	40
Monoterpenes	30	120
Isoprene	410	600
SOA production from all BVOCs	20	380
Anthropogenic		
Non-methane VOCs	98.2	157.9
Black carbon	3.6	6
Primary organic aerosols	6.3	15.3
SO_2	43.3	77.9
NH_3	34.5	49.6
Biomass burning aerosols	29	85.3

Table 1. Global natural and anthropogenic aerosol and aerosol precursor emissions adapted from Boucher et al., 2013. The following acronyms are used: primary biological aerosol particle-PBAP; secondary organic aerosol-SOA; biogenic volatile organic compounds-BVOC and volatile organic compounds-VOC. N.B. DMS and SO_2 are measured in TgS yr^{-1} and Isoprene and SOA from BVOCs are measured in TgC yr^{-1}.

As evident in Table 1, the two most prevalent types of atmospheric aerosol are marine aerosol and mineral dust, both natural in source. Marine aerosol is emitted into the atmosphere at 1400-6800 Tg yr^{-1} and mineral dust aerosol is emitted at 1000-4000 Tg yr^{-1} (Boucher et al., 2013). Marine aerosol is produced from breaking waves and subsequent bubble bursting in the ocean (e.g. Woodcock et al., 1953, Mason, 1954, Blanchard and Woodcock, 1957, MacIntyre, 1974, O'Dowd and de Leeuw, 2007 etc.) and is typically within the size range sub μm to tens of μm (Fitzgerald, 1991). Marine aerosol consists of inorganic salts as well as a number of organic components (Marty et al., 1979, Middlebrook et al., 1998). Mineral dust aerosol is emitted into the

atmosphere by wind action over large desert areas such as the Sahara and Gobi (Usher et al., 2003) in the form of sand or silica particles, in the size range > 2.5 μm.

Both aerosol optical properties such as the ability to scatter and absorb solar radiation and chemical properties are determined by aerosol chemical composition, morphology and size (e.g. Pöschl, 2005, Zhang et al., 2008). It is therefore important to characterise aerosols in order to fully understand their behaviour. Organic material found in tropospheric aerosols can consist of a large complex mixture of organic compounds (Seinfeld and Pandis, 1998) which have the potential to interact with atmospheric aerosols during their lifetime. Such reactions could influence aerosol morphology i.e. the formation of coatings, which in turn could impact on how an aerosol reacts with other atmospheric chemicals (Donaldson and Vaida, 2006).

1.5. Coated aerosols

Amphiphiles are a common component of organic material found in atmospheric aerosols (Donaldson and Vaida, 2006, Gill et al., 1983) and consist of a polar hydrophilic head group (the water-soluble part of the molecule) and a hydrophobic hydrocarbon tail group (the water insoluble part of the molecule). If the hydrophobic part of an amphiphile strongly dominates over the hydrophilic part of the amiphiphile, then the amphiphile will be insoluble in water and can form an insoluble monolayer at the air-water interface (Barnes and Gentle, 2005). Owing to the abundance of amphiphilic organic material in atmospheric aerosols it is therefore possible for aerosols to exist that have core-shell morphology, i.e. a core aerosol coated in a thin film of organic material at the air-water interface. At an air-aqueous interface such as the surface of the ocean or the core of a water droplet, the hydrophilic head group of the amphiphile would be immersed in the aqueous phase which would typically contain polar organic molecules and dissolved inorganic species. The hydrophobic tail would protrude into the atmosphere where it could be exposed to reactive radicals and solar radiation (Barnes and Gentle, 2005, Donaldson and Vaida, 2006). Amphiphiles that have longer carbon chain lengths tend to have a higher propensity for the surface (Gill et al. 1983). Compounds such as long chain fatty acids, fatty alcohols, lipids, and sterols are all amphiphiles and have the ability to form films at the air-water interface.

As highlighted previously both marine aerosol and mineral dust are major sources of atmospheric aerosol (Boucher et al., 2013). One of the main sources of surface active material in marine aerosols arises from the film forming material present in the top microlayer of the ocean (Donaldson and George, 2012). The origin of surfactant

material in the microlayer is oceanic biota enriched in fatty acids, amines, alcohols and sterols (Donaldson and Vaida, 2006 and references therein).

All bodies of water including fresh water are covered by an organic film or a surface microlayer of 1-1000 μm in thickness (Donaldson and Vaida, 2006), and this film can be incorporated into atmospheric aerosols (Seinfeld and Pandis, 1998). Bubbles are formed in the ocean when waves break and whitecaps form. As bubbles rise to the surface of the ocean, surface active organics present in the microlayer can partition to the bubble interface. Bubbles provide a large surface area for partitioning to occur. Such bubbles then burst at the ocean's surface, and in doing so release jet and film drops that are highly enriched in surface active material (Blanchard and Woodcock 1957, Blanchard 1989, MacIntyre, 1972, 1974). It is possible for a breaking bubble to remove a sample of the ocean surface on the order of a tenth of a micrometer. Given that bubbles cover approximately 3-4 % of the ocean's surface at any time, bubbles are a major source of marine aerosol (MacIntyre, 1974). In 1962, Blanchard investigated the components of a heavy surf in Hawaii and found that the droplets released in the surf carried a highly compressed surface active film on their surface (Blanchard, 1964).

Another significant method for the formation of surface active coatings is adsorption by solid aerosols such as mineral dust. When dust particles pass over areas of pollution, forested regions and biomass burning, organic compounds (polar and non polar) may be adsorbed on to their surface (Falkovich, 2004).

1.6. Evidence for organic coatings

A number of field studies have sampled atmospheric aerosol and used a variety of analytical techniques to determine aerosol chemical composition and morphology (Husar and Shu, 75, Posfai et al., 1998, Capel et al., 1990, Facchini et al., 1999, 2000, Tervahattu et al., 2002, 2005, Russell et al., 2002, Peterson and Tyler, 2002, Takahama et al., 2010). Older studies typically inferred the presence of organic coatings on the surface of aerosols (Husar and Shu, 1975, Posfai et al., 1998, Capel et al., 1990, Facchini et al., 1999, 2000) whereas more recent studies using surface analysis techniques have provided more direct evidence (Tervahattu et al., 2002, 2005, Russell et al., 2002, Peterson and Tyler, 2002, Takahama et al., 2010). It is important to remember that many of these methods used contact techniques, often where the aerosol samples were collected on either a filter or an impactor (e.g. Facchini et al., 2000, Peterson and Tyler, 2002, Russell et al., 2002 etc.), which could affect the aerosol morphology.

1.6.1. Inferred evidence for organic coatings

Husar and Shu, 1975 and Posfai et al., 1998, both used electron microscopy to infer the presence of organic coatings on the surface of aerosol samples. Husar and Shu, 1975, collected smog and haze aerosol samples in Los Angeles and observed different light scattering behaviour for each aerosol type. The difference in behaviour indicated different chemical composition or morphology for the different aerosol types. Electron microscopy studies showed the smog aerosol to be solid and spherical. Whereas the haze aerosol was described as resembling a thick walled rubber ball with an evacuated centre following heating. The authors thus proposed that the haze aerosol had been an aqueous core which had evaporated. The study therefore represents indirect evidence that the sampled haze aerosol consisted of an aqueous core surrounded by a non-volatile coating. Posfai et al., 1998 also used electron microscopy to infer the presence of an organic coating on ammonium sulfate particles collected over the North Atlantic Ocean. The electron beam used in microscopy caused the particles to evaporate leaving behind a residue. Subsequent analysis of the residue by Energy Dispersive Spectrometry (EDS) showed high concentrations of C, O and S which were interpreted as evidence of an organic coating.

Other studies have used surface tension measurements to infer the presence of an organic coating (Capel et al., 1990, Facchini et al., 1999, 2000). Water soluble organic carbon (WSOC) content was determined for aerosol, fog and cloud water samples and the surface tension of the WSOC was measured and compared to that of pure water. In all cases the determined values of surface tension for the WSOC were lower than that of pure water and thus the presence of surfactant materials and surface active films in aerosol, fog and cloud water droplets was inferred.

1.6.2. More recent evidence for organic coatings

Tervahattu et al., 2002 reported analysis of aerosol samples collected prior to, during and following a ‘fine particle episode’ that occurred in Helsinki, Finland in 1998. Aerosol samples were adhered to an indium substrate and analysed using scanning electron microscopy (SEM) coupled with an energy dispersive X-ray microanalyzer (EDX). Adhesion to an indium substrate meant that the aerosol particles did not have to be coated and exposed to a vacuum, which helped to preserve their natural morphology. During SEM analysis, the particles were observed to bubble and/or pulsate which led the authors to conclude that the particles were surrounded by an organic membrane. Further analysis by mass spectrometry (MS) was performed using a direct insertion probe for sample introduction and the results indicated a very high

content of fragmented aliphatic hydrocarbon chains, indicative of a lipid film. Combining the observations from SEM with the MS results, Tervahattu et al., 2002 concluded that the samples were marine aerosols that had accumulated anthropogenic emissions, lost chloride and were coated in a lipid membrane. The authors also stated that the presence of such a lipid membrane would 'likely' impact on CCN formation because CCN formation is a strong function of surface properties.

Tervahattu et al., 2005 determined the presence of fatty acids at the surface of continental and marine aerosol samples using the surface sensitive technique, Time of Flight Mass Spectrometry (TOF-SIMS). Fatty acids with carbon chain lengths peaking at C22 were found at the surface of continental aerosols whereas fatty acids with slightly smaller carbon chain lengths, peaking at C16 were found at the surface of marine aerosols. Sputtering by TOF-SIMS was used to gradually remove the surface of the aerosol samples and fatty acids were observed to sputter the most, indicating their presence at the aerosol surface. Russell et al., 2002, used X-ray spectromicroscopy to create maps of organic coatings on continental and marine aerosols collected by a research aircraft. Results showed that the surface of the aerosol particles (0.3-1 μm in diameter) was enhanced in surface active carboxylic acids R(C=O)OH groups, whereas the interior of the particles was enhanced with groups such as R(C-O)R, indicating the presence of surface active organic coatings. Peterson and Tyler, 2002 analysed a number of aerosol samples from continental and marine sources using a combination of techniques (TOF-SIMS, X-ray photoelectron spectroscopy (XPS) and SEM). Positive evidence of surface active coatings was obtained from the determination of fatty acid amides of stearic and palmitic acid on the surface of forest fire emissions. Organic haloes were also observed to overlie the aqueous phase in marine aerosol samples.

Takahama et al., 2010 analysed the distribution of chemical compounds and the shape of a large number of aerosols collected during six field campaigns from 2004-2008 using Scanning Transmission X-Ray Microscopy with Near-Edge X-Ray Absorption Fine Structure Spectroscopy. The majority of the particles were found to be chemically heterogeneous. Black carbon aerosols were covered with aqueous phase components including carboxylic acids. In some cases, the black carbon was present as an inclusion in a liquid droplet i.e. it was surrounded by a liquid film ranging from <30 nm to 600 nm in thickness. Notably, spherical inorganic core-organic shell particles were also observed. Ten particles were found to have an organic shell composed of carboxylic acids surrounding an inorganic core. The thickness of the organic coatings was determined to range from 70 nm-1.7 μm with the coating making up 30-80 % of the

particle volume. Takahama et al., 2010 also noted how such organic coatings could significantly impact on CCN ability.

Both inferred and direct evidence of the existence of organic coatings at the surface of atmospheric aerosol have been presented. The presence of an organic film on the surface of an aerosol can have a significant impact on the core aerosol properties (e.g. Gill et al., 1983, Saxena et al., 1995, Donaldson and Vaida, 2006), specifically CCN formation and the chemical reactions that an aerosol will undergo during its lifetime.

1.7. Chemical reactions

The troposphere is chemically complex and many heterogeneous reactions occur that involve aerosols (Pandis et al., 1995). The troposphere contains a large number of gaseous and aqueous phase oxidants, the most common gaseous phase oxidants are ozone (O_3), the hydroxyl radical $^{\cdot}OH$, and hydrogen peroxide H_2O_2 (Thompson, 1992). Aqueous phase reactions can also occur in cloud water and the most important aqueous phase oxidants are; the hydroxyl radical ($^{\cdot}OH$), the nitrate radical ($NO_3^{\cdot}$) and the sulfate radical ($SO_4^{\cdot-}$) (Herrman et al., 2003, 2010). Aqueous phase oxidants are formed from photochemical processes or absorption from the gaseous phase (Finlayson-Pitts and Pitts Jr, 1997).

The aqueous phase hydroxyl radical is the most predominant species and can be formed by several mechanisms (Herrman et al., 2010). Gas-phase partitioning of $^{\cdot}OH$ to an aqueous droplet and gas to drop partitioning of O_3 followed by subsequent reaction with O_2^- both result in the formation of the aqueous hydroxyl radical (Arakaki and Faust, 1998, Seinfeld and Pandis, 1998). The aqueous phase hydroxyl radical can also be formed from the photolysis of H_2O_2, NO_3^-, NO_2^- and $Fe(OH)^{2+}$ which are commonly found in water droplets (Arakaki and Faust, 1998. Faust and Allen, 1993 and references therein). Another source of the aqueous phase hydroxyl radical is from Fenton's reagent, i.e. combination of an iron salt and H_2O_2 (Walling, 1975):

$$Fe^{2+} + H_2O_2 \longrightarrow Fe^{3+} + OH + OH^- \qquad 4$$

The aqueous phase $NO_3^{\cdot}$ radical is formed by gas to droplet transfer from electron transfer reactions between nitrate anions and other radicals such as $SO_x^{\cdot-}$ (Herrman et al., 2010). The aqueous phase sulfate radical, $SO_4^{\cdot-}$ has been proposed to form from diffusion of gas phase $NO_3^{\cdot}$ into cloud droplets (Chameides, 1986) and from the oxidation chain of S(IV) in the aqueous phase (Herrman et al., 2010, Hayon et al., 1972).

Given that a typical aerosol lifetime is in the order of days it is likely that an aerosol will undergo oxidation within its lifetime. The presence of both gaseous and aqueous phase radicals means that oxidation of an organic coating present on the surface of an aerosol could occur either from the gaseous or bulk aerosol phase depending on the aerosol constituents. Karagulian et al., 2008 demonstrated oxidation from the 'bottom up' by photolysis of a mixture of NaCl and $NaNO_2$ particles coated with the lipid 1-oleoyl-2-palmitoyl-sn-glycero-3-phosphocholine (OPPC). Photolysis of the particles generated hydroxyl radicals at the interface which resulted in the oxidation of the OPPC coating.

As mentioned previously, the presence of an organic coating on an aerosol can affect a number of aerosol properties (Donaldson and Vaida, 2006), such as CCN formation and gas phase diffusion into the bulk. Oxidation of a coated aerosol will result in a change in aerosol properties and ultimately aerosol influence on the Earth's climate. It is therefore important to study coated aerosols and understand how common tropospheric reactions such as oxidation can change aerosol properties. This thesis covers the formation and characterisation of core-shell aerosol, including gaseous and aqueous phase oxidation studies of relevant aerosol coating material.

1.8. Techniques to study coated aerosols and their oxidation reactions

In order to study aerosol properties and specifically aerosol morphology, a non-contact technique is required that simulates the natural environment in which aerosols are found in the atmosphere (dispersed in a gaseous phase) and does not change the aerosol morphology. Aerosol optical tweezers or optical trapping is a well established technique that allows individual aerosol particles or droplets to be levitated and manipulated using a laser beam in a gaseous environment, thereby reproducing the non-contact environment that atmospheric aerosols exist in and preserving the morphology of the aerosol.

A surface technique is required to study oxidation reactions of thin films at the surface of aerosols, and the techniques of neutron and X-ray reflectivity provide complementary methods to gain insight into thin film behaviour during oxidation at the air-water interface.

Thus microscopic laboratory generated aerosols were studied using optical trapping combined with white light Mie scattering and the oxidation of monolayer films at the air-water interface were studied using neutron and X-ray reflectivity. The following section describes the relevant background and theory necessary to understand the techniques

and data interpretation described in the subsequent papers and also includes an evaluation of the experimental methods used.

1.9. Introduction references

Alexis, N., Barnes, C., Bernstein, I. L., Nel, A., Peden, D., Diaz-Sanchez, D., Tarlo, S. M. and Williams, P. B.: Health effects of air pollution, J. Allergy Clin. Immunol., 114(5), 1116–23, 2004.

Andreae, M. and Crutzen, P. J.: Atmospheric Aerosols : Biogeochemical Sources and in Atmospheric Chemistry Role, Science, 276 (5315), 1052–1058, 1997.

Arakaki, T. and Faust, B. C.: Sources, sinks, and mechanisms of hydroxyl radical (˙OH) photoproduction and consumption in authentic acidic continental cloud waters from Whiteface Mountain, New York : The role of the Fe(r) (r=II, III) photochemical cycle, J. Geophys. Res., 103(D3), 3487–3504, 1998.

Barnes, G. T. and Gentle, I.R.: Interfacial Science: An Introduction, Oxford University Press, 2005.

Blanchard, D. C.: Sea-to-Air Transport of Surface Active Material, Science, 146(13), 396–397, 1964.

Blanchard, D. C. and Woodcock, A.: Bubble formation and modification in the sea and its meteorological significance, Tellus, 9(2), 1957.

Boucher, O., D. Randall, P. Artaxo, C. Bretherton, G. Feingold, P. Forster, V.-M. Kerminen, Y. Kondo, H. Liao, U. Lohmann, P. Rasch, S.K. Satheesh, S. Sherwood, B. Stevens and X.Y. Zhang, 2013: Clouds and Aerosols. In: Climate Change 2013: The Physical Science Basis. Contribution of Working Group I to the Fifth Assessment Report of the Intergovernmental Panel on Climate Change [Stocker, T.F., D. Qin, G.-K. Plattner, M. Tignor, S.K. Allen, J. Boschung, A. Nauels, Y. Xia, V. Bex and P.M. Midgley (eds.)]. Cambridge University Press, Cambridge, United Kingdom and New York, NY, USA.

Capel, P. D., Gunde, R., Ziircher, F. and Gigert, W.: Carbon Speciation and Surface Tension of Fog, Environ. Sci. Technol., 24(5), 722–727, 1990.

Chameides, W. L.: Possible role of NO_3 in the nighttime chemistry of a cloud, J. Geophys. Res., 91, D5, 5331-5337, 1986.

Chang, D., Song, Y. and Liu, B.: Visibility trends in six megacities in China 1973-2007, Atmos. Res., 94(2), 161–167, 2009.

Dickerson, R. R., Kondragunta, S., Stenchikov, G., Civerolo, K. L., Doddridge, B. G. and Holben, B. N.: The Impact of Aerosols on Solar Ultraviolet Radiation and Photochemical Smog, Science, 278(5339), 827–830, 1997.

Donaldson, D. J. and Vaida, V.: The influence of organic films at the air-aqueous boundary on atmospheric processes., Chem. Rev., 106(4), 1445–61, 2006.

Donaldson, D. J. and George, C.: Sea-Surface Chemistry and Its Impact on the Marine Boundary Layer, Environ. Sci. Technol., 46(19), 10385–10389, 2012.

Facchini, M. C., Mircea, M., Fuzzi, S. and Charlson, R. J.: Cloud albedo enhancement by surface-active organic solutes in growing droplets, Nature, 401(September), 257–259, 1999.

Facchini, M. C., Decesari, S., Mircea, M., Fuzzi, S. and Loglio, G.: Surface tension of atmospheric wet aerosol and cloud / fog droplets in relation to their organic carbon content and chemical composition, Atmos. Environ., 34, 4853–4857, 2000.

Falkovich, A. H.: Adsorption of organic compounds pertinent to urban environments onto mineral dust particles, J. Geophys. Res., 109(D2), D02208, 2004.

Faust, B. C. and Allen, J. M.: Aqueous-phase photochemical formation of hydroxyl radical in authentic cloudwaters and fogwaters, Environ. Sci. Technol., 27(6), 1221–1224, 1993.

Finlayson-Pitts, B. J. and Jr, J. N. P.: Tropospheric Air Pollution: Ozone, Airborne Toxics, Polycyclic Aromatic Hydrocarbons, and Particles, Science, 276(5315), 1045–1052, 1997.

Finlayson-Pitts, B. J.: Reactions at surfaces in the atmosphere: integration of experiments and theory as necessary (but not necessarily sufficient) for predicting the physical chemistry of aerosols, Phys. Chem. Chem. Phys., 11, 7760–7779, 2009.

Finlayson-Pitts, B. J. and Pitts, Jr. J.N.: Chemistry of the Upper and Lower Atmosphere: Theory, Experiments and Applications, Academic Press, 2000.

Fitzgerald, J. W.: Marine Aerosols: A Review, Atmos. Environ., 25(3/4), 533–545, 1991.

Fuzzi, S., Andreae, M. O., Huebert, B. J., Kulmala, M., Bond, T. C., Boy, M., Doherty, S. J., Guenther, A. and Nazionale, C.: Critical assessment of the current state of scientific knowledge, terminology, and research needs concerning the role of organic aerosols in the atmosphere, climate, and global change, Atmos. Chem. Phys., 6, 2017–2038, 2006.

Gill, P. S., Gradel, T. E. and Weschler, C. J.: Organic Films on Atmospheric Aerosol Particles, Fog Droplets, Cloud Droplets, Raindrops and Snowflakes, Rev. Geophys. Sp. Phys., 21(4), 903–920, 1983.

Hayon, E., Treinin, A. and Wilf, J.: Electronic spectra, photochemistry, and autoxidation mechanism of the sulfite-bisulfite-pyrosulfite systems. SO_2^-, SO_3^-, SO_4^-, and SO_5^- radicals, J. Am. Chem. Soc., 94(1), 47–57, 1972.

Herrmann, H.: Kinetics of aqueous phase reactions relevant for atmospheric chemistry, Chem. Rev., 103(12), 4691–716, 2003.

Herrmann, H., Hoffmann, D., Schaefer, T. and Tilgner, A.: Tropospheric aqueous-phase free-radical chemistry: Radical sources, spectra, reaction kinetics and prediction tools, ChemPhysChem, 11(18), 3796–3822, 2010.

Hobbs, P.V.: Introduction to Atmospheric Chemistry, Cambridge University Press, 2000.

Husar, R. and Shu, W.: Thermal analyses of the Los Angeles smog aerosol, J. Appl. Meteorol., 14, 1558–1565, 1975.

IPCC, 2013: Summary for Policymakers. In: Climate Change 2013: The Physical Science Basis. Contribution of Working Group I to the Fifth Assessment Report of the Intergovernmental Panel on Climate Change [Stocker, T.F., D. Qin, G.-K. Plattner, M. Tignor, S.K. Allen, J. Boschung, A. Nauels, Y. Xia, V. Bex and P.M. Midgley (eds.)]. Cambridge University Press, Cambridge, United Kingdom and New York, NY, USA.

Jacob, J.: Chemistry of OH in Remote Clouds and Its Role in the Production of Formic Acid and Peroxymonosulfate, J. Geophys. Res., 91(D9), 9807–9826, 1986.

Karagulian, F., Dilbeck, C. W. and Finlayson-pitts, B. J.: Unusual Oxidation of Organics at Interfaces from the Bottom Up and Atmospheric Implications, J. Am. Chem. Soc., 130(34), 11272–11273, 2008.

Lohmann, U. and Feichter, J.: Global indirect aerosol effects : a review, Atmos. Chem. Phys., 5, 715–737, 2005.

MacIntyre, F.: Flow patterns in breaking bubbles, J. Geophys. Res., 77(27), 5211–5227, 1972.

MacIntyre, F.: The Top Millimeter of the Ocean, Scientific American, 230(5), 62-77, 1974.

Malm, W. C.: Introduction to Visibility, 1–70, 1999.

Marty, J. C., Saliot, A., Buat-Ménard, P., Chesselet, R. and Hunter, K. A.: Relationship between the lipid compositions of marine aerosols, the sea surface microlayer, and subsurface water, J. Geophys. Res., 84(C9), 5707, 1979.

Mason, B. J.: Bursting of Air Bubbles at the Surface of Sea Water, Nature, 174, 470–471, 1954.

Middlebrook, A. M., Murphy, D. M. and Thomson, D. S.: Observations of organic material in individual marine particles at Cape Grim during the First Aerosol Characterization Experiment (ACE 1), 103(97), 475–483, 1998.

O'Dowd, C. D. and de Leeuw, G.: Marine aerosol production: a review of the current knowledge, Philos. Trans. A. Math. Phys. Eng. Sci., 365(1856), 1753–74, 2007.

Pandis, S. N., Wexler, A. S. and Seinfeld, J. H.: Dynamics of Tropospheric Aerosols, J. Phys. Chem., 99(24), 9646–9659, 1995.

Peterson, R. E. and Tyler, B. J.: Analysis of organic and inorganic species on the surface of atmospheric aerosol using time-of-flight secondary ion mass spectrometry (TOF-SIMS), Atmos. Environ., 36, 6041–6049, 2002.

Pöschl, U.: Atmospheric aerosols: composition, transformation, climate and health effects, Angew. Chem. Int. Ed. Engl., 44(46), 7520–40, 2005.

Posfai, M., Huifang, X., Anderson, J. R. and Buseck, P. R.: Wet and dry sizes of atmospheric aerosol particles- An AFM-TEM study, Geophys. Res. Lett., 25(11), 1907–1910, 1998.

Ramanathan, V., Crutzen, P. J., Kiehl, J. T. and Rosenfeld, D.: Aerosols, Climate, and the Hydrological Cycle, Science, 294(December), 2119–2125, 2001.

Rudich, Y.: Laboratory Perspectives on the Chemical Transformations of Organic Matter, Chem. Rev., 103(12), 5097–5124, 2003.

Russell, L. M., Maria, S. F. and Myneni, S. C. B.: Mapping organic coatings on atmospheric particles, Geophys. Res. Lett., 29(16), 1–4, 2002.

Saxena, P., Hildemann, L., McMurry, P. H. and Seinfeld, J. H.: Organics alter hygroscopic behavior of atmospheric particles, J. Geophys. Res., 100(95), 18755–18770, 1995.

Seinfeld, J. H. Pandis, S.N.: Atmospheric Chemistry and Physics: From Air Pollution to Climate Change, Wiley, 1998.

Takahama, S., Liu, S. and Russell, L. M.: Coatings and clusters of carboxylic acids in carbon-containing atmospheric particles from spectromicroscopy and their implications for cloud-nucleating and optical properties, J. Geophys. Res. Atmos., 115(D01202), 1–21, 2010.

Thompson, A. M.: The oxidizing capacity of the earth's atmosphere: probable past and future changes, Science, 256, 1157–1165, 1992.

Tervahattu, H., Hartonen, K., Kerminen, V., Kupiainen, K., Koskentalo, T., Tuck, A. F. and Vaida, V.: New evidence of an organic layer on marine aerosols, J. Geophys. Res., 107(D7), AAC 1-1-AAC 1-8, 2002.

Tervahattu, H., Juhanoja, J., Vaida, V., Tuck, A. F., Niemi, J. V., Kupiainen, K., Kulmala, M. and Vehkamaki, H.: Fatty acids on continental sulfate aerosol particles, J. Geophys. Res., 110(D6), D06207, 2005.

Usher, C. R., Michel, A. E. and Grassian, V. H.: Reactions on Mineral Dust, Chem. Rev., 103(12), 4883–4939, 2003.

Wallace, J.M. and Hobbs, P.V.: Atmospheric Science An Introductory Survey, Academic Press, Burlington, MA, USA, 2006.

Walling, C.: Fenton's reagent revisited, Acc. Chem. Res., 8(4), 125–131, 1975.

Whitby K.T. and Sverdrup G. M. California Aerosols: Their Physics and Chemical Characteristics. Adv. Environ.Sci Tech. 8, 477-525, 1980.

Woodcock, A., Kientzler, C., Arons, A. and Blanchard, D. C.: Giant Condensation Nuclei from Bursting Bubbles, Nature, 172, 1144–1145, 1953.

Zhang, R., Khalizov, A. F., Pagels, J., Zhang, D., Xue, H. and McMurry, P. H.: Variability in morphology, hygroscopicity, and optical properties of soot aerosols during atmospheric processing., Proc. Natl. Acad. Sci. U. S. A., 105(30), 10291–6, 2008.

2. Theory and evaluation of methods

2.1. Introduction to optical tweezers

In 1970, Ashkin published a paper detailing the levitation and acceleration of micron sized particles by a laser beam (Ashkin, 1970). The radiation pressure associated with light from a continuous wave Argon laser at 514.5 nm was observed to accelerate transparent latex spheres in water. A dual beam trap was also described in the same paper; two Gaussian laser beams were pointed directly at each other and a particle was trapped symmetrically between the two beams. This was the first demonstration of a counter-propagating optical trap. Ashkin et al. in 1986 also demonstrated the trapping of particles in the size range 10 μm to 25 nm in water using a single beam gradient trap. Photons of light carry momentum and when light is refracted through an object, a change in the momentum of the photons occurs. The change in momentum of the photons is equal to a force and thus a reaction force also occurs, which acts on the trapped object that the light is refracted through.

The forces involved in trapping a particle can be considered differently depending on the size of the trapped object compared to the wavelength of the trapping laser. When the object is much larger than the trapping laser wavelength, a ray optics approach can be taken, whereas when the object is much smaller than the wavelength of light, Rayleigh scattering is valid and the trapping forces can be considered in terms of the electric field close to the trapped object. However, when the size of the object is similar to the wavelength of the trapping laser, Mie scattering is valid for spherical objects (Bowman and Padgett, 2013, Molloy and Padgett, 2002, Neuman and Block, 2004).

Two main types of optical trap will be described, a single beam gradient trap and a counter-propagating trap. The forces involved in a single beam gradient trap are the scattering force and the gradient force. The scattering force is associated with the scattering of light and is proportional to the light intensity and acts in the propagation direction of the laser. The gradient force arises from the gradient in light intensity associated with the beam of light. Figure 1 aids in understanding how the gradient force works. Figure 1 is adapted from Neuman and Block, 2004 and part a) shows the interaction of two light rays that increase in intensity from left to right and are incident on a sphere. The light rays are refracted through the sphere causing a change in momentum of the incident photons which results in a force on the sphere which is represented by the arrows originating from the centre of the sphere and pointing downwards. The thickness of the arrows indicates the strength of the forces, and the resultant force in this diagram acts to push the particle downwards and to the right.

Part b) illustrates the axial trapping force and shows two rays originating from a focussed light source incident on a transparent sphere and their refraction through the sphere. Again, the change in momentum of light causes a reaction force which is depicted by the two arrows originating from the centre of the sphere and pointing upwards. For stable trapping to occur, the gradient force must exceed the scattering force and this is achieved by focussing the incident laser light and slightly overfilling the back aperture of a high Numerical Aperture (NA) objective lens in the trapping set up.

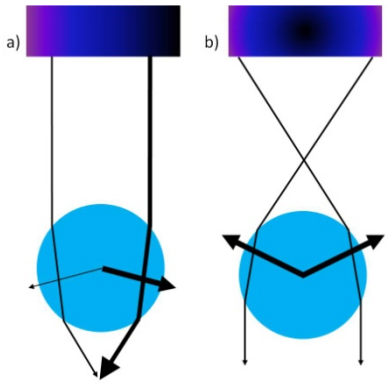

Figure 1. Depiction of the gradient force in a single-beam gradient trap. Diagram a) represents the lateral part of the gradient force and diagram b) represents the axial part of the gradient force. Light rays originate from a source and are diffracted through a transparent trapped sphere which results in a reaction force on the trapped bead as depicted by force arrows originating from the centre of the bead.

The review papers by Molloy and Padgett, 2002, Neuman and Block, 2004 and McGloin, 2006 each describe general optical trapping, trapping forces and the wide range of subject areas that employ optical trapping and potential future use of the technique. The technique is widely used in the biological sciences (e.g. Svoboda and Block, 1994, Neuman et al., 1999) as well as in the study of aerosol science and atmospheric chemistry (e.g. King et al., 2004). A large amount of research is invested in technique development and capabilities, some examples of research areas are measurement and calibration of trapping forces (e.g. Neuman and Block, 2004), orbital angular momentum (Friese et al., 1998, Molloy and Padgett, 2002) and use in microfluidic devices (McGloin, 2006 and Leach et al., 2006).

A counter-propagating optical trap is used for all trapping experiments conducted in this thesis in which two laser beams are pointed directly at each other. A counter-propagating trap was selected because it allows the facile and reproducible trapping of solid particles in air (studied in this thesis) compared to a single beam gradient trap. The scattering force from each beam balances out to stably trap an aerosol in between the focus of the two laser beams. The Gaussian profile of the beams acts to keep the

aerosol on axis. Figure 2 represents a cartoon depiction of a counter-propagating optical trap.

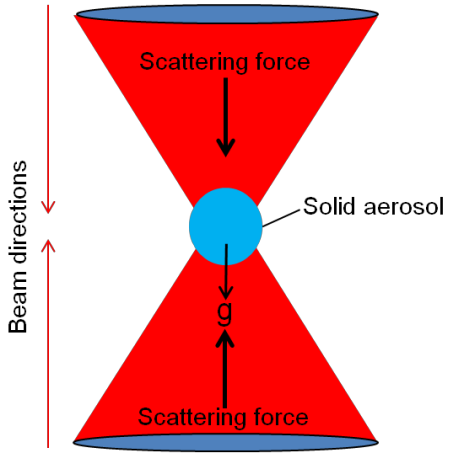

Figure 2. Counter-propagating optical trap, highlighting the two opposed scattering forces to trap a solid aerosol in between the focal point of two Gaussian laser beams.

The experiments conducted in this thesis combined white light Mie scattering with a counter-propagating optical trap and used Mie theory to determine the size and wavelength dependent refractive index of the trapped aerosol.

2.2. Experimental trapping procedure

Two main optical trapping studies were performed in this thesis, one involving the trapping of solid polystyrene beads in air (Jones et al., 2013) and the other involving the trapping of solid silica beads in air and coating them in a thin film of oleic acid as a proxy for mineral dust aerosol with an organic coating (Jones et al., 2015). A brief description of the trapping procedure will be given here to aid understanding. The detailed experimental methodology for the trapping and characterisation of polystyrene beads is described in paper 1 and the detailed methodology for trapping silica beads coated in oleic acid is described in paper 2.

Polystyrene beads were selected as a proxy for solid aerosol and were atomised and passed through a diffusion dryer into an experimental cell containing the two counter-propagating laser beams. The polystyrene beads fell under gravity and their motion was monitored on a side image. The position of the cell was subsequently adjusted using micrometer positioning stages to align a falling bead with the laser focal point in order to optically trap it. Once stably trapped, the bead was illuminated with a white LED and the backscattered light was collected and directed into a spectrograph to produce a spectrum of the backscattered light as a function of wavelength.

In order to trap silica beads coated in oleic acid, core silica beads were initially trapped in the same way as the polystyrene beads described previously. Nitrogen carrier gas was then passed over a hot oleic acid reservoir to carry hot oleic acid vapour to the experimental cell containing the trapped silica bead. The experimental cell was at room temperature and pressure and thus a supersaturation of oleic acid was created and the oleic acid consequently condensed on to the surface of the trapped silica bead to produce a thin film. Again, the backscattered spectrum was collected with time from the point when the silica bead was initially trapped and throughout the coating process. A diagram of the experimental set-up used to trap polystyrene beads and silica beads coated in a film of oleic acid can be seen in Figure 3. Mie theory and core-shell Mie theory were used to characterise the trapped aerosol.

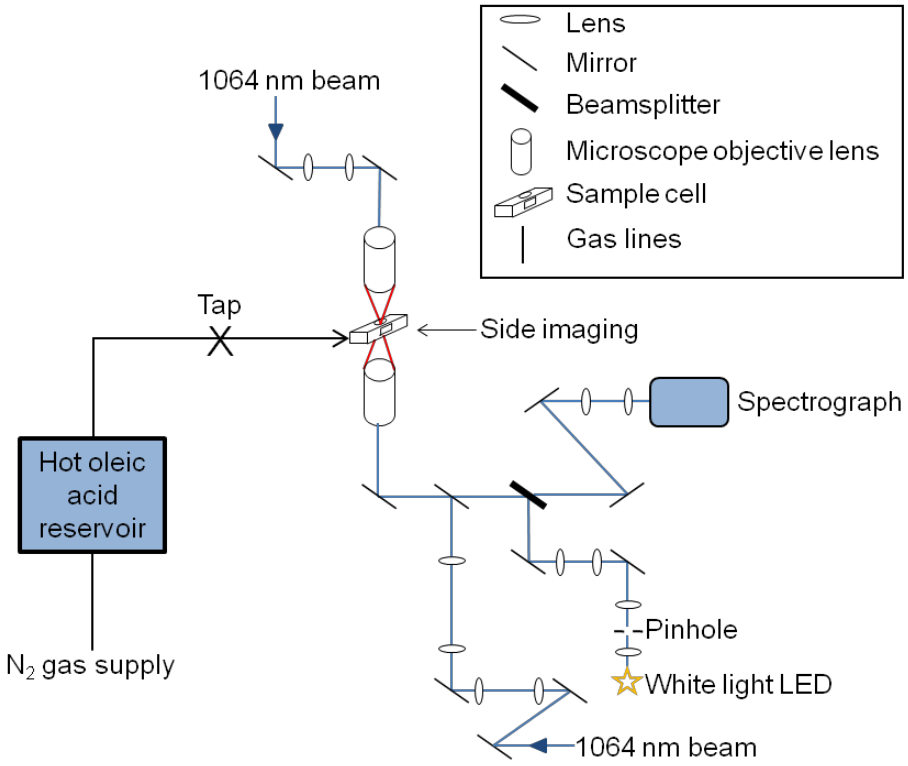

Figure 3. Counter-propagating optical set up used to trap solid polystyrene beads and silica beads coated in a thin film of oleic acid.

2.3. Mie theory

Mie theory was used to determine the size and wavelength dependent refractive index of solid polystyrene beads, liquid oleic acid droplets and solid silica beads. Core-shell Mie theory was used to determine the thickness of an oleic acid coating on an optically trapped silica bead coated in oleic acid. In all cases, the trapped aerosol must be spherical to apply Mie theory accurately and the shell of a core-shell aerosol must be uniform and symmetric to apply core-shell Mie theory. In all optical trapping experiments, the trapped aerosol was illuminated with white light from an LED and the resultant spectrum obtained.

Mie theory is used to describe the scattering and absorption of light by spherical particles whose size is comparable to the wavelength of light. It is commonly used to describe the scattering from a spherical dielectric homogeneous particle illuminated by a plane wave (Wriedt, 2012). A solution to Maxwell's equations is used to compute the incident, internal and scattered fields associated with a small spherical particle.

There are a number of outputs that can be calculated, specifically the extinction and scattering efficiencies of a homogeneous sphere can be written as (Petty, 2004):

$$\mathrm{Q_{ext}} = \frac{2}{x^2}\sum_{k=1}^{\infty}(2\mathrm{n}+1)\Re(\mathrm{a_n}+\mathrm{b_n}) \quad (1)$$

$$\mathrm{Q_{sca}} = \frac{2}{x^2}\sum_{k=1}^{\infty}(2\mathrm{n}+1)(|\mathrm{a_n}|^2+|\mathrm{b_n}|^2) \quad (2)$$

Where x is the size parameter and is defined as $x = \frac{2\pi \mathrm{r}}{\lambda}$, where r is the radius of the sphere and λ is the wavelength. The real part of a_n and b_n is denoted by $\Re$ where a_n and b_n are the Mie scattering coefficients and can also be referred to as partial wave scattering amplitudes. The Mie scattering coefficients are functions of both the size parameter x and the refractive index of the sphere, and by imposing boundary conditions between the sphere and the surrounding medium a_n and b_n can be written as (Bohren and Huffman, 1983):

$$a_n = \frac{m\psi_n(mx)\psi_n'(x)-\psi_n(x)\psi_n'(mx)}{m\psi_n(mx)\xi_n'(x)-\xi_n(x)\psi_n'(mx)} \quad (3)$$

$$b_n = \frac{\psi_n(mx)\psi_n'(x)-m\psi_n(x)\psi_n'(mx)}{\psi_n(mx)\xi_n'(x)-m\xi_n(x)\psi_n'(mx)} \quad (4)$$

where x is the size parameter as previously defined and m is the relative refractive index of the sphere to the surrounding medium. ψ_n and ξ_n are Riccati-Bessel functions defined by:

$$\psi_n(x) = x j_n(x) \quad (5)$$

$$\xi_n(x) = x h_n^{(1)}(x) \quad (6)$$

Where $j_n(x)$ is a spherical Bessel function and $h_n^{(1)}(x)$ is a spherical Hankel function (Bohren and Huffman, 1983).

A typical plot of the extinction efficiency for a water droplet in air plotted as function of size parameter is shown in Figure 4. The figure shows a clear ripple structure in the extinction efficiency which occurs at specific values of the size parameter in the real part of the Mie scattering coefficients, a_n and b_n (Chýlek, 1976).

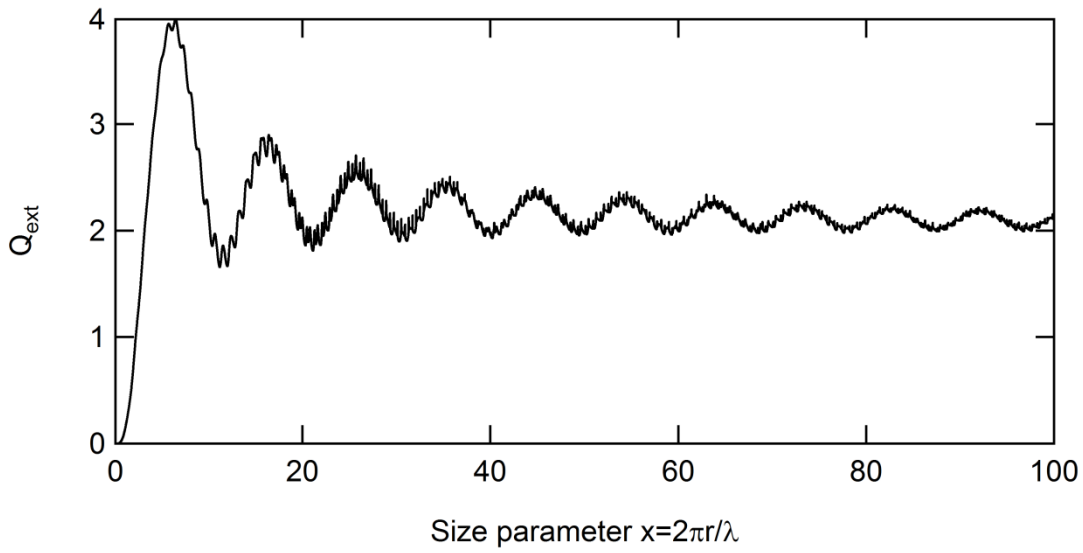

Figure 4. The extinction efficiency plotted as function of size parameter for a non-absorbing sphere in air with a real refractive index of 1.33.

The ripple structure in Figure 4 is more commonly referred to as Mie resonances, morphology dependent resonances (MDR) or whispering gallery modes (WGM) (Hill and Benner, 1988). When an optically trapped spherical aerosol is illuminated by a plane wave, light of a whole number of wavelengths can couple into the optical cavity and undergo total internal reflection around the circumference of the trapped aerosol to form a standing wave. The formation of such a standing wave is known as a MDR or a WGM (Hill and Benner, 1988). A cartoon depiction of an MDR is shown in figure 5.

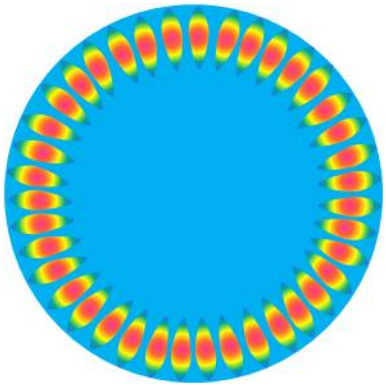

Figure 5. Cartoon representation depicting the internal intensity distribution of an MDR in an optically trapped droplet (shown in blue). The intensity increases in colour from blue < green < yellow < red, with red being the most intense.

MDRs can be described in terms of their mode number-n, the total number of wavelengths that form the standing wave around the aerosol circumference (Symes et al., 2004) and their mode order-l, the number of radial maxima (from the surface of the sphere inwards) in the distribution of the electromagnetic field (Reid et al., 2006).

For the work presented in this thesis, the trapped aerosol was illuminated with light from a white LED and the backscattered light was collected over a solid angle as a function of wavelength. The resultant spectrum was plotted as a function of intensity versus wavelength and will be referred to as a Mie spectrum or Mie resonance spectrum from here on. Figure 6 shows an example calculated Mie spectrum for a water droplet of radius 2 μm in air.

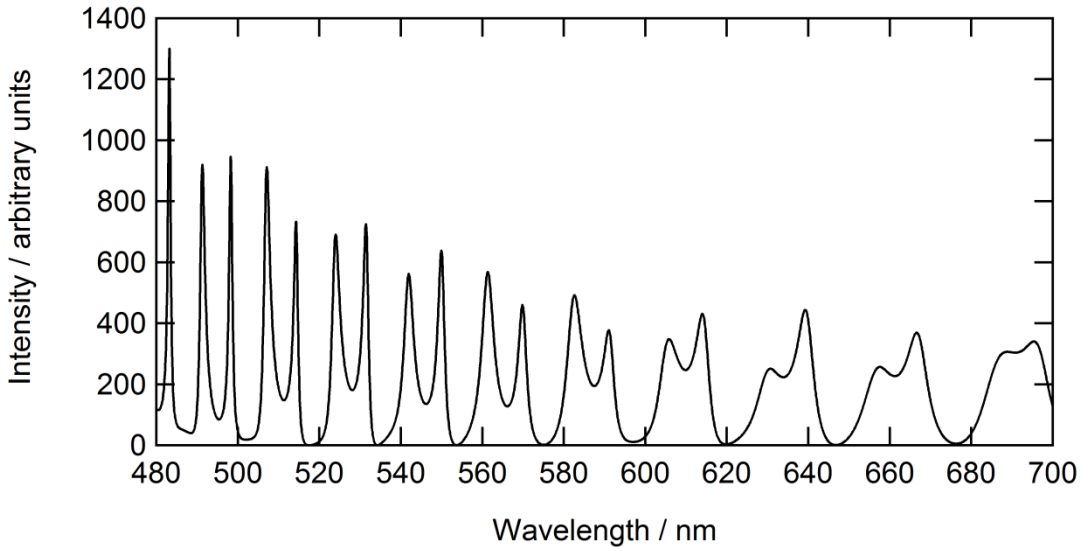

Figure 6. Calculated Mie spectrum for a 2 μm radius droplet of water in air, showing clear resonances at specific wavelengths.

The collection of light as function of wavelength enables accurate determination of the wavelength dependent refractive index of the trapped aerosol as well as facile

monitoring of the physical and chemical changes in the trapped aerosol during the experiment. Thus, when an optically trapped aerosol is illuminated by white light from an LED, the resultant wavelength resolved backscattered spectrum consists of a series of MDRs like those in Figure 6. The wavelengths at which the resonances occur are dependent on the size, shape and refractive index of the trapped aerosol. Larger aerosol will have a higher number of resonances in their spectrum and contain a finer structure compared to smaller aerosols owing to the difference in the whole number of wavelengths that can form a standing wave around the circumference of a larger aerosol compared to a smaller aerosol. Backscattered light can also be collected as a function of angle; however such a method is not optimised to monitor the physical or chemical changes in an optically trapped aerosol because of the time taken to obtain a spectrum over the desired angular range.

2.3.1. Optical characterisation of a homogeneous aerosol

Mie scattering was computed for spherical aerosols of a given size and refractive index dispersion (Bohren and Huffman, 1983) and the positions of the calculated resonances were compared to the position of the experimental resonances obtained from the Mie spectrum of an optically trapped aerosol. The real part of the wavelength dependent refractive index was defined by the Cauchy equation (Jenkins, 1976),

$$n = A + \frac{B}{\lambda^2} + \frac{C}{\lambda^4} \qquad 7$$

Where n is the wavelength dependent refractive index, A, B and C are empirical coefficients and λ is the wavelength. In order to fit the calculated Mie resonances to the experimental Mie resonances, the radius of the aerosol and the empirical coefficients, A, B and C of the Cauchy equation were iterated until the position and shape of the calculated Mie resonances matched the experimental Mie resonances and thus the unique size and wavelength dependent refractive index of the individually optically trapped aerosol was determined.

2.3.2. Optical characterisation of a core-shell aerosol

The Mie scattering coefficients for a coated sphere, A_n and B_n have a different functional form to those of a homogeneous sphere as stated in equations 3 and 4. The scattering coefficients for a coated sphere are (Bohren and Huffman, 1983):

$$A_n = \frac{m_2\psi_n(m_2x)\psi_n^{'}(m_1x) - m_1\psi_n^{'}(m_2x)\psi_n(m_1x)}{m_2\chi_n(m_2x)\psi_n^{'}(m_1x) - m_1\chi_n^{'}(m_2x)\psi_n(m_1x)} \qquad 8$$

$$B_n = \frac{m_2\psi_n(m_1x)\psi_n'(m_2x) - m_1\psi_n(m_2x)\psi_n'(m_1x)}{m_2\chi_n'(m_2x)\psi_n(m_1x) - m_1\psi_n'(m_1x)\chi_n(m_2x)} \quad 9$$

Where m_1 and m_2 are the refractive indices of the core and coating material relative to the surrounding medium. ψ_n and χ_n are Riccati-Bessel functions and χ_n is defined by (Bohren and Huffman, 1983):

$$\chi_n(x) = -xy_n(x) \quad 10$$

where $y_n(x)$ is a spherical Bessel function.

In order to fit the calculated core-shell Mie resonances to the experimentally obtained core-shell Mie resonances, the wavelength dependent refractive index of the coating material was initially characterised so that it could be fixed in the core-shell Mie calculations. A droplet of coating material was optically trapped and its size and refractive index as a function of wavelength determined as described in the previous section for homogenous aerosols. The next step was to optically trap the core aerosol and determine its size and wavelength dependent refractive index using Mie theory again as described in the previous section. The final step was to coat the core aerosol with a thin film and obtain an experimental core-shell Mie resonance spectrum. Core-shell Mie spectra were calculated (Aden and Kerker, 1951 and Toon and Ackerman, 1981) for films of differing thicknesses until the position and shape of the calculated core-shell Mie resonances matched the experimentally obtained core-shell Mie resonances. The only variable to be iterated in the core-shell fitting process was the thickness of the film; the radius and refractive index of the core aerosol as well as the refractive index of the coating were fixed.

2.4. Evaluation of optical trapping and white light Mie scattering

2.4.1. Particle shape and absorption

Mie theory is strictly only applicable to spherical particles. Spherical liquid droplets and solid spheres are used as proxies for atmospheric aerosol, however not all atmospheric aerosol is perfectly spherical i.e. some aerosols will be agglomerations of smaller solid particulates such as black carbon or consist of liquid droplets with solid inclusions (Takahama et al., 2010). The characterisation of both spherical and non-spherical aerosols would be the ideal situation but standard Mie theory cannot be applied to calculate the scattering from non-spherical particles and such calculations are computationally intense (Mishchenko et al., 2000).

A more realistic experiment would be to optically trap and characterise real samples of atmospheric aerosol. However, it is difficult to preserve the natural geometry of atmospheric aerosol samples due to the contact techniques involved in sampling e.g. contact with filters. Optical trapping of non-spherical aerosol may cause the trapped aerosol to spin in the trap which would affect the interaction of light with the trapped object thus changing the backscattered light. Real atmospheric aerosol is also likely to be chemically complex and thus its refractive index would also be difficult to accurately model. Therefore studies on spherical aerosol proxies consisting of one or two model chemicals are necessary to provide insight into the effect of chemical composition on the optical properties of atmospheric aerosol.

A non-contact method of sampling atmospheric aerosols would be required to study the natural geometry of coated atmospheric aerosols but is currently not possible. Therefore proxies for coated aerosol are studied as described in the paper 2. Nitrogen carrier gas is passed over a reservoir of hot oleic acid to carry hot oleic acid vapour into the experimental cell containing an optically trapped silica bead in order to coat its surface. Depending on the coating material and temperature of the oleic acid reservoir, it is possible that the refractive index of the coating could be slightly changed from the bulk material. The coating reservoir was regularly emptied, cleaned and re-filled to avoid any degradation of the coating material due to heating. It was also possible that the coatings formed could be slightly uneven in thickness, have a high level of roughness or contain excess coating droplets on top of the coated surface of the aerosol. Core-shell Mie theory cannot be used to characterise such uneven coatings because the ability of light to couple into the droplet will be impaired causing either a reduction in intensity of the core-shell Mie resonances or their complete disappearance (Reid et al., 2011). Therefore if there was a non-contact method of sampling atmospheric aerosol, core-shell Mie theory could only be used to characterise aerosols coated in a spherical uniform coating which may not always be the case in the atmosphere.

Another limitation of using a counter-propagating optical trap with Gaussian laser beams to study atmospheric aerosol proxies is that the trapped aerosol does not absorb at the same wavelength as the trapping laser. Absorbing aerosol undergoes heating which results in unstable trapping owing to the larger photophoretic force compared to radiation pressure (Pan et al., 2012). Heating can also cause potential damage to the aerosol and will affect physical properties such as the refractive index of the aerosol, therefore making determination of the refractive index unrealistic. Aerosol particles such as black carbon are absorbing and currently cannot be characterised

using conventional optical trapping configurations such as those described in this thesis.

2.4.2. Particle size

The experimentally obtained spectrum must contain enough (typically, at least four for the work conducted in this thesis) resonances to facilitate comparison to the calculated Mie spectrum. The larger the aerosol or larger the refractive index of the material, the more accurate the comparison to calculated resonances will be, owing to a larger number of Mie resonances and increased fine structure (sharp peaks). The Mie spectrum of the polystyrene beads (manufacturer size, 1.25 μm radius) in paper 1 contained approximately fifteen resonances which facilitated accurate determination of the particle size and refractive index. Whereas the Mie spectrum of the silica beads (manufacturer size, 1.035 μm radius) in paper 2 consisted of approximately four broad resonances. Larger silica beads would have given more resonances in the Mie spectrum but would have been less atmospherically relevant. The size specification of the atomiser used to deliver solid beads to the experimental trapping cell also had to be taken into account, which was stated as <2 μm for polystyrene latex aerosol. Atomisers capable of delivering larger beads are commercially available and the resultant spectrum would contain an increased number of Mie resonances and facilitate modelling but larger beads would be less atmospherically relevant as outlined in the discussion. A bead with a larger refractive index would have also provided more structure in the Mie resonance spectrum, but silica was selected as a proxy for mineral dust aerosol. There is therefore a balance to be considered between the atmospheric relevance of the sample and the ease of analysis.

2.4.3. Collection of spectra

The backscattered light from the optically trapped aerosol is collected over a solid angle to give an output of intensity versus wavelength as shown in Figure 6. The wavelength range is determined by the spectrometer grating and the optics used to direct the white light to the trapped aerosol and the optics used to collect the backscattered light and direct it to the spectrometer. The quantum efficiency of the CCD detector is 92-95 % over the wavelength range used in papers 1 and 2 and determines the signal to noise ratio. Preliminary spectra were assessed for both polystyrene and silica beads and the spectrometer grating that gave the most resonances for the trapped bead was selected. The advantage of collecting the backscattered light as a function of wavelength is that chemical reactions can be followed in real time whereas if the signal was collected as a function of scattering

angle, the chemistry and thus the spectrum would have changed before all the angles could be collected and a full measurement could have been obtained.

2.4.4. Mie analysis

For analysis conducted in this thesis, the wavelength of the experimental Mie resonances was compared to the modelled Mie resonances to obtain the size and refractive index dispersion of an optically trapped proxy aerosol. The shape of the broader resonances such as those observed in the Mie spectra for silica beads and oleic acid droplets was slightly influenced by the collection angle of the backscattered light. Therefore the position of the experimental resonances was followed and the shape of the resonances was reproduced closely where possible. An improvement in the technique would be to fit the entire modelled Mie resonance spectrum to the experimentally obtained Mie resonance spectrum rather than just the positions of the Mie resonances. The calculated Mie resonance spectrum could be subtracted from the experimental Mie resonance spectrum and the difference minimised to determine the optimum calculated Mie resonance spectrum. Caution would need to be taken to ensure that the calculated Mie resonance positions still aligned with the experimental Mie resonance positions when subtracting the data.

The combination of a counter-propagating optical trap with white light Mie scattering is the first technique to be able to uniquely determine the refractive index of relevant aerosol proxies as a function of wavelength quickly and precisely. Combining the determined refractive index with the accurate determination of aerosol size marks a significant step in further understanding aerosol optical properties for use in climate models.

2.5. Neutron and X-Ray reflectometry experiments

Surface reflection techniques provide an ideal way to study monolayer films at an interface. Neutron and X-Ray reflectometry were employed as complementary techniques to study the oxidation of monolayer organic films at the air-water interface. These techniques were selected because they provided information on the amount and thickness of material at the air-water interface. The following section will cover the theory behind neutron and X-Ray reflectometry experiments and compare the two techniques.

2.5.1. Neutron and X-Ray reflection theory

Neutron and X-Ray reflection experiments provide information on properties of a monolayer film perpendicular to the interface. In the case of neutron reflectivity, information on the neutron refractive index of the film perpendicular to the interface is obtained, whereas in the case of X-Ray reflectivity, information on the electron density of the film perpendicular to the interface is obtained.

A beam of neutrons or X-rays incident on a thin film at the air-water interface at a grazing angle of incidence is specularly reflected (angle of incidence = angle of reflection) from the film on to a detector. The reflectivity of the beam for a film of deuterated material at the air-water interface, R is measured as a function of Q, which is the momentum transfer of the neutron or X-ray as defined in equation 11 (Penfold et al., 1997).

$$Q = \frac{4\pi \sin\theta}{\lambda} \qquad 11$$

$$R = \frac{16\pi^2}{Q^4}(2\rho)^2 \sin\left(\frac{Q\delta}{2}\right)^2 \qquad 12$$

where θ is the incident angle of the neutron or X-Ray beam to the horizontal, λ is the neutron or X-ray wavelength, δ is the film thickness and ρ is the neutron or X-ray scattering length density is defined as:

$$\rho = \Sigma\, \mathrm{nb} \qquad 13$$

where b is the scattering length of an element (neutron or X-ray) and n is the number density of that element (Penfold et al., 1997). Therefore scattering length density may be related to the identity of material at the air-water interface if the chemical composition of the film is unknown. The scattering length density and film thickness can also be related to the amount of material at the air-water interface by:

$$\Gamma = \frac{\rho\delta}{b} \quad (14)$$

where Γ is the surface coverage or amount of material at the air-water interface, and δ is the thickness of the film. Neutron and X-ray reflectivity studies therefore provide information on the scattering length density and thickness of a monolayer film as a function of depth from the interface. The detailed experimental methodology required to study different systems is described in papers 3-6.

2.5.2. Neutron experiments and time-of-flight technique

Neutron reflectivity experiments were conducted on the reflectometers SURF at ISIS in Oxfordshire UK (Penfold et al., 1997) and FIGARO at the ILL in Grenoble, France (Campbell et al., 2011). ISIS is a pulsed neutron source and the ILL is a continuous neutron source. SURF and FIGARO are both time-of-flight reflectometers with vertical scattering planes. FIGARO is a high flux instrument, and can deliver a beam of incoming neutrons with wavelengths between 2-30 Å, whereas SURF can deliver neutrons in the wavelength range 0.55-6.8 Å. Neutrons were specularly reflected from a monolayer film at the air-water interface.

Choppers are used on SURF to shield the instrument from fast neutrons and gamma rays when the proton beam hits the target and to select the wavelength range of neutrons delivered to the sample (Penfold et al., 1997). Whereas on FIGARO, choppers are used to both pulse the source and select the wavelength range of the neutrons delivered to the sample (Campbell et al., 2011). The time of origin of the neutrons and the detection time are both known as well as the distance travelled from the chopper to the sample and from the sample to the detector. Time is proportional to the reciprocal velocity of the neutron and velocity is proportional to the neutron wavelength. Reflectivity can therefore be calculated and binned in terms of Q (equation 11), to produce a reflectivity profile (Daillant et al., 2009) as shown in Figures 7 and 8. The experimentally obtained reflectivity profile can then be modelled to determine the thickness and amount of material at the air-water interface as detailed in the previous section and in papers 3-5.

2.5.3. X-ray experiments

X-ray reflectivity measurements were conducted on I07 at the Diamond Light Source, Oxfordshire, UK. X-rays of 12.5 keV energy, ~1 Å wavelength were used and the incident angle of the X-ray beam on the monolayer surface was adjusted using a double crystal deflector (DCD) scheme (Arnold et al., 2012). The DCD was adjusted to

give a range of incident angles which were specularly reflected on to the detector. By varying the incident angle of the X-rays, reflectivity measurements over a specified Q range were obtained (equation 11). As with the neutron reflectivity experiments, the experimentally obtained reflectivity was modelled to determine the thickness and amount of material at the air-water interface as detailed in paper 6.

2.6. Comparing neutron and X-ray reflectometry studies

Neutron and X-ray reflectometry are complementary techniques used to study the oxidation of monolayer films at the air-water interface. The use of both techniques allows the study of a wide range of samples that would not be possible using one technique alone. The following sections compare the two techniques then evaluate various aspects of the experiments conducted in the body of the thesis in further detail.

X-ray reflectivity provides a more intense signal than neutron reflectivity because it has a much lower background signal owing to the higher absorption of X-rays by the liquid (Lu et al., 2000) compared to neutron reflectivity. Neutron reflectivity suffers from a large background signal owing to incoherent neutron scattering. It is therefore possible to measure a higher Q range, from ~0.015-0.8 $Å^{-1}$ using X-ray reflectivity because of the larger signal to background ratio. However, owing to the intense signal, X-rays also have the possibility to damage the film under study. Depending on the susceptibility of the film to damage, the exposure time to the X-rays can be decreased and the position of the X-ray beam on a monolayer film can be adjusted so that reflectivity measurements are consistently made on undamaged film. A drawback of X-ray reflectivity is that it can sometimes be difficult to distinguish between the monolayer film and the liquid subphase that the film is present on, as explained in the following paragraphs. Figure 7 highlights the small difference in the X-ray reflectivity signal for a monolayer of film forming material extracted from an atmospheric aerosol sample and a pure water subphase. Figure 7 also highlights the large Q range that can be obtained using X-ray reflectivity.

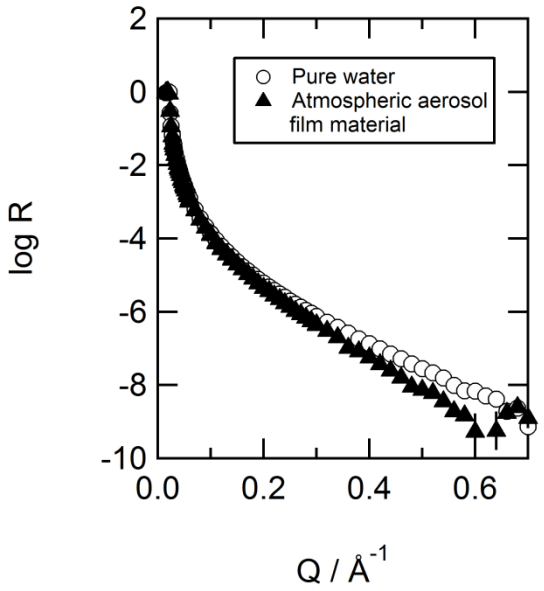

Figure 7. X-ray reflectivity profile highlighting the small difference in reflectivity between a film of organic material extracted from an atmospheric aerosol sample and a pure water subphase.

The aim of the reflectivity experiments conducted in this thesis was to gain information about the oxidation of real thin films at the air-water interface. Therefore X-ray reflectivity was used to study the oxidation of monolayer films of organic material extracted from atmospheric aerosol and sea water samples as detailed in paper 6. X-ray reflectivity was selected because of its higher flux and sensitivity to the electron density of the film.

Neutron reflectivity experiments do not have as intense a signal as in X-ray reflectivity experiments, owing to the large background arising from incoherent neutron scattering and the higher absorption of X-rays by the liquid as discussed previously. Neutron reflectivity is therefore not as suited to the study of real atmospheric films at the air-water interface which may not have a strong signal. The large background signal consequently results in a lower Q range as depicted in Figure 8. However, neutron reflectivity is a non-destructive technique and measurements can be made without damage to the monolayer film at the air-water interface. An advantage of the technique over X-ray reflectivity is that contrast variation can be used to enhance or diminish the reflectivity of a monolayer film at the air-water interface. Hydrogen and Deuterium have significantly different scattering lengths (b_H = -3.74 × 10^{-5} Å and b_D = 6.67 × 10^{-5} Å) but are chemically the same and therefore selective deuteration can be used to enhance the neutron reflectivity signal of a monolayer film with respect to the air and the aqueous subphase. The ratio of D_2O to H_2O in the aqueous subphase can also be adjusted to make the aqueous subphase effectively vanish. Such a subphase is known as air contrast matched water (ACMW) and consists of D_2O to H_2O in the volume ratio

8.1% to 91.9%. Figure 8 highlights the difference in reflectivity between ACMW and a fully deuterated monolayer of oleic acid.

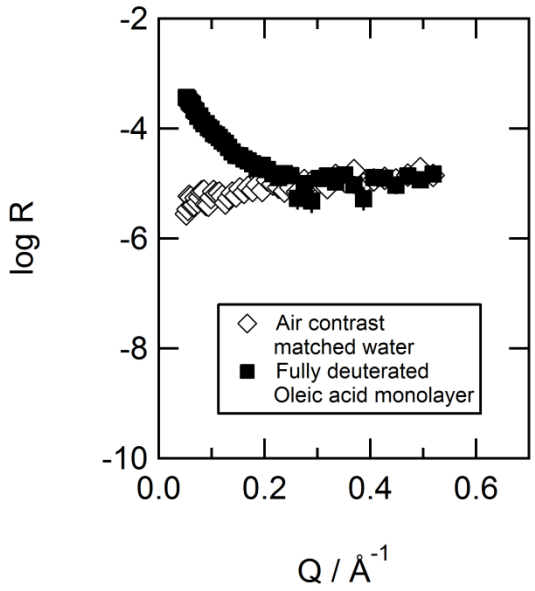

Figure 8. Neutron reflectivity profile highlighting the benefit of contrast variation for a film of fully deuterated oleic acid present on a subphase of ACMW. The reflectivity data has been plotted on the same log scale as Figure 7 to allow comparison between neutron and X-ray experiments. The large background signal arising from incoherent scattering is also emphasised resulting in a reduced Q range compared to X-ray reflectivity. The sloping baseline is an artefact of the instrument (SURF) used to collect the data.

Selective deuteration is useful in studying reaction mechanisms when monolayer films at the air-water interface undergo a chemical reaction. An example of the technique was reported in paper 3 (Thompson et al., 2013) where a film of 1-palmitoyl-2-oleoyl-sn-glycero-3-phosphocholine (POPC) at the air-water interface was exposed to gaseous ozone. The oleoyl tail of POPC was selectively deuterated and during reaction with gaseous ozone the oleoyl tail was observed to break at the terminal C9 position. Combining neutron reflectivity with surface pressure measurements, the remaining tail was interpreted to reverse its orientation and penetrate the air-water interface. A limitation of X-ray reflectivity studies is that contrast variation cannot be employed so mechanistic studies cannot be conducted using X-ray reflectivity alone.

2.7. Evaluation of neutron and X-ray reflectometry experiments

2.7.1. Equipment limitations

For both neutron and X-ray reflectivity experiments a Langmuir trough was employed to study monolayer films at the air-water interface. The Langmuir trough used in the

experiments described in papers 4-6 does not have barriers or a tensiometer to either compress the film or measure the surface pressure during the experiment. The reason for the lack of barriers and a tensiometer was because of beamline geometry constraints and the use of chemicals and UV lights. For the X-ray reflectivity experiments conducted using real atmospheric aerosol and sea water samples described in paper 6, it would have been useful to monitor the surface pressure alongside the oxidation reaction. The change in surface coverage of the monolayer films of atmospheric aerosol material and sea water material on exposure to gaseous ozone was negligible. Additional surface pressure data may have been helpful in observing whether any change occurred in the coverage of the monolayer film, even if it was a very small change. The use of Brewster Angle Microscopy (BAM) may also have been useful for the X-ray reflectivity experiments; where any prior knowledge of the sample composition was lacking, BAM could have provided information on potential phase changes and film partitioning into the subphase.

2.7.2. Modelling the neutron and X-ray reflectivity data

In order to model the experimental data obtained in both neutron and X-ray reflectivity experiments, a slab model was proposed consisting of a monolayer film at the air-water interface present on a liquid subphase as depicted in Figure 1 in paper 6. The surface coverage and film thickness were determined from fitting the modelled data to the experimental reflectivity data. For a monolayer of deuterated material at the air-water interface of a null reflecting solution, the neutron signal is due solely to the deuterated species present at the surface i.e. the scattering length density of the air and liquid subphase are both equal to zero. Therefore the determined values of surface coverage of the film for neutron reflectivity experiments are independent of the model used to fit the data because there can be no contribution from the aqueous subphase or air above the monolayer film. However, contrast variation cannot be used in X-ray reflectivity, and it is possible that the determined values of surface coverage of the film could be influenced by the aqueous subphase and are thus dependent on the model used, i.e. how the layers in the model are defined. However, an accurate determination of surface coverage may still be possible given a distinct difference in reflectivity between the monolayer film and the subphase, and given the general increased sensitivity of an X-ray experiment.

The slab model was used to determine the amount of material at the air-water interface for the data obtained in papers 3-6. The scattering length density and thickness of material at the air-water interface was varied whilst the roughness of the film at the air-water interface and the background signal (once fitted) were kept constant. Other fitting

options were trialled that involved varying different parameters including the area per head group, the film thickness and the scattering length of the film. For these alternative fits, the scattering length was typically fixed and the area per head group and film thickness were varied in order to obtain acceptable fits of the modelled reflectivity to the experimental reflectivity. Such fits were discounted because the scattering length of the film will change as the film is oxidised and thus constraining the scattering length was not realistic. Therefore all fits of modelled reflectivity to the experimental reflectivity data in the aforementioned papers were achieved by varying the scattering length density and film thickness because those variables will change during oxidation of a monolayer film.

2.7.3. Sample collection methods

For all neutron reflectivity experiments conducted, the samples were supplied by Avanti polar lipids or Sigma Aldrich and 1 mgmL^{-1} solutions were made in chloroform. However, for the X-ray reflectivity experiments, atmospheric aerosol and sea water samples were collected using the methods described in the experimental section of paper 6. Oxidation reactions were performed on organic film forming material extracted from both atmospheric aerosol and sea water samples using gaseous ozone and aqueous phase hydroxyl and nitrate radicals. The composition of the organic films will determine whether the film is oxidised by different oxidants. Gas Chromatography Mass Spectrometry, GC-MS and Electrospray Ionization Mass Spectrometry, ESI-MS analysis of the atmospheric aerosol and sea water samples did not show the high numbers of unsaturated compounds-fatty acids and high concentration of phospholipids (Marty et al., 1979) that were anticipated. It is possible that the sampling or extraction methods used could have influenced the compounds that were detected by GC-MS and ESI-MS. Both the aerosol and seawater samples were extracted in chloroform only. Chloroform should extract phospholipids well as manufacturers supply phospholipids in chloroform such as Avanti Polar Lipids Inc., so perhaps the ratio of phospholipids to other compounds in the collected sea surface microlayer samples was low. Future work will involve the extraction of samples using different solvents such as methanol. Several samples could also be collected in parallel and extracted using different solvents to determine the effect on film composition using GC-MS and ESI-MS. The method by which the samples were collected could also have affected the compounds observed in the analysis. In comparison to the sampling methods described in paper 6 for atmospheric aerosol samples, larger flow rates and collection times could be employed to sample greater volumes of atmospheric aerosol. More specialised sampling equipment for collection

of sea water samples could also be used, such as a rotating drum or glass plate etc. (Garrett and Duce, 1980) in order to selectively sample the sea surface microlayer.

2.7.4. Combining optical trapping studies with neutron and X-ray reflectivity studies

The optical properties of thin films present on the surface of aerosols can be accurately characterised using a counter-propagating optical trap combined with white light Mie scattering. As coated aerosols are likely to undergo oxidation in the atmosphere it is important to study the oxidation of thin films and the associated change in aerosol properties. Neutron and X-ray reflectometry are used to study the oxidation of monolayer films at the air-water interface in this thesis. Optical trapping and white light Mie scattering provide information on the optical properties of aerosols and neutron and X-ray reflectivity provide information on the oxidation of thin films at the flat air-water interface. However, thin films present at the surface of aerosols are present on a curved surface and it would therefore be beneficial to study the oxidation of thin films on the surface of an optically trapped aerosol. A thin film changes in both thickness and chemical composition as it is oxidised. Core-shell Mie theory could be used to follow the change in film thickness with time during oxidation of a film on the surface of an optically trapped core-shell aerosol. The change in film thickness on an optically trapped aerosol could then be compared to the change in film thickness of a flat monolayer film during oxidation determined using neutron and X-ray reflectivity. The oxidation of thin films on a curved and flat surface could therefore be compared to determine whether geometry has an effect on the oxidation kinetics of thin films.

2.8. Conclusion

For the studies in this thesis, optical trapping combined with white light Mie spectroscopy was used to characterise the properties of proxy aerosol. Neutron and X-ray reflectometry were used to study the oxidation of monolayer films at the air-water interface on a larger scale compared to studies on the surface of optically trapped aerosol. Information on the amount and thickness of the material at the air-water interface during oxidation was obtained as well as some mechanistic information from subsequent kinetic modelling of the experimental data. Thus the use of optical trapping and neutron and X-ray reflectivity provides information on both the optical properties of coated aerosols and the physical properties of a film during oxidation at the air-water interface.

2.9. Methodology references

Aden, A. L. and Kerker, M.: Scattering of Electromagnetic Waves from Two Concentric Spheres, J. Appl. Phys., 22(10), 1242-1246, 1951.

Arnold, T., Nicklin, C., Rawle, J., Sutter, J., Bates, T., Nutter, B., McIntyre, G. and Burt, M.: Implementation of a beam deflection system for studies of liquid interfaces on beamline I07 at Diamond., J. Synchrotron Radiat., 19, 408–416, 2012.

Ashkin, A.: Acceleration and trapping of particles by radiation pressure, Phys. Rev. Lett., 24(4), 156–159, 1970.

Ashkin, A., Dziedzic, J. M., Bjorkholm, J. E. and Chu, S.: Observation of a single-beam gradient force optical trap for dielectric particles., Opt. Lett., 11(5), 288–290, 1986.

Bohren, C.F.: and Huffman, D.R.: Absorption and Scattering of Light by Small Particles, Wiley, 1983.

Bowman, R. W. and Padgett, M. J.: Optical trapping and binding, Reports Prog. Phys., 76(2), 026401, 2013.

Campbell, R. A., Wacklin, H. P., Sutton, I., Cubitt, R. and Fragneto, G.: FIGARO: The new horizontal neutron reflectometer at the ILL, Eur. Phys. J. Plus, 126(11), 107, 2011.

Chýlek, P.: Partial-wave resonances and the ripple structure in the Mie normalized extinction cross section, J. Opt. Soc. Am. A., 66(3), 285-287, 1976.

Daillant, J., Gibaud, A. (Eds.), X-ray and Neutron Reflectivity: Principlies and Applications, Lect. Notes Phys. 770 (Springer, Berling Heidelberg 2009) ISBN: 978-3-540-88587-0.

Friese, M., Nieminen, T., Heckenberg, N. and Rubinsztein-Dunlop, H.: Optical alignment and spinning of laser-trapped microscopic particles, Nature, 394(October), 348–350, 1998.

Garrett, W.D, and Duce, R. A.: Surface microlayer samplers in Air-sea interaction: instruments and methods, eds., Dobson, F, Hasse, L. and Davis, R., Plenum, New York, London, 1980.

Hill, S. C. and Benner, R. E. in Optical Effects Associated with Small Particles, P. W Barber and R. K. Chang, eds. (World Scientific, Singapore, 1988), p. 3.

Jenkins, F. A.: Fundamentals of optics, McGraw-Hill, 4th edition, 1976.

Jones, S. H., King, M. D. and Ward, A. D.: Determining the unique refractive index properties of solid polystyrene aerosol using broadband Mie scattering from optically trapped beads., Phys. Chem. Chem. Phys., 15(47), 20735–41, 2013.

Jones, S. H., King, M. D. and Ward, A. D.: Atmospherically relevant core–shell aerosol studied using optical trapping and Mie scattering, Chem. Commun., 51, 4914–4917, 2015.

King, M. D., Thompson, K. C. and Ward, A. D.: Laser Tweezers Raman Study of Optically Trapped Aerosol Droplets of Seawater and Oleic Acid Reacting with Ozone : Implications for Cloud-Droplet Properties, J. Am. Chem. Soc., 126(51), 16710–16711, 2004.

Leach, J., Mushfique, H., di Leonardo, R., Padgett, M. and Cooper, J.: An optically driven pump for microfluidics, Lab Chip, 6, 735–739, 2006.

Lu, J. R., Thomas, R. K. and Penfold, J.: Surfactant layers at the air/water interface: structure and composition, Adv. Colloid Interface Sci., 84(1-3), 143–304, 2000.

Marty, J. C., Saliot, A., Buat-Ménard, P., Chesselet, R. and Hunter, K. a.: Relationship between the lipid compositions of marine aerosols, the sea surface microlayer, and subsurface water, J. Geophys. Res., 84(C9), 5707–5716, 1979.

McGloin, D.: Optical tweezers: 20 years on., Philos. Trans. A. Math. Phys. Eng. Sci., 364(1849), 3521–37, 2006.

Mishchenko, M.I, Hovenier, J.W and Travis, L.D: Light Scattering by Nonspherical Particles: Theory, Measurements, and Applications, Academic Press, San Diego, 2000.

Molloy, J. E. and Padgett, M. J.: Lights, action: optical tweezers, Contemp. Phys., 43(4), 241–258, 2002.

Neuman, K. C., Chadd, E. H., Liou, G. F., Bergman, K. and Block, S. M.: Characterization of photodamage to Escherichia coli in optical traps., Biophys. J., 77(5), 2856–2863, 1999.

Neuman, K. C. and Block, S. M.: Optical trapping, Rev. Sci. Instrum., 75(9), 2787–2809, 2004.

Pan, Y.-L., Hill, S. C. and Coleman, M.: Photophoretic trapping of absorbing particles in air and measurement of their single-particle Raman spectra., Opt. Express, 20(5), 5325–34, 2012.

Penfold, J., Richardson, R. M., Zarbakhsh, a., Webster, J. R. P., Bucknall, D. G., Rennie, A. R., Jones, R. A. L., Cosgrove, T., Thomas, R. K., Higgins, J. S., Fletcher, P. D. I., Dickinson, E., Roser, S. J., McLure, I. a., Hillman, a. R., Richards, R. W., Staples, E. J., Burgess, A. N., Simister, E. A. and White, J. W.: Recent advances in the study of chemical surfaces and interfaces by specular neutron reflection, J. Chem. Soc. Faraday Trans., 93(22), 3899–3917, 1997.

Petty, G.W, A first course in atmospheric radiation, Sundog publishing, Madison, Wisconsin, 2004.

Reid, J. P. and Mitchem, L.: Laser probing of single-aerosol droplet dynamics, Annu. Rev. Phys. Chem., 57, 245–71, 2006.

Reid, J. P., Dennis-Smither, B. J., Kwamena, N.-O. a, Miles, R. E. H., Hanford, K. L. and Homer, C. J.: The morphology of aerosol particles consisting of hydrophobic and hydrophilic phases: hydrocarbons, alcohols and fatty acids as the hydrophobic component., Phys. Chem. Chem. Phys., 13(34), 15559–72, 2011.

Svoboda, K. and Block, S. M.: Biological applications of optical forces, Annu. Rev. Biophys. Biomol. Struct., 23, 247–85, 1994.

Symes, R., Sayer, R. R. M. and Reid, J. J. P.: Cavity enhanced droplet spectroscopy: Principles, perspectives and prospects, Phys. Chem. Chem. Phys., 6, 474–487, 2004.

Takahama, S., Liu, S. and Russell, L. M.: Coatings and clusters of carboxylic acids in carbon-containing atmospheric particles from spectromicroscopy and their implications for cloud-nucleating and optical properties, J. Geophys. Res. Atmos., 115(D01202), 1–21, 2010.

Thompson, K. C., Jones, S. H., Rennie, A. R., King, M. D., Ward, A. D., Hughes, B. R., Lucas, C. O. M., Campbell, R. A., and Hughes, A. V: Degradation and rearrangement of a lung surfactant lipid at the air-water interface during exposure to the pollutant gas ozone., Langmuir, 29(14), 2013.

Toon, O. B. and Ackerman, T. P.: Algorithms for the calculation of scattering by stratified spheres., Appl. Opt., 20(20), 3657–60, 1981.

Wriedt, T Mie Theory: A review in Hergert, W. and Wriedt, T.: The Mie Theory Basics and Applications, Springer, 2012.

Paper 1: Determining the unique refractive index properties of solid polystyrene aerosol using broadband Mie scattering from optically trapped beads

S. H. Jones, M. D. King, and A. D. Ward

Physical Chemistry Chemical Physics, 2013, 15, 20735–20741.

Within this partly co-authored work, I declare that the following contributions are entirely my own work:

- Conducted the experiments and collected and analysed all the polystyrene bead data.
- Authored the paper.
- Contributed significantly to the design of the experiment.
- Contributed to drawing the conclusions of the paper.

PCCP

RSC Publishing

PAPER

View Article Online
View Journal | View Issue

Cite this: *Phys. Chem. Chem. Phys.*, 2013, **15**, 20735

Determining the unique refractive index properties of solid polystyrene aerosol using broadband Mie scattering from optically trapped beads

Stephanie H. Jones,[ab] Martin D. King[a] and Andrew D. Ward*[b]

Received 16th August 2013,
Accepted 21st October 2013

DOI: 10.1039/c3cp53498g

www.rsc.org/pccp

A method is described to measure the refractive index dispersion with wavelength of optically trapped solid particles in air. Knowledge of the refraction properties of solid particles is critical for the study of aerosol; both in the laboratory and in the atmosphere for climate studies. Single micron-sized polystyrene beads were optically trapped in air using a vertically aligned counter-propagating configuration of focussed laser beams. Each bead was illuminated using white light from a broadband light emitting diode (LED) and elastic scattering within the bead was collected onto a spectrograph. The resulting Mie spectra were analysed to accurately determine polystyrene bead radii to ±0.4 nm and values of the refractive index to ±0.0005 over a wavelength range of 480–700 nm. We demonstrate that optical trapping combined with elastic scattering can be used to both accurately size polystyrene beads suspended in air and determine their wavelength dependent refractive index. The refractive index dispersions are in close agreement with reported values for polystyrene beads in aqueous dispersion. Our results also demonstrate a variation in the refractive index of polystyrene, from bead to bead, in a commercial sample. The measured variation highlights that care must be taken when using polystyrene beads as a calibration aerosol.

1 Introduction

Atmospheric aerosol is known to impact on many areas of life, such as air pollution, human health, and modern climate change.[1,2] The climate of the Earth is directly affected by aerosols scattering and absorbing solar radiation and indirectly affected by aerosols acting as cloud condensation nuclei. There is a significant amount of uncertainty regarding aerosol contribution to both effects and characterisation of the physical properties of atmospheric aerosol such as radius and refractive index are necessary to reduce the uncertainty.

Polystyrene beads are often used as a test aerosol to calibrate instruments used to size aerosols with light scattering techniques.[3] The refractive index of the beads controls, in part, the elastic scattering of light as a function of scattering angle and wavelength. Therefore, knowledge of the bead's refractive index as a function of wavelength is critical for the use of polystyrene beads as test aerosol. Refractive index varies with wavelength and the variation can be described by a Cauchy equation.[4] The variation in refractive index with wavelength can also be referred to as a dispersion of the refractive index. The Cauchy equation is of the form;

$$n = A + \frac{B}{\lambda^2} + \frac{C}{\lambda^4} \quad (1)$$

Where, n is the refractive index at wavelength, λ, and A, B and C are empirical coefficients.

To date, a number of studies have focussed on the characterisation of the refractive index dispersion of polystyrene either as bulk material or as an aqueous suspension.[5–8] For polystyrene bead suspensions, the dispersions of the refractive index with wavelength are broadly in agreement. Miles *et al.*,[9] performed a cavity-ring-down study looking at polystyrene beads in air and reported a value of the real component of refractive index of 1.627 ± 0.027 at a single illumination wavelength of 560 nm. The reported value was larger, but within the uncertainty of the measurement, when compared to those obtained from studies of aqueous polystyrene bead suspensions.[5–8]

The study presented here demonstrates the technique of optical trapping of polystyrene beads in air combined with white-light scattering[10–13] and the application of Mie theory,[14–16] to determine the radius and wavelength-dependent values of refractive index. Details for application of Mie theory for spectral

[a] *STFC, Central Laser Facility, Research Complex at Harwell, Rutherford Appleton Laboratory, Harwell Oxford, Didcot, Oxfordshire, OX11 0FA, U.K. E-mail: andy.ward@stfc.ac.uk, stephanie.jones@stfc.ac.uk*
[b] *Department of Earth Sciences, Royal Holloway University of London, Egham, Surrey, TW20 0EX, U.K. E-mail: m.king@es.rhul.ac.uk*

analysis are given in Ward *et al.*[10] and in Moore *et al.*[11] and references therein.

The refractive index dispersion with wavelength for polystyrene beads in air were investigated and compared to polystyrene beads in water. Beads were individually characterised to determine the variation in size and refractive index within the sample of polystyrene beads.

Bateman *et al.*[5] used transmission photospectrometer measurements to determine the size and refractive index dispersion of a suspension of polystyrene beads in water as preliminary work towards the characterisation of biological hydrosols. Polystyrene microspheres were chosen for Ma *et al.*'s[6] investigation as a proxy for turbid media used in the development of biomedical optics and the calibration of optical instrumentation. Ma *et al.*[6] determined the complex and real values of the refractive indices as a function of wavelength using reflectance and transmission measurements of the suspensions of polystyrene beads in water using an integrating sphere. Other researcher's motivations for studying polystyrene were to provide optical reference data for bulk polystyrene[7] and to contribute to bulk optical plastic data.[8] The National Institute of Standards and Technology (NIST) have also used an integrating sphere to make absorption measurements to determine the refractive index dispersions of polystyrene suspensions.[17] NIST selected polystyrene as a generic micro bead and their results indicated slightly different refractive index dispersions for different sized polystyrene beads, resulting in a difference of 0.001 in refractive index between beads of different radii. A further study[18] of individual polystyrene beads has been undertaken in solution. Philips *et al.*[18] nebulised a solution of polystyrene beads and used electric fields to control the resultant charged beads in order to isolate one bead. The bead was illuminated using a laser and the size and refractive index values of polystyrene fitted.

In the study presented here single polystyrene beads in air have been optically trapped using a vertically aligned counter-propagating configuration of focussed laser beams. The technique provides a contact free method of studying single aerosol particles and is an ideal way to model aerosols in the climate and their related atmospheric chemistry.[19,20] Optical trapping is suitable for the analysis of laboratory generated aerosol but is, to our knowledge, untested against atmospheric aerosol sources. Complications may arise for particles that strongly absorb light at the laser trapping wavelength. Whilst different laser wavelengths can be used to address this problem there are materials such as black carbon and humic acids that may remain unsuited for use in optical trapping studies. Optical trapping of liquid aerosol droplets has been reported by a number of authors and is reviewed by McGloin.[21] However, the trapping of microscopic solid spheres (<5 μm) is not as prevalent and was first reported by Summers *et al.*,[22] using a single beam gradient trap. Summers *et al.* showed that stable trapping of the bead was achieved for a few seconds. Li *et al.*,[23] have subsequently reported success in trapping such beads using a horizontally orientated counter-propagating trap with significant stability in trapping even under low pressure conditions. Flynn *et al.*[24] and Lindballe *et al.*[25] have trapped polystyrene beads in aqueous suspension using horizontal counter-propagating optical traps. Flynn *et al.*[24] analysed the forward scattered laser light at different laser power ratios to determine the size and refractive index at low resolution.

Building on the initial work of Ward *et al.*[10] and then Moore *et al.*[11] this study demonstrates that light scattering from a white LED and application of Mie theory can be used to accurately size polystyrene beads suspended in air and determine the refractive index dispersion over a broadband wavelength range.

2 Experimental

2.1 Apparatus and aerosol generation

A vertically aligned counter-propagating optical trap was used to trap forty-six individual polystyrene beads. A diagram of the apparatus is shown in Fig. 1. The equipment consists of a 1.50 W, 1064 nm, continuous wave Nd:YAG laser (Laser Quantum) coupled to two fibre-optic cables using a beamsplitter coupling port (Oz Optics). The laser beam was fibre-delivered to two opposed objective lenses (Mitutoyo M Plan Apo 50×, NA = 0.42) using simple beam expansion optics to match the beam diameter to the back aperture of the objective lens.[26]

The focussed beams were aligned in x, y and z dimensions using differential micrometer control on the top objective to create a counter-propagating optical trap. Vertical focal separation between the two beams was set at 10 μm. The laser power of the upwards pointing beam was 10 mW and the downwards beam 15 mW at the point of focus. These laser powers permitted stable optical trapping combined with an in-focus brightfield image of the trapped bead. The larger radiation pressure from

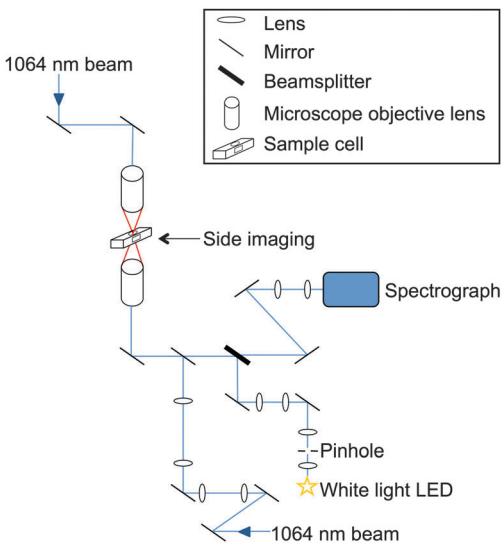

Fig. 1 Schematic diagram of the experimental apparatus. Two laser beams (1064 nm) from a twin-coupled fibre output are focussed through opposing objective lenses to form an optical trap in an aluminium cell. White light from an LED of wavelength range 480–700 nm is focussed on to the trapped bead and backscattered light collected onto a spectrograph.

the downwards beam was used to force the bead into the image plane of the lower objective lens.[23] A brightfield side image of the bead, orthogonal to the previous image of the trapped bead, was also obtained to assist bead trapping. An aluminium cell is used for bead trapping and was placed between the two objective lenses. The windows in the top and bottom faces of the cell were coverslips which allowed the laser beams to focus into the cell with minimal aberration. The cell also contained inlet and outlet ports orthogonal to the laser beam paths to allow delivery and exhaust of aerosols.

An atomiser (Topas, ATM 220) with a diffusion dryer (Topas, DDU 570/L) was used to deliver dry polystyrene beads, of approximately 1.25 μm radius, into the trapping cell. The beads were obtained from Bangs Laboratories (PS05N, Batch 5893) and are specified at 1.25 μm radius with 0.08 μm standard deviation. Transmission Electron Microscopy analysis was also performed on the polystyrene bead sample using a JEOL JEM-2100/HT electron microscope in low-magnification mode. The average particle radius was determined as 1.216 μm with a standard deviation of 0.015 μm. A number of beads were delivered into the cell and the cell position was adjusted relative to the laser beams until a single bead was trapped. The remaining beads were removed by collisions with the cell walls. All beads were from the same commercial sample and each bead was studied individually.

No control was made for humidity or temperature. Room humidity was typically 30% RH and room temperature was 21 °C and kept constant by air conditioning. To allow inspection of the beads after trapping they were placed on the lower coverslip by raising the sample cell relative to the trapping position. The inspection was to confirm that a solid polystyrene bead was trapped rather than dust, a small fragment of the silica gel from the diffusion dryer or an aqueous liquid droplet.

Light from a white LED (Comar 01 LD 555, 6 V) was focussed on the trapped bead as shown in Fig. 1. An iris was placed in the optical train in such a position that the edge of the iris was in focus in the microscope imaging plane. The area of the imaged iris was adjusted to be of a size slightly greater than that of the trapped bead. A portion of the white light was backscattered by the polystyrene bead and collected across a 25 degree cone angle by the objective lens before exiting along the same optics through the microscope towards a beamsplitter where it was focussed into a spectrograph (Acton SP2500i) *via* a series of mirrors (Semrock Max Mirror). The light was subsequently imaged on to a charge-coupled device (CCD) detector (Princeton Instrument Spec 10:400 BR). Spectra were collected by scanning from 480–700 nm using a 1200 groove mm^{-1} grating with a resolution of 0.028 nm. The spectrograph and CCD were calibrated for wavelength using the spectral lines of Ar and Xe gas lamps (reference lines from NIST database[27]).

2.2 Imaging

The optically trapped polystyrene bead was imaged using brightfield illumination such that the upper objective lens acted as a condenser. The bead was also imaged horizontally, through two coverslip windows in the cell, to provide both horizontal and vertical views of the bead respectively as shown in Fig. 2. Side-imaging aided optical trapping as the falling polystyrene beads were observed approaching the laser focus allowing the cell position to be adjusted accordingly. Illumination sources used for imaging were turned off during acquisition of elastically backscattered light.

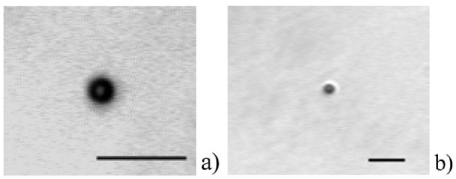

Fig. 2 Brightfield images of a trapped polystyrene bead showing views from (a) the lower objective lens (Mitutoyo M Plan Apo 50×, NA 0.42) and (b) the side-imaging lens (Mitutoyo M Plan Apo 20×, NA 0.42). Optical filters placed in front of each camera have blocked the laser light from the image. Scale bar on each image represents 10 microns.

2.3 Data fitting

The recorded spectrum of the intensity of elastically backscattered light with wavelength, henceforth the ''Mie spectrum'', was compared to the predicted spectrum calculated from Mie theory using two processes. Initially four different sets of empirical constants (A, B and C) for the wavelength-dependent dispersion of refractive index from the literature were used to determine the radii of the trapped polystyrene beads using eqn (1). The second process of fitting used the determined radii as a starting value for iteration of both the empirical constants A, B and C and also the particle size to determine whether better fits could be determined, and enable bead-to-bead comparison.

2.3.1 Radii determination using literature wavelength dependent refractive indices. Forty-six different polystyrene beads were optically trapped and their Mie spectra recorded. A typical backscattered Mie spectrum from a single polystyrene bead collected in this study is shown in Fig. 3. Resonance wavelengths were taken from the spectrum of each bead which has at least 15 first-order resonances[28] in the wavelength range 480–700 nm. The resonance positions obtained experimentally were then compared to calculated wavelengths from Mie theory, the values of which are dependent on both refractive index and size. All calculated Mie spectra were integrated across the 25 degree collection angle.[10]

The initial calculation of Mie resonance wavelengths were performed using literature values[5–8] to define the wavelength dispersion of the refractive index of polystyrene. The values of the coefficients A, B and C in these studies are valid over the experimental wavelength range of 480–700 nm. The imaginary part of the refractive index for polystyrene is typically small and constant in the visible region[29] and in this work was fixed at $0.0003i$. The refractive index of air was also assumed constant over this wavelength range at 1.00027.[30] Calculated resonance wavelengths were altered by varying only the particle size in 0.1 nm increments and the resulting positions compared to experimental resonance wavelengths.[11] The minimum value in

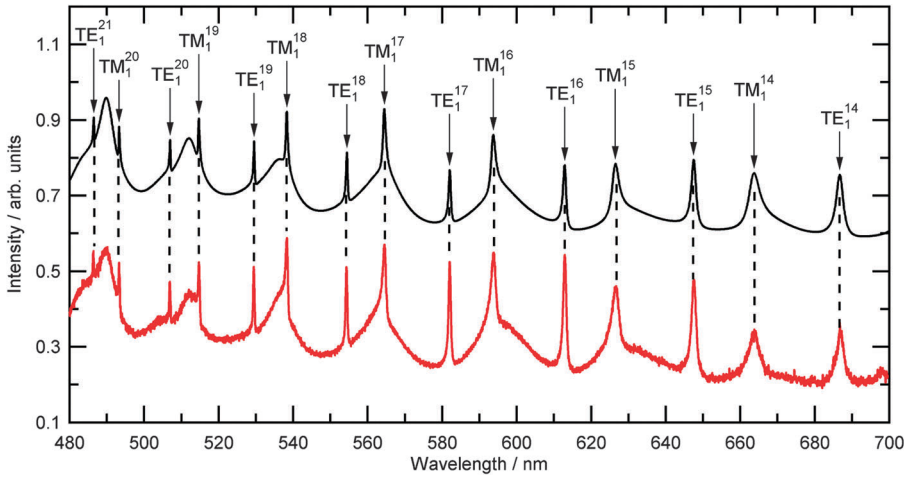

Fig. 3 A typical recorded experimental Mie spectrum for an optically trapped polystyrene bead (Table 2, number 13) is shown in red. The background signal from the white LED has been divided through the collected signal but no other processing or modifications have been made. The calculated Mie spectra for a polystyrene bead of size 1.227 μm, and a dispersion of refractive index as detailed in Table 2 is shown in black and is offset by 0.5 arbitrary units.

the average difference per resonance, χ_r as defined in eqn (2), was used to determine the best fit for particle size.

$$\chi_r = \frac{\sum \sqrt{(\lambda_{experimental} - \lambda_{calculated})^2}}{N} \quad (2)$$

Where, for N resonance positions, each measured resonance wavelength, $\lambda_{experimental}$ from the recorded Mie spectrum was compared to the corresponding calculated resonance wavelength, $\lambda_{calculated}$ determined using Mie theory for given values of particle radius and empirical constants A, B and C. The particle size is reported to the nearest nanometer.

2.3.2 Iterative fitting of size and refractive index dispersion. The aim of the second fitting process was to obtain the best value of refractive index dispersion (*i.e.* values A, B and C) and particle radius to fit the calculated Mie resonance wavelengths to the experimental resonance wavelengths. Ten polystyrene beads were selected at random from the forty-six original beads. The bead radius was initially set at the value of the average radius obtained from the initial fitting process described in Section 2.3.1. Whilst it was possible to determine χ_r for all the values of A, B, C and radius within known boundary conditions this was found computationally intensive. As an alternative, for each particle size we considered the refractive index, n_{ABC}, required to match the calculated and experimental resonance wavelengths for each resonance position. The typical result was a plot of 15 data points showing the dispersion of refractive index, n_{exp} with wavelength that is required to exactly fit the selected particle size to the experimental resonance wavelengths (see Fig. 4 for an example). A set of empirical constants A, B and C were fitted to the values of n_{ABC} for all the resonances using a Levenberg–Marquardt algorithm.[31,32] The residual, φ, from the Levenberg–Marquardt algorithm was used to assess the quality of the fit. To determine the particle size the value of particle radius was varied in 0.5 nm increments and the above procedure repeated until the minimum in the plot of φ against particle radius was obtained, as shown in Fig. 5. Each of the recorded Mie spectra from the ten selected polystyrene beads was fitted in this way (see Table 2).

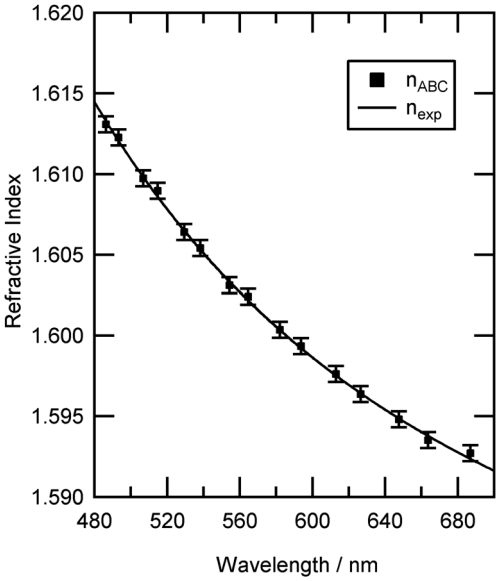

Fig. 4 The determined values of refractive index for individual resonance positions of an optically trapped polystyrene bead in air (Table 2, number 13) are shown as points, n_{ABC}. The refractive index dispersion is shown as a solid line. The uncertainty in refractive index, ±0.0005, results from an uncertainty of ±0.4 nm in bead radius.

3 Results and discussion

3.1 Comparison with literature refractive index dispersions

Table 1 lists the summarised average and standard deviation of the optimum radii for the forty-six optically trapped beads using literature constants for the Cauchy equation to describe

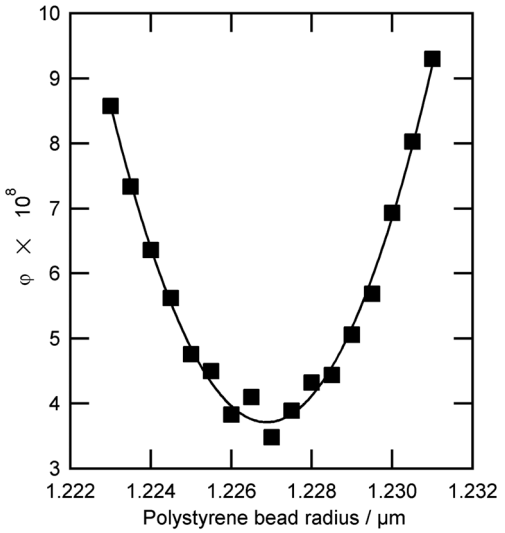

Fig. 5 The value of the Levenberg–Marquardt residual, φ, as a function of bead radius for an optically trapped polystyrene bead (Table 2, number 13). The uncertainty in determination of optimum bead radius is ±0.4 nm.

Table 1 Summary of the fitted bead radii for 46 different polystyrene beads using wavelength dependent refractive index equations from the literature

Literature source	Average radius/μm	χ_r/nm
Bateman *et al.*[5]	1.227 ± 0.009	0.056
Ma *et al.*[6]	1.299[a]	2.089
Matheson *et al.*[7]	1.231 ± 0.009	0.077
Sultanova *et al.*[8]	1.232 ± 0.009	0.092
This work	1.227 ± 0.008	0.046

[a] Variations in radii are standard deviations. The uncertainty for the average radius using the equation from Ma *et al.* is not stated as the particle sizing process results in a poor fit as indicated by the large value of χ_r.

the variation of refractive index with wavelength. Also listed in Table 1 is the average value of, χ_r (eqn (2)), the figure of merit for comparing experimental and calculated resonance positions. Bateman *et al.*'s[5] wavelength-dependent equation to describe refractive index gives the best quality of fit to the experimental data. However, with the exception of Ma *et al.*[6] all fits are similar.

3.2 Iterative fitting results for individual polystyrene beads

The results for single polystyrene beads will now be considered. Fig. 3 compares a typical Mie spectrum from the experiment (bead number 13) with a calculated Mie spectrum and shows excellent agreement in resonance wavelength values. The difference in wavelength of the resonance positions for the spectra in Fig. 3 was an average of 0.049 nm which was less than 2 pixels on the detector. The calculated Mie spectrum in Fig. 3 was calculated for values of radius and A, B and C as detailed in Table 2.

To obtain the radius of the polystyrene bead, a number of radii were fitted as described in Section 2.3.2. For bead 13, the value of the Levenberg–Marquardt residual, φ was plotted as a function of radius close to the optimum size value, as shown in Fig. 5, demonstrating a clear minimum that corresponds to a

Table 2 Polystyrene bead radii and Cauchy empirical constants determined for ten different polystyrene beads

Bead	Radius/μm	χ_r/nm	A	B/nm^2	C/10^8 nm^4
1	1.238	0.049	1.5716	8272	2.48
4	1.240	0.037	1.5700	8631	2.09
7	1.219	0.042	1.5702	8299	2.74
13	1.227	0.049	1.5736	8300	2.58
18	1.229	0.050	1.5723	8772	1.76
19	1.231	0.041	1.5747	7305	3.94
22	1.225	0.043	1.5712	8793	1.74
26	1.219	0.045	1.5720	8481	2.28
29	1.227	0.045	1.5725	8145	2.66
39	1.211	0.048	1.5698	9122	1.27

radius of 1.227 μm. As the bead radius was altered away from the optimum position the change in refractive index required to match the calculated Mie spectrum resonances to the experimental Mie spectrum resonances became more exaggerated and the residual value, φ, increased. The above procedure results in an uncertainty of ±0.4 nm in particle radius (determined from Fig. 5) which propagates to an uncertainty in refractive index of ±0.0005 as shown in Fig. 4.

3.3 Data fitting results for ten polystyrene beads

The values of the radius and empirical constants A, B and C for each of the ten beads are listed in Table 2. A range of values for both the radius and A, B and C were determined when the beads were fitted using an identical procedure (see 2.3.2). The difference in values of size and refractive index was greater than the error in these quantities and therefore significant. The individual values of refractive index for the beads are plotted as a function of wavelength in Fig. 6 to illustrate the differences

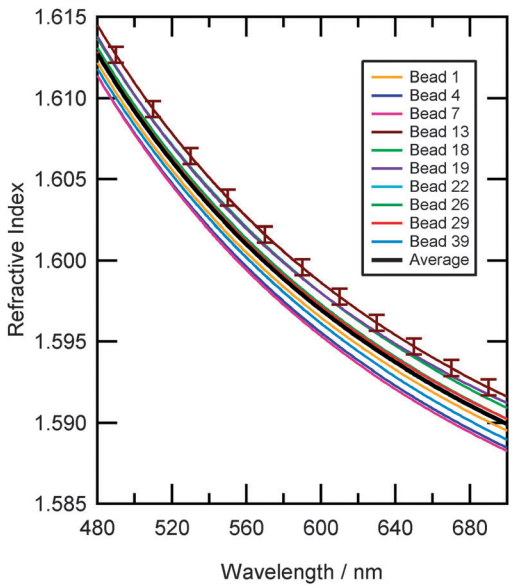

Fig. 6 Refractive index dispersions for ten individual polystyrene beads taken from Table 2. Each bead has a unique radius and wavelength dependent refractive index. Indicative error bars show the variation of refractive index for each bead arising from the measurement and data fitting process. The average refractive index dispersion of the ten beads is shown as a black line.

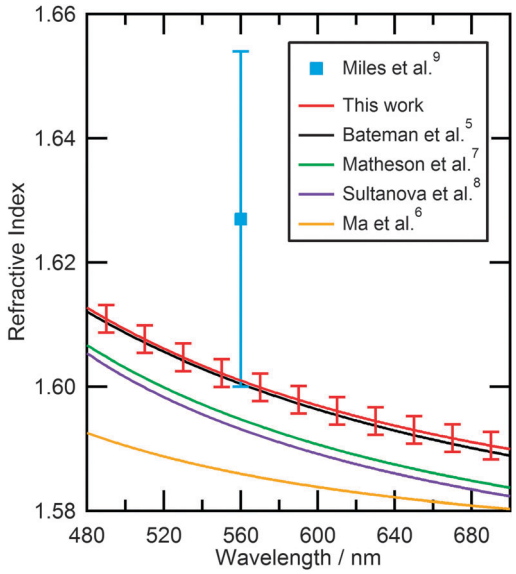

Fig. 7 Comparison of the refractive index dispersions from literature with the refractive index dispersion obtained in this study over the wavelength range 480–700 nm. Error bars indicate the variation of refractive index dispersion for the polystyrene bead sample.

between the ten beads. Thus, the size and more interestingly the composition of each test aerosol was different for each bead, clearly showing that individual polystyrene beads would not be a suitable choice for instrument calibration at high resolution.

The average dispersion of the ten beads can be seen as the black line in Fig. 6, and was calculated by averaging the values of the coefficients A, B and C for the ten beads in Table 2 which resulted in eqn (3). The overall variation (two standard deviations) of the refractive indices for the sample of polystyrene beads was 0.0022, and is shown in Fig. 7. Eqn (3) agrees well with that of Bateman *et al.*[5]

$$n = 1.5718 + \frac{8412}{\lambda^2} + \frac{(2.35 \times 10^8)}{\lambda^4} + 0.0003i \qquad (3)$$

The average values of A, B and C were used to re-fit particle size as defined in Section 2.3.1 to the set of forty-six beads and the results are shown in Tables 1 and 3. A smaller average value of χ_r was determined using these A, B and C values in comparison to those obtained from literature. Thus, for the sample of polystyrene beads used in this study, the description of the refractive index dispersion presented in eqn (3) was more accurate.

The average polystyrene bead radius measured from the Mie scattering analysis (1.227 ± 0.008 μm) is within error of that measured by electron microscopy (1.216 ± 0.015 μm) and has a similar deviation in particle size.

Fig. 7 is a comparison of different refractive index dispersions from literature to the average dispersion obtained in this study. The dispersion used to describe our study lies close to that of Bateman *et al.*[5] indicating that our result agrees well with their study of polystyrene beads in aqueous suspension.

Table 3 Calculated sizes for 46 polystyrene beads using the average refractive index dispersion determined in this study (eqn (3))

Bead	Radius/nm	χ_r/nm	Bead	Radius/nm	χ_r/nm
1	1.237	0.050	24	1.230	0.038
2	1.223	0.039	25	1.224	0.050
3	1.223	0.055	26	1.219	0.044
4	1.239	0.039	27	1.216	0.059
5	1.229	0.041	28	1.232	0.045
6	1.235	0.048	29	1.227	0.049
7	1.218	0.042	30	1.235	0.043
8	1.225	0.040	31	1.214	0.054
9	1.232	0.041	32	1.229	0.051
10	1.214	0.042	33	1.224	0.047
11	1.239	0.041	34	1.236	0.045
12	1.219	0.052	35	1.226	0.040
13	1.228	0.050	36	1.221	0.059
14	1.224	0.045	37	1.231	0.059
15	1.237	0.047	38	1.229	0.037
16	1.237	0.058	39	1.210	0.050
17	1.211	0.042	40	1.229	0.035
18	1.230	0.046	41	1.212	0.054
19	1.231	0.036	42	1.231	0.058
20	1.219	0.055	43	1.215	0.046
21	1.229	0.045	44	1.236	0.037
22	1.225	0.041	45	1.233	0.033
23	1.237	0.051	46	1.230	0.044

Other studies[6–8] have slightly lower values of refractive index for polystyrene, Matheson *et al.*[7] and Sultanova *et al.*[8] being closer to our value than Ma *et al.*[6]

The result that is the most relevant to our study is that of Miles *et al.*[9] who determined the refractive index of different sized polystyrene beads. Whilst the values reported by Miles *et al.* and this work agree within error, the larger value of Miles *et al.* compared to all previous works[5–8] cannot be repeated in our fitting process by including values of real refractive indices in the range 1.62–1.65.

The variation of refractive index dispersion for the different polystyrene beads shown in Fig. 6 could indicate small chemical or physical differences in the polymer material during synthesis of the bead. However, there were two assumptions made in the fitting of Mie resonance wavelengths that could also lead to artefacts when considering individual beads. The first assumption was that the polystyrene beads were all perfectly spherical. Mie scattering of droplets under small deformation is shown[33,34] to result in resonances which shift, broaden and split as the droplet asymmetry increases. Careful inspection of the experimental Mie spectra for polystyrene beads showed no discernible splitting or broadening of the narrow first-order resonances. The second assumption was that the wavelength dependent refractive index was described accurately by a three-term Cauchy equation; however, there could be a function to the curve which was not taken into account that requires a wavelength-dependent refractive index equation of a different form *i.e.* with more terms.

Conclusions

Forty-six polystyrene beads were optically trapped in air using a counter-propagating trap. Analysis of backscattered light and application of Mie scattering theory resulted in a determination

of radius and new empirical constants for the wavelength dispersion of refractive index for polystyrene beads in air. From an iterative fitting process the polystyrene bead radius was determined with an uncertainty of ±0.4 nm and refractive index dispersion with an uncertainty of ±0.0005. Each polystyrene bead from the same batch was found to have a different radius and refractive index dispersion over the 480–700 nm range. Therefore, the use of a monodisperse value of refractive index for polystyrene bead samples could be problematic when conducting high accuracy work.

This study has demonstrated the successful use of a technique to determine wavelength dependent refractive indices and radii for forty-six polystyrene beads. Comparison to literature indicates that the values of refractive index for polystyrene beads in air and polystyrene beads in aqueous suspension, determined by Bateman *et al.*,[5] are in close agreement. Our analysis demonstrated that the technique is very sensitive and is capable of characterising polydispersity in size and composition for polystyrene beads. Therefore, we recommend that the use of polystyrene beads to calibrate light scattering instruments, for aerosol size measurements, should be treated with caution with regards to the variation in particle size and refractive index within the calibration sample. The study has shown the use of optically trapped polystyrene beads as a solid test aerosol and future studies will investigate different types of solid aerosol.

Acknowledgements

SHJ wishes to thank NERC for funding of grant (NE/HC19I03/1). We thank Wilm Jones (Cardiff University) for assistance in obtaining TEM images. We are also grateful to STFC for support under grants 12130016 and 12230019 for access to the laboratories of the Central Laser Facility at the Research Complex at Harwell.

Notes and references

1 IPCC, Climate Change 2007: The Physical Science Basis. Contribution of Working Group I to the Fourth Assessment Report of the Intergovernmental Panel on Climate Change, Cambridge University Press, Cambridge, UK, 2007.
2 U. Pöschl, *Angew. Chem., Int. Ed.*, 2005, **44**, 7520–7540.
3 R. Friehmelt and S. Heidenreich, *J. Aerosol Sci.*, 1999, **30**, 1271–1279.
4 F. A. Jenkins, *Fundamentals of optics*, McGraw-Hill, 4th edn, 1976.
5 J. B. Bateman, E. J. Weneck and D. C. Eshler, *J. Colloid Sci.*, 1959, **14**, 308–329.
6 X. Ma, J. W. Lu, R. S. Brock, K. M. Jacobs, P. Yang and X.-H. Hu, *Phys. Med. Biol.*, 2003, **48**, 4165–4172.
7 L. A. Matheson and J. L. Saunderson, *Styrene: Its polymers and copolymers and derivatives in Optical and Electrical Properties of Polystyrene*, American Chemical Society, 1952.
8 N. G. Sultanova, I. D. Nikolov and C. D. Ivanov, *Opt. Quantum Electron.*, 2003, **35**, 21–34.
9 R. E. H. Miles, S. Rudić, A. J. Orr-Ewing and J. P. Reid, *J. Phys. Chem. A*, 2010, **114**, 7077–7084.
10 A. D. Ward, M. Zhang and O. Hunt, *Opt. Express*, 2008, **16**, 16390–16403.
11 L. J. Moore, M. D. Summers and G. A. D. Ritchie, *Phys. Chem. Chem. Phys.*, 2013, **15**, 13489–13498.
12 Y. Liu, X. Li, Y. L. Kim and V. Backman, *Opt. Lett.*, 2005, **30**, 2445.
13 A. A. Zardini, U. K. Krieger and C. Marcolli, *Opt. Express*, 2006, **14**, 6951.
14 C. F. Bohren and D. R. Huffman, *Absorption and Scattering of Light by Small Beads*, Wiley Scientific, 1998.
15 P. Chylek, V. Ramaswamy, A. Ashkin and J. M. Dziedzic, *Appl. Opt.*, 1983, **22**, 2302–2307.
16 J. D. Eversole, H.-B. Lin, A. L. Huston, A. J. Campillo, P. T. Leung, S. Y. Liu and K. Young, *J. Opt. Soc. Am. B*, 1993, **10**, 1955.
17 A. K. Gaiglas, L. Wang, V. Karpiak, Y.-Z. Zhang and S. Choquette, *J. Res. NIST*, 2012, **117**, 202–215.
18 D. T. Philips, P. J. Wyatt and R. M. Berkman, *J. Colloid Interface Sci.*, 1970, **34**, 159–162.
19 M. D. King, K. C. Thompson, A. D. Ward, C. Pfrang and B. R. Hughes, *Faraday Discuss.*, 2008, **137**, 173.
20 O. R. Hunt, A. D. Ward and M. D. King, *RSC Adv.*, 2013, **3**, 19448–19454.
21 D. McGloin, *Philos. Trans. R. Soc., A*, 2006, **364**, 3521–3537.
22 M. D. Summers, D. R. Burnham and D. McGloin, *Opt. Express*, 2008, **16**, 11.
23 T. Li, S. Kheifets, D. Medellin and M. G. Raizen, *Science*, 2010, **328**, 1673–1675.
24 R. A. Flynn, B. Shao, M. Chachisvilis, M. Ozkan and S. C. Esener, *Biosens. Bioelectron.*, 2006, **21**, 1029–1036.
25 T. B. Lindballe, M. V. Kristensen, A. P. Kylling, D. Z. Palima, J. Gluckstad, S. R. Keiding and H. Stapelfeldt, *J. Eur. Opt. Soc.-Rapid*, 2011, **6**, 11057.
26 E. Fallman and O. Axner, *Appl. Opt.*, 1997, **36**, 2107–2113.
27 NIST Atomic Spectra Database Lines Data, Ar I and Xe I, http://physics.nist.gov/cgi-bin/ASD/lines1.pl accessed on 03.04.2012.
28 C. Mätzler, IAP Res. Rep., 2002.
29 Duke Scientific Corporation, Technical Note 007B, December 1, 1996.
30 R. J. Mathar, *J. Opt. A: Pure Appl. Opt.*, 2007, **9**, 470.
31 W. H. Press, S. A. Teukolsky, W. T. Vetterling and B. P. Flannery, *Numerical recipes – the art of scientific computing*, Cambridge University Press, 2007.
32 J. L. Huckaby, A. K. Ray and B. Das, *Appl. Opt.*, 1994, **33**, 7112.
33 S. Arnold, D. E. Spock and L. M. Folan, *Opt. Lett.*, 1990, **15**, 1111.
34 G. Schweiger, *Opt. Lett.*, 1990, **15**, 156.

Paper 2: Atmospherically relevant core–shell aerosol studied using optical trapping and Mie scattering

S. H. Jones, M. D. King, and A. D. Ward

Chemical Communications, 2015, 51, 4914-4917.

Within this partly co-authored work, I declare that the following contributions are entirely my own work:

- Conducted the experiments and collected and analysed the data.
- Authored the paper.
- Contributed significantly to the design of the experiment.
- Contributed to drawing the conclusions of the paper.

ChemComm

COMMUNICATION

View Article Online
View Journal | View Issue

Cite this: *Chem. Commun.*, 2015, **51**, 4914

Received 9th December 2014,
Accepted 13th February 2015

DOI: 10.1039/c4cc09835h

www.rsc.org/chemcomm

Atmospherically relevant core–shell aerosol studied using optical trapping and Mie scattering

S. H. Jones,[ab] M. D. King[b] and A. D. Ward*[a]

Solid core–liquid shell aerosols have been trapped in a counter-propagating optical trap confirming potential core–shell morphology in the atmosphere. Mie spectroscopy can be used to measure the core radius and film thickness to 0.5 and 1 nm precision respectively and to measure the wavelength dependent refractive indices of silica (core) and oleic acid (shell).

An atmospherically relevant core–shell aerosol has been generated and studied in the laboratory with precise (±1 nm) determination of shell thickness. The combination of optical trapping and Mie scattering has been used to study oleic acid coated silica beads and to determine the core silica size to ±0.5 nm and the wavelength dependent refractive index to an uncertainty of ~0.0008 at 589 nm. Oleic acid shell thickness has been determined to ±1 nm and the wavelength dependent refractive index of the shell can be described by an uncertainty of ~0.0007 at 589 nm.

The prevalence of aerosols in the lowest layer of the atmosphere, the troposphere, is well known,[1] however, their contribution to the Earth's climate remains uncertain.[1] Aerosols contribute to the climate in two ways; directly, by scattering and absorbing solar radiation, and indirectly, by acting as cloud condensation nuclei (CCN) and influencing cloud radiative properties.[1] Aerosols exist as a complex mixture of chemicals[2] and morphologies, which influences their ability to form CCN and scatter or absorb radiation. Organic coatings are thought to exist on the surface of aerosols[3–11] but direct evidence is difficult to obtain as atmospheric sampling and subsequent analytical techniques such as Electron Microscopy (EM) often require contact methods which can change the morphology of the sampled aerosol. The presence of an organic coating or shell surrounding the aerosol core has the ability to influence water uptake of an aerosol,[11] the amount of scattered light[12] or the amount of absorbed solar radiation and to affect how the aerosol behaves in subsequent heterogeneous reaction with gas-phase oxidants. It is therefore important to characterise the optical properties of coated aerosols to further understand their effect on the climate.

Mineral dust aerosol is one of the most prevalent sources of solid atmospheric aerosol, it is emitted into the atmosphere at around 1000–4000 Tg per year.[1] Typical mineral particle diameters range from 0.5 μm to 100 μm and contain silica.[13] Silica beads of approximately 1 μm radius were therefore selected to represent solid aerosol. Once airborne, mineral aerosol may come into contact with a large variety of chemical species and can become coated. Oleic acid is a typical organic component found in the troposphere,[14] and was selected as the coating material for the silica beads in this experiment. The study reported here details the use of a counter-propagating optical trap and Mie scattering to study and characterise laboratory generated aerosol of silica beads coated with oleic acid.

There have been a number of contact and non-contact studies on core–shell systems reported in the literature, *e.g.*[15–27] The most relevant study is that by Hightower *et al.*,[18] who trapped glass microspheres of ~4 μm radius in vacuum using a quadrupole trap. The glass beads were coated in glycerine and the scattered light intensity was recorded at a fixed angle during the evaporation of glycerine. Changes in intensity were compared to calculations based on Mie theory to confirm that a concentric layered sphere was trapped. Other associated core–shell studies[22,23] have also been conducted on chemicals not commonly found in the atmosphere; ~20 μm radius Santovac 5 (polyphenol ether) droplets coated in a layer of Fomblin (perfluorinated polyether) levitated in an Electrodynamic balance (EDB).

In the current study we report, to the best of our knowledge, the first optical trapping study of an atmospherically relevant (in terms of composition, size and trapping medium) coated solid aerosol, characterised using white light Mie scattering. The wavelength dependent refractive indices of both the material that forms the coating and the core have been determined as well as the core aerosol radius and coating thickness. We demonstrate that core–shell aerosol may form in the atmosphere.

[a] *Central Laser Facility, Research Complex at Harwell, Rutherford Appleton Laboratory, Didcot, Oxon, OX11 0FA, UK. E-mail: andy.ward@stfc.ac.uk*
[b] *Department of Earth Sciences, Royal Holloway University of London, Egham, Surrey, TW20 0EX, UK*

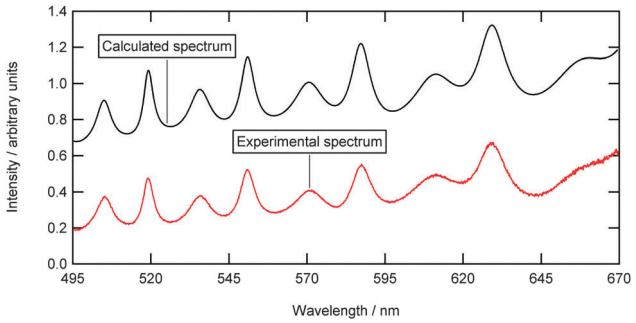

Fig. 1 A typical experimental Mie spectrum is shown in the lower trace (red) for an optically trapped oleic acid droplet. The upper trace (black) is the calculated Mie theory model for a trapped droplet of radius 1.0551 μm, having a refractive index dispersion of, $n = 1.4554 + \frac{4565}{\lambda^2} + \frac{1 \times 10^8}{\lambda^4}$.

A vertically aligned counter-propagating optical trap was used to trap individual silica beads (Bangs Laboratories, SS04N, Lot number 7920, non-porous, 1.035 μm radius) in dry nitrogen (relative humidity $< 10\%$) as a proxy for mineral dust. The optical trapping of silica beads has been studied in detail by Rkiouak *et al.*[28] Of the 35 silica beads captured in our study, the surface of 17 beads were coated with a thin film of oleic acid. Three of these coated beads were selected, at random, for detailed characterisation and analysis. The optical set-up has been described in detail in a previous publication[29] and will only be briefly discussed here. Once trapped, the aerosol is illuminated with white light from an LED, and the backscattered light from the particle is collected and directed into a spectrograph to produce a Mie spectrum as shown in Fig. 1.

To use core–shell Mie theory to determine the oleic acid shell thickness, the refractive index dispersion of silica particles and oleic acid droplets were measured separately and these values were then applied to the core–shell Mie calculation without further change. Silica is optically well characterised; however, the refractive index of a silica bead can vary depending on the method of manufacture, specifically at the surface of the bead. Values of refractive index for oleic acid at the sodium D line are widely available in the literature[30] but the wavelength dependent dispersion is not well reported.

To determine the refractive index dispersion of oleic acid, a 0.1 g L^{-1} solution of sodium chloride was atomised and dried to produce Aitken nuclei in nitrogen which were passed over a heated oleic acid reservoir held at a temperature of between 120–130 °C. The flow was then cooled to produce oleic acid droplets that were carried in nitrogen into the trapping cell. An oleic acid droplet was trapped and grown in size through collisions with other oleic acid droplets until it was $\sim$2 μm in diameter. A typical Mie spectrum for the resulting trapped droplet of oleic acid is shown in Fig. 1. Mie theory[31] was used to model the measured Mie spectrum and determine the droplet radius and the wavelength dependent refractive index of oleic acid. The refractive index dispersion was found by numerically determining the global minimum in deviation between the experimental data and the calculated Mie spectrum when varying size and refractive index dispersion.[29,32] The error in identifying the position of the global minimum was propagated to the reported errors in particle size and refractive index. There is an excellent agreement between the calculated and experimental Mie spectrum, as evidenced by the root mean square value of χ = 0.1764 nm, (the average difference in wavelength per peak between the calculated and experimental peak positions[29]) and the traces in Fig. 1. The determination of the wavelength dependent dispersion for the oleic acid is specific to our experimental conditions and, as such, is ideally suited for application to the core–shell model rather than using the literature value reported at a single wavelength.

Following the determination of the wavelength dependent dispersion of an oleic acid droplet, the next step was to trap a silica bead and characterise its size and wavelength dependent refractive index. The trapping cell was cleaned and dried and silica beads were atomised and carried to the cell in nitrogen. A single silica bead was optically trapped in air and illuminated with white LED light, resulting in a Mie spectrum, as shown in Fig. 2. Mie theory was then used to model the experimental data. The determined refractive index for the silica bead shown in Fig. 2 is 1.3664 at 589 nm which is in agreement with other studies[33,34] (1.37 and 1.39) conducted on silica beads from the same manufacturer.

Following determination of the parameters in Table 1, the trapped silica beads were coated with oleic acid by producing a supersaturation of oleic acid vapour in the trapping environment. A flow of nitrogen was passed over a heated oleic acid reservoir (between 110–130 °C) and subsequently cooled to room temperature and directed into the trapping cell, where the oleic acid condensed on to the surface of the silica bead to form a uniform thin film. Mie spectra were recorded throughout the coating process to assess film formation and measure film thickness.

On exposure to a supersaturated environment of gaseous oleic acid the position of the Mie peaks shifted to longer wavelengths in comparison to that of uncoated silica, which was indicative of thin film formation. An example spectrum

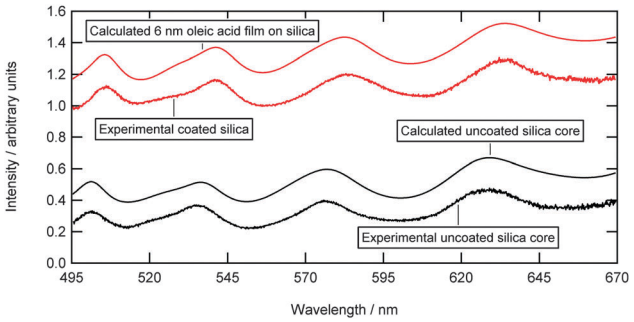

Fig. 2 The lower two traces (black) show a typical experimental Mie spectrum for an optically trapped silica bead (lowest trace) and its Mie model (trace above) for a silica bead of 0.9559 μm radius, with a refractive index dispersion of, $n = 1.3548 + \frac{3720}{\lambda^2} + \frac{1 \times 10^8}{\lambda^4}$. The upper two traces (red) represent a coated experimental Mie spectrum (lower trace) after 140 seconds exposure of the trapped silica bead to oleic acid vapour and the core–shell Mie model (uppermost trace) for a 6 nm thick oleic acid film on the core silica bead.

Table 1 Radii and refractive index dispersions for an oleic acid droplet and three individual silica beads obtained using Mie theory[a 31]

Species	Radius/μm	A	B/nm^2	C/nm^4	χ/nm
Oleic acid	1.0551 ± 0.0004	1.4554 ± 0.0005	4565 ± 70	1×10^8	0.1764
Silica 1	0.9570 ± 0.0005	1.3587 ± 0.0007	3250 ± 100	1×10^8	0.3715
Silica 2	0.9493 ± 0.0005	1.3609 ± 0.001	2995 ± 35	1×10^8	0.3729
Silica 3	0.9559 ± 0.0005	1.3548 ± 0.001	3720 ± 50	1×10^8	0.3136

[a] A, B and C are calculated empirical coefficients in the Cauchy equation.

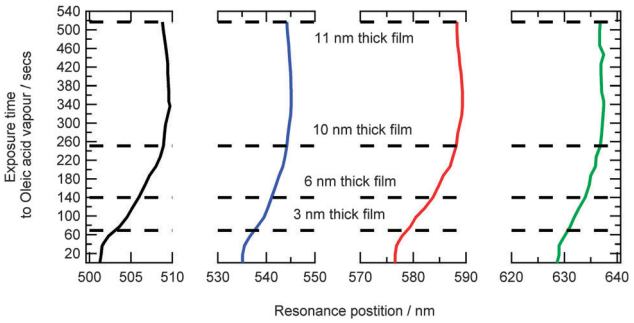

Fig. 3 The solid lines show the four peak positions shifting with increasing exposure time to gaseous oleic acid for Silica bead 3 in Table 1. The dashed lines indicate where experimental peaks shifts correspond to the stated oleic acid film thicknesses calculated from core–shell Mie theory.[35,36]

illustrating the shift is shown in Fig. 2 for a 6 nm oleic acid film. The experimental shifts for each peak in the spectrum throughout the coating process can be seen in Fig. 3. With increasing exposure time to gaseous oleic acid, the experimental peak positions shifted to longer wavelengths, indicative of an increase in film thickness. Core–shell Mie theory[35,36] was used to determine the film thickness at selected time points throughout the experiment, as shown in Fig. 3. The film thickness increases with prolonged exposure time to oleic acid and the measured film thickness increases from 3 nm to 11 nm ± 1 nm for the selected time points in Fig. 3. Previous studies on larger particles have observed a poorer quality of fit with increasing film thickness for thicker films.[17,20] Kaiser *et al.*,[20] stated the different densities of the coating and core material could influence formation of a non-concentric coating.

From the agreement between experimental and calculated data for a core–shell system we conclude that the silica bead is uniformly coated. If the bead were non-uniformly coated, *e.g.* if a 'droplet' of coating material was present only on one part of the silica surface, there would be a reduction in intensity of the experimental positions. Depending on the exact geometry of the system, it could also be possible to observe almost a complete disappearance of the Mie spectrum.[37] Neither of these effects was observed experimentally.

Other effects were also considered, such as, laser heating, a change in the refractive index of the surrounding medium, or loss of symmetry in aerosol morphology. Laser heating from 25 mW of laser trapping power could cause a temperature increase in the trapped uncoated silica bead. Assuming a conservative 1 °C temperature increase,[38] the associated thermal expansion of the silica bead would cause the peak positions to shift wavelength by <1 nm, which is negligible when compared to the peak shifts arising from the presence of a 1 nm oleic acid film on a trapped silica bead >1 nm. Peak shifts arising from changes in the refractive index of the surrounding medium *i.e.* the difference of a bead being trapped in dry or moist air result in peak shifts of <1 nm. It is also assumed that the trapped particle is spherical, as we do not observe splitting or broadening of the Mie peaks.[39,40]

From the detailed analysis of three experimental spectra, the agreement between our calculated results using core–shell Mie theory[35,36] and our experimental data indicates that we have successfully formed a concentric coating of oleic acid on an optically trapped silica bead. The coating is also seen to increase in thickness with increasing exposure time to a supersaturated vapour of oleic acid. It is likely that this geometry will exist naturally if it formed in the laboratory from atmospheric proxies of silica and oleic acid and therefore could be influential in the atmosphere.

The ability to generate core–shell aerosol and assess shell growth combined with the determination of the wavelength dependent refractive index of both the core aerosol and the shell indicates an important step in atmospheric chemistry, towards further understanding the impact of coated aerosol on the atmosphere. Further studies into different core–shell systems and heterogeneous reactions are required to verify the hypothesis.

The authors would like to thank the Central Laser Facility for laboratory access at the Research Complex at Harwell under grants 13230007, 12230019 and 12130016. SHJ would like to acknowledge NERC for PhD funding grant NE/H019103/1.

Notes and references

1 IPCC, 2013: *Climate Change 2013: The Physical Science Basis. Contribution of Working Group I to the Fifth Assessment Report of the Intergovernmental Panel on Climate Change*, ed. T. F. Stocker, D. Qin, G.-K. Plattner, M. Tignor, S. K. Allen, J. Boschung, A. Nauels, Y. Xia, V. Bex and P. M. Midgley, Cambridge University Press, Cambridge, United Kingdom and New York, NY, USA, pp. 1535.
2 U. Pöschl, *Angew. Chem., Int. Ed. Engl.*, 2005, **44**, 7520–7540.
3 D. C. Blanchard, *Science*, 1964, **146**, 396–397.
4 G. B. Ellison, F. Tuck and V. Vaida, *J. Geophys. Res.*, 1999, **104**, 11633–11641.
5 D. J. Donaldson and V. Vaida, *Chem. Rev.*, 2006, **106**, 1445–1461.
6 P. S. Gill, T. E. Gradel and C. J. Weschler, *Rev. Geophys. Space Phys.*, 1983, **21**, 903–920.
7 H. Tervahattu, K. Hartonen, V. Kerminen, K. Kupiainen, T. Koskentalo, A. F. Tuck and V. Vaida, *J. Geophys. Res.*, 2002, **107**, AAC 1-1–AAC 1-8.
8 B. E. Wyslouzil, G. Wilemski, R. Strey, C. H. Heath and U. Dieregsweiler, *Phys. Chem. Chem. Phys.*, 2006, **8**, 54–57.
9 A. H. Falkovich, *J. Geophys. Res.*, 2004, **109**, D02208.
10 D. M. Cwiertny, M. A. Young and V. H. Grassian, *Annu. Rev. Phys. Chem.*, 2008, **59**, 27–51.

11 M. D. King, K. C. Thompson and A. D. Ward, *J. Am. Chem. Soc.*, 2004, **126**, 16710–16711.
12 Y. Li, M. J. Ezell and B. J. Finlayson-pitts, *Atmos. Environ.*, 2011, **45**, 4123–4132.
13 K. H. Wedepohl, *Geochim. Cosmochim. Acta*, 1995, **59**, 1217–1232.
14 W. F. Rogge, L. Hildemann, M. A. Mazurek, G. R. Cass and B. Simoneit, *Environ. Sci. Technol.*, 1991, **25**, 1112–1125.
15 E. R. Garland, A. D. Lee, T. Baer and L. I. Clarke, *J. Phys. Chem. C*, 2009, **113**, 2141–2148.
16 Y. Katrib, S. Martin, H. Hung, Y. Rudich, H. Zhang, J. G. Slowik, P. Davidovits, J. T. Jayne and D. R. Worsnop, *J. Phys. Chem. A*, 2004, **108**, 6686–6695.
17 A. Abo Riziq, M. Trainic, C. Erlick, E. Segre and Y. Rudich, *Atmos. Chem. Phys.*, 2008, **8**, 1823–1833.
18 R. L. Hightower, C. B. Richardson, H. B. Lin, J. D. Eversole and A. J. Campillo, *Opt. Lett.*, 1988, **13**, 946–948.
19 W. Li, S. Rassat, W. Foss and E. Davis, *J. Colloid Interface Sci.*, 1994, **162**, 267–278.
20 T. Kaiser, G. Roll and G. Schweiger, *Appl. Opt.*, 1996, **35**, 5918–5924.
21 J. F. Widmann, C. L. Aardahl, T. J. Johnson and E. J. Davis, *J. Colloid Interface Sci.*, 1998, **199**, 197–205.
22 J. Huckaby and A. Ray, *Langmuir*, 1995, **11**, 80–86.
23 A. K. Ray and R. Nandakumar, *Appl. Opt.*, 1995, **34**, 7759–7770.
24 D. P. Veghte, M. B. Altaf and M. A. Freedman, *J. Am. Chem. Soc.*, 2013, **135**, 16046–16049.
25 J. Buajarern, L. Mitchem and J. P. Reid, *J. Phys. Chem. A*, 2007, **111**, 9054–9061.
26 B. J. Dennis-Smither, K. L. Hanford, N.-O. A. Kwamena, R. E. H. Miles and J. P. Reid, *J. Phys. Chem. A*, 2012, **116**, 6159–6168.
27 M. Song, C. Marcolli, U. K. Krieger, D. M. Lienhard and T. Peter, *Faraday Discuss.*, 2013, **165**, 289–316.
28 L. Rkiouak, M. J. Tang, J. C. J. Camp, J. McGregor, I. M. Watson, R. A. Cox, M. Kalberer, A. D. Ward and F. D. Pope, *Phys. Chem. Chem. Phys.*, 2014, **16**, 11426–11434.
29 S. H. Jones, M. D. King and A. D. Ward, *Phys. Chem. Chem. Phys.*, 2013, **15**, 20735–20741.
30 *CRC Handbook of Chemistry and Physics*, CRC Press, Taylor and Francis, Boca Raton, FL, 86th edn, 3-406 and 10-249, 2005.
31 C. F. Bohren and D. R. Huffman, *Absorption and Scattering of Light by Small Particles*, Wiley, 1998.
32 J. L. Huckaby, A. K. Ray and B. Das, *Appl. Opt.*, 1994, **33**, 7112–7125.
33 J. J. Valle-Delgado, J. A. Molina-Bolívar, F. Galisteo-González, M. J. Gálvez-Ruiz, a. Feiler and M. W. Rutland, *J. Chem. Phys.*, 2005, **123**, 034708.
34 R. S. Conroy, B. T. Mayers, D. V. Vezenov, D. B. Wolfe, M. G. Prentiss and G. M. Whitesides, *Appl. Opt.*, 2005, **44**, 7853–7857.
35 A. L. Aden and M. Kerker, *J. Appl. Phys.*, 1951, **22**, 1242–1246.
36 O. B. Toon and T. P. Ackerman, *Appl. Opt.*, 1981, **20**, 3657–3660.
37 J. P. Reid, B. J. Dennis-Smither, N.-O. A. Kwamena, R. E. H. Miles, K. L. Hanford and C. J. Homer, *Phys. Chem. Chem. Phys.*, 2011, **13**, 15559–15572.
38 R. J. Hopkins, L. Mitchem, A. D. Ward and J. P. Reid, *Phys. Chem. Chem. Phys.*, 2004, **6**, 4924–4927.
39 S. Arnold, D. E. Spock and L. M. Folan, *Opt. Lett.*, 1990, **15**, 1111–1113.
40 G. Schweiger, *Opt. Lett.*, 1990, **15**, 156–158.

Paper 3: Degradation and rearrangement of a lung surfactant lipid at the air-water interface during exposure to the pollutant gas ozone

K. C. Thompson, **S. H. Jones**, A. R. Rennie, M. D. King, A. D. Ward, B. R. Hughes, C. O. M. Lucas, R. A. Campbell and A. V. Hughes

Langmuir, 2013, 29 (14), 4594-4602.

Within this partly co-authored work, I declare that the following contributions are entirely my own work:

- Conducted the experiments on different deuterations of POPC and collected and analysed the subsequent data.
- Commented on drafts of the paper.

Langmuir

Article

pubs.acs.org/Langmuir

Degradation and Rearrangement of a Lung Surfactant Lipid at the Air−Water Interface during Exposure to the Pollutant Gas Ozone

Katherine C. Thompson,*[,†] Stephanie H. Jones,[‡,§] Adrian R. Rennie,[∥] Martin D. King,[‡] Andrew D. Ward,[§] Brian R. Hughes,[†] Claire O. M. Lucas,[‡,⊥] Richard A. Campbell,[#] and Arwel V. Hughes[⊥]

[†]Department of Biological Sciences and Institute of Structural and Molecular Biology, Birkbeck College, University of London, Malet Street, London WC1E 7HX, U.K.

[‡]Department of Earth Sciences, Royal Holloway University of London, Egham, Surrey TW20 0EX, U.K.

[§]STFC, Lasers for Science Facility, Central Laser Facility, Research Complex at Harwell, Rutherford Appleton Laboratory, Harwell Oxford, Didcot, Oxfordshire OX11 0FA, U.K.

[∥]Materials Physics, Department of Physics and Astronomy, Uppsala University, 75120 Uppsala, Sweden

[⊥]ISIS Pulsed Neutron and Muon Source, STFC Rutherford Appleton Laboratory, Harwell Oxford, Didcot, Oxfordshire OX11 0QX, U.K.

[#]Institut Laue Langevin, 6 Rue Jules Horowitz F-38042, Grenoble, Cedex 09, France

Supporting Information

ABSTRACT: The presence of unsaturated lipids in lung surfactant is important for proper respiratory function. In this work, we have used neutron reflection and surface pressure measurements to study the reaction of the ubiquitous pollutant gas-phase ozone, O_3, with pure and mixed phospholipid monolayers at the air−water interface. The results reveal that the reaction of the unsaturated lipid 1-palmitoyl-2-oleoyl-*sn*-glycero-3-phosphocholine, POPC, with ozone leads to the rapid loss of the terminal C9 portion of the oleoyl strand of POPC from the air−water interface. The loss of the C9 portion from the interface is accompanied by an increase in the surface pressure (decrease in surface tension) of the film at the air−water interface. The results suggest that the portion of the oxidized oleoyl strand that is still attached to the lipid headgroup rapidly reverses its orientation and penetrates the air−water interface alongside the original headgroup, thus increasing the surface pressure. The reaction of POPC with ozone also leads to a loss of material from the palmitoyl strand, but the loss of palmitoyl material occurs after the loss of the terminal C9 portion from the oleoyl strand of the molecule, suggesting that the palmitoyl material is lost in a secondary reaction step. Further experiments studying the reaction of mixed monolayers composed of unsaturated lipid POPC and saturated lipid dipalmitoyl-*sn*-glycero-3-phosphocholine, DPPC, revealed that no loss of DPPC from the air−water interface occurs, eliminating the possibility that a reactive species such as an OH radical is formed and is able to attack nearby lipid chains. The reaction of ozone with the mixed films does cause a significant change in the surface pressure of the air−water interface. Thus, the reaction of unsaturated lipids in lung surfactant changes and impairs the physical properties of the film at the air−water interface.

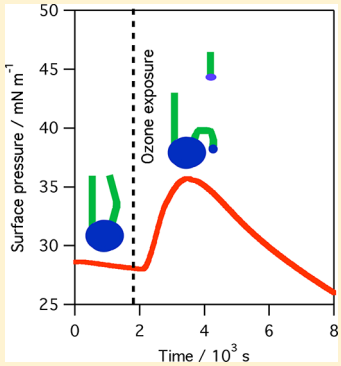

INTRODUCTION

The air−liquid interface of the lung consists of an aqueous fluid subphase, on the surface of which lies a self-assembled mixture of lipids and proteins that protrude into the air. The collective mixture is known as lung surfactant.[1] Avery and Mead first suggested in 1959 that the death of prematurely born babies from respiratory failure was related to a deficiency in lung surfactant.[2] It is now known that the surfactant plays the vital role of lowering the surface tension of the lung fluid, thus allowing proper respiratory function.[1,3] The main components of lung surfactant are lipids (∼90% by weight) and proteins (∼10%). Of the lipid fraction about 70−80% by weight are phosphocholine lipids, with the major species being the fully saturated lipid dipalmitoyl-*sn*-glycero-3-phosphocholine, DPPC. Unsaturated phospholipids such as 1-palmitoyl-2-oleoyl-*sn*-glycero-3-phosphocholine, POPC, make up 30−50% of the total phospholipid content.[1,3] The role of the unsaturated lipids is thought to be to fluidize the monolayer at body temperature and thus increase the rate of spreading across the interface and to facilitate the readsorption of surface-active material during the expansion of the lung.[4,5] The exact composition of the lipid mixture appears to be of great importance, as shown by Walther et al. who looked at the oxygenation of rats treated with a synthetic mimic of lung surfactant protein with lipid mixtures containing different ratios of saturated to unsaturated lipids and found significant improvement when the higher ratios of unsaturated lipids, as are found in natural lung surfactant, were used.[6] Other studies have revealed the importance of lung

Received: October 31, 2012
Revised: March 11, 2013
Published: March 12, 2013

   dx.doi.org/10.1021/la304312y | *Langmuir* 2013, 29, 4594−4602

Scheme 1. Initial Reaction of POPC with Gaseous Ozone Leading to the Cleavage of the Carbon−Carbon Double Bond of the Oleoyl Strand[a]

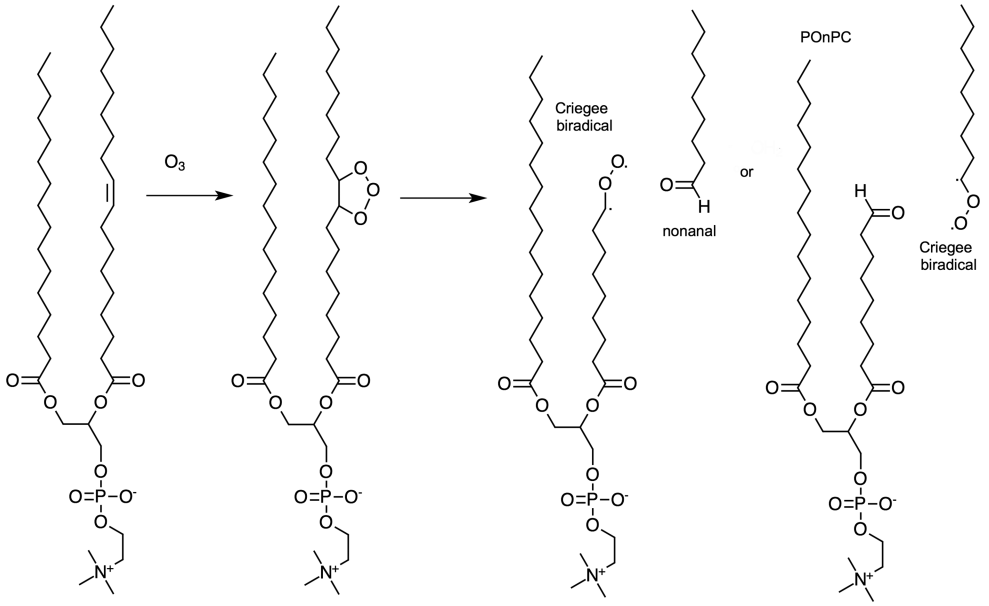

[a]The scheme shows the products formed to be a Criegee biradical and an aldehyde. The aldehydes formed would be expected to be further oxidized to carboxylic acids given the experimental conditions.[13]

surfactant proteins that associate with the more fluid lipids and thus prevent the loss of these lipids when high surface pressures are reached.[5,7] A change to the chemical structure of the unsaturated lipids would be expected to alter both the physical properties of the lipids themselves and also the degree of association between the lipid and the surfactant proteins.

The inhalation of the ubiquitous gas-phase air pollutant ozone, O_3, is known to lead to an increase in deaths from respiratory causes.[8] The initial mechanism by which ozone exposure leads to respiratory distress is not fully understood, but it is widely believed that ozone reacts with various species present in lung surfactant including unsaturated lipids.[9,10] In contrast to saturated lipids such as DPPC, monolayers of unsaturated lipids spread at the air−water interface have been shown to react rapidly when exposed to laboratory air but are unreactive when exposed to an inert gas.[11,12] Other workers have shown that the pollutant gas ozone, present in low concentrations in laboratory air, reacts with POPC and its structural isomer 1-oleoyl-2-palmitoyl-*sn*-glycero-3-phosphocholine, OPPC, but not DPPC, at the air−water interface, leading to a range of products.[13,14] In our previous study, we showed that when a film of POPC is exposed to pure oxygen no reaction is observed but when gaseous ozone is present a reaction occurs that leads to a very rapid increase in surface pressure (i.e., a rapid decrease in surface tension).[15] The rapid increase in surface pressure was followed by a relatively slow decrease in surface pressure. Neutron reflection studies were used to follow the amount of lipid residing at the air−water interface as a function of time. The studies demonstrated that the slow decrease in surface pressure was accompanied by a loss of material from the palmitoyl strand of the POPC lipid from the air−water interface, indicating either degradation of the palmitoyl strand or the loss of whole lipid molecules from the interface.[15] The chemical or structural changes that cause the surface pressure to increase initially could not be elucidated on the basis of the experiments performed in our earlier work. Hence we have used a different approach in the experiments presented here that provides new insight into the changes occurring at the interface causing the surface pressure to rise. Our new neutron reflection experiments on labeled (partially deuterated) lipids were designed to determine the relative amounts of different moieties of the lipid that could be directly related to the kinetics of reaction and provide mechanistic information.

The initial steps in the reaction of ozone with POPC are expected to lead to the cleavage of the carbon−carbon double bond on the oleoyl chain and either nonanal and a Criegee biradical or 1-palmitoyl-2-(9′-oxo-nonanoyl)-*sn*-glycero-3-phosphocholine, POnPC, and a Criegee biradical, as shown in Scheme 1.[16] The aldehydes formed would be expected to oxidize further to yield carboxylic acids under the experimental conditions used, hence POnPC would oxidize to yield 1-palmitoyl-2-azelaoyl-*sn*-glycero-3-phosphocholine, PAzPC.[13] Lai et al. used PTFE tape to remove (skim) material from the air−water interface after a monolayer of POPC was exposed to gas-phase ozone. The material from several runs was removed from the PTFE tape and pooled together before analysis by mass spectrometry. Lai et al. found evidence for the presence of both POnPC and PAzPC at the interface following the reaction of POPC with gas-phase ozone, with the relative amounts of PAzPC to POnPC increasing with the extent of ozone exposure.[13]

In the present study, we have used neutron reflection with the selective deuteration of POPC to understand more fully the reaction mechanism and related changes in surface pressure. In particular, we want to determine whether the initial increase in surface pressure observed when POPC monolayers are exposed to ozone is caused by the insertion of the newly formed C9 fragment into the lipid monolayer or by a rearrangement of the oxidized lipid left at the interface. We also investigate whether the oxidation of POPC in a mixture of POPC and DPPC leads to the loss of saturated lipid DPPC, a major component of lung

dx.doi.org/10.1021/la304312y | *Langmuir* 2013, 29, 4594−4602

lining fluid, from the interface. DPPC alone does not react with ozone at the air−water interface,[15] but the Criegee intermediates formed from the reaction of ozone with POPC will react further and may attack nearby saturated lipid chains or may decompose, generating very reactive OH radicals that could go on to react with DPPC.[17] Experiments were therefore performed on mixed films of POPC and DPPC to determine whether exposure to ozone causes damage to the saturated lipid DPPC when present in the monolayer with unsaturated lipid POPC.

EXPERIMENTAL METHODS

The reaction between gas-phase ozone and phosphocholine lipid monolayers, either pure POPC or a mixture of POPC and DPPC, at the air−water interface was studied by recording the neutron reflectivity of the interface and the surface pressure simultaneously as the monolayers were exposed to a dilute gaseous mixture of ozone in molecular oxygen. The monolayers were prepared on an aqueous subphase contained in a PTFE-lined Langmuir trough (Nima Technology) housed in an approximately 45 L, gastight aluminum chamber with a glass lid. The chamber lid was removed to allow the addition of the lipid, as a 1 mg mL^{-1} solution in chloroform, to the surface of the subphase. In the case of experiments with POPC and DPPC, binary lipid mixtures in chloroform were prepared with a total lipid concentration of 1 mg mL^{-1}. The chloroform was allowed to evaporate under a flow of oxygen gas before the experiments commenced. The experiments were performed by continuously flowing a dilute (∼0.1 − 2 ppm) mixture of ozone in oxygen (BOC, ≥ 99.5%) at a constant flow rate of between 1 and 5 L min^{-1}, with 5 L min^{-1} used for all experiments on Pd_{17}OPC (structure shown in Figure 1) through the chamber. A continuous flow was used to ensure

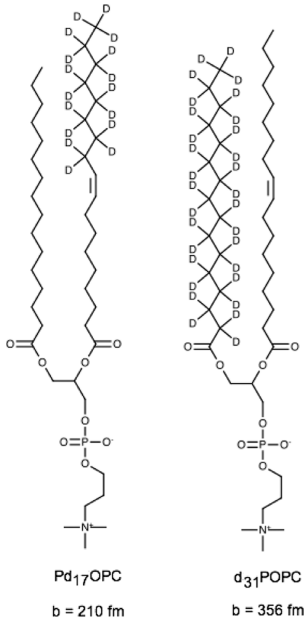

Figure 1. Structure and deuteration schemes of Pd_{17}OPC (left) and d_{31}POPC (right).

that the ozone concentration was not depleted over the course of the experiment. The ozone was generated by passing dry oxygen through a commercial ozonizer (UVP) that was initially switched off. Switching on the ozonizer generated ozone from the photolysis of molecular oxygen. The surface pressure, equal to the difference between the surface tension of the gas−water interface of pure water and the surface tension of the interface under study, was measured using a Wilhelmy plate made from filter paper (Whatman). In most experiments, the film was added to the surface, compressed to a surface pressure that was about 5 mN m^{-1} greater than the starting surface pressure and then expanded back to the starting surface pressure. Starting surface pressures of 10 to 40 mN m^{-1} were used. The surface pressure and neutron reflectivity of the film were then monitored continuously while the surface area was held constant and the film was exposed to gas-phase ozone. In a typical experiment, the neutron reflectivity data was recorded continuously for 30 min before the ozonizer was switched on. Control runs were performed in which monolayers of the lipids were exposed to oxygen only.

The neutrons entered and exited the chamber via fused quartz windows. For experiments performed above room temperature, the windows were heated to prevent the condensation of water vapor. The reflection of visible laser light at the interface was used to check the height alignment of the interface with respect to the neutron beam. The reflectivity of the gas−liquid interface to neutrons was monitored using either the SURF reflectometer at ISIS, Rutherford Appleton Laboratory, Didcot, U.K.[18] or the FIGARO reflectometer at the Insitut Laue Langevin, Grenoble, France.[19] The incident neutron beam, containing neutrons with a range of wavelengths, λ (0.5 to 6.5 Å for SURF and 2.2 to 25 Å for FIGARO), was collimated and inclined so that it fell at a grazing angle of incidence, θ, of either 1.5° (SURF) or 0.624° and 3.78° (FIGARO) with respect to the horizontal of the air−liquid interface. The reflectivity R is recorded as a function of momentum transfer normal to the interface, q, given by $q = (4\pi/\lambda)\sin\theta$. All reflectivity data were normalized for the intensity spectrum of the incident beam, and the absolute reflectivity was derived by using a scale factor obtained by measuring the known reflectivity of pure D_2O contained in the trough. The background reflectivity signal, attributed to incoherent scattering, was either subtracted from the recorded reflectivity (FIGARO) using data from the area detector recorded from both sides of the specular ridge or included in the model used to fit the reflectivity data (SURF).

The reflectivity of an interface for neutrons depends upon the neutron scattering length density of the material at the interface, ρ, and the thickness of the interfacial material, δ.[20] The neutron scattering length density is given by eq I below

$$\rho = \frac{\sum_i b_i}{V} \quad \text{(I)}$$

where b_i represents the coherent neutron scattering lengths of the individual nuclei in the compound and V is the volume occupied by one molecule.[20] The coherent scattering lengths of hydrogen, H, and deuterium, D, are of opposite sign with $b = -3.74$ fm in the case of H and 6.67 fm in the case of D.[21] A solution of null reflecting water (NRW) is one that contains 8% by volume D_2O (92% H_2O) and has a scattering length and a scattering length density of zero. No reflection of neutrons occurs from the gas−NRW interface alone. When a monolayer of material such as a lipid is present on an NRW subphase, the reflection of neutrons occurs from the lipid monolayer only. Because the scattering length b of material containing mainly CH_2 groups is very low, $b = -0.8$ fm for CH_2 compared to material containing CD_2 groups, $b = +20$ fm for CD_2, selective deuteration is often used in neutron reflection to highlight different parts of a molecule. In this work, we used two different deuterated isotopologs of POPC-labeled Pd_{17}OPC and d_{31}POPC. See Figure 1 for an illustration of the deuteration schemes.

The number of molecules per unit area, surface coverage Γ, present at an interface is given by

$$\Gamma = \frac{\rho\delta}{b_m} \quad \text{(II)}$$

where ρ is the neutron scattering length density, δ is the film thickness, and b_m is the scattering length of the species in the adsorbed layer.[20] Values for ρ and δ may be obtained from the model fits to measured neutron reflectivity as a function of q. In the case of films containing only one chemical species, b can be calculated using

$$b_m = \sum_i b_i \quad \text{(III)}$$

dx.doi.org/10.1021/la304312y | Langmuir 2013, 29, 4594−4602

where b_i represents the coherent neutron scattering lengths of the individual nuclei in the compound. Thus, the measured neutron reflectivity of the interface can be used to obtain the surface coverage, Γ. In the case where the exact chemical (or rather elemental) composition of the interface is not known, for instance, at any instant during a chemical reaction where there is an unknown amount of reactant and product present, the measured reflectivity can provide the average $\rho\delta$ for the interfacial material.

For the lipid molecules considered in this work, although all parts of the lipid molecule contribute to the observed reflectivity, reflection from monolayers composed of d_{31}POPC is most sensitive to changes to the amount of the palmitoyl strand present, where the scattering length, b, for the palmitoyl tail (306 fm) accounts for 86% of the overall b value. Reflection from monolayers of Pd_{17}OPC is most sensitive to changes in the amount of the terminal portion of the oleoyl chain present, where b for the deuterated C9 tail (169 fm) accounts for 80% of the overall b value for the molecule. In the case of experiments on monolayers initially containing both POPC and DPPC lipids, either deuterated DPPC, d_{62}DPPC, was used with non-deuterated POPC, ^{1}H-POPC, or nondeuterated DPPC, ^{1}H-DPPC, was used with deuterated POPC, d_{31}POPC. Table 1 provides details of the scattering lengths for the different lipid compositions employed in the experiments described here.

Table 1. Formulae and Scattering Lengths, b_m, for the Lipids Used in This Work and an Expected Product, POnPC

lipid	formula	b_m/fm
^{1}H-POPC	$C_{42}H_{82}NO_8P$	33
Pd_{17}OPC	$C_{42}H_{65}D_{17}NO_8P$	210
d_{31}POPC	$C_{42}H_{51}D_{31}NO_8P$	356
^{1}H-DPPC	$C_{40}H_{80}NO_8P$	28
d_{62}DPPC	$C_{40}H_{18}D_{62}NO_8P$	673
^{1}H-POnPC	$C_{33}H_{64}NO_9P$	47
d_{31}POnPC	$C_{33}H_{33}D_{31}NO_9P$	369

Mixed-film experiments were performed with a 1:1 by mass ratio of DPPC and POPC with initial starting pressures of about 20 mN m^{-1} at 31 °C and 40 mN m^{-1} at 21 °C. An experiment with ^{1}H-POPC and d_{62}DPPC in a 1:5 ratio was also performed. The surface pressure versus molecular area isotherm for a 1:1 mixture of DPPC and POPC, shown in Figure 2, differs considerably from that of pure DPPC for which sharp phase transitions can be seen. It has previously been shown that for multilamellar dispersions (i.e., bilayer structures) of 1:1 mixtures of DPPC and POPC in water the liquid crystalline to gel phase transition occurs gradually over the temperature range of 0 to 37 °C.[22] Within this temperature range, the lipid layers exist as inhomogeneous mixtures of a liquid-crystalline phase containing both POPC and DPPC, with domains containing just DPPC in the gel phase. In the case of lipid monolayers, the degree of domain formation will depend on both the temperature and the surface pressure of the monolayer, hence our decision to study the 1:1 DPPC/POPC monolayers both at about 40 mN m^{-1}, 21 °C, and at about 17 mN m^{-1}, 31 °C.

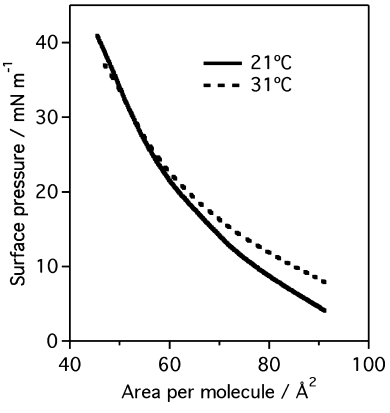

Figure 2. Surface pressure vs mean molecular area isotherms obtained by compressing a fixed amount of a 1:1 mixture of DPPC and POPC on the water surface at 21 and 31 °C.

Avanti Polar Lipids supplied all lipids: ^{1}H-POPC, Pd_{17}OPC (custom synthesis using d_{17}-oleic acid provided by Oxford Isotope Facility), d_{31}POPC, ^{1}H-DPPC, and d_{62}DPPC. The chloroform was from Chromasolv (≥99%, stabilized with ethanol), the D_2O was from Aldrich or EUR-ISOTOP, CEA, Saclay (99.9 atom % D), and the H_2O (18 MΩ cm resistivity) was from a Millipore system.

Typically, the measured neutron reflectivity data was continuously recorded and then coadded in 5 min intervals for each time point. For data interpretation, a least-squares fitting procedure was used to compare the measured reflectivity as a function of q at each time point, and the reflectivity versus q curve was calculated according to Abelès' optical matrix method,[23] assuming a single uniform layer between two semi-infinite media with neutron refractive indices of 1. The layer of material at the interface is characterized by its thickness, δ, and scattering length density, ρ, at each time. The reaction of the lipid monolayer with ozone will cause changes in the chemical composition of the interfacial material, changing the scattering length, b_m, and hence the scattering length density ρ ($\rho = b_m/V$) and potentially the thickness of the layer. Data were fitted using programs that are described elsewhere.[24] Monolayers composed initially of Pd_{17}OPC gave only a weak initial reflectivity signal, and the signal decayed rapidly when the film was exposed to ozone. For the case of thin layers with no refractive index difference between the two bulk phases that are measured at small values of q, the reflectivity changes very little with thickness but depends primarily on the amount of material in the interfacial layer. When fitting the Pd_{17}OPC data, the approach used was as follows: the data for the initial film was fitted by setting the scattering length density to the theoretical value for the whole lipid (1.69×10^{-6} Å^{-2} using a molecular volume of 1247 Å^3 [25]) and fitting the thickness of the layer between the air and the null reflecting water. The thickness, δ, obtained for the layer, (17 ± 2) Å, was then held constant, and the scattering-length density, ρ, was fitted to the remaining data sets. Constraining the thickness to different values between 15 and 20 Å changed the value of the product $\delta\rho$, the amount of material at the surface, by less than 10%. In the case of experiments with mixed lipid films, the decay in the reflectivity of the interface was not large and the data were fitted, allowing both the scattering-length density and the thickness to vary. In all cases, it is the product $\delta\rho$ that is presented because this is the property that can be directly related to surface coverage and is fitted most precisely. Data were collected to provide rapid identification of the changes in surface coverage rather than detailed structural information. The fitting of single data sets measured in a limited range of q was found to be insensitive to details of the structure and to the roughness of the interface (values of up to 6 Å were tested), so all fit results presented used a roughness at the interface of zero.

RESULTS

Reaction of POPC Monolayers with Ozone. The exposure of a monolayer film of Pd_{17}OPC to pure oxygen caused no significant change in the reflectivity of the monolayer, in agreement with our previous work on d_{31}POPC.[15] In contrast, the exposure of a monolayer of Pd_{17}OPC to ozone led to a rapid decrease in the reflectivity of the monolayer film. An example of the change in reflectivity measured when a Pd_{17}OPC monolayer is exposed to ozone is shown in Figure 3.

Fitting the reflectivity data as described previously shows that the product $\rho\delta$ for the interfacial material drops to a factor of ≤0.2 of its initial value, as expected if the deuterated C9 portion of the lipid were lost from the interface and the undeuterated

dx.doi.org/10.1021/la304312y | Langmuir 2013, 29, 4594−4602

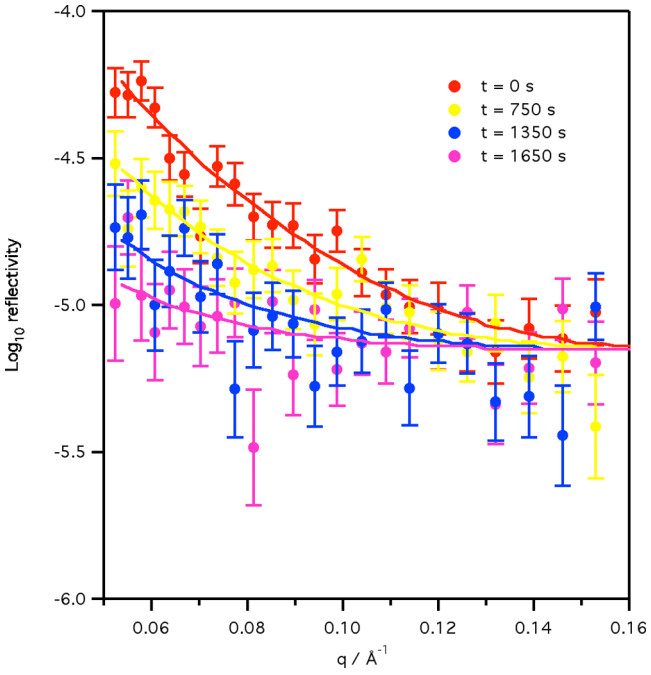

Figure 3. Examples of the reflectivity profiles obtained when a monolayer of $Pd_{17}OPC$ was exposed to gas-phase ozone. The time, *t*, refers to the time since the film was first exposed to a flow of ozone. For this experiment, the starting surface pressure was 28 mN m^{-1}. The data are presented without background subtraction.

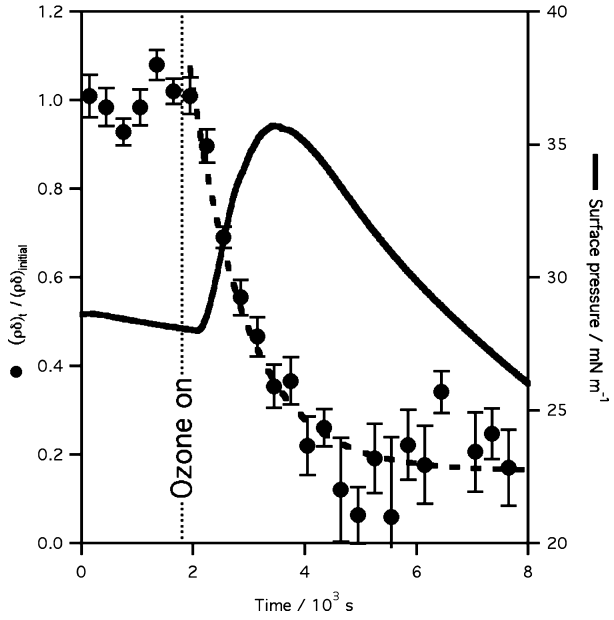

Figure 4. Typical kinetic plot that shows the rapid loss of the deuterated portion of $Pd_{17}OPC$ from the air–water interface (change in $\rho\delta$) and the simultaneous increase in surface pressure with time when a film of $Pd_{17}OPC$ is exposed to gas-phase ozone. The product of the scattering length density and the thickness, $\rho\delta$, falls to a factor of about 0.2 of the initial value. The dashed line indicates an exponential fit to the data giving a lifetime of ~17 min for the $Pd_{17}OPC$ with respect to reaction with ozone. Note that the surface pressure and product $\rho\delta$ are initially anticorrelated. By the time the surface pressure has reached its peak the product $\rho\delta$ has already reduced to a low value, a factor of ~0.3 of its initial value. Although the product $\rho\delta$ has reached a minimum, a factor of ~0.2 of its initial value, after 4000 s exposure to ozone the surface pressure continues to decay further.

portion of the lipid remains at the interface over the time scale studied. The reduction in $\rho\delta$ for the material at the interface occurs rapidly and fits to a single-exponential decay function

$$(\rho\delta)_t = Ae^{-t/\tau} + B \qquad \text{(IV)}$$

where τ is the lifetime of the lipid. The changes in $\rho\delta$ are anticorrelated with the changes in the surface pressure, with the decay in $\rho\delta$ occurring as the surface pressure increases. An example of the change in the fitted value of $\rho\delta$ and the surface pressure with time is shown in Figure 4.

In all cases the decay of $\rho\delta$ observed when $Pd_{17}OPC$ monolayers were exposed to gas-phase ozone fitted well to a single exponential function (IV) suggesting that first-order or pseudofirst order kinetics are followed. The physical interpretation of this is that the reaction of ozone with POPC leads directly to loss of the terminal portion of the oleoyl strand from the air–water interface. Table 2 summarizes the lifetimes of $Pd_{17}OPC$ observed when monolayers of $Pd_{17}OPC$ are exposed to gas-phase ozone.

The experiments on $Pd_{17}OPC$ clearly show that the terminal portion of the oleoyl strand of POPC is rapidly lost from the interface when POPC reacts with gas-phase ozone. The rapid loss of material from the oleoyl strand is correlated with the increase in the surface pressure of the film, with the surface pressure peaking as the amount of C9 material left at the interface approaches its lower limit. To provide a ready comparison with the slow change in reflectivity observed when $d_{31}POPC$ is exposed to ozone a pair of experiments, one using $Pd_{17}OPC$ and one using $d_{31}POPC$, were performed under identical gas-flow conditions and both with a starting surface pressure of ~20 mN m^{-1}. The results are shown in Figure 5.

As Figure 5 clearly shows, when POPC reacts with gas-phase ozone at the air–water interface the loss of material from the C9 terminal portion of the oleoyl strand of POPC occurs on a different time scale from the loss of material from the palmitoyl strand. The loss of material from the oleoyl strand occurs rapidly, and this process is correlated with a rapid increase in surface pressure, as can be seen in Figure 5 by inspecting the data for $Pd_{17}OPC$. In contrast, the reaction of ozone with POPC leads to only a very limited amount of material from the palmitoyl strand of POPC being lost from the interface over the same time scale. The loss occurs very slowly and does not commence until after the surface pressure has peaked and has started its decline, as revealed by the data for $d_{31}POPC$ shown in Figure 5.

Table 2. Lifetimes Obtained from Fitting a Single-Exponential Function to the Decay in the Product $\rho\delta$ Obtained from Fitting the Neutron Reflectivity Data as Described in the Text

initial surface pressure/ mN m^{-1}	ozone mixing ratio/ ppm	lifetime ($\pm\sigma$)/ min
12	0.4	(8 ± 2)
17	~0.1	(16 ± 4)
19	~0.1	(24 ± 8)
28	~0.1	(17 ± 3)

Reaction of Mixed Films of POPC and DPPC with Ozone. Our previous work has shown that when monolayers of the saturated lipid DPPC at the air–water interface are exposed to gas-phase ozone at mixing ratios of a few parts per million, no loss of DPPC from the interface was observed.[15] However, we wished to investigate whether the oxidation of

dx.doi.org/10.1021/la304312y | *Langmuir* 2013, 29, 4594–4602

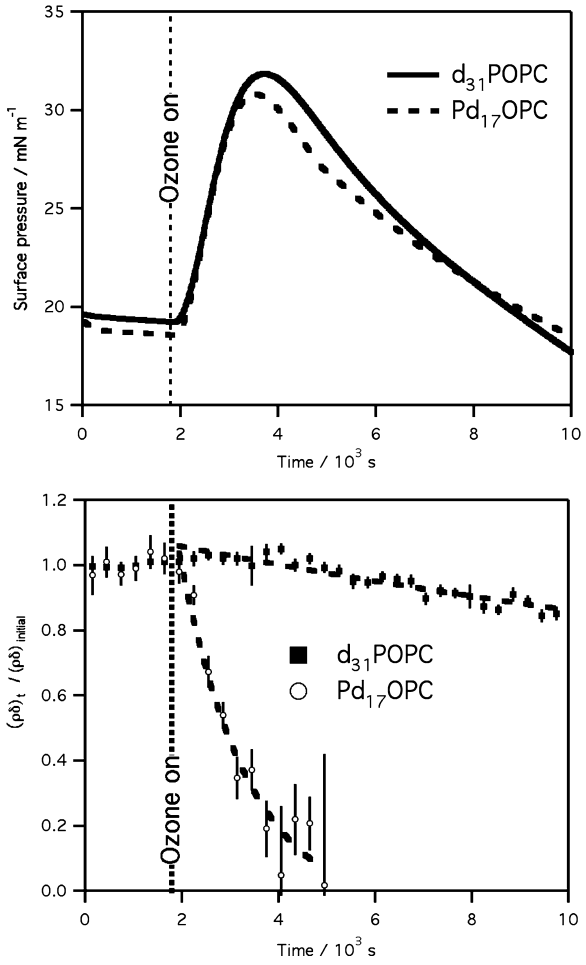

Figure 5. Surface pressure (upper) and fitted $\rho\delta$ (lower) when d_{31}POPC and Pd_{17}OPC are exposed to gas-phase ozone. The changes in surface pressure are almost identical in the two cases, but the change in the neutron reflection signal with time is very different for the two isotopologues. For the reaction of ozone with d_{31}POPC, the reduction in $\rho\delta$ is only slight, the process is slow (lifetime 354 min), and loss from the interface is seen only after the surface pressure has started to decline whereas for the reaction of ozone with Pd_{17}OPC the product $\rho\delta$ for the material at the interface decreases very rapidly (lifetime 24 min) to very low values and the decrease in scattering length occurs simultaneously with the increase in surface pressure. The dashed lines in the lower panel represent the fit to a single-exponential decay function in the case of d_{31}POPC and Pd_{17}OPC.

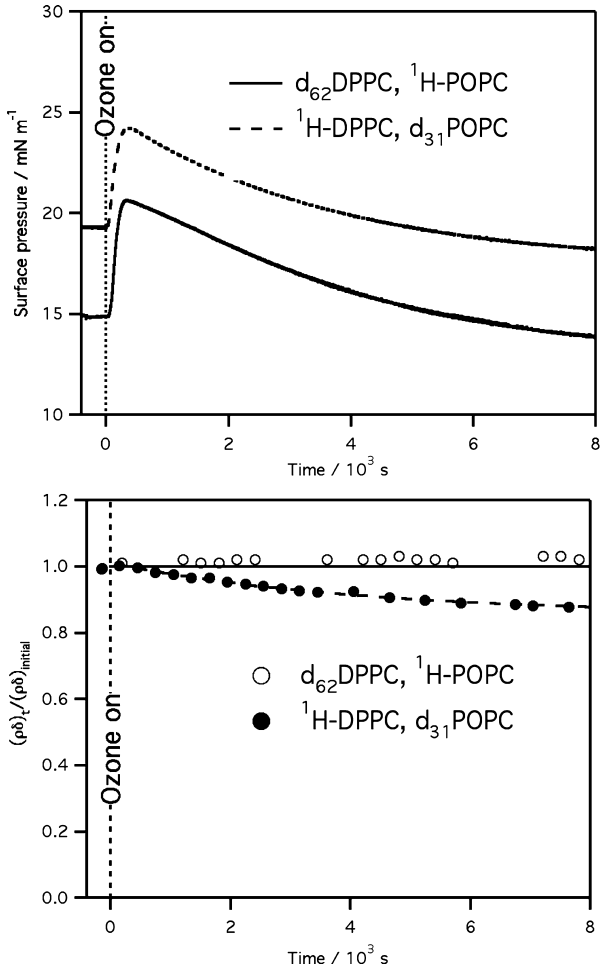

Figure 6. Plots showing the different results obtained when binary mixtures of (i) ^{1}H-DPPC and d_{31}POPC and (ii) d_{62}DPPC and ^{1}H-POPC are exposed to gas-phase ozone at the air−water interface with an initial surface pressure of about 17 mN m^{-1} at 31 °C. The upper panel shows the changes in surface pressure with time. The lower panel shows the values of $(\rho\delta)_t/(\rho\delta)_{initial}$ with time obtained by fitting the neutron reflectivity data. The quantity $\rho\delta$ is dominated by the changes in the amount of deuterated palmitoyl material at the interface. The dashed line through the data for ^{1}H-DPPC, d_{31}POPC is an exponential fit to the data and shows the slow loss of some of the palmitoyl portion of POPC from the interface. The solid line in the lower panel illustrates a constant ratio of $(\rho\delta)_t/(\rho\delta)_{initial}$ = 1 (i.e., no loss of deuterated material is observed when ^{1}H-POPC is exposed to ozone in the presence of d_{62}DPPC).

POPC by ozone-generated reactive species could lead to the degradation of DPPC molecules when both species, POPC and DPPC, were present at the air−water interface, as occurs in a real lung lining. Other authors have used neutron reflection to show that severe damage to DPPC bilayers does occur when DPPC is subject to more general oxidative stress conditions generated by exposure to ultraviolet light of <258 nm.[26] In the work presented here, two sets of experiments were performed: one with ^{1}H-DPPC and d_{31}POPC, which would reveal changes in the amount of POPC at the interface when in the presence of DPPC, and another set with d_{62}DPPC and ^{1}H-POPC, which would reveal any changes in the amount of DPPC at the interface when POPC was reacted with ozone. A loss of DPPC from the interface was not observed during any experiments in which mixtures of POPC and DPPC were exposed to ozone gas, regardless of the extent that DPPC was expected to mix with POPC in the monolayer. Figure 6 shows the change in surface pressure and surface composition when a 1:1 mixture of POPC/DPPC with an initial starting surface pressure of about 17 mN m^{-1} at 31 °C was exposed to 2 ppm of ozone, and Figure 7 shows the results obtained when a 1:1 mixture of POPC/DPPC with an initial starting pressure of about 40 mN m^{-1} at 21 °C was exposed to 2 ppm of ozone.

As can be seen from Figures 6 and 7, the reaction of POPC with ozone in mixed films of POPC and DPPC leads to an increase in the surface pressure, followed by a much slower decrease in surface pressure. When the initial pressure is fairly high, the reaction ultimately causes the surface pressure to decay to a much lower value than the initial value, as shown in Figure 7. Both the initial rapid increase and the slower decrease in surface pressure are much less pronounced in the mixed films than in films of pure POPC. Loss of material from the palmitoyl

dx.doi.org/10.1021/la304312y | Langmuir 2013, 29, 4594−4602

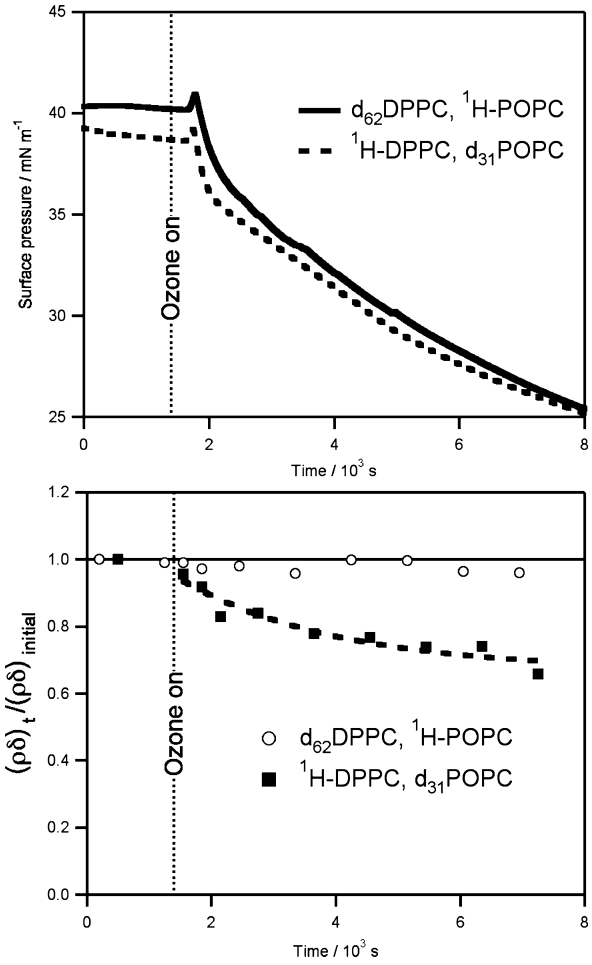

Figure 7. Plots showing the different results obtained when binary mixtures of (i) ^{1}H-DPPC and d_{31}POPC and (ii) d_{62}DPPC and ^{1}H-POPC are exposed to gas-phase ozone at the air−water interface with an initial surface pressure of about 40 mN m^{-1} at 21 °C. The upper panel shows the changes in surface pressure. The lower panel shows the values of $(\rho\delta)_t/(\rho\delta)_{initial}$ obtained by fitting the neutron reflectivity data. The $\rho\delta$ term is dominated by changes in the amount of deuterated palmitoyl material at the interface. The dashed line through the data for ^{1}H-DPPC, d_{31}POPC is an exponential fit to the data and shows a slow decay, as expected for the loss of the palmitoyl portion of POPC from the interface. The solid line in the lower panel illustrates a constant ratio of $(\rho\delta)_{initial}/(\rho\delta)_t = 1$ (i.e., no loss of deuterated material is observed when ^{1}H-POPC is exposed to ozone in the presence of d_{62}DPPC). The surface pressure of the film decreases to well below the initial value during exposure to ozone.

strand of POPC is observed when the mixed films are exposed to ozone; however, no measurable loss of material from the palmitoyl strands of DPPC was observed.

DISCUSSION

The results presented for the oxidation of films of pure POPC by ozone show that the lipid reacts rapidly with ozone at the air−water interface. For a concentration of ozone of about 0.1 ppm, a concentration frequently encountered in polluted cities in the summer months, the lifetime of the lipid is about 20 min. No clear trend was observed between the initial surface pressure of the lipid film and the lifetime. When a higher concentration of ozone was used, 0.4 ppm, a shorter lifetime, 8 min, was obtained as expected. The lifetimes reported here relate explicitly to the loss of the terminal C9 portion of the oleoyl strand from the interface. The lifetime of 8 min when the concentration of ozone is 0.4 ppm is in good agreement with the work of Wadia et al.[14] Wadia followed the generation of gas-phase product nonanal from the oleoyl strand of the lipid OPPC when reacted with ozone and reported that the formation of nonanal was observed over a period of 6.6 min when the concentration of ozone was 0.5 ppm.

In this work and in our previous paper,[15] we have shown that there is a rapid and dramatic rise in the surface pressure (decrease in surface tension) when gas-phase ozone reacts with POPC. The results from the neutron reflection studies presented here clearly show that the rapid increase in surface pressure occurs on the same time scale as the loss of the terminal portion of the oleoyl strand of POPC from the interface, with the surface pressure peaking as the product $\rho\delta$ reaches the minimum. The C9 portion of the molecule must either be released into the gas phase or dissolve into the bulk phase on the same time scale as the surface pressure increases. Thus the data reveal that the surface pressure increase cannot be caused by the incorporation of the C9 product into the air−water interface but instead is likely to be caused by a change in the arrangement of the remaining, damaged, lipid molecule at the air−water interface, an idea consistent with the recent results of Khabiri et al.[27] Khabiri et al., based on computational simulations of oxidized dioleoyl-*sn*-glycero-3-phosphocholine, DOPC, suggested that the orientation reversal of the oxidized acyl chain could occur (i.e., that the formation of an aldehyde or acid functional group at the position of the double bond would cause the lipid tail to bend over into the subphase). The addition of an extra group to the water would increase the molecular crowding at the interface and thus increase the surface pressure. The fact that the surface pressure does not remain high but instead decreases on a very slow time scale (hours) indicates that a secondary, slow process then occurs, as we have discussed in a previous paper.[15] It can be concluded that, under these static conditions, some form of damaged lipid remains at the interface for several hours. We and others have previously studied monolayers of oxidized lipid species POnPC and PAzPC. These oxidized lipids form monolayers at the air−water interface, which at the surface pressures used in this work are stable for at least several hours.[15,28] Several studies have shown that lysophospholipids (similar to the oxidized lipids produced here but completely lacking a fatty acid residue at position 2 on the glycerol backbone) remain at the interface along with undamaged lipids and significantly impair the performance of the surfactant film. The presence of 10% lysophospholipid with 90% undamaged lipids significantly increases both the minimum achievable surface tension of the film and the rate at which the surface tension is reduced.[29,30] Thus, the presence of the oxidatively damaged lipids generated by the reaction of ozone with lung surfactant could lead to significant health effects, the extent of which will be dependent upon how long the damaged lipids remain at the interface when subject to the continuous compression and expansion cycles experienced in the lung, something that we will investigate in the future.

When ozone reacts with unsaturated organic molecules in the gas phase, the highly reactive OH radical can be formed as a side product.[17] It is possible that OH radicals are formed when ozone reacts with POPC at the air−water interface. The formation of OH radicals in this way would be significant because OH radicals are much more reactive than ozone and would readily attack saturated alkyl chains, either on the

dx.doi.org/10.1021/la304312y | *Langmuir* 2013, 29, 4594−4602

remaining portion of the original POPC molecule or on a neighboring lipid molecule. To determine whether OH radicals capable of attacking neighboring lipids are formed, we studied the reaction of ozone with mixtures of POPC and DPPC. Our experiments on mixed POPC/DPPC monolayers reveal that DPPC remains unaffected by exposure to ozone, even in the presence of reactive lipids such as POPC. This is in agreement with the work of Kim et al.,[31] who used mass spectrometry to study the reaction of mixtures of saturated and unsaturated lipids with ozone and did not see any change in the saturated lipid species. Thus, either OH radicals are not produced when ozone reacts with POPC at the air−water interface or the radicals are produced but are not sufficiently long-lived to react with nearby lipids. In further studies, we will look at mixed films of Pd_{17}OPC and DPPC to determine if the presence of DPPC changes the rate of reaction of POPC with ozone, for instance, by altering the accessibility of the oleoyl chain to the incoming ozone. The reaction of POPC in mixed films of POPC and DPPC does lead to a measurable change in the surface pressure of the film. The air−water interface of the lung naturally contains both saturated and unsaturated lipids as well as proteins. The damage and/or loss of the unsaturated components following exposure to ozone will alter the physical properties of the film, including its fluidity and the ability of the film to readsorb to the air−water interface following monolayer collapse.

CONCLUSIONS

We have studied the reaction of monolayers of the unsaturated lipid POPC with ozone gas at the air−water interface both as a film of pure POPC and when present in mixtures of POPC and DPPC. Our results obtained from the pure monolayers of POPC reveal that when POPC reacts with ozone the cleavage of the carbon−carbon double bond occurs rapidly and the C9 terminal portion of the oleoyl strand is very rapidly lost from the air−water interface, with a lifetime of about 20 min when the ozone concentration is 0.1 ppm. The loss of the C9 portion occurs at the same time as the surface pressure of the air−water interface increases, indicating that the surface pressure increase is not caused by the incorporation of the cleaved C9 product. Instead, we suggest that the remaining damaged tail of the lipid molecule quickly reorients itself at the interface and inserts into the aqueous subphase, leading to an increase in molecular crowding and hence an increase in the surface pressure. Experiments performed on the mixed films of DPPC and POPC reveal that no measurable loss of saturated lipid DPPC from the interface occurs when unsaturated lipid POPC reacts with ozone, but the lipid film that remains at the interface has a reduced surface pressure (i.e., increased surface tension). Thus, we conclude that although the saturated lipids present in lung surfactant are not damaged when the unsaturated lipids present react with gas-phase ozone, exposure to the toxic gas ozone does cause a rapid and dramatic damage to the unsaturated components of lung surfactant and hence dramatically changes the organization of material at the interface and the physical properties of the film.

ASSOCIATED CONTENT

Supporting Information

Example of a fit to the neutron reflectivity data along with the 1D neutron scattering length density profile and a brief explanation of the layer thickness. This material is available free of charge via the Internet at http://pubs.acs.org.

AUTHOR INFORMATION

Notes

The authors declare no competing financial interest.

ACKNOWLEDGMENTS

We thank Simon Wood, Institut Laue-Langevin, for all his technical support and assistance in commissioning the gas chamber. We gratefully acknowledge the award of beam time at the Institut Laue-Langevin and at the ISIS Neutron Facility. S.H.J. and C.O.M.L. gratefully acknowledge the NERC and STFC for the provision of studentships NE/F0007116/1 and NE/H019103/1.

REFERENCES

(1) Creuwels, L. A.; van Golde, L. M.; Haagsman, H. P. The pulmonary surfactant system: biochemical and clinical aspects. *Lung* **1997**, *175*, 1−39.
(2) Avery, M. E.; Mead, J. Surface properties in relation to atelectasis and hyaline membrane disease. *AMA J. Dis. Child* **1959**, *97*, 517−523.
(3) Zuo, Y. Y.; Veldhuizen, R. A. W.; Neumann, A. W.; Petersen, N. O.; Possmayer, F. Current perspectives in pulmonary surfactant−inhibition, enhancement and evaluation. *Biochim. Biophys. Acta* **2008**, *1778*, 1947−77.
(4) Notter, R. H.; Tabak, S. A.; Mavis, R. D. Surface properties of binary mixtures of some pulmonary surfactant components. *J. Lipid Res.* **1980**, *2*, 509−515.
(5) Pérez-Gil, J. Structure of pulmonary surfactant membranes and films: The role of proteins and lipid−protein interactions. *Biochim. Biophys. Acta* **2008**, *1778*, 1676−1695.
(6) Walther, F. J.; Hernández-Juviel, J. M.; Gordon, L. M.; Waring, A. J.; Stenger, P.; Zasadzinski, J. A. Comparison of three lipid formulations for synthetic surfactant with a surfactant protein B analog. *Exp. Lung Res.* **2005**, *31*, 563−579.
(7) Ding, J.; Takamoto, D. Y.; von Nahmen, A.; Lipp, M. M.; Lee, K. Y.; Waring, A. J.; Zasadzinski, J. A. Effects of lung surfactant proteins, SP-B and SP-C, and palmitic acid on monolayer stability. *Biophys. J.* **2001**, *80*, 2262−2272.
(8) Jerrett, M.; Burnett, R. T.; Pope, C. A.; Ito, K.; Thurston, G.; Krewski, D.; Shi, Y.; Calle, E.; Thun, M. Long-term ozone exposure and mortality. *New Engl. J. Med.* **2009**, *360*, 1085−1095.
(9) Langford, S. D.; Bidani, A.; Postlethwait, E. M. Ozone-reactive absorption by pulmonary epithelial lining fluid constituents. *Toxicol. Appl. Pharmacol.* **1995**, *132*, 122−130.
(10) Pryor, W. A. How far does ozone penetrate into the pulmonary air/tissue boundary before it reacts? *Free Radical Biol. Med.* **1992**, *12*, 83−88.
(11) Liljeblad, J. F. D.; Bulone, V.; Tyrode, E.; Rutland, M. W.; Johnson, C. M. Phospholipid monolayers probed by vibrational sum frequency spectroscopy: instability of unsaturated phospholipids. *Biophys. J.* **2010**, *98*, L50−L52.
(12) Stottrup, B. L.; Stevens, D. S.; Keller, S. L. Miscibility of ternary mixtures of phospholipids and cholesterol in monolayers, and application to bilayer systems. *Biophys. J.* **2005**, *88*, 269−276.
(13) Lai, C. C.; Yang, S. H.; Finlayson-Pitts, B. J. Interactions of monolayers of unsaturated phosphocholines with ozone at the air−water interface. *Langmuir* **1994**, *10*, 4637−4644.
(14) Wadia, Y.; Tobias, D. J.; Stafford, R.; Finlayson-Pitts, B. J. Real-time monitoring of the kinetics and gas-phase products of the reaction of ozone with an unsaturated phospholipid at the air−water interface. *Langmuir* **2000**, *16*, 9321−9330.
(15) Thompson, K. C.; Rennie, A. R.; King, M. D.; Hardman, S. J. O.; Lucas, C. O. M.; Pfrang, C.; Hughes, B. R.; Hughes, A. V. Reaction of a phospholipid monolayer with gas-phase ozone at the air−water interface: measurement of surface excess and surface pressure in real time. *Langmuir* **2010**, *26*, 17295−17303.
(16) Criegee, R. Mechanism of ozonolysis. *Angew. Chem., Int. Ed.* **1975**, *14*, 745−752.

(17) Atkinson, R.; Aschmann, S. M.; Arey, J.; Shorees, B. Formation of OH radicals in the gas-phase reactions of O_3 with a series of terpenes. *J. Geophys. Res. Atmos.* **1992**, *97*, 6065−6073.
(18) Penfold, J.; Richardson, R. M.; Zarbakhsh, A.; Webster, J. R. P.; Bucknall, D. G.; Rennie, A. R.; Jones, R. A. L.; Cosgrove, T.; Thomas, R. K.; Higgins, J. S.; Fletcher, P. D. I.; Dickinson, E.; Roser, S. J.; McLure, I. A.; Hillman, A. R.; Richards, R. W.; Staples, E. J.; Burgess, A. N.; Simister, E. A.; White, J. W. Recent advances in the study of chemical surfaces and interfaces by specular neutron reflection. *J. Chem. Soc., Faraday Trans.* **1997**, *93*, 3899−3917.
(19) Campbell, R. A.; Wacklin, H. P.; Sutton, I.; Cubitt, R.; Fragneto, G. FIGARO: The new horizontal neutron reflectometer at the ILL. *Eur. Phys. J. Plus* **2011**, *126*, 107.
(20) Lu, J. R.; Thomas, R. K.; Penfold, J. Surfactant layers at the air/water interface: structure and composition. *Adv. Colloid Interface Sci.* **2000**, *84*, 14−304.
(21) Sears, V. F. Neutron scattering lengths and cross sections. *Neutron News* **1992**, *3*, 26−37.
(22) Curatolo, W.; Sears, B.; Neuringer, L. J. A calorimetry and deuterium NMR study of mixed model membranes of 1-palmitoyl-2-oleylphosphatidylcholine and saturated phosphatidylcholines. *Biochim. Biophys. Acta* **1985**, *817*, 261−270.
(23) Abelès, F. La théorie générale des couches minces. *J. Phys. Radium* **1950**, *11*, 307−310.
(24) Rennie, A. R. *Neutron Reflection Analysis Programs*; http://material.fysik.uu.se/Group_members/adrian/refprog.htm accessed July 2012.
(25) Koenig, B. W.; Gawrisch, K. Specific volumes of unsaturated phosphatidylcholines in the liquid crystalline lamellar phase. *Biochim. Biophys. Acta* **2005**, *1715*, 65−70.
(26) Smith, H. L.; Howland, M. C.; Szmodis, A. W.; Li, Q.; Daemen, L. L.; Parikh, A. N.; Majewski, J. Early stages of oxidative stress-induced membrane permeabilization: a neutron reflectometry study. *J. Am. Chem. Soc.* **2009**, *131*, 3631−3638.
(27) Khabiri, M.; Roeselova, M.; Cwiklik, L. Properties of oxidized phospholipid monolayers: an atomistic molecular dynamics study. *Chem. Phys. Lett.* **2012**, *519*−*520*, 93−99.
(28) Sabatini, K.; Mattila, J.-P.; Megli, F. M.; Kinnunen, P. K. J. Characterization of two oxidatively modified phospholipids in mixed monolayers with DPPC. *Biophys. J.* **2006**, *90*, 4488−4499.
(29) Hite, R. D.; Seeds, M. C.; Jacinto, R. B.; Grier, B. L.; Waite, B. M.; Bass, D. A. Lysophospholipid and fatty acid inhibition of pulmonary surfactant: non-enzymatic models of phospholipase A_2 surfactant hydrolysis. *Biochim. Biophys. Acta* **2005**, *1720*, 14−21.
(30) Holm, B. A.; Keicher, L.; Liu, M. Y.; Sokolowski, J.; Enhorning, G. Inhibition of pulmonary surfactant function by phospholipases. *J. Appl. Physiol.* **1991**, *71*, 317−321.
(31) Kim, H. I.; Kim, H.; Shin, Y. S.; Beegle, L. W.; Jang, S. S.; Neidholdt, E. L.; Goddard, W. A.; Heath, J. R.; Kanik, I.; Beauchamp, J. L. Interfacial reactions of ozone with surfactant protein B in a model lung surfactant system. *J. Am. Chem. Soc.* **2010**, *132*, 2254−2263.

Paper 4: The atmospheric importance of aqueous radical initiated oxidation of an organic monolayer at the air-water interface studied by neutron reflectivity

S. H. Jones, M. D. King, A. R. Rennie, A. D. Ward, R. A. Campbell and A. V. Hughes

To be submitted to Physical Chemistry Chemical Physics, 14 pages.

Within this partly co-authored work, I declare that the following contributions are entirely my own work:

- Conducted the neutron and photolysis experiments and collected and analysed the data.
- Authored the paper.
- Contributed significantly to the design of the experiment.
- Contributed to drawing the conclusions of the paper.

Journal Name

Dynamic Article Links ►

Cite this: DOI: 10.1039/c0xx00000x

www.rsc.org/xxxxxx

ARTICLE TYPE

The atmospheric importance of aqueous radical initiated oxidation of an organic monolayer at the air-water interface studied by neutron reflectivity

Stephanie H. Jones [a,b], Martin D. King*[a] Adrian R. Rennie[c], Andrew D. Ward[b], Richard A. Campbell[d] and Arwel V. Hughes[e]

Received (in XXX, XXX) Xth XXXXXXXXX 20XX, Accepted Xth XXXXXXXXX 20XX
DOI: 10.1039/b000000x

Neutron reflectivity has been used to study the radical initiated oxidation of a monolayer film of the lipid 1,2-distearoyl-*sn*-glycero-3-phosphocholine (DSPC) at the air-water interface, by the aqueous-phase hydroxyl, sulfate and nitrate radicals. Radical-initiated oxidation of organic films at the surface of atmospheric aqueous aerosols can influence the optical properties of aerosol and consequently can impact on the Earth's radiative balance and contribute to modern climate change. The amount of material at the air-water interface was found to decrease on exposure to aqueous-phase radicals following a multi-step degradation mechanism. Results indicate that each aqueous radical reacts with the DSPC film via the same multi-step mechanism. The multi-step degradation mechanism suggests that individual film molecules are reactive and produce surface active products and therefore several steps are required to remove the film from the air-water interface. Film lifetime calculations indicate that it will take ~1.5 days for the film to decay to 50 % of its initial amount. Therefore attack of aqueous radicals on organic films present at the air-water interface of atmospheric aerosol, which have an atmospheric lifetime of 4-10 days, is important.

Introduction

Atmospheric aerosols can exist as complex chemical mixtures in the troposphere e.g. Saxena and Hildemann[1] and Pöschl[2] etc. and are known to influence the Earth's climate both directly, by scattering and absorbing radiation and indirectly, by acting as cloud condensation nuclei (CCN). A large amount of uncertainty is attributed to aerosol contribution to cloud properties and therefore aerosol contribution to the indirect effect[3]. In order to reduce this uncertainty it is necessary to investigate common reactions that aerosols will undergo in the troposphere such as oxidation, and characterise important aerosol properties, such as atmospheric lifetime.

Thin organic films are believed to exist on the surface of aerosols at the air-water interface and air-solid interface e.g. references 4-11. An abundant tropospheric aerosol, marine aerosol, is commonly formed with an organic surface active film[4,5,7]. As marine aerosol forms by bubble bursting action over the ocean, an organic coating can be formed on the surface of the aerosol that arises from the presence of organic material in the sea surface microlayer (tens to hundreds of micrometers of the uppermost ocean)[5,12,13]. Another common source of surface active coating is lipids that are present in plant waxes and become airborne by wind action[14]. Such coatings are believed to form an encapsulating monolayer around the aerosol surface, and hence play a central role in aerosol chemistry and hygroscopic properties e.g. references 4 and 5.

A number of gas and liquid-phase oxidants are present in the troposphere[15] that can oxidise atmospheric aerosol, resulting in a change in aerosol physical and optical properties. Thin films on aerosol may also be readily oxidised which would cause an associated change in coated aerosol properties, such as: hygroscopicity (ability to uptake water), aerosol atmospheric lifetime and aerosol ability to form a CCN. It has been suggested that the oxidation of an organic film at the air-water interface may influence the formation and activation of cloud droplets e.g. references 16-19. King et al.[19] demonstrated this for the oxidation of an oleic acid film at the air-water interface as a proxy for an organic coating on an aerosol. Thus, characterisation of the aerosol coating and determination of the atmospheric lifetime with respect to oxidation at the air-water interface is central to the further understanding of aerosol contribution to the indirect climate effect.

Common atmospheric oxidants include gas-phase ozone[20,21], nitrate[22] and the cloud water aqueous phase radicals, hydroxyl ($^{\cdot}OH$), sulfate ($SO_4^{\cdot-}$) and nitrate ($NO_3^{\cdot}$)[15]. In order to assess whether organic coatings present at the air-water interface of aerosols are susceptible to attack by aqueous phase radicals, a series of neutron reflectivity experiments were performed. Neutron reflectivity is a surface reflection technique that provides information on the physical properties of a monolayer film at the

air-water interface. For the work described here, neutron reflectivity was used to measure surface coverage and estimate thickness of monolayer films at the air-water interface. Previous neutron reflection studies have been successfully conducted on the oxidation of atmospherically relevant thin films at the air-water interface[19,23,24]. The lipid 1,2-distearoyl-*sn*-glycero-3-phosphocholine (DSPC) is a naturally occurring phosphocholine lipid and was selected as a saturated proxy thin film material to represent film forming organic matter found in the troposphere e.g. references 25-27.

Neutron reflectometry was used to study the decay of material (DSPC film and resultant products) at the air-water interface for the following reactions:

$$OH_{(aq)} + DSPC_{(Surf)} \longrightarrow Products \quad \text{R1}$$

$$SO_4^{\cdot-}{}_{(aq)} + DSPC_{(Surf)} \longrightarrow Products \quad \text{R2}$$

$$NO_3^{\cdot}{}_{(aq)} + DSPC_{(Surf)} \longrightarrow Products \quad \text{R3}$$

where *Surf* is used to indicate presence at the air-water interface.

The oxidative loss of DSPC from the air-water interface was subsequently kinetically modelled and a bimolecular rate constant was determined for the loss of surface active material at the air-water interface, thus allowing calculation of a film lifetime with respect to radical oxidation. Comparison of the film lifetime with typical atmospheric aerosol residence times enables the importance of such aqueous phase radical reactions to be assessed.

Experimental

The experimental section includes an introduction to neutron reflectometry and the associated experimental set-up used in the neutron reflection experiments. An explanation of aqueous radical generation is provided as well as a description of the calculation of the radical steady-state concentration. The section ends with a description of the multi-step degradation mechanism that was used to kinetically model the data.

Neutron reflectometry

Neutron reflectometry was used to study a monolayer film at the air-water interface[28]. Specular neutron reflection allows the determination of the neutron refractive index profile normal to the air-water interface[29]. The reflectivity of the film can be modelled to obtain information on the amount and thickness of material at the air-water interface. A Langmuir trough was used as the sample environment to study the neutron reflection of deuterated material at the air-water interface.

Measurements were made at the ISIS neutron source at the Rutherford Appleton Laboratory, Oxfordshire, UK using the SURF reflectometer[30] and at the ILL in Grenoble, France using the FIGARO reflectometer[31]. At ISIS, neutron reflection was recorded at an angle of 1.5° to the horizontal using a wavelength range of 0.5-6 Å. At the ILL, neutron reflection was recorded at an incident angle of 0.62° to the horizontal with a wavelength range of 2-20 Å and at an incident angle of 3.8° to the horizontal with a wavelength range of 2-30 Å.

The application of the neutron reflection technique to species at the air-water interface has been described by Lu et al.[28] and has been specifically applied to the oxidation of species at the air-water interface in King et al.[19] and therefore will only be described briefly here. Neutron reflectivity, R, is measured as a function of the momentum transfer, Q, of the neutron[30] where Q is defined as:

$$Q = \frac{4\pi \sin\theta}{\lambda} \quad \text{A}$$

λ is the neutron wavelength and θ is the incident angle of the neutron beam.

Neutron reflectivity[28] for a monolayer of deuterated material at the air-water interface is defined as:

$$R = \frac{16\pi^2}{Q^4}(2\rho)^2 \sin\left(\frac{Q\delta}{2}\right)^2 \quad \text{B}$$

where δ is the film thickness and ρ, is the scattering length density[29] defined as:

$$\rho = \sum_i nb_i \quad \text{C}$$

b is the scattering length of an element and n is the number density of that element[30]. The value of b for fully deuterated DSPC ($C_{44}H_5NO_8PD_{83}$) used in this study is 888 fm based on values of b for individual elements obtained from Sears[32]. The reflectivity data was normalised using the intensity spectrum of an unreflected beam of neutrons and the absolute reflectivity was determined using a scale factor obtained from measuring the reflectivity of pure D_2O in the Langmuir trough.

Isotopes typically have different scattering lengths[32] where b is a measure of the interaction between the nucleus of an atom and a neutron[33]. The difference in bound coherent scattering length between hydrogen and deuterium is distinct, b = −3.74 fm for hydrogen and b = 6.67 fm for deuterium, whereas the chemical properties are the same. Specific chemical moieties of a molecule can be selectively deuterated in order to highlight the deuterated parts by producing a strong contrast between the film, subphase and the air[28]. The subphase is the phase below the film i.e. the monolayer film to be studied is spread on top of the subphase. In our study, the reflectivity of the film was increased relative to the air and water by using fully deuterated DSPC ($C_{44}H_5NO_8PD_{83}$) in order to achieve a large scattering length density (ρ = 7.17 × 10^{-6} $Å^{-2}$, calculated from values given in Hollinshead et al.[34]) in comparison to that of the subphase. The subphase had a scattering length density of zero (effectively the same as the air above the film) and was therefore null reflecting. A solution of null reflecting water (NRW), also known as Air contrast matched water (ACMW) consists of D_2O and H_2O in the volume proportion 8.1% and 91.9% respectively. In the current experiment, aqueous radicals were generated photolytically from the subphase and consequently the volume ratio of D_2O and H_2O in the subphase was slightly adjusted to account for the scattering length density of the radical precursor chemicals. A monolayer film of fully deuterated DSPC was placed on top of the radical precursor subphase (null reflecting) contained in the Langmuir trough and the specular neutron reflection signal was dominated by reflection from the monolayer film.

In the current study, neutron reflectivity was used to estimate the surface coverage or amount of deuterated material at the air-

water interface as a monolayer film of DSPC ($C_{44}H_5NO_8PD_{83}$) was exposed to aqueous phase radicals. Neutron reflectivity as a function of momentum transfer, Q, was typically recorded continuously in intervals of 300 s or 900 s, and each kinetic run was between 15 000 to 40 000 s in duration. The experimental reflectivity versus the momentum transfer was modelled with an Abelès formalism,[35] which allows determination of the scattering length density and thickness of the deuterated material at the air-water interface. The scattering length density ρ, and film thickness δ, can be related to the amount of deuterated material or surface coverage Γ, at the air-water interface using the following equation:

$$\Gamma = \frac{\rho\delta}{b} \quad \text{D}$$

where b, is the scattering length of material at the air-water interface. The relative surface coverage of deuterated material at the air-water interface was followed and defined as:

$$\frac{\Gamma_t}{\Gamma_0} = \frac{\rho_t\delta_t}{\rho_0\delta_0} \quad \text{E}$$

where Γ_t is the surface coverage at time t and Γ_0 is the surface coverage at time zero and thus $\rho_t\delta_t$ is the product of the scattering length density and thickness at time t, and $\rho_0\delta_0$ is the product of the scattering length density and thickness at time zero.

The Abelès formalism was used to compute an initial model of the reflectivity versus momentum transfer data, and the model parameters were then adjusted to achieve a better match of the modelled reflectivity data to the experimental reflectivity data by eye. Two programs were used to compute the models, Motofit[36] and mono[37]. Typical fits were optimised using a least squares algorithm in mono and a genetic algorithm followed by a Levenberg-Marquardt algorithm in Motofit. The data presented here is from Motofit.

Experimental set-up

A custom PTFE Langmuir trough of dimensions 240 mm × 70 mm with a liquid depth of approximately 3.5 mm was used to study the oxidation of a monolayer of fully deuterated DSPC initiated by radical attack on three different null reflecting solutions (different radical precursors). UV lamps were suspended above the trough along its length to photolytically generate the radicals and provide even illumination of the whole air-water interface. Two types of UV lamps were used, black lamps centred on ~360 nm to generate $SO_4^{\cdot-}$ and $NO_3^{\cdot}$ radicals and germicidal lamps that used Hg lines to provide a significant output at ~254 nm to generate $^{\cdot}OH$ radicals. In both cases, the bulbs were situated in a retro reflector within the lamp body at a fixed height above the air-water interface, depending on the neutron source and number of lamps required.

A monolayer of fully deuterated DSPC ($C_{44}H_5NO_8PD_{83}$) >99 % atom purity from Avanti Polar Lipids Inc. was spread on the surface of the radical precursor subphase as a 1 mg mL^{-1} solution in chloroform (Sigma Aldrich, 0.5-1 % EtOH as stabiliser) using a micro-litre syringe. In each experiment, 40 μL was typically added to the air-water interface. Previously it had been determined that 40 μL provided a surface pressure of ~20 mNm^{-1} on this trough. Surface pressure was not measured during the neutron studies because the UV radiation degraded the tensiometer and would have blocked the neutron beam on the small Langmuir trough used to provide even illumination. Neutron reflectivity as a function of momentum transfer, Q, was recorded before and during photolysis of the subphase to monitor the change in reflectivity of the DSPC monolayer on exposure to aqueous phase radicals[30,31].

Radical Generation

Aqueous radicals were synthesised photolytically from the subphase using aqueous phase photochemistry[15,38-41].

Hydroxyl radicals were generated by photolysis of a 0.03 $moldm^{-3}$ aqueous solution of KNO_3 after Mack and Bolton[38] using two UV bulbs centred at ~254 nm at a height of ~83 mm above the trough.

$$NO_{3(aq)}^- + h\nu\ (\lambda{\sim}254\ nm) \rightarrow NO_{2(aq)}^- + O_{(aq)} \quad \text{R4}$$

$$NO_{3(aq)}^- + h\nu\ (\lambda{\sim}254\ nm) \rightarrow NO_{2(aq)} + O^{\cdot-}{}_{(aq)} \quad \text{R5}$$

$$O^{\cdot-}{}_{(aq)} + H_2O_{(aq)} \rightarrow OH_{(aq)} + OH^-{}_{(aq)} \quad \text{R6}$$

Sulfate radical anions were generated by photolysis of a 0.03 $moldm^{-3}$ aqueous solution of $K_2S_2O_8$[39] using four black bulbs centred at ~360 nm at a height of 128 mm above the trough.

$$S_2O_{8(aq)}^{2-} + h\nu\ (\lambda{\sim}360\ nm) \rightarrow SO_{4(aq)}^{\cdot-} + SO_{4(aq)}^{\cdot-} \quad \text{R7}$$

Nitrate radicals were generated by photolysis of an aqueous solution subphase containing 0.03 $moldm^{-3}$ $K_2S_2O_8$ and 0.1 $moldm^{-3}$ KNO_3 after Herrmann[15], using four black bulbs centred at ~360 nm at a height of 128 mm above the trough at ISIS and 115 mm above the trough at the ILL. The height of the lamps was used to control the rate of reaction. Photolysis of $S_2O_8^{2-}$ yielded two $SO_4^{\cdot-}$ radicals as detailed in equation R7 and subsequent titration of $SO_4^{\cdot-}$ with an excess of NO_3^- resulted in the production of the nitrate radical, $NO_3^{\cdot}$ after Herrmann[15].

$$SO_{4(aq)}^{\cdot-} + NO_{3(aq)}^- \rightarrow NO_{3(aq)}^{\cdot} + SO_{4(aq)}^{2-} \quad \text{R8}$$

The UV lamps used to initiate photolysis were switched on and off remotely and produced a stable irradiance after three minutes[42]. The concentration of aqueous radical precursor was chosen to maintain a constant steady-state radical concentration throughout the entire kinetic run. The calculation of the steady-state radical concentration is described in a following section.

Blank experiments were performed on a monolayer of DSPC on the following aqueous solution subphases: 0.03 $moldm^{-3}$ KNO_3; 0.03 $moldm^{-3}$ $K_2S_2O_8$ with 0.1 $moldm^{-3}$ KNO_3 and 0.03 $moldm^{-3}$ $K_2S_2O_8$. All were conducted without UV light and were termed dark blanks. Blanks were also conducted on a monolayer of DSPC on ACMW with UV light only, and termed light or photolysis only blanks.

Kinetic modelling

Two kinetic models were developed in the work presented here: a

multi-step degradation of material at the air-water interface and a steady-state analysis of the radical concentration. A multi-step degradation mechanism was proposed for the radical initiated oxidation of a monolayer of DSPC and kinetically modelled to determine pseudo-first-order rate constants for each step of the mechanism. Steady-state concentrations of the $SO_4^{\cdot-}$ and $^{\cdot}OH$ radicals were also determined by kinetic modelling of offline photolysis work using the UV lamps and trough in the same set-up as on the beam line. Bimolecular rate constants for reactions R1 and R2 were subsequently calculated from the pseudo-first order rate constants and steady state concentrations. Unfortunately the secondary radical chemistry following photolysis to generate the nitrate radical is not well known enough to kinetically model.

Determination of radical steady-state concentrations

In order to determine the steady-state radical concentrations, photolysis of the radical precursors was performed offline from the neutron experiments in exactly the same conditions as on the beam line. The loss of radical precursor was measured as a function of photolysis time to determine the photolysis rate constant, J, for equations R4, R5 and R7. The offline set-up was exactly the same as that used for the neutron experiments and is described in the notes and references section[‡]. Kinetic modelling was required because the photolysis rates of the NO_3^- and $S_2O_8^{2-}$ anions were unknown. During the neutron reflectivity experiments, the concentration of radical precursors (NO_3^- and $S_2O_8^{2-}$) was kept large to maintain an almost constant concentration of radical precursor and thus constant concentration of radicals in steady-state concentration throughout the reaction. However, in order to calculate the photolysis rate constant for NO_3^- and $S_2O_8^{2-}$, the precursor solutions were photolysed at concentrations of 0.0003 moldm^{-3} KNO_3 aqueous solution and 0.0003 moldm^{-3} $K_2S_2O_8$ aqueous solution to observe and model the loss of radical precursor. Loss of KNO_3 or $K_2S_2O_8$ was followed by UV-visible spectrometry for up to ten hours for $K_2S_2O_8$ and up to 16.5 hours for KNO_3. The following photolysis reaction schemes were kinetically modelled using a Backward Differentiation Formula (BDF) method to handle stiff systems[43-45] and the appropriate photolysis rate constants, J, were varied until the modelled temporal variation of the concentrations of $S_2O_8^{2-}$ and NO_3^- fitted the experimentally determined temporal profile of the concentrations. Rate constants for the reactions in the photolysis schemes were obtained from the literature where possible and the following rate constants were determined from kinetic modelling: J_4; J_5; J_7; J_{11} and k_{12}.

Hydroxyl radicals are produced from the photolysis of nitrate from the following photochemistry:

$$NO_3^-{}_{(aq)} + h\nu\ (\lambda{\sim}254\ nm) \rightarrow NO_2^-{}_{(aq)} + O_{(aq)} \quad \text{R4}$$

$J_4=5.8 \times 10^{-6}$ M^{-1} s^{-1}

$$NO_3^-{}_{(aq)} + h\nu\ (\lambda{\sim}254\ nm) \xrightarrow{H_2O} NO_{2(aq)} + OH_{(aq)} \quad \text{R5}$$

$J_5=6 \times 10^{-17}$ M^{-1} s^{-1}

$$OH_{(aq)} + NO_3^-{}_{(aq)} \rightarrow NO_{3(aq)} + OH^-{}_{(aq)} \quad \text{R9}$$

$k_9=1.3 \times 10^8$ M^{-1} s^{-1} [46]

$$OH_{(aq)} + NO_2^-{}_{(aq)} \rightarrow NO_{2(aq)} + OH^-{}_{(aq)} \quad \text{R10}$$

$k_{10}=6.0 \times 10^9$ M^{-1} s^{-1} [47]

$$NO_2^-{}_{(aq)} + h\nu\ (\lambda{\sim}254\ nm) \xrightarrow{H_2O} NO^{\cdot}{}_{(aq)} + OH_{(aq)} \quad \text{R11}$$

$J_{11}=2.2 \times 10^{-5}$ M^{-1} s^{-1}

$$OH_{(aq)} + wall \rightarrow \quad \text{R12}$$

$k_{12}=1\times 10^{-10}$ M^{-1} s^{-1}

$$NO_2^-{}_{(aq)} + NO_{3(aq)} \rightarrow NO_3^-{}_{(aq)} + NO_{2(aq)} \quad \text{R13}$$

$k_{13}=6.0 \times 10^9$ M^{-1} s^{-1} [47]

The concentrations of NO_3^- and NO_2^- were independently measured as a function of photolysis time by UV-Visible spectrometry over the wavelength range ~200-500 nm in a long path length liquid cell (17.5 cm) for a series of time intervals from 2 hours up to 16.5 hours. The steady state concentration of $^{\cdot}OH$ radicals was then determined from kinetically modelling the above reactions (4, 5 and 9-13) as a series of first-order differential equations and varying J_4, J_5, J_{11} and k_{12}. Once a fit was obtained, the rate constants were fixed and the concentration of the radical precursor changed to represent the concentration used in neutron experimental concentrations, 0.03 moldm^{-3}, and the kinetic model was re-run to determine the hydroxyl radical steady-state concentration used in the neutron experiments.

The photolysis of persulfate, $K_2S_2O_8$ in aqueous solution, leading to the production of sulfate radical anions derives from the following photochemistry[39]:

$$S_2O_8^{2-}{}_{(aq)} + h\nu\ (\lambda{\sim}360\ nm) \rightarrow SO_4^{\cdot-}{}_{(aq)} + SO_4^{\cdot-}{}_{(aq)} \quad \text{R7}$$

$J_7=1.32 \times 10^{-5}$ M^{-1} s^{-1}

$$SO_4^{\cdot-}{}_{(aq)} + SO_4^{\cdot-}{}_{(aq)} \rightarrow S_2O_8^{2-}{}_{(aq)} \quad \text{R14}$$

$k_{14}=6.1 \times 10^8$ M^{-1} s^{-1} [39]

$$SO_4^{\cdot-}{}_{(aq)} + S_2O_8^{2-}{}_{(aq)} \rightarrow SO_4^{2-}{}_{(aq)} + S_2O_8^{\cdot-}{}_{(aq)} \quad \text{R15}$$

$k_{15}=5.5\times 10^5$ M^{-1} s^{-1} [39]

$$SO_4^{\cdot-}{}_{(aq)} + H_2O_{(aq)} \rightarrow H^+{}_{(aq)} + SO_4^{2-}{}_{(aq)} + OH^{\cdot}{}_{(aq)} \quad \text{R16}$$

$k_{16}[H_2O]=460$s^{-1} [39]

Owing to the weak absorption of the SO_4^{2-} anion, the decrease in concentration of $S_2O_8^{2-}$ was followed instead of the SO_4^{2-} anion as a function of photolysis time by UV-Visible spectrometry over the wavelength range ~200-300 nm. The steady state concentration of $SO_4^{\cdot-}$ radicals was then determined from kinetically modelling the above reactions (7 and 14-16) as a series of first order differential equations and varying J_7. Once the photolysis rate constant, J_7, had been determined, the initial persulfate concentration was set at the same concentration used in the neutron experiments (0.03 M) and the kinetic model was re-run to determine the sulfate radical steady-state concentration used in the neutron experiments.

The nitrate radical is produced by photolysis of persulfate in the presence of an excess of nitrate. The associated secondary radical chemistry following photolysis is not well defined in the

literature and therefore the steady-state concentration of the nitrate radical was not kinetically modelled.

It was noted that UV radiation from the lamps could be absorbed by either water or the aqueous radical precursor solution at 254 or 360 nm and consequently attenuate the light with increasing trough depth causing a decreasing irradiance with depth profile. If this were the case, the radical steady-state concentration would mirror the decreasing profile. In order to assess the effect of light attenuation with increasing trough depth, the depth for incident light to decay to ~37% (1/e), the e-folding depth was calculated. e-folding depth values are shown in Table 1 and are greater than the trough depth; therefore, light attenuation was not an issue. The trough is also PTFE and a lambertian reflector, therefore aiding in reflection to further reduce any depth irradiance profile.

Table 1 e-folding depth

Photolysis wavelength / nm	Absorption coefficient of water[48-49] / cm^{-1}	UV e-folding depth in water / cm	Radical precursor	Radical precursor absorption cross section[38,41,50] / cm^2 $molecule^{-1}$	Concentration of precursor solution / $moldm^{-3}$	UV e-folding depth for radical precursor / cm
360 nm	6.56×10^{-5}	6620	NO_3^- and $S_2O_8^{2-}$	NO_3^- ~ 0 $S_2O_8^{2-}$ = 2.42×10^{-21} this work	0.1 and 0.03	23
360 nm	6.56×10^{-5}	6620	$S_2O_8^{2-}$	2.42×10^{-21} this work	0.03	23
254 nm	4.49×10^{-4}	968	NO_3^-	1.45×10^{-20}	0.03	4

[a] Absorption coefficients for water, absorption cross sections for radical precursors and concentrations used to calculate the values of e-folding depth for water and each radical precursor system at the photolysis wavelengths. Both the calculated values for water and radical precursor e-folding depths are significantly greater than the depth of the Langmuir trough, ~3.5 mm and therefore light is effectively not attenuated over the depth of the trough.

Multi-step degradation kinetics

As will be detailed in the results section, a multi-step degradation scheme was required to kinetically model decays of the surface coverage of material at the air-water interface as a function of photolysis time.

The degradation scheme is described here to facilitate its easy application in the results section. A multi-step degradation mechanism was fitted to the experimentally determined decrease in surface coverage of material with time at the air-water interface. The following mechanism is proposed:

$$DSPC_{(Surf)} + X^{\cdot}{}_{(aq)} \longrightarrow A_{(Surf)} \longrightarrow B_{(Surf)} \longrightarrow C_{(Surf)} \longrightarrow D_{(aq)} \quad \text{R17}$$

where $DSPC_{(Surf)}$ is a monolayer of DSPC at the air-water interface; $X^{\cdot}{}_{(aq)}$ is an aqueous radical oxidant (either $^{\cdot}OH$, $NO_3^{\cdot}$ or $SO_4^{\cdot-}$); $A_{(Surf)}$, $B_{(Surf)}$ and $C_{(Surf)}$ are surface active deuterated products at the air-water interface and $D_{(aq)}$ is a non-surface active deuterated product, i.e. A, B and C reside at the air-water interface whereas product D partitions to the gas-phase or aqueous subphase. Experimentally determined surface coverage was defined as the weighted sum of the surface coverage of all deuterated species at the air-water interface including the original DSPC film and any other deuterated surface active products that may have formed from reaction with the radical species i.e. products A, B and C. Each deuterated component of the experimentally determined surface coverage was weighted by its estimated scattering length density or its approximate degree of deuteration, and the total surface coverage at the air-water interface determined by neutron reflection was defined as the weighted sum of Γ_{DSPC} and Γ_A, Γ_B and Γ_C:

$$\Gamma_{tot} = \Gamma_{DSPC} + \alpha\Gamma_A + \beta\Gamma_B + \gamma\Gamma_C \quad \text{R18}$$

where α, β and γ are the weightings relating to the scattering length density, ρ, of each surface active decay product, i.e.

$$\alpha = \frac{\rho_A}{\rho_{DSPC}} \quad \text{R19}$$

$$\beta = \frac{\rho_B}{\rho_{DSPC}} \quad \text{R20}$$

$$\gamma = \frac{\rho_C}{\rho_{DSPC}} \quad \text{R21}$$

Values of α, β and γ were taken as 0.95, 0.83 and 0.41 to represent stylised decay steps where an initial 5% decrease in the scattering length density occurred followed by the loss of a head moiety and finally the loss of a hydrocarbon tail from a DSPC molecule. Values of α, β and γ were the result of trial and error during the fitting process and were selected to achieve a good fit between the model and experimental data.

$$\Gamma_{tot} = \Gamma_{DSPC} + 0.95\Gamma_A + 0.83\Gamma_B + 0.41\Gamma_C \quad \text{R22}$$

The experimentally determined surface coverage (equation D) as a function of reaction time was fitted to the following degradation scheme.

$$DSPC_{(Surf)} + X^{\cdot}{}_{(aq)} \longrightarrow A_{(Surf)} \quad \text{R23}$$

$$A_{(Surf)} + X^{\cdot}{}_{(aq)} \longrightarrow B_{(Surf)} \quad \text{R24}$$

$$B_{(Surf)} + X^{\cdot}{}_{(aq)} \longrightarrow C_{(Surf)} \quad \text{R25}$$

$$C_{(Surf)} + X^{\cdot}{}_{(aq)} \longrightarrow D_{(aq)} \quad \text{R26}$$

The number of degradation steps was also a result of trial and error to obtain good agreement between the modelled and calculated temporal profiles of deuterated material at the air-water interface. Reactions R23-R26 are stylised multi-step reactions simplified to show stable (non-radical) products and the justification of the reaction mechanism will be covered in the discussion section. Reactions R23-R26 have the following rate laws[51]:

$$\frac{d\Gamma_{DSPC}}{dt} = -k_{23}\Gamma_{DSPC}[X] \quad \text{R27}$$

$$\frac{d\Gamma_A}{dt} = k_{23}\Gamma_{DSPC}[X] - k_{24}\Gamma_A[X] \quad \text{R28}$$

$$\frac{d\Gamma_B}{dt} = k_{24}\Gamma_A[X] - k_{25}\Gamma_B[X] \quad \text{R29}$$

$$\frac{d\Gamma_C}{dt} = k_{25}\Gamma_B[X] - k_{26}\Gamma_C[X] \quad \text{R30}$$

The concentration of the radicals [X] are in steady-state during

the reaction, i.e. $d[X]/dt = 0$, thus a series of pseudo-first order rate constants, k' can be defined as:

$$k'_n = k_n[X] \quad \text{R31}$$

where n = 23, 24, 25 and 26 and equations R27-R30 become:

$$\frac{d\Gamma_{DSPC}}{dt} = -k'_{32}\Gamma_{DSPC} \quad \text{R32}$$

$$\frac{d\Gamma_A}{dt} = k'_{32}\Gamma_{DSPC} - k'_{33}\Gamma_A \quad \text{R33}$$

$$\frac{d\Gamma_B}{dt} = k'_{33}\Gamma_A - k'_{34}\Gamma_B \quad \text{R34}$$

$$\frac{d\Gamma_C}{dt} = k'_{34}\Gamma_B - k'_{35}\Gamma_C \quad \text{R35}$$

Equations R32-R35 were kinetically modelled using a Runge-Kutta method[43] and values of the pseudo-first-order rate constants were varied until the modelled temporal variation of the total surface coverage, Γ_{tot}, R22 fitted the experimentally determined temporal profile of surface coverage for each neutron experiment.

Results

Figure 1 shows a typical decay in the neutron reflectivity profile with time as a monolayer film of DSPC at the air-water interface is exposed to the aqueous phase hydroxyl radical.

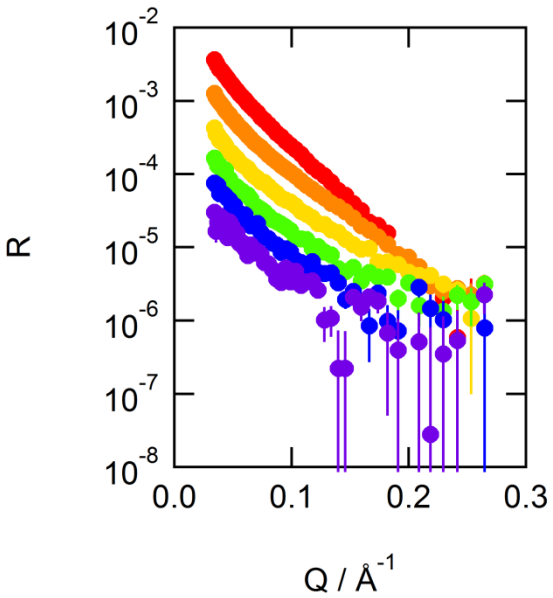

Fig.1. A typical neutron reflectivity profile for a monolayer film of fully deuterated DSPC at the air-water interface on exposure to the aqueous phase hydroxyl radical. The reflectivity signal of the film prior to exposure to the hydroxyl radical is the largest signal (red and orange circles) and as the UV lights are switched on and the hydroxyl radical is generated, the reflectivity signal decreases from the red/orange circles to the purple circles (lowest reflectivity signal).

For all experiments, data collection was stopped prior to complete removal of the film from the air-water interface as the focus of the experiment was on the initial reaction mechanism. The amount of material at the air-water interface therefore does not completely decrease to zero in Figure 1 and Figures 4-6.

Table 3 details the neutron reflectivity experiments undertaken in the available beam time at ISIS and the ILL, and the pseudo-first order rate constants determined from the kinetic model for each experimental radical initiated oxidation of a monolayer film of DSPC by one of the aqueous phase radicals $^{\cdot}OH$, $SO_4^{\cdot-}$ or $NO_3^{\cdot}$.

Cite this: DOI: 10.1039/c0xx00000x

www.rsc.org/xxxxxx

ARTICLE TYPE

Table 2 Neutron reflectivity experiments conducted

Run Number	$\Gamma_{initial}$ / 10^{18} moelcule m^{-2}	Radical	pH of subphase	k'_{32} / 10^{-04} s^{-1}	k'_{33} / 10^{-04} s^{-1}	k'_{34} / 10^{-04} s^{-1}	k'_{35} / 10^{-04} s^{-1}
1	1.70	$NO_3^{\cdot}$	4.7	4.4	2.2	2.2	2.2
2 dark blank	1.64	$NO_3^{\cdot}$	4.7	-	-	-	-
3	1.65	$NO_3^{\cdot}$	4.7	1.1	1.0	1.0	1.0
3 light blank	1.68		-	-	-	-	-
4	1.52	$NO_3^{\cdot}$	4.7	1.9	1.8	1.8	1.8
5	1.62	$NO_3^{\cdot}$	5.5	2.1	2.0	2.0	2.0
6	1.60	$NO_3^{\cdot}$	5.5	1.4	1.3	1.3	1.3
7	1.63	$NO_3^{\cdot}$	5.5	2.2	2.0	2.0	2.0
8	1.64	$NO_3^{\cdot}$	5.5	2.4	2.2	2.2	2.2
9	1.63	$NO_3^{\cdot}$	5.5	1.6	1.5	1.5	1.5
10	1.74	$SO_4^{\cdot-}$	5.5	1.8	1.5	1.5	1.5
11	1.59	$SO_4^{\cdot-}$	5.5	2.2	1.8	1.8	1.83
12	1.62	$SO_4^{\cdot-}$	-	2.7	2.2	2.2	2.2
13	1.63	$SO_4^{\cdot-}$	-	2.7	2.2	2.2	2.2
14	1.64	$SO_4^{\cdot-}$	-	2.7	2.2	2.2	2.2
15 light blank	1.58		5.5	-	-	-	-
16 dark blank	1.58	$SO_4^{\cdot-}$	-	-	-	-	-
17	1.59	$SO_4^{\cdot-}$	-	1.3	1.1	1.1	1.1
18	1.59	$^{\cdot}OH$	5.5	3.7	2.2	2.4	2.0
19 light blank	1.59		5.5	-	-	-	-
20	1.62	$^{\cdot}OH$	5.5	3.3	2.0	2.2	1.8

[a] Table of pseudo-first order rate constants for each neutron experiment conducted, including the initial values of surface coverage and the pH of the precursor solution. It was assumed that all neutron reflectivity was due to DSPC.

Determination of steady state radical concentrations

The steady-state concentrations listed in Table 3 were calculated by fitting the temporal decay of NO_3^-, NO_2^- and $S_2O_8^{2-}$ as described in the determination of radical steady-state concentration in the experimental section and are shown in Figures 2 and 3. Unfortunately, the secondary radical chemistry that is required to form nitrate radicals following photolysis is not well characterised enough to calculate the nitrate radical steady-state concentration. Determination of the steady-state concentration was the largest measured source of uncertainty in the experiment. Analysis suggests that both the hydroxyl and sulfate steady-state concentrations are within 40 % of the values given in Table 3.

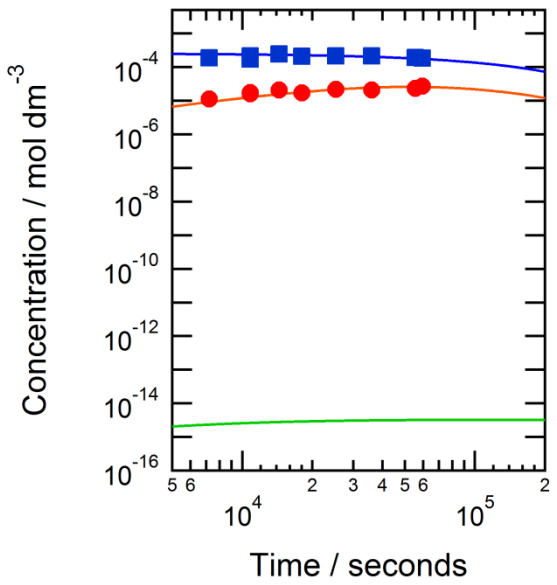

Fig. 2. The experimental decay of the NO_3^- anion and the production of the NO_2^- anion for the offline photolysis of KNO_3 are shown by the blue squares and the red circles respectively. The kinetically modelled fits are shown as lines through the points and the resultant steady-state hydroxyl radical concentration is represented by the green line.

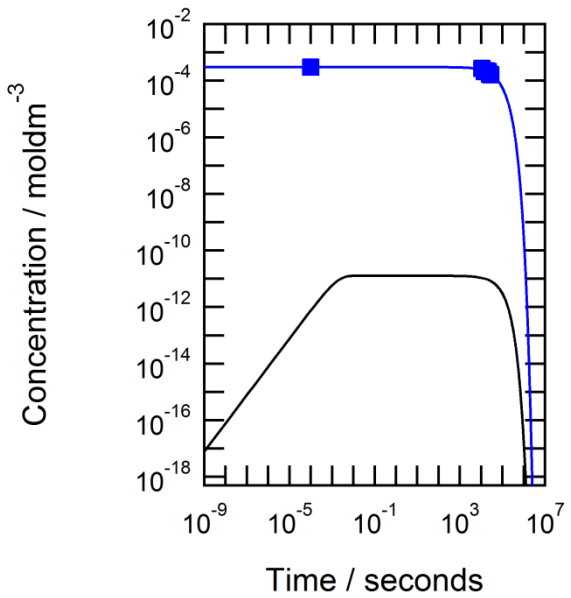

Fig. 3. The experimental decay of the $S_2O_8^{2-}$ anion for the offline photolysis of $K_2S_2O_8$ is shown by the blue squares and the kinetically modelled fit as the line through the markers. The resultant steady-state sulfate radical anion $SO_4^{\cdot-}$ concentration is shown as the black line.

Multi-step degradation kinetic fits

Figures 4-6 show the experimental decays of deuterated material at the air-water interface when a monolayer film of DSPC is exposed to the aqueous phase radicals, $NO_3^{\cdot}$, $SO_4^{\cdot-}$ and $^{\cdot}OH$ respectively. The experimental data is reproduced by calculation of equation R22 by varying k'_{32}-k'_{35} using kinetic modelling. Table 3 highlights the modelled values of k′ for each degradation step for each radical system ($^{\cdot}OH$ and $SO_4^{\cdot-}$).

Figures 4-6 demonstrate that the surface coverage of material at the air-water interface follows a degradation mechanism. Individual amounts of the surface active degradation products A, B, and C, are also shown in Figures 4-6 as well as blank runs, which emphasise the difference between degradation and no reaction. Figure 4 includes a dark blank, a monolayer film of DSPC on a radical precursor subphase with no light source i.e. no photolysis. Figures 5 and 6 both show light blanks i.e. photolysis only, for a monolayer film of DSPC on ACMW with UV light.

Figure 4 shows a ~93 % decay in the initial amount of deuterated material at the air-water interface in ~ 8 hours and a dark blank (red squares).

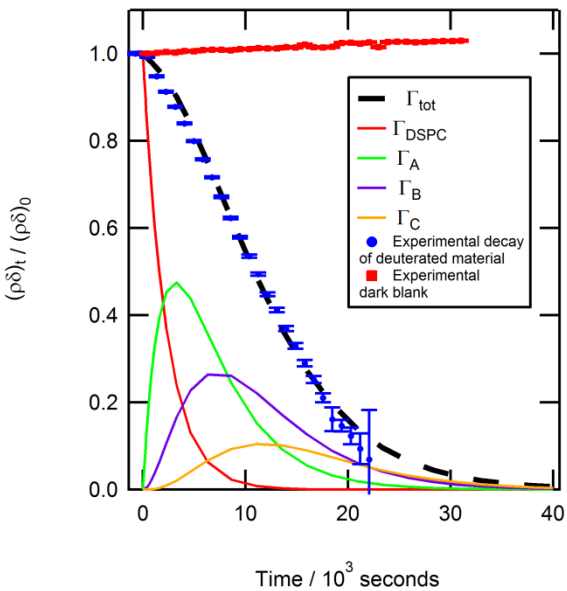

Fig 4. The experimental decay in relative surface coverage of deuterated material at the air-water interface due to $NO_3^{\cdot}$ radical initiated oxidation is shown by the blue circles. The figure also shows the modelled fit of the degradation mechanism to the experimental data as a dashed black line. The remaining curves represent the decay of the initial DSPC film (red line) and the build up and decay of the individual reaction products. A dark blank is represented by the red squares, which confirms that the reaction required the presence of UV light.

Figure 5 shows an ~89 % decrease in the initial amount of deuterated material at the air-water interface (blue circles) over ~7 hours of exposure to the aqueous sulfate radical. An exponential function has been fitted to the photolysis blank (red squares) which is indicative of a very slow decay in relative surface coverage with time. Decaying by ~4 % in ~5.3 hrs arising from a small degradation owing to the presence of UV light only.

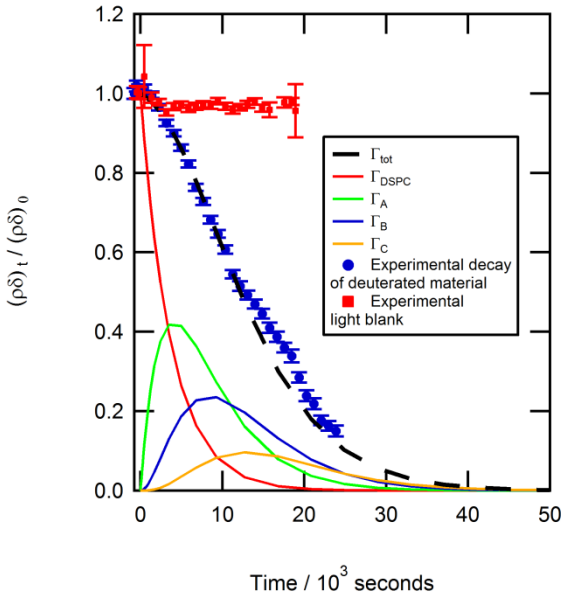

Fig 5. The decay in relative surface coverage of deuterated material at the air-water interface due to $SO_4^{\cdot-}$ radical initiated oxidation is shown by the blue circles. The dashed black line is the modelled fit of the degradation mechanism to the experimental data. The remaining curves represent the relative coverage of the individual steps of the degradation mechanism. The red squares represent a photolysis blank experiment, conducted on a monolayer film of DSPC on an ACMW subphase with UV light only (~254 nm). No radicals are knowingly generated from the subphase in the blank run but some degradation of the film does occur owing to the presence of UV light.

Figure 6 shows the decrease in the amount of deuterated material at the air-water interface on exposure to the aqueous hydroxyl radical. A 92 % decrease in the initial relative surface coverage was observed in 7.8 hours of photolysis time. As in Figure 5, there was a slight decrease in the amount of material for the photolysis blank (red squares) and so an exponential function was fitted to the decay. The exponential function indicated a ~15% decay in the initial relative surface coverage during ~5 hours of exposure to UV light which was a greater decay than that observed for the light blank in Figure 5. Comparing the decay from the light blank to the decay observed for the radical reaction after 5 hours of photolysis time, the amount of deuterated material at the air-water interface had decayed to 68% of its initial value in the presence of sulphate radical anions, which is significantly more than the 15% decay that occurred in the same time for the light blank. Therefore, the decrease in relative surface coverage induced by the UV light alone is not enough to account for the decay in surface coverage observed for the radical reaction.

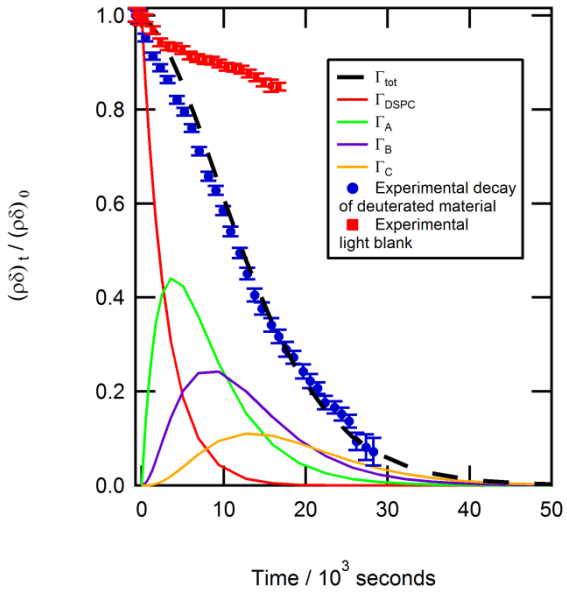

Fig 6. The decay in relative surface coverage of deuterated material at the air-water interface due to $^{\cdot}OH$ radical initiated oxidation is shown by blue circles. The modelled fit of the degradation mechanism to the experimental data is shown as a dashed black line through the experimental fit points. The remaining curves show the decrease in relative surface coverage of a monolayer film of DSPC (red) and the build up and decrease in relative surface coverage of the reaction products. A light blank is shown by the red squares which represent the relative surface coverage of a monolayer film of DSPC with time on an ACMW subphase with UV light (~360 nm). A ~15% decay is induced by radiation from the UV lights alone in 5 hours compared to ~68% decay induced for the radical reaction in the same time frame.

Table 3 Determined values of pseudo-first order and bimolecular rate constants and aqueous steady-state radical concentrations for the multi-step degradation mechanism for the aqueous phase hydroxyl and sulfate radical systems.

Radical Reaction	k' / 10^{-4} s^{-1}	Steady-state radical concentration / mol dm^{-3}	Radical Reaction	k / mol^{-1} dm^3 s^{-1}
	Range			Range
$^{\cdot}OH$ R32	0.33	3×10^{-15}	$^{\cdot}OH$ R27	11.1×10^9
	Range			Range
$^{\cdot}OH$ R33	0.20	3×10^{-15}	$^{\cdot}OH$ R28	6.64×10^9
	Range			Range
$^{\cdot}OH$ R34	0.22	3×10^{-15}	$^{\cdot}OH$ R29	7.20×10^9
	Range			Range
$^{\cdot}OH$ R35	0.18	3×10^{-15}	$^{\cdot}OH$ R30	6.09×10^9
	2.22 ±		$SO_4^{\cdot-}$	(3.77 ±
$SO_4^{\cdot-}$ R32	0.56	4.7×10^{-11}	R27	2.15) × 10^6
	1.85±		$SO_4^{\cdot-}$	(3.93 ±
$SO_4^{\cdot-}$ R33	0.47	4.7×10^{-11}	R28	0.99) × 10^6
	1.85 ±		$SO_4^{\cdot-}$	(3.93 ±
$SO_4^{\cdot-}$ R34	0.47	4.7×10^{-11}	R29	0.99) × 10^6
	1.85 ±		$SO_4^{\cdot-}$	(3.93 ±
$SO_4^{\cdot-}$ R35	0.47	4.7×10^{-11}	R30	0.99) × 10^6

[a] Range and average of the pseudo-first order (R32-35) and bimolecular rate constants (determined using equation R31 and the modelled aqueous radical steady-state concentrations) for each degradation step in the multi-step degradation mechanism for $^{\cdot}OH$ and $SO_4^{\cdot-}$ respectively. Two experiments were conducted using $^{\cdot}OH$, hence the range of the values rather than the average is given. The associated standard deviation is also reported for the sulfate system.

The pseudo-first order and bimolecular rate constants reported in Table 3 are averaged for each degradation step for all of the experiments conducted using the aqueous sulfate radical. Whereas the range is given for the pseudo-first order and bimolecular rate constants for each degradation step for the two experiments conducted using the aqueous hydroxyl radical. The uncertainty reported for the sulfate pseudo-first order and bimolecular rate constants is the standard deviation of the average value. No uncertainties are reported for the hydroxyl system as owing to time constraints at the neutron source, two experiments only were conducted. All the pseudo-first order rate constants for each radical system were also varied by a fixed percentage and the resultant fit through the experimental data points assessed by eye. Increments of k′ that provided a reasonable fit by eye were ± 5% for the hydroxyl system, ± 10% for the sulfate system and ± 20% for the nitrate system. For the nitrate system, a sensitivity analysis was performed; each pseudo-first order rate constant was varied individually by a fixed percentage and the remaining rate constants subsequently adjusted to maintain a good fit through the data points. From variation of individual pseudo-first order rate constants, it was deemed that no one rate constant was more or less significant in determining the reaction profile.

Determination of bimolecular rate constants, k

Bimolecular rate constants for reactions R27-R30 were calculated using the determined radical steady-state concentration and equation R31, and are listed in Table 3 with their associated standard deviations where possible.

Discussion

In the discussion, we shall consider the proposed multi-step degradation scheme, the values of the bimolecular rate constants, any Kinetic Isotope Effects, a brief comparison to the few other studies and the atmospheric implications of our work.

Proposed multi-step degradation mechanism

The degradation mechanism proposed in the multi-step degradation kinetics section can be described by the cartoon shown in Figure 7. The mechanism was invoked owing to its characteristic temporal profile and complete lack of exponential curve. The first step in the proposed mechanism is radical attack of the DSPC monolayer film by an aqueous phase radical ($NO_3^{\cdot}$, $SO_4^{\cdot-}$, $^{\cdot}OH$) to form a surface active product, A. Product A can be thought of as DSPC with a small deuterocarbon unit removed. Product A then reacts with another aqueous radical to undergo a further deuterium abstraction which results in the loss of the DSPC head group to leave a new surface active product at the air-water interface, B. The surface active product B can also undergo radical attack causing a third deuterium abstraction which finally results in the removal of one of the tail groups of DSPC to form surface active product C. Component C remains surface active but it is proposed that any further radical reactions will result in a non-surface active product, D that will partition into either the aqueous or gaseous phase. Figure 7 approximates these steps as a cartoon showing an interpretation of the ensemble surface coverage at the air-water interface following each step. The largest source of uncertainty in the experiment is assumed to arise from the number of steps in the degradation mechanism and the individual weightings of each step. However, this cannot be resolved by neutron reflectivity.

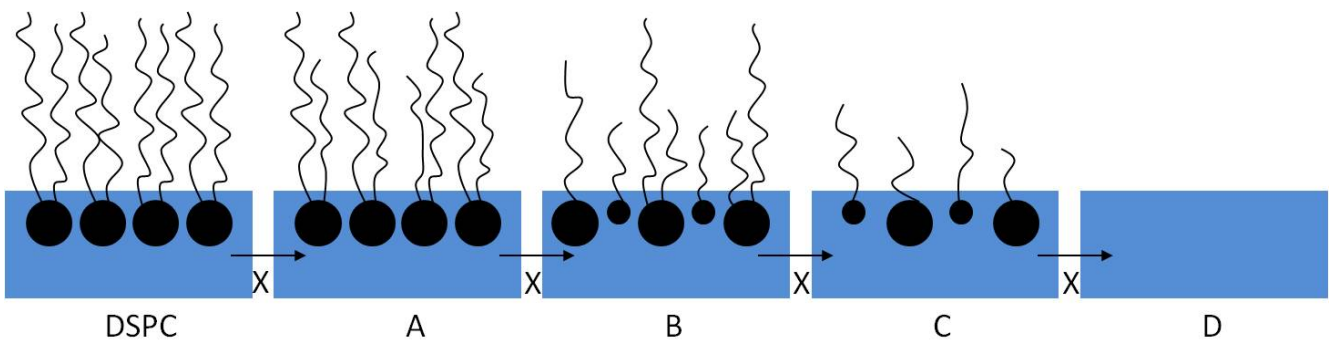

Fig.7 Cartoon of multi-step degradation mechanism approximating the ensemble surface coverage of material at the air-water interface following each step in the proposed degradation mechanism for the attack of a monolayer film of DSPC by an aqueous phase radical, X.

Figure 7 is a cartoon interpretation of the degradation mechanism whereas Figure 8 represents a molecular interpretation of the mechanism. Figures 4-6 showed the decay of material at the air-water interface and were consistent with a degradation mechanism resulting in degradation products that remained at the air-water interface. The decays in Figures 4-6 are consistent with an ensemble of DSPC molecules that required four radical initiated attacks to remove the film at the air-water interface. It is probable that for some of the DSPC molecules, less than four separate attacks are needed and for other DSPC molecules, more than four attacks are required. However, overall the results are commensurate with an ensemble of molecules that require four radical attacks. Likewise the change in scattering length density of an ensemble of DSPC molecules is consistent with (not necessarily equal to) 5 % loss of a CD_2 tail, loss of a head group and complete loss of a tail for each subsequent radical attack.

Figure 8 details the proposed chemical mechanism for initial aqueous radical $X^{\cdot}$ ($SO_4^{\cdot-}$, $^{\cdot}OH$) attack and subsequent secondary reactions resulting in C-C bond cleavage and carbonyl formation.

The chemistry in Figure 8 is based on radical chemistry from The Chemistry of Free Radicals[52] and details a deuterium abstraction followed by addition of ambient O_2 to form a peroxy radical. Peroxy self-reaction can occur or a secondary cross reaction with another peroxy radical; in both cases an alkoxy radical is formed. The alkoxy radicals can undergo carbon-carbon bond scission to form stable surface active products with shorter hydrocarbon tails than the original material or non surface active products that are soluble in the gaseous or aqueous phase.

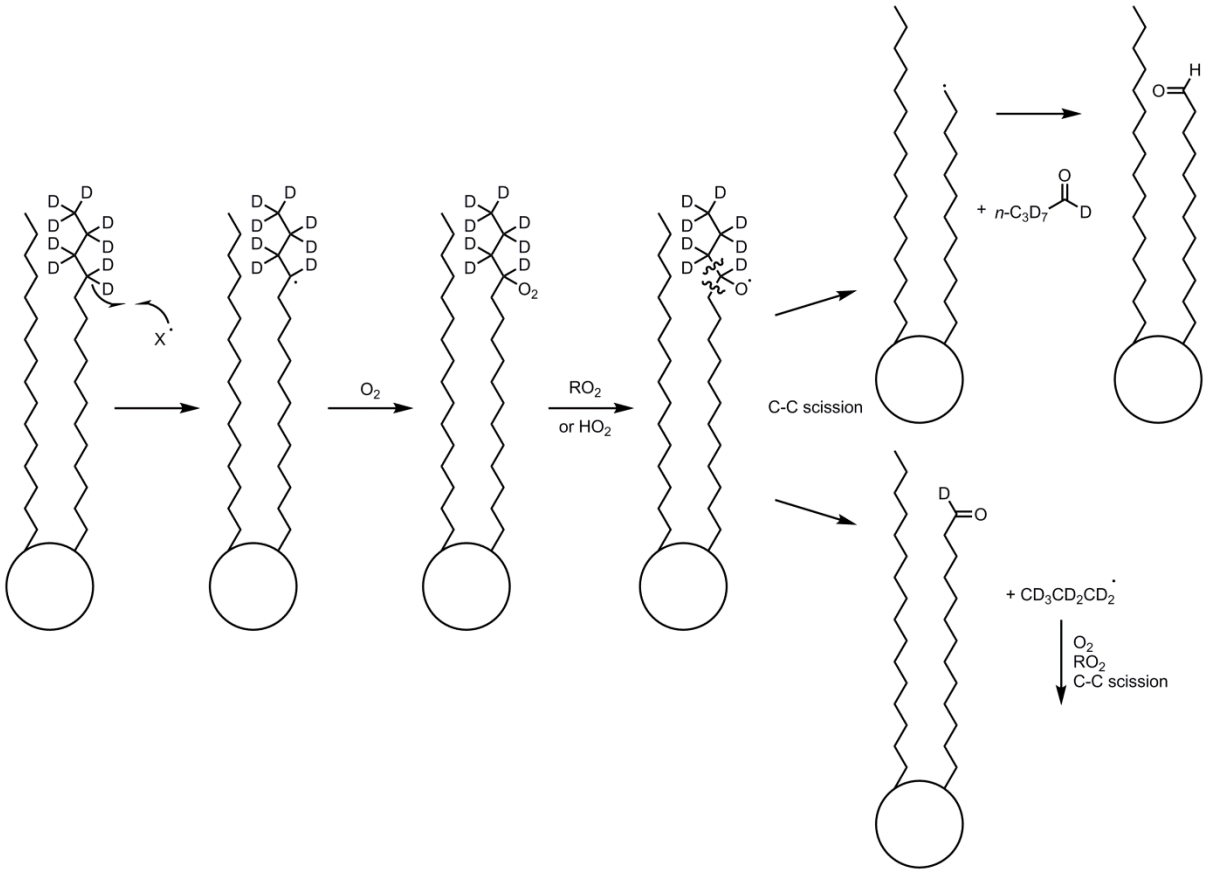

Fig.8 Stylised mechanism for aqueous radial initiated oxidation of a DSPC molecule showing the proposed reaction products.

Figure 8 allows the visualisation of the degradation mechanism in greater detail with respect to radical abstraction of a deuterium from one of the deuterocarbon chains on the lipid. Note the chemical mechanism is proposed to suggest how the chemistry proceeds and other mechanisms may also give similar results.

Bimolecular rate constants

The bimolecular rate constants determined for each step in the degradation mechanism (R27-R30) of a DSPC film initiated by aqueous phase ·OH radical attack, are larger than the bimolecular rate constants determined for oxidation initiated by aqueous phase sulfate radical attack. Attack by the ·OH radical is therefore faster than attack by the sulfate radical as well as being non-selective. Following the initial radical attack, the subsequent bimolecular rate constants for each step of the degradation mechanism are similar to each other, which is what is expected given that A, B and C are similar molecules, i.e. the radical can easily abstract a deuterium from the remaining deuterocarbon tail.

Kinetic Isotope Effect

Owing to the deuteration of the DSPC film, there will be a potential kinetic isotope effect on the determined values of the rate constants. Statistical mechanics has shown the kinetic isotope effect to be up to a factor of 7.2[51] for initial Hydrogen abstraction but the kinetic isotope effect is generally 6.1 for a C-H bond.

Comparison to other literature studies

There have been several studies on the oxidation of thin films by gaseous phase oxidants in the literature e.g. references 19, 23, 53-56 but few studies using non-gaseous oxidants.

Karagulian et al.[57-58] coated a solid mixture of NaCl and $NaNO_2$ particles, 2 μm in diameter with the lipid 1-oleoyl-2-palmitoyl-sn-glycero-3-phosphocholine (OPPC). The mixture was photolysed at ~290 nm and O^- and ·OH were subsequently generated at the interface from the photolysis of NO_2^-. The O^- and ·OH radicals were able to react with the OPPC coating and the reaction was followed using diffuse reflection infrared Fourier transform spectroscopy (DRIFTS). The loss of OPPC and the formation of oxidation products consistent with the reaction of

˙OH with the OPPC coating were identified using Matrix-assisted laser desorption/ionization mass spectrometry (MALDI-MS). The authors concluded that generation of the ˙OH radical at the coating interface resulted in oxidation from the 'bottom up'. It was also proposed that similar chemistry would occur for aqueous droplets coated in an organic film.

Atmospheric implications

Determination of atmospheric lifetime

The lifetime of DSPC with respect to aqueous ˙OH radical attack was calculated to be ~ 6 hours using the following equation.

$$\tau = \frac{1}{k[OH]} \qquad \text{R36}$$

The atmospheric steady state concentration for aqueous ˙OH radicals obtained from Anastasio and Newburg[59] was 3.80×10^{-16} moldm^{-3}. It proved difficult to locate typical atmospheric concentrations for both the $NO_3^{\cdot}$ and $SO_4^{\cdot-}$ radicals in the literature owing to the difficulty of making such measurements experimentally; therefore, the lifetime of DSPC with respect to $NO_3^{\cdot}$ and $SO_4^{\cdot-}$ radical attack was not calculated.

The lifetime of DSPC is interesting because it provides an idea of the importance of a lipid coating on atmospheric aerosol and gives an idea of how easy it would be to detect a lipid in the atmosphere. A lifetime of 6 hours is relatively short compared to a typical aerosol lifetime of ~4-10 days. The steady-state concentration of ˙OH radicals determined in the current experiment was $\sim 3 \times 10^{-15}$ moldm^{-3} which gives a lifetime of ~0.8 hours, in keeping with the lifetime of DSPC obtained in the degradation model of ~0.7 hours. However, determination of the film lifetime is more important in order to assess the effect of a film on the optical and hygroscopic properties of an aerosol.

Owing to the fact that the shape of the decay for aqueous radical attack of a thin film of DSPC at the air-water interface was not an exponential decay, a degradation mechanism was kinetically modelled as described in the experimental section. The differential equations used to describe the degradation mechanism were also solved analytically (see supplementary information) and the relative amount of the film at the air-water interface with time was calculated using the bimolecular rate constants listed in Table 3 and ˙OH concentrations[59] of 3.80×10^{-16} moldm^{-3}, 3.80×10^{-17} and 3.80×10^{-15} moldm^{-3} to provide an envelope of film lifetimes. The determined lifetimes are plotted in Figure 9 for the three different ˙OH concentrations.

The solid black line in Figure 9 (˙OH concentration, 3.80×10^{-16} moldm^{-3}) indicates that it takes ~1.5 days for the amount of film material to decay to half of its initial amount, which is of the same order of magnitude as a typical aqueous aerosol lifetime and could suggest that oxidation initiated by the ˙OH radical may be important in the atmosphere. The vertical dashed line emphasises the film half-lives and indicates that oxidation of the film critically depends on the ˙OH radical concentration. An ˙OH concentration of 3.80×10^{-15} moldm^{-3} gives a half-life of less than one day whereas an ˙OH concentration of 3.80×10^{-17} moldm^{-3} gives a half-life greater than four days which is comparable to a typical aerosol lifetime. Few studies of ambient ˙OH in droplets have been conducted so few values of the atmospheric concentration of aqueous radicals have been determined.

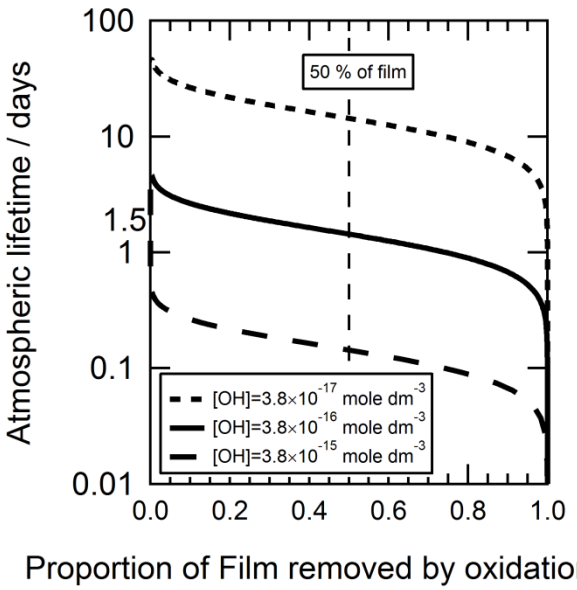

Fig. 9. Atmospheric lifetime of the film versus proportion of the film removed by oxidation for three different ˙OH radical concentrations. The vertical dashed line highlights the atmospheric half life. The importance of the ˙OH concentration is emphasised by the figure considering a typical aerosol lifetime is in the order of a few days.

Conclusions

The amount of deuterated material at the air-water interface was observed to decay when a monolayer film of fully deuterated DSPC was exposed to the aqueous phase radicals, ˙OH, $SO_4^{\cdot-}$ and $NO_3^{\cdot}$. The decay was consistent with a multi-step degradation mechanism that could be described by initial removal of a small unit from the deuterocarbon tail, followed by the removal of a head group and finally complete removal of a tail. The initial loss of DSPC was determined to be the fastest step in the degradation mechanism.

An atmospheric lifetime of ~6 hours was calculated for a DSPC molecule with respect to attack by an aqueous phase hydroxyl radical using a typical atmospheric concentration of aqueous hydroxyl radicals[59].

The overall film lifetime was determined to critically depend on the atmospheric radical concentration. A film half life of ~1.5 days was calculated using the literature concentration of 3.80×10^{-16} moldm^{-3} for aqueous hydroxyl radicals[59]. Therefore, oxidation of thin films in the atmosphere by aqueous radicals may be important and their reactions are consistent with a multi-step degradation mechanism.

Acknowledgments

We thank STFC ISIS and the ILL for the award of beam time under the grants RB1320137, RB1310415, 9-10-1287, 9-10-1288. SHJ is grateful to NERC for PhD funding grant NE/H019103/1.

Notes and references

‡The UV-Visible measurements were conducted using a long path

length (17.5 cm) stainless steel cell (inner diameter 0.25 inches) with CaF_2 windows and collimating lenses (Ocean Optics 74-series). A deuterium tungsten halogen light source (Ocean Optics DT-mini-2-GS) was fibre coupled (Ocean Optics premium-grade patch cord) to the long path length cell and a spectrometer (Ocean Optics USB 2000+). The UV-Visible spectrum of the photolysed solution was recorded over the wavelength range 180-877 nm by averaging over 100 scans using a 220 ms integration time. The UV lamps were placed at the same height above the same trough as used in the neutron experiments and a syringe was used to add and remove the radical precursor solution from the trough. Prior to and following photolysis the radical precursor solution was weighed to account for any changes in weight due to evaporation during photolysis. Initially, the UV-Visible spectrum of pure water was measured three times then the system was rinsed with the photolysed solution before measuring the spectrum of the photolysed solution three times. The long path length cell was subsequently rinsed with pure water to ensure complete removal of the measured solution. Three measurements of the stock radical precursor solution were also taken each time a photolysis measurement was taken.

[a] *Department of Earth Sciences, Royal Holloway University of London, Egham, Surrey, TW20 0EX, U.K. Fax: XX XXXX XXXX; Tel: XX XXXX XXXX; E-mail: m.king@es.rhul.ac.uk, stephanie.jones.2011@live.rhul.ac.uk*
[b] *STFC, Central Laser Facility, Research Complex at Harwell, Rutherford Appleton Laboratory, Harwell Oxford, Didcot, Oxfordshire, OX11 0FA, U.K. E-mail: andy.ward@stfc.ac.uk*
[c] *Department of Physics and Astronomy, Uppsala University, 75120 Uppsala, Sweden.*
[d] *Institut Laue-Langevin, BP 156, 6, rue Jules Horowitz, 38042 Grenoble Cedex 9, France.*
[e] *ISIS pulsed neutron and Muon source, Rutherford Appleton Laboratory, Harwell Oxford, Oxfordshire, OX11 0QX.*

† Electronic Supplementary Information (ESI) available: [Analytical solutions to the differential equations used to describe the multi-step degradtion mechanism can be found in the supplementary information]. See DOI: 10.1039/b000000x/

1. P. Saxena and L. M. Hildemann, *J. Atmos. Chem.*, 1996, **24**, 57–109.
2. U. Poschl, *Angew. Chem. Int. Ed.* 2005, **44**, 7520-7540.
3. IPCC, 2013: Climate Change 2013: The Physical Science Basis. Contribution of Working Group I to the Fifth Assessment Report of the Intergovernmental Panel on Climate Change [Stocker, T.F., D. Qin, G.-K. Plattner, M. Tignor, S.K. Allen, J. Boschung, A. Nauels, Y. Xia, V. Bex and P.M. Midgley (eds.)]. Cambridge University Press, Cambridge, United Kingdom and New York, NY, USA, 1535 pp.
4. D. J. Donaldson and V. Vaida, *Chem. Rev.*, 2006, **106**, 1445-1461.
5. G. Ellison, A. Tuck, and V. Vaida, *J. Geophys. Res.*, 1999, **104**, 11633-11641.
6. P. Gill, T. Graedel, and C. Weschler, *Rev. Geophys.*, 1983, **21**, 903–920.
7. H. Tervahattu, K. Hartonen, V. Kerminen, K. Kupiainen, T. Koskentalo, A. F. Tuck, and V. Vaida, *J. Geophys. Res.*, 2002, **107**, AAC 1-1-AAC 1-8.
8. H. Tervahattu, J. Juhanoja, V. Vaida, A. Tuck, J. Niemi, K. Kupiainen, M. Kulmala, and H. Vehkamaki, *J. Geophys. Res.*, 2005, **110**, D06207.
9. B. E. Wyslouzil, G. Wilemski, R. Strey, C. H. Heath, and U. Dieregsweiler, *Phys. Chem. Chem. Phys.*, 2006, **8**, 54–7.
10. A. H. Falkovich, *J. Geophys. Res.*, 2004, **109**, D02208.
11. L. M. Russell, S. F. Maria, and S. C. B. Myneni, *Geophys. Res. Lett.*, 2002, **29**, 26–1–26–4.
12. D. C. Blanchard, *Science*, 1964, **146**, 396–397.
13. 1D. J. Donaldson and C. George, *Environ. Sci. Technol.*, 2012, **46**, 10385–10389.
14. B. Simoneit, *Mar. Chem.*, 1977, **5**, 443–464.
15. H. Herrmann, *Chem. Rev.*, 2003, **103**, 4691–716.
16. P. Saxena, L. Hildemann, P. H. McMurry, and J. H. Seinfeld, *J. Geophys. Res.*, 1995, **100**, 18755–18770.
17. B. M. Mircea, M. C. Facchini, S. Decesari, and R. J. Charlson, *Tellus Ser. B-Chemical Phys. Meteorol.*, 2002, **54**, 74–81.
18. G. McFiggans, P. Artaxo, U. Baltensperger, H. Coe, M. C. Facchini, G. Feingold, S. Fuzzi, M. Gysel, A. Laaksonen, U. Lohmann, T. F. Mentel, D. M. Murphy, C. D. O'Dowd, J. R. Snider, and E. Weingartner, *Atmos. Chem. Phys. Discuss.*, 2005, **6**, 2593–2649.
19. M. D. King, A. R. Rennie, K. C. Thompson, F. N. Fisher, C. C. Dong, R. K. Thomas, C. Pfrang, and A. V. Hughes, *Phys. Chem. Chem. Phys.*, 2009, **11**, 7699–7707.
20. A. M. Thompson, *Science*, 1992, **256**, 1157–1165.
21. M. Andreae and P. J. Crutzen, *Science*, 1997, **276**, 1052–1058.
22. R. Wayne, I. Barnes, P. Biggs, J. Burrows, C. Canosa-Mas, J. Hjorth, G. Le Bras, G. Moortgat, D. Perner, G. Poulet, G. Restelli, and H. Sidebottom, *Atmos. Environ., Part A*, 1991, **25**, 1–203.
23. M. D. King, A. R. Rennie, C. Pfrang, A. V. Hughes, and K. C. Thompson, *Atmos. Environ.*, 2010, **44**, 1822–1825.
24. C. Pfrang, F. Sebastiani, C. O. M. Lucas, M. D. King, I. D. Hoare, D. Chang, and R. A. Campbell, *Phys. Chem. Chem. Phys.*, 2014, **16**, 13220–13228.
25. W. D. Garrett, *Deep. Res.*, 1967, **14**, 221–227.
26. K. Larsson, G. Odham, and A. Södergren, *Mar. Chem.*, 1974, **2**, 49–57.
27. J. C. Marty, A. Saliot, P. Buat-Ménard, R. Chesselet, and K. A. Hunter, *J. Geophys. Res.*, 1979, **84**, 5707–5716.
28. J. R. Lu, R. K. Thomas, and J. Penfold, *Adv. Colloid Interface Sci.*, 2000, **84**, 143–304.
29. J. Penfold and R. K. Thomas, *J. Phys. Condens. Matter*, 1990, **2**, 1369-1412.
30. J. Penfold, R. M. Richardson, A. Zarbakhsh, J. R. P. Webster, D. G. Bucknall, A. R. Rennie, R. A. L. Jones, T. Cosgrove, R. K. Thomas, J. S. Higgins, P. D. I. Fletcher, E. Dickinson, S. J. Roser, I. A. McLure, A. R. Hillman, R. W. Richards, E. J. Staples, a. N. Burgess, E. A. Simister, and J. W. White, *J. Chem. Soc. Faraday Trans.*, 1997, **93**, 3899–3917.
31. R. A. Campbell, H. P. Wacklin, I. Sutton, R. Cubitt, and G. Fragneto, *Eur. Phys. J. Plus*, 2011, **126**, 107.
32. V. Sears, *Neutron news*, 1992, **3**, 26–37.
33. R. Pynn, in *Neutron Scattering-A Non-destructive Microscope for Seeing Inside Matter in Neutron Applications in Earth, Energy and Environmental Sciences*, Neutron Scattering Applications and Techniques, ed. L. Liang, R. Rinaldi and H. Schober, Springer US, 2009, pp 15-36.
34. C. M. Hollinshead, R. D. Harvey, D. J. Barlow, J. R. P. Webster, A. V Hughes, A. Weston, and M. J. Lawrence, *Langmuir*, 2009, **25**, 4070–4077.
35. F. Abelès, Le Journal de Physique et le Radium,1950, **11**, 307-310.
36. A. Nelson, *J. Appl. Crystallogr.*, 2006, **39**, 273–276.
37. A.R. Rennie, Neutron Reflection Analysis Programs; http://material.fysik.uu.se/Group_members/adrian/refprog.htm accessed March 2013.
38. J. Mack and J. Bolton, *J. Photochem. Photobiol. A chem.*, 1999, **128**, 1–13.
39. X. Yu, Z. Bao, and J. R. Barker, *J. Phys. Chem. A*, 2004, **108**, 295–308.
40. L. Chu and C. Anastasio, *J. Phys. Chem. A*, 2003, **107**, 9594–9602.
41. L. Chu and C. Anastasio, *Environ. Sci. Technol.*, 2007, **41**, 3626–32.

42. C.O.M. Lucas, Ph.D. Thesis, Royal Holloway University of London, 2012.
43. W. H. Press, B. P. Flannery, S. A. Teukolsky, and W.T. Vetterling, *Numerical Recipes in C*, Cambridge University Press, New York, 2nd edn., 1992, pp. 994.
44. S. D. Cohen, A. C. Hindmarsh, *CVODE User Guide*, LLNL Report UCRL-MA-118618, September 1994.
45. P. N. Brown, G. D. Byrne, A. C. Hindmarsh, VODE, a Variable-Coefficient ODE Solver, *SIAM J. Sci. Stat. Comput.*, 1989, ***10***, 1038-1051.
46. Y. Katsumura and P. Jiang, *J. Phys. Chem.,* 1991, **95**, 4435–4439.
47. T. Løgager and K. Sehested, *J. Phys. Chem.*, 1993, **97**, 6664–6669.
48. H. Buiteveld, J. H. . Hakvoort, and M. Donze, *SPIE Ocean Opt. XII 2258*, 1994, **2258**, 174–183.
49. L. Kröckel and M. A. Schmidt, *Opt. Mater. Express*, 2014, **4**, 559–567.
50. R.P. Buck, S. Singhadeja and L.B. Rogers, *Anal. Chem.*, 1954, **26**(7), 1240-1242.
51. K. J. Laidler, *Kinetic Isotope Effects in Chemical Kinetics*, Harper and Row, 1987.
52. *The Chemistry of Free Radicals*: Peroxyl Radicals, ed. Z. B. Alfassi, Wiley, 1997.
53. L. F. Voss, M. F. Bazerbashi, C. P. Beekman, C. M. Hadad, and H. C. Allen, *J. Geophys. Res.*, 2007, **112**, D06209.
54. E. González-Labrada, R. Schmidt, and C. E. DeWolf, *Chem. Commun.*, 2006, **23**, 2471–2473.
55. E. González-Labrada, R. Schmidt, and C. E. DeWolf, *Phys. Chem. Chem. Phys.*, 2007, **9**, 5814-5821.
56. K. C. Thompson, S. H. Jones, A. R. Rennie, M. D. King, A. D. Ward, B. R. Hughes, C. O. M. Lucas, R. A. Campbell, and A. V Hughes, *Langmuir*, 2013, **29**, 4594–4602.
57. F. Karagulian, A. Scott Lea, C. W. Dilbeck, and B. J. Finlayson-Pitts, *Phys. Chem. Chem. Phys.*, 2008, **10**, 528–541.
58. F. Karagulian, C. W. Dilbeck, and B. J. Finlayson-pitts, *J. Am. Chem. Soc.*, 2008, **130**, 11272–11273.
59. C. Anastasio and J. T. Newberg, *J. Geophys. Res.*, 2007, **112**, D10306.

Electronic Supplementary Information for "The atmospheric importance of aqueous radical initiated oxidation of an organic monolayer at the air-water interface studied by neutron reflectivity" by S. H. Jones, M. D. King, A. R. Rennie, A. D. Ward, R. A. Campbell and A. V. Hughes.

The multi-step degradation mechanism,

$$DSPC \longrightarrow A \longrightarrow B \longrightarrow C \longrightarrow D$$

can be described by the following differential equations:

$$\frac{-d[A]}{dt} = k_1[A]$$

$$\frac{d[B]}{dt} = k_1[A] - k_2[B]$$

$$\frac{d[C]}{dt} = k_2[B] - k_3[C]$$

$$\frac{d[D]}{dt} = k_3[C] - k_4[D]$$

An integrating factor was used to solve the differential equations and the following solutions were obtained:

$$[A] = [A_0]e^{-k_1 t}$$

$$[B] = \frac{k_1[A_0]}{(k_2 - k_1)}(e^{-k_1 t} - e^{-k_2 t})$$

$$[C] = \frac{k_1 k_2[A_0]}{(k_2 - k_{1)}}\left(\frac{e^{-k_1 t}}{(k_3 - k_1)} - \frac{e^{-k_2 t}}{(k_3 - k_2)} - \frac{e^{-k_3 t}}{(k_3 - k_1)} + \frac{e^{-k_3 t}}{(k_3 - k_2)}\right)$$

$$[D] = \frac{k_1 k_2 k_3[A_0]}{(k_2 - k_{1)}}\left(\frac{e^{-k_1 t}}{(k_3 - k_1)(k_4 - k_1)} - \frac{e^{-k_2 t}}{(k_3 - k_2)(k_4 - k_2)} - \frac{e^{-k_3 t}}{(k_3 - k_1)(k_4 - k_3)} + \frac{e^{-k_3 t}}{(k_3 - k_2)(k_4 - k_3)} - \frac{e^{-k_4 t}}{(k_3 - k_1)(k_4 - k_1)} + \frac{e^{-k_4 t}}{(k_3 - k_2)(k_4 - k_2)} + \frac{e^{-k_4 t}}{(k_3 - k_1)(k_4 - k_3)} - \frac{e^{-k_4 t}}{(k_3 - k_2)(k_4 - k_3)}\right)$$

Paper 5: The reaction of a monolayer of oleic acid with gas-phase ozone at the air-water interface: The effect of solution viscosity

M. D. King, **S. H. Jones**, A. R. Rennie, A. D. Ward, A. V. Hughes and R. A. Campbell

To be submitted to Physical Chemistry Chemical Physics, 6 pages.

Within this partly co-authored work, I declare that the following contributions are entirely my own work:

- Conducted the neutron experiments and collected and analysed the data.
- Contributed significantly to the design of the experiment.
- Contributed to drawing the conclusions of the paper.

The reaction of a monolayer of oleic acid with gas-phase ozone at the air-water interface: The effect of solution viscosity.

Martin D. King,[a*], Stephanie H. Jones,[a] Adrian R. Rennie,[c] Andrew D. Ward,[d], Arwel V. Hughes,[g] Richard Campbell,[h]

Received Xth XXXXXXXXXX 20XX, Accepted Xth XXXXXXXXX 20XX
First published on the web Xth XXXXXXXXXX 200X
DOI: 10.1039/b000000x

The oxidation of oleic acid at the air-water interface is an important model reaction for oxidation of organic matter at the interface of aqueous atmospheric aerosol. Organic films on atmospheric particulate matter affect the optical and hygrodynamic properties of atmospheric matter and affect modern climate change. The oxidation of a monolayer of oleic acid by gas-phase ozone at the air-aqueous solution interface studied by neutron reflection is shown to be independent of solution viscosity and ionic strength over the relative viscosity range 1–7.4, demonstrating that the rate-determining step of this multi-step heterogeneous reaction does not involve the solution. As a first approximation for proxy organic films - (such as oleic acid) on atmospheric aerosol, the viscosity of the core aerosol, over the relative range 1–7.4, does not affect the lifetime of the film with respect to oxidation by ozone and can be neglected in atmospheric chemistry models.

1 Introduction

The oxidation of oleic acid at the air-water interface is an important model reaction for oxidation of the organic matter at the interface of aqueous atmospheric aerosol.[1–3] Organic films on atmospheric particulate matter affect the optical and hygrodynamic properties of atmospheric matter and affect modern climate change.[1,4]

The oxidation of oleic acid at the air-water interface by gas-phase ozone can be broken into a multi-step process. The gas-phase ozone must first diffuse to the interface, accommodate at the interface (in this case the oleic acid) and then diffuse to the reaction site (the double bond of the oleic acid) and react. Characteristic times (or rate constants) for these processes can be calculated (as to be shown in section 2.7). The process with the longest characteristic time will be the rate limiting step and control the lifetime of oleic acid owing to chemical oxidation by ozone at the air-water interface. Such knowledge allows atmospheric researchers to assess the importance of organic films at the air-water interface of airborne aqueous aerosols in the atmosphere by only considering the rate limiting process. Due care must be afforded to the conversion of laboratory processes to the atmosphere[5]. The ozone may also diffuse to the water beneath the oleic acid and attack the oleic acid "from below"[6,7]. Ozone is very soluble in water[8]. To assess whether diffusion into the sub-phase was important a series of experiments were performed to measure the first-order decay of oleic acid at the air-aqueous solution interface as the viscosity of the aqueous solution was increased. Increasing the viscosity of the solution will hinder the diffusion of ozone in the aqueous solution, and if the diffusion is important it will retard the rate of oxidation of the oleic acid film. The chemical used to increase the solution viscosity will also increase the ionic strength. Atmospheric aerosol may be of very large viscosity[9–12] and ionic strength[13,14]. Thus the aim of this work is to assess whether the reaction of oleic acid at the air-water interface is retarded by an increase in the viscosity of the solution phase below the oleic acid.

[a] *Department of Earth Sciences, Royal Holloway University of London, Egham, Surrey. Fax: 44 1784 471780; Tel: 44 1784 414038; E-mail: m.king@es.rhul.ac.uk*
[b] *Central Laser Facility, Research Complex at Harwell, Rutherford Appleton Laboratory, Harwell Innovation Campus, Chilton, Didcot, OX11 0FA, UK*

2 Experimental

The experimental section will describe the separate parts of the method individually.

2.1 Neutron reflection

Specular neutron reflection can be used to probe the composition and potentially the thickness of a series of parallel layers normal to an interface. A good description of the use of neutron scattering for the study of interface can be found elsewhere[15,16]. However a brief description will be given here.

The specular reflection of neutrons from thinly layered media can be used to determine the composition of those layers normal to the reflecting beam. The composition is deduced from the effective refractive index of neutrons in these

layers. The refractive index being calculated from the wavelength of the neutron and the scattering length density of the layers. The coherent scattering length of a chemical compound may be calculated by summing up the coherent scattering lengths of the different nuclei within a chemical compound and the scattering length density is calculated as the scattering length per unit molecular volume[17]. Coherent scattering lengths densities are well known and tabulated[17]. The chemical system in the experiments described here may be described by a thick layer aqueous of subphase of sodium perchlorate with a thin (tens of angstrom) layer of perdeuterated oleic acid ($(CD_2)_8CD{=}CD(CD_2)_7CO_2H$), topped with a thick layer of air. The scattering length density of the air (relative to the condensed phase layers) is effectively zero. The scattering length densities of the oleic acid monolayer and bulk aqueous subphase of aqueous sodium perchlorate have scattering length densities highly dependent on the relative amount of deuterium to hydrogen in the samples. A strong contrast in the effective refractive index of the oleic acid monolayer can be achieved by perdeuterating the oleic acid, to create a large scattering length density, and mixing the proportion of D_2O and H_2O in the aqueous subphase, to make a small or zero scattering length density for the subphase (8% v/v D_2O in H_2O for pure water), also known as constrast matching. Thus the neutron reflection data may be modelled as a single uniform thin layer between two semi-infinite layers with zero (or small) refractive index. The scattering lengths, b, of H (b=-3.74 fm) and D (b=6.68 fm) are very different and careful use of deuteration can be used to provide strong contrast in neutron reflection experiments.

Neutron reflection measurements were made at the ISIS pulsed neutron and muon spallation source at the Rutherford Appleton Laboratory with preliminary measurements conducted at the Institute Laue Langevin in Grenoble. The SURF reflectometer[18] was used at ISIS and the FIGARO reflectometer at the ILL[19]. The SURF reflectometer has an incident neutron beam at 1.5° to the horizontal of the air-liquid interface. The time of flight instrument illuminates with a range of neutron wavelengths, λ to give the reflectivity as function of the momentum transfer, Q, $Q = \frac{4\pi sin(\theta)}{\lambda}$, over the wavelength range 0.06 to 0.5 Å. Reflectivity data from all measurements were normalised to the intensity of the incident beam and absolute reflectivity data were obtained relative to a measurement of pure D_2O.

Modelled reflectivity data was compared to experimental data to determine the scattering length density and thickness of the perdeuterated layer using an Abelès optical matrix method[20–22]. A least-squares fitting procedure was used to vary the values of the scattering length density, ρ, and layer thickness, δ to calculate the modelled data and compare to the experimental reflectivity curve. A layer at the air-water interface of thickness, δ and scattering length density, ρ, may be related to the surface coverage, Γ, of material at the air-water interface with scattering length, b by

$$\Gamma = \frac{\rho\delta}{b} \quad (1)$$

Thus neutron reflection can be measured as the surface coverage of the material at the air-water interface for known compounds. In the work presented here the oleic acid will react with ozone and the composition, and thus scattering length of the material will change during the reaction. The product $\rho\delta$ (equal to Γb) will be followed kinetically as $\frac{\rho\delta}{\rho_o\delta_o}$, where $\rho_o\delta_o$ is the initial value of $\rho\delta$ before reaction and $\rho\delta$ is the value at some time, t, later. See section 2.6 for further information.

2.2 Generation of ozone

A 0.13 ppm of gas-phase ozone in oxygen was generated by flowing pure oxygen (2 L min^{-1}) through a quartz glass tube and photolysing the oxygen with a mercury pen-ray lamp in a commercial ozoniser from UVP. The flow was directed by PFA tubing to a Tedlar bag containing a custom-made Langmuir trough constructed from pure PTFE (surface area = 168 cm^2, depth ~4 mm). The volume of the Tedlar bag was 25 L and the flow of oxygen was maintained throughout the experiment. The gas exhausted the bag via PFA tubing and was bubbled through aqueous potassium hydroxide solution and to a local exhaust vent. The bag was approximately half inflated. An approximately half-inflated bag was achieved by sealing the bag once approximately half-inflated and allowing an equilibrium to be achieved between the input and output gas flows. The mixing time in the bag was $\sim \frac{10\pm2L}{2\text{L min}^{-1}} = 5\pm1$ minute. The mixing ratio of ozone within the flow was controlled (0.13 ppm or zero ppm) by switching the mercury pen ray lamp on and off. The mixing ratio of ozone was calibrated offline by UV-Vis spectrometry using the absorption maxima around a wavelength of 254 nm.

2.3 Application of surface active species

The deuterated oleic acid was placed at the air-water interface using a Hamilton syringe as a 1 mg mL^{-1} solution in chloroform. Approximately 20 μL was added. The chloroform was allowed to evaporate and purged from the Tedlar bag by the oxygen flow. Two blank experiments were performed: (1) monitoring the surface active species (deuterated oleic acid) in a flow of oxygen only (no ozone) and (2) monitoring the air-water interface of the sodium perchlorate solution in the absence of the deuterated film. The surface pressure of the interface was not monitored during the experiment as the Wilhemy plate tensiometer may have been damaged by ozone and would have blocked the neutron beam on the small Langmuir trough.

2.4 Viscosity of the aqueous subphase

The reaction between ozone and oleic acid has been shown to be consistent with the diffusion of the ozone to the organic monolayer, accommodation of the ozone within the monolayer and then reaction of accommodated ozone with the oleic acid film.[3,23] However, the dissolving of ozone into the aqueous subphase and subsequent reaction with the monolayer film , *i.e.* "attack from below"[6,7] may also be important. Thus the rate-limiting step may be the diffusion of ozone in the water. By increasing the viscosity of the subphase it can be shown that the diffusion of ozone in water is not the rate limiting step and potentially provides evidence that the subphase ozone is not involved in the reaction. The viscosities of atmospheric aerosol are large and these experiments may represent real conditions in atmospheric aerosol.

The viscosity of the subphase was increased by the addition of sodium perchlorate ($NaClO_4$). Sodium perchlorate is inert to ozone, dissolves readily, and increases the viscosity and the ionic strength, of the solution. The solutions used in the work described here are shown in table 2. The relative visicosities (to pure water) were calculated from[24,25] for the solutions in table 2. The ionic strength, and pH (measured with pH paper owing to the presence of D_2O) are given in table 2

2.5 Samples

Deutereated oleic acid ($(CD_2)_8CD{=}CD(CD_2)_7CO_2H$) was obtained from Sigma Aldrich as a special synthesis at a stated isotopic purity of 98% and used without further purification. Sodium perchlorate was also obtained from Sigma Aldrich. H_2O was purified on site to a resistivity greater than 18MΩ cm, D_2O was supplied by ISIS and the ILL. Oxygen was BOC technical grade with a stated purity greater than 99%

2.6 Kinetic analysis

King et al[3] studied the kinetic decay of oleic acid at the air-water interface (using neutron reflection) and determined bimolecular rate constants for the reaction

$$O_3 + (CD_2)_8CD{=}CD(CD_2)_7CO_2H \rightarrow \text{products} \qquad (2)$$

In the work presented here it was not the aim to repeat the determination of the value of the bimolecular rate constant but to investigate whether the temporal decay of the surface coverage of oleic acid with ozone is different with with increasing viscosity of the subphase. Thus a detailed kinetic analysis after King et al[3] will not be performed but the temporal decay *e.g.* $\frac{\Gamma_t}{\Gamma_{t=0}}$ versus reaction time will be plotted for each experiment at a different subphase viscosity and the same ozone mixing ratio. The ratio of the surface coverage, Γ_t, at a time, t, to the initial surface coverage, $\Gamma_{t=0}$ is taken from the measurements of $\rho_t\delta_t$ at time, t, and initial measurements of $\rho_o\delta_o$, i.e. $\frac{\Gamma_t}{\Gamma_{t=0}} = \frac{\rho_t\delta_t}{\rho_o\delta_o}$.

Table 1 The characteristic times for chemical reaction and transport in the oxidation of oleic acid by gas-phase O_3. The following values were used in this work: The diffusion constant for ozone in water, D_l, was estimated from the diffusion constants for oxygen in water as $2.1\times10^{-9}m^2s^{-1}$,[26], the diffusion constant for ozone in an organic liquid (*i.e.* oleic acid) was $\sim 1.0\times10^{-9}m^2s^{-1}$ [3,27], a mass accommodation coefficient, α, for ozone on an aqueous solution was 1×10^{-2},[28] the average molecular speed in the gas-phase, $\bar{\nu}$ was 470 ms^{-1} the rate coefficient for reaction 2, k, was $7.3\times10^{-11}cm^2\,molecule^{-1}s^{-1}$,[3], a typical surface coverage of oleic acid was taken as $2\times10^{18}molecule\,cm^{-2}$, a typical diffusion distance was taken as 20 Å, the approximate thickness of the oleic acid film, the diffusion coefficient of ozone in the gas-phase, D_g, was $1.76\times10^{-5}\,m^2\,s^{-1}$,[26]. A Henry's law coefficient, H, for ozone with an organic liquid was $480\,mol\,m^{-3}\,atm^{-1}$,[29,28]. A gas constant, R, of $8.205\times10^{-5}\,m^3\,atm\,K^{-1}\,mol^{-1}$ for a temperature of 298 K was used.

Quantity	Estimate	Characteristic dimension
Ozone mixing time	$\frac{v}{f}$	5 minutes
Diffuso-reactive length in film	$l=\sqrt{\frac{D_l}{k\Gamma_{Oleic}}}$	350 nm
Gas-phase diffusion of ozone	$\frac{r^2}{\pi^2 D_g}$	$\sim$ 20 fs
Interfacial equilibrium	$\frac{d^2}{\pi^2 D_l}$	$\sim$ 0.3 ns
Accommodation	$D_l(\frac{4HRT}{\alpha\bar{\nu}})^2$	$\sim$ 10 ns
Liquid-phase diffusion of ozone through the oleic acid film	$\frac{r^2}{\pi^2 D_l}$	$\sim$ 0.4 ns
Liquid-phase diffusion of ozone through the water at a distance of 0.01 mm	$\frac{r^2}{\pi^2 D_l}$	$\sim$ 6 ms
Reaction	$\frac{1}{k_{surf}\Gamma_{Oleic}}$	$\sim$ 7 ns

2.7 Characteristic times

As highlighted in section 1 the characteristic times can be used to estimate the rate limiting process. The calculations are contained in table 1. The gas-phase diffusion, interfacial equilibration and accommodation of ozone are all fast processes and effectively instantaneous on the timescale of the remaining processes. Examination of the characteristic time for reaction and diffusion of ozone (and the diffuso-reactive length) with and through the 20 Å film demonstrates that a portion of the ozone molecules may diffuse through the film to the aqueous subphase without reaction with the oleic acid. Reaction of these ozone molecules with the water subphase may then be important and will be tested in the experiments

described here.

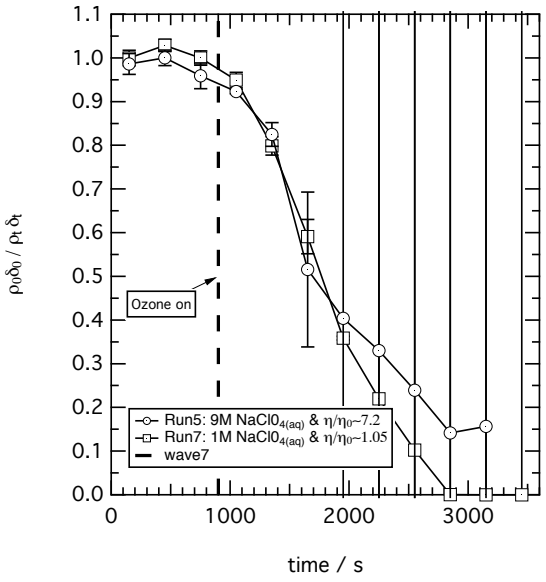

Fig. 1 The kinetic decays of deuterated Oleic acid at the air-water interface in the presence of 0.13 ppm of gas-phase ozone. The abscissa plots the relative product of the scattering length density, ρ, and thickness, δ, for the deuterated materials at the air-water interface for reactions upon viscous ($\frac{\eta}{\eta_o} \sim 7.24$) and non-viscous ($\frac{\eta}{\eta_o} \sim 1.03$) aqueous subphases containing an aqueous solution of sodium perchlorate. The abscissa plots the the ratio of $\rho\delta$ at a time, t to an initial value at time $t = 0$. The ozone was switched on after 900 seconds.

3 Results

The general results will be discussed followed by the results of the blank runs.

3.1 Reaction with increasing viscosity

Typical decays in the product of the film scattering length density and film thickness, $\rho\delta$, with time t are shown in Figure 1 for viscous ($\frac{\eta}{\eta_o} \sim 7.24$) and non-viscous ($\frac{\eta}{\eta_o} \sim 1.03$) subphases. The quantity, $\rho\delta$, representing the amount of deuterated material (oleic acid) at the interface. The decays are characteristic exponential decays with the initial decay modified by the mixing ratio of ozone in the bag increasing during the first few minutes of reaction to a constant value of 0.13 ppm.[30] The characteristic mixing time, defined as the ratio of the bag volume to gas flow rate, in the bag is 5 ± 1 minute. The initial surface coverage of deuterated oleic acid on the interface was different for each experiment and thus the ratio of values of $\rho\delta$ relative to the initial values of $\rho_0\delta_0$, before the addition of ozone are plotted to demonstrate that the decay, and thus the reaction rate are the same. Figure 1 demonstrates that a seven-fold increase in viscosity does not affect the decay kinetics for the reaction between gas-phase ozone and oleic acid at the air-water interface. Figure 1 shows there is significant uncertainty in the product of ρ and δ at long reaction times, with the uncertainty being larger than the calculated value of $\rho\delta$. Therefore the values of $\rho\delta$ at long reaction times should be considered with caution. At larger values of viscosity, more sodium perchlorate is present and therefore it was not possible to contrast-match to air.

Further confirmation that the viscosity of the subphase does not affect the kinetics of the reaction between oleic acid at the air-water interface and ozone is provided by Figure 2 which displays a kinetic decay for every relative viscosity of subphase studied. The kinetic decays are all similar. An assessment of uncertainty in the individual points plotted in the figure is shown for the blank kinetic run in the absence of ozone (squares in figure 2). The uncertainty is derived from statistical fitting of computed reflectivity curves (reflectivity *vs* momentum transfer) to experimental reflectivity curves to determine values of ρ and δ from the neutron reflectivity profiles with momentum transfer.

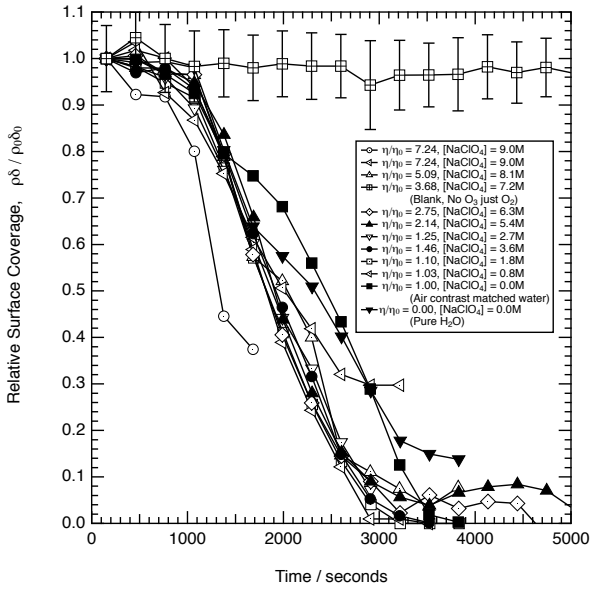

Fig. 2 The kinetic decays of deuterated oleic acid at the air-water interface in the presence of 0.13 ppm of gas-phase ozone. The ozone was switched on after 900 seconds. Data are shown for all subphase solution viscosities measured. A blank run demonstrating the stability of the oleic acid film in the absence of ozone and the presence of molecular oxygen demonstrates no loss of material (unfilled squares).

Table 2 Viscosity experiment. Relative viscosities calculated from concentration of sodium perchlorate.[25]

$[ClO_4^-]$ / Mol dm^{-3}	$\frac{\eta}{\eta_0}$	Ionic Strength / Mol dm^{-3}	pH
9.0	7.24	9.0	4.5
8.1	5.09	8.1	-
7.2	3.68	7.2	5.0
6.3	2.75	6.3	-
5.4	2.14	5.4	5.5
3.6	1.46	3.6	-
2.7	1.25	2.7	-
1.8	1.10	1.8	5.5
0.8	1.03	0.8	6.0
0.0	1.00	0	6.0

3.2 Blank experiments, reaction with oxygen and aqueous sodium perchlorate

The ozone is produced in a bath gas of oxygen and oleic acid and reacts very slowly with molecular oxygen, but the loss of oleic acid is insignificant on the timescale of this experiment as shown previously for these type of experiments using the same equipment[3,31].

Two blank experiments were performed: Figure 2 demonstrates that the deuterated oleic acid is stable at the air-water interface in the absence of ozone and in the presence of molecular oxygen. The unfilled squares with uncertainty bars in figure 2 show that no loss of deuterated material occurs from the air-water interface on the timescale of the experiment. The second blank experiment was the monitoring of the air-water interface of the aqueous perchlorate subphase in the absence of the oleic acid but in the presence of ozone. No change was observed.

4 Discussion

The study is reasonably straight forward with a clear result: thus the discussion concentrates on experimental uncertainty, comparison with other studies and importantly the atmospheric implications.

4.1 Experimental uncertainty

The agreement between the experimental kinetic decays in figure 2 is convincing and the uncertainty bars plotted in the figure demonstrate that the agreement is within the uncertainty considered. It was not possible to increase the range of viscosities further as the large concentrations of sodium perchlorate required would have contributed significantly to the background neutron reflectivity signal.

4.2 Interpreting the results compared to literature

Other studies of the reaction of ozone with oleic acid at the air-water interface have not considered the effect of the subphase viscosity on the reaction, but have have tentatively considered the effect of ionic strength and the results agree with those presented here.[3] Smith et al.[23] considered the oxidation of oleic acid by ozone, specifically the reaction between gas-phase ozone and oleic acid particles. Smith et al.[23] demonstrated that the reaction probably occurred at the surface and may have been limited by the diffusion of oleic acid through oleic acid[23] to the surface, i.e. a different mechanism to the monolayer of oleic acid presented here.

4.3 The effect of large ozone mixing ratios

The mixing ratios of ozone in the study presented here are large and not typical of the ambient atmosphere. However similar studies have considered different ozone mixing ratios and obtained similar exponential behaviour to that demonstrated here.[3,30]

4.4 Implications for atmospheric scientists

For atmospheric scientists studying the effect of oxidation of aerosol particulate matter the work presents two simplifications for the modelling of the oxidation of thin film material by the prevalent oxidising agent, gaseous ozone: The kinetics (and thus the timescale) of the atmospheric oxidation of model thin film material on atmospheric aerosol may, as a first approximation be considered to be independent of the ionic strength and viscosity over the relative viscosity range 1–7 of the aerosol, assuming the components increasing the ionic strength and viscosity of the aerosol are unreactive to ozone in relevant concentration and timescales. Secondly it may be inferred that the kinetics of reaction between oleic acid and ozone at the air-water interface do not need to consider the dissolution of the ozone into the aqueous subphase. These two simplifications will considerably simplify the modelling

of the oxidation of atmospheric films on atmospheric aerosol, provided oleic acid is a good proxy for thin film material on atmospheric aerosols.

5 Conclusions

The work presented here has demonstrated that the reaction between gas-phase ozone and a monolayer of oleic acid at the air-water interface is independent of the ionic strength and viscosity over the relative range 1–7.4 of the aqueous subphase. It may be concluded that dissolution of ozone into the aqueous subphase is not a rate limiting step and may be ignored for the atmospheric modelling of aqueous aerosol similar to oleic acid over the viscosity range 1–7.4, and simply considered as a surface reaction.

6 Acknowledgements

We gratefully acknowledge the support of the STFC ISIS (RB1310383) and ILL (9-10-1288). The majority of the experiments were undertaken at the ISIS Pulsed Neutron and Muon Source with other, preliminary, experiments undertaken at the Institute Laue-Langevin. SHJ wishes to express gratitude to NERC (NE/H019103/1) for studentship support.

References

1 D. Donaldson and V. Vaida, *Chem Rev*, 2006, **106**, 1445–1461.
2 M. D. King, K. C. Thompson and A. D. Ward, *J Am Chem Soc*, 2004, **126**, 16710–16711.
3 M. D. King, A. R. Rennie, K. C. Thompson, F. N. Fisher, C. C. Dong, R. K. Thomas, C. Pfrang and A. V. Hughes, *Phys. Chem. Chem. Phys*, 2009, **11**, 7699–7707.
4 *IPCC, 2013: Climate Change 2013: The Physical Science Basis. Contribution of Working Group I to the Fifth Assessment Report of the Intergovern- mental Panel on Climate Change*, ed. T. F. Stocker, D. Qin, G.-K. Plattner, M. Tignor, S. K. Allen, J. Boschung, A. Nauels, Y. Xia, V. Bex and P. M. Midgley, Cambridge University Press, Cambridge, United Kingdom and New York, NY, USA, 2013.
5 D. R. Hanson, A. R. Ravishankara and S. Solomon, *Journal of Geophysical Research. D. Atmospheres*, 1994, **99**, 3615–3629.
6 F. Karagulian, C. W. Dilbeck and B. J. Finlayson-Pitts, *J Am Chem Soc*, 2008, **130**, 11272–11273.
7 F. Karagulian, C. W. Dilbeck and B. J. Finlayson-Pitts, *J Phys Chem A*, 2009, **113**, 7205–7212.
8 R. Battino, T. Rettich and T. Tominaga, *J Phys Chem Ref Data*, 1983, **12**, 163–178.
9 L. Renbaum-Wolff, J. W. Grayson, A. P. Bateman, M. Kuwata, M. Sellier, B. J. Murray, J. E. Shilling, S. T. Martin and A. K. Bertram, *Proceedings of the National Academy of Sciences*, 2013, **110**, 8014–8019.
10 E. Abramson, D. Imre, J. Beranek, J. Wilson and A. Zelenyuk, *Phys. Chem. Chem. Phys.*, 2013, **15**, 2983–2991.
11 T. Koop, J. Bookhold, M. Shiraiwa and U. Poschl, *Phys. Chem. Chem. Phys.*, 2011, **13**, 19238–19255.
12 E. Mikhailov, S. Vlasenko, S. T. Martin, T. Koop and U. Pöschl, *Atmos Chem Phys*, 2009, **9**, 9491–9522.
13 H. M. Ali, M. Iedema, X. Y. Yu and J. P. Cowin, *Atmos Environ*, 2014, **89**, 731–738.
14 L. Giulianelli, S. Gilardoni, L. Tarozzi, M. Rinaldi, S. Decesari, C. Carbone, M. C. Facchini and S. Fuzzi, *Atmos Environ*, 2014, **98**, 394–401.
15 J. Penfold and R. K. Thomas, *Current Opinion in Colloid & Interface Science*, 2014, **19**, 198–206.
16 J. R. Lu, R. K. Thomas and J. Penfold, *Advances in Colloid and Interface Science*, 2000, **84**, 143–304.
17 V. F. Sears, *Neutron optics*, Oxford University Press, 1989.
18 J. Penfold, R. Richardson, A. Zarbakhsh, J. Webster, D. Bucknall, A. Rennie, R. Jones, T. Cosgrove, R. Thomas, J. Higgins, P. Fletcher, E. Dickinson, S. Roser, I. McLure, A. Hillman, R. Richards, E. Staples, A. Burgess, E. Simister and J. White, *J Chem Soc Faraday T*, 1999, **93**, 3899–3917.
19 R. A. Campbell, H. P. Wacklin, I. Sutton, R. Cubitt and G. Fragneto, *Eur Phys J Plus*, 2011, **126**, 107.
20 F. Abelés, *Ann. Phys. (Paris)*, 1948, **3**, 504–.
21 A. F, *Ann. Phys. (Paris)*, 1950, **5**, 596–706.
22 L. G. Parrat, *Phys. Rev.*, 1954, **95**, 359–.
23 G. D. Smith, E. W. III, C. DeForest, T. Baer and R. E. Miller, *J. Phys. Chem. A.*, 2002, **106**, 8085–8095.
24 L. H. Clark and G. L. Putnam, *Journal of American Chemical Society*, 1949, **71**, 3445–3447.
25 G. J. Janz, B. G. Oliver, G. R. Lakshminarayanan and G. E. Mayer, *J Phys Chem*, 1970, **74**, 1285–1289.
26 E. L. Cussler, *Diffusion mass tranfer in fluid systems*, Cambridge University Press, 1999.
27 M. D. King, K. C. Thompson, A. D. Ward, C. Pfrang and B. R. Hughes, *Faraday Discussions*, 2007, **137**, 173–192.
28 S. Sander, R. Friedl, D. Golden, M. Kurylo, P. Wine, J. Abbatt, J. Burkholder, C. Kolb and G. Moortgat, *Chemical kinetics and photochemical data for use in Atmospheric Studies Evaluation Number 17*, Jet Propulsion Laboratory California Institute of Technology Pasadena, California Technical Report 17, 2011.
29 T. Moise and Y. Rudich, *J Geophys Res-Atmos*, 2000, **105**, 14667–14676.
30 C. Pfrang, F. Sebastiani, C. O. M. Lucas, M. D. King, I. D. Hoare, D. Chang and R. A. Campbell, *Phys. Chem. Chem. Phys.*, 2014, **16**, 13220–13228.
31 M. D. King, A. R. Rennie, C. Pfrang, A. V. Hughes and K. C. Thompson, *Atmos Environ*, 2010, **44**, 1822–1825.

Paper 6: Are atmospheric aerosol and sea-water film forming materials at the air-water interface inert to oxidation?

S. H. Jones, M. D. King, A. D. Ward, A. R. Rennie, A. C. Jones and T. Arnold

To be submitted to Atmospheric Chemistry and Physics, 42 pages.

Within this partly co-authored work, I declare that the following contributions are entirely my own work:

- Collected and extracted the sea-water samples.
- Conducted the X-ray experiments and collected and analysed the data.
- Authored the paper.
- Contributed significantly to the design of the experiment.
- Contributed significantly to drawing the conclusions of the paper.

Are atmospheric aerosol and sea-water film forming materials at the air-water interface inert to oxidation?

S. H. Jones[1,2], M. D. King[1], A. D. Ward[2], A. R. Rennie[3], A. C. Jones[1] and T. Arnold[4]

[1]{Department of Earth Sciences, Royal Holloway, University of London, Egham, Surrey, TW20 0EX United Kingdom}

[2]{STFC, Central Laser Facility, Research Complex at Harwell, Rutherford Appleton Laboratory, Harwell Oxford, Didcot, Oxfordshire, OX11 0FA, United Kingdom}

[3]{Department of Physics and Astronomy, Uppsala University, 75120 Uppsala, Sweden}

[4]{Diamond Light Source, Harwell Oxford, Didcot, OX11 0DE, United Kingdom}

Correspondence to: M. D. King (m.king@es.rhul.ac.uk)

Abstract

The heterogeneous oxidation of thin films of organic material extracted from real aerosol and sea-water samples at the air-water interface was studied using X-ray reflectivity. Films of atmospheric aerosol material and sea-water material were both exposed to gas-phase ozone and the amount of material at the air-water interface was modelled with time. No change in the amount of material at the air-water interface was observed on exposure to gas-phase ozone, indicating that no reaction occurred and a potential lack of unsaturated organic material in the samples. Gas chromatography, GC-MS, and Electrospray Ionization Mass Spectrometry, ESI-MS, showed the presence of saturated compounds in the samples. It is proposed that the amount of unsaturated compounds as compared to saturated compounds in atmospheric material is so low that both GC-MS and ESI-MS analysis as well as gas-phase oxidation are dominated by saturated material. Reactions were also conducted using the atmospherically relevant aqueous radicals, hydroxyl and nitrate. On exposure of a film of atmospheric aerosol material to the aqueous hydroxyl radical and exposure of a film of sea-water film material to the aqueous nitrate radical, a decrease in the amount of material at the air-water interface was observed. A thinning mechanism for the film forming surface active

material is proposed, but more studies on different samples are required to verify the reaction. It can be tentatively suggested that oxidation by gas-phase ozone is not important in the atmosphere and further studies should focus on radical induced oxidation of saturated organic material.

1 Introduction

Atmospheric aerosols play a critical role in the Earth's climate, by directly scattering and absorbing solar radiation, and indirectly, through their involvement in cloud formation and their associated influence on cloud radiative properties (e.g. Stocker et al., 2013). The indirect effect remains largely uncertain i.e. aerosol contribution to cloud condensation nuclei formation (CCN) and cloud properties (Stocker et al., 2013). Studies have been conducted to reduce the level of uncertainty of aerosol contribution to the indirect effect and to improve understanding of aerosol processes e.g. Lohman et al., 2005, Pandis et al., 1995, Poschl, 2005, Ramanathan et al., 2001. Aerosols may be naturally chemically complex (Poschl, 2005) and it is difficult to accurately represent their composition when conducting laboratory experiments using proxy chemicals. Studies are often carried out using simplified proxies consisting of only one chemical, and the chemicals chosen for these proxies are often based on the findings of analytical studies conducted on ensemble aerosol samples (e.g. Tervahattu et al., 2002, Ebben et al., 2012, Rogge et al., 1991, 1993). Whilst studies conducted using simple aerosol proxies provide useful insight into aerosol behaviour and properties in the atmosphere, the question remains as to whether the chosen materials chemically react and behave in the same way as atmospheric aerosols. The work presented here identifies whether thin films on atmospheric aerosol are appropriately modelled with specific proxy chemicals by investigating the oxidation behaviour of real atmospheric materials.

Studies have shown that a significant number of tropospheric aerosols are coated with a thin organic film that can affect the properties and behaviour of the aerosol and therefore impact on aerosol contribution to the climate (Blanchard, 1964, Donaldson and Vaida, 2006, Gill et al., 1983, Tervahattu et al., 2002 a), 2002 b)). One of the major types of natural aerosol, sea-salt aerosol, forms by wave breaking and/or bubble bursting action over the ocean (e.g. Woodcock et al., 1953, Mason, 1954, etc). During formation, sea-salt aerosol becomes coated in a thin organic film that originates from the sea surface microlayer (e.g. Donaldson and Vaida, 2006 and references therein). The sea surface microlayer consists of organic

components, specifically lipids and fatty acids arising from oceanic biota that have decayed and the resultant chemicals accumulate in the sea surface microlayer (Donaldson et al., 2012 and references therein). Owing to the variety of chemicals present in the troposphere, it is also possible for uncoated aerosols to become coated in their lifetime, when low volatility compounds partition to a particle, (e.g. Andrews and Larson, 1993, Falkovich et al., 2004). Aerosols coated in a thin organic film are naturally abundant in the atmosphere and in order to better understand aerosol behaviour, it is pertinent to study coated aerosols and the reactions that they may undergo in order to assess the impact of the presence of a thin film on aerosol behaviour. One method to study such aerosol coatings is at the air-water interface.

Tropospheric aerosol will undergo oxidation by common gas and liquid phase oxidants, such as O_3, $OH\cdot$ and $NO_3\cdot$ radicals respectively (e.g. Herrmannn, 2003). Chemical oxidation of an aerosol will alter the hygroscopic properties of the aerosol which in turn can affect aerosol ability to act as CCN as well as the surface tension of the aerosol. It is therefore very important to study oxidation of thin films at the air-water interface.

To date, as far as the authors are aware, no previous studies have been conducted on the oxidation of organic films extracted from real atmospheric aerosol or sea water samples at the air-water interface. The aim of this experiment was to study the oxidation of real organic thin films (organics extracted from aerosol and sea-water samples) at the air-water interface. Oxidation with gas-phase ozone, a prevalent gas-phase atmospheric oxidant, was initially studied, with thin films of material extracted from either atmospheric aerosol or sea-water samples. Following the study with gas-phase ozone, studies of thin film material extracted from atmospheric aerosol with the aqueous OH radical (Herrmannn, 2003), and thin film material extracted from sea-water with the aqueous $NO_3^{\cdot}$ radical (Herrmannn, 2003) were conducted.

$$\text{Organic film} + \mathrm{O_{3(g)}} \rightarrow \text{Products} \quad \text{(R1)}$$

$$\text{Organic film} + \mathrm{OH^{\cdot}_{(aq)}} \rightarrow \text{Products} \quad \text{(R2)}$$

$$\text{Organic film} + \mathrm{NO^{\cdot}_{3(aq)}} \rightarrow \text{Products} \quad \text{(R3)}$$

The above radical reactions were studied to observe the difference between addition to a carbon-carbon double bond (reaction with ozone) and a hydrogen abstraction. The overall study will allow comparison between the oxidation of films of material extracted from real

atmospheric samples at the air-water interface and oxidation studies conducted using thin films of atmospheric proxies.

In order to achieve such a comparison, organic film forming material was extracted in chloroform from both atmospheric aerosol and sea water samples and the resultant organic material studied and oxidised at the air-water interface. A thin film of material extracted from atmospheric aerosol in chloroform will be referred to as 'atmospheric film material' and a thin film of material extracted from sea-water in chloroform will be referred to as 'sea-water film material'. To study the oxidation of a thin film (~10-50 Å in thickness) at the air-water interface X-ray reflectivity was used. X-ray reflectivity allows the determination of film thickness and scattering length density which may be related to surface coverage at the air-water interface.

2 Experimental

The experimental describes the different techniques required to study the oxidation of organic film material, extracted from aerosol and sea water samples, at the air-water interface. The experimental will be broken down into sections containing information on the sampling and extraction of aerosol and sea-water samples, thin film formation at the air-water interface using a Langmuir trough, oxidant generation, a typical experimental procedure and X-ray reflectivity and the associated experimental data modelling.

2.1 Aerosol and sea water sampling

Samples of film forming organic compounds were collected from atmospheric aerosol and coastal sea water. The organic film-forming material was subsequently extracted in chloroform. A bubble extraction process (Gevod, 2008) was not employed as it would have been inefficient for the small aerosol samples.

2.1.1 Aerosol sampling and extraction

Atmospheric aerosol samples were collected using two different sampling methods. Tropospheric air was drawn through clean stainless steel into either an inline flow through filter sampler (Savillex, 47 mm Stage Filter Assembly) or a ChemComb Model 3500 speciation sampling cartridge, using an SKC flow metred aerosol pump at a controlled flow

rate of 10 L min^{-1}, at ambient temperature (~10-20°C) and pressure. Samples were collected on 47 mm pre combusted quartz filters (SKC, Type R-100, 380 µm thick).

The ChemComb sampling cartridge consisted of two glass denuders which were either coated or uncoated (e.g. Helmig, 1997) and a quartz filter. ChemComb denuders coated in sodium thiosulphate were used to remove ambient gas-phase ozone from the sampled air in order to prevent oxidation of material on the filter by ambient ozone. The ChemComb sampling cartridge also had a built in PM-2.5 impactor at the inlet. All samples were collected on site at Royal Holloway University of London, in Egham, Surrey, UK, 51.4289 N, 0.5479 W, approximately 20 m above the ground (see Table 1). Samples were collected for time periods ranging from one to five weeks between September 2013 and February 2014.

To determine the origin of the sampled air masses archived back trajectories were run using the online NOAA HYSPLITT model (Draxler and Rolph, 2015, Rolph, 2015). A basic map of air mass sources was devised to estimate the origin of the sampled air masses, three air mass regions were allocated; marine (originating from the Atlantic ocean), polluted/European and arctic. For each day that a sample was collected, the NOAA HYSPLITT model was used to calculate a normal trajectory from one starting location using GDAS meteorology for 240 hours, starting in Egham, at 100 m above ground level with isentropic vertical motion. A back trajectory map was produced and the general air mass character of the source for each sample was allocated.

The materials used during the sampling collection and preparation were either Pyrex or PTFE and had been thoroughly washed and rinsed with chloroform prior to use. The quartz filters had also been heat treated by the manufacturer to remove any organics prior to use. All sample manipulation, assembly and disassembly using both methods i.e. filter sampler and ChemComb sampling cartridge were performed in a controlled clean atmosphere in a glove bag to prevent any contamination. The collected aerosol samples were visible as particulate matter that appeared black in colour on the quartz filters. The samples were frozen at ~ -18°C post sampling and were usually extracted within 1-2 weeks of being frozen and within at least 6 weeks of being frozen. To extract the film forming organic material, the used quartz filters were halved and one half was cut into small pieces using a stainless steel knife on a clean PTFE cutting block in a glove bag. The pieces were subsequently placed into a flask and pure water (>18 MΩ) and chloroform (Sigma-Aldrich, Chromosolv Plus, for HPLC, ≥99.9%, contains 0.5-1.0% ethanol as stabilizer) were added in a 1:1 ratio and the mixture was

thoroughly shaken. A separating funnel was then used to extract the organics dissolved in chloroform from the water. Once separated, the chloroform was evaporated under a flow of pure dry nitrogen to leave the organics. Following evaporation, ~2 ml of chloroform was subsequently added to each dry sample and the samples frozen at ~ -18°C, before analysis by X-ray reflection. Filter blanks were also prepared, i.e. blank quartz filters were cut up and chloroform and water added in the same ratio (1:1) used for the aerosol samples and the same separation and drying procedure performed. To summarise, atmospheric film material extracted from quartz air filters that had been collected; without a denuder, with a coated and with an uncoated denuder as well as blank quartz filters were all studied as detailed in Table 1.

2.1.2 Sea water sampling and extraction

Surface sea-water samples (top ~10 cm of the ocean) were collected from the English channel using a clean polypropylene bucket attached to a long reach (2-3 m) sampler at Milford-on-Sea on the south coast of England in April 2013, 50.7260° N, 1.5890° W. Samples were collected on shore by skimming the bucket over the top of incoming waves. Samples were then transferred to clean glass bottles for transport and storage. The glass bottles had been thoroughly cleaned and rinsed with chloroform prior to use. Approximately twenty × 1 L samples were collected.

In order to extract the organics, samples were coarsely filtered using Whatman filter paper, (grade 1) into a clean glass beaker to remove any macro coastal detritus that may have been present, and freeze dried to remove water. Once freeze dried, ~100 ml chloroform (Sigma-Aldrich, Chromosolv, Plus, for HPLC, ≥99.9%, contains amylenes as stabilizer) was added to ~500 ml of freeze dried sea water to dissolve any organic material that was present as well as ~50 ml of pure water to dissolve the sea salt. The chloroform (containing organic film forming material) was removed from the water with a separating funnel. The chloroform was subsequently evaporated under a flow of dry nitrogen. The organics remained as a clear or pale yellow oily residue and samples were frozen until use on the beamline. Processing of approximately 2 L of sea water produced < 1 mg of organic material. Prior to use on the beamline, chloroform (between 5-20 ml) was added to the sea water samples to form sea-water film material. Further experimental details are provided in Table 2.

2.1.3 GC-MS and ESI-MS analysis

Following the experiments, the samples were sent for GC-MS and ESI-MS analysis. Two atmospheric aerosol samples, one filter blank and a chloroform blank (the same chloroform used to extract the organics) were analysed by GC-MS at King‘s College, London with the standards oleic, stearic and linoleic acid. Two sea-water samples were also analysed using GC-MS and ESI-MS with a chloroform blank. The spectra can be seen in the appendix and it is noted that the siloxanes and phthalates identified in the spectra are plasticisers that have leached from the septums of the sample storage bottles.

2.2 Film formation using a Langmuir trough

Thin films can be studied at the air-water interface using a Langmuir trough and their use has been described by Barnes and Gentle, 2005. The trough is made from PTFE and has a shallow indentation into which a liquid can be added such as water. The liquid in the trough is often referred to as the subphase because a thin film can be added to its surface, i.e. at the air-water interface. The liquid sits proud of the trough owing to surface tension and the surface pressure of a thin film can be monitored with a Wilhemy plate tensiometer. Film forming material typically consists of long chain amphiphilic molecules with a hydrophilic head group that is oriented into the aqueous subphase and a hydrophobic tail group that sticks up into the air. The film forming material is typically dissolved in chloroform and spread on the surface of the subphase by adding drops using a micro-litre syringe. The chloroform evaporates in ambient air to leave a film at the air-water interface.

Two Langmuir troughs were used in the work presented here. A model 302A Nima Langmuir trough (dimensions: 354 mm x 98 mm x 5 mm) fitted with a PS4 Wilhelmy plate tensiometer and Delrin barriers to measure isotherms, typical values ~13-25 mNm^{-1}, and a smaller custom trough having dimensions, 140 mm × 70 mm and a liquid depth of approximately 3.5 mm, fitted with a 25 L Tedlar gas bag for use on the beamline for X-ray reflectivity. The latter trough had no tensiometer or barriers to keep the volume small and prevent interaction with the X-ray beam. Gas-phase ozone and UV radiation (required to photolytically generate the aqueous radicals) will also degrade the barriers and the tensiometer.

2.3 Oxidant generation

Ozone was generated using a commercial ozoniser (UVP) by the photolysis of molecular oxygen. A flow of dry oxygen at a flow rate of 1 L min^{-1} passed through the ozoniser and was admitted to the Tedlar bag containing the Langmuir trough from the start of the experiment. The ozoniser was switched on and off remotely. A constant mixing ratio of 0.1 or 1 ppm (dependent on the settings) of ozone was produced within three minutes of switching on the ozoniser, and mixing time in the bag was estimated to be ten minutes. The ozone mixing ratio was measured prior to use on the beamline with a calibrated electrochemical sensor (Eco sensors A-22 Portable Ozone Meter).

Aqueous nitrate and hydroxyl radicals were generated in the subphase from photolysis of precursors, also in the aqueous subphase. UV fluorescent lamps were located directly above the trough and along its length using 16 cm bulbs to evenly illuminate the liquid subphase. The hydroxyl radical was generated from the photolysis of a 0.03 M KNO_3 solution (Mack and Bolton 1999) using a germicidal lamp (two bulbs centred at ~254 nm) at a height of ~90 mm above the trough surface. Whereas the nitrate radical was generated from photolysis of 0.1 M $NaNO_3$ and 0.02997 M $K_2S_2O_8$ solution using two black lamps (four bulbs centred at 360 nm) at a height of 195 mm above the trough (base) (Herrmann, 2003). All bulbs were situated in a retro reflector.

$$S_2O_{8(aq)}^{2-} + h\nu(\lambda \sim 360\text{nm}) \rightarrow SO_{4(aq)}^{\cdot -} + SO_{4(aq)}^{\cdot -} \quad \text{R4}$$

$$SO_{4(aq)}^{\cdot -} + NO_{3(aq)}^{-} \rightarrow SO_{4(aq)}^{2-} + NO_{3(aq)}^{\cdot} \quad \text{R5}$$

$$NO_{3(aq)}^{-} + h\nu(\lambda \sim 254\text{nm}) \rightarrow NO_{2(aq)}^{-} + O_{(aq)} \quad \text{R6}$$

$$NO_{3(aq)}^{-} + h\nu(\lambda \sim 254\text{nm}) \rightarrow NO_{2(aq)} + O_{(aq)}^{\cdot -} \quad \text{R7}$$

$$O_{(aq)}^{\cdot -} + H_2O_{(l)} \rightarrow OH_{(aq)} + OH_{(aq)}^{-} \quad \text{R8}$$

2.4 Typical experimental procedure

The custom Langmuir trough was thoroughly cleaned with chloroform prior to use and was filled with ~80 ml pure water (>18 MΩcm) and the surface of the water was cleaned using a pipette attached to a pump. A monolayer of either atmospheric film material or sea-water

film material was added using a micro-litre syringe. Typically ~40 µl of atmospheric film material was added and the chloroform was allowed to evaporate or ~600 µl of sea-water film material was added and the chloroform was allowed to evaporate. These volumes were used because they were assumed to give surface pressures of ~14-25 mNm^{-1} and ~25 mNm^{-1} for atmospheric film material and sea-water film material respectively from preliminary measurements conducted prior to X-ray experiments. The trough was contained in a 25 L Tedlar bag with input and output PFA tubing for addition and exhaust of gas-phase ozone in order to maintain a constant mixing ratio of ozone in the trough environment. The Tedlar bag was cut open for the experiments conducted using the hydroxyl radical because the bag would attenuate the radiation from the lamps at ~254 nm. The bag remained closed for the experiments conducted using the nitrate radical as the bag would not significantly attenuate the radiation from the lamps at ~360 nm.

2.4.1 Aerosol sample experiments

Experiments were performed with gas-phase ozone as the reactant and three different types of atmospheric film material sampled with; no denuder, a coated denuder and an uncoated denuder. Experiments were also conducted with the hydroxyl radical and atmospheric film material sampled with a coated and uncoated denuder.

Specific blank experiments were also performed to ensure that any reaction that did occur was due to the presence of either gas-phase ozone or the hydroxyl radical. The following blank experiments were conducted, an oxygen blank with O_2 only and a UV blank with UV light only at ~254 nm (no radical precursor subphase). A filter blank was also performed to verify that the surface coverage of the atmospheric film material was not influenced by the extraction process from the quartz filters. A film at the air-water interface was generated from unused quartz filters and exposed to oxygen only.

2.4.2 Sea-water sample experiments

Experiments were performed with both gas-phase ozone and the nitrate radical. Similarly to the experiments performed with atmospheric film material, blank experiments were also conducted. An oxygen blank with O_2 only, a UV blank with UV light only at ~360 nm (no radical precursor subphase), and a nitrate anion subphase blank, using the nitrate anion subphase only without UV radiation were all performed.

3 X-Ray Reflectivity

X-ray reflectivity is a surface specular reflection technique that uses X-rays to study the electron density of a thin film perpendicular to the surface (Arnold et al., 2012). Information on the film thickness, amount of material, and morphological roughness of the film may be obtained. The reflectivity is measured as a function of the incident X-ray angle.

X-ray reflectivity measurements were conducted at the I07 beamline at the Diamond Light Source, Didcot, UK (Arnold et al., 2012). The energy of the X-ray beam was 12 keV or 12.5 keV for the sea-water and atmospheric film material respectively which provided X-rays of wavelength 1.033 Å and 0.992 Å respectively. The custom Langmuir trough was used for the sample environment and mounted on an anti-vibration table. Two thin Kapton windows were located at either end of the trough to allow X-rays to pass into the Tedlar gas bag. The I07 Double-Crystal-Deflector (DCD) (Arnold et al., 2012) was used to define the grazing angle of incidence at which the X-rays hit the air-water interface where they were specularly reflected on to a Pilatus detector (Arnold et al., 2012).

The reflectivity of the film is measured as a function of Q. Q is the momentum transfer of the X-rays perpendicular to the interface, and is defined as:

$$Q = \frac{4\pi \sin\theta}{\lambda} \tag{1}$$

where θ is the grazing angle of specular reflection and λ is the X-ray wavelength. Q is varied by changing the angle of incidence of the X-ray beam. The reflectivity of the film was recorded before and during reaction with gas-phase ozone and the aqueous radicals. The X-ray reflectivity was recorded continuously in intervals of approximately 1200 s and the duration of each kinetic run (reaction with oxidant) was between 9000 to 24000 s.

3.1 Thin film model and data analysis

In order to model the resulting experimental X-ray data, the following model was employed. The thin film of either atmospheric film material or sea-water film material at the air-water interface was thought of as a series of parallel layers or a slab. The thin film was located between two semi-infinite media; air and the aqueous subphase as depicted in Figure 1.

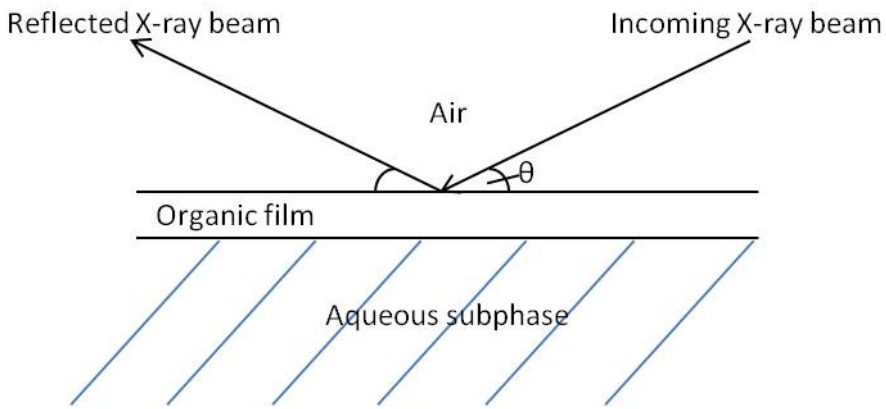

Figure 1- Slab model for an organic thin film at the air-water interface.

The X-ray reflectivity data as a function of Q was reduced by calculating R vs Q. Reflectivity data as a function of Q may be used to model the scattering length density and thickness of a series of layered media normal to an X-ray beam using Abelès method (Abelès, 1950). The data described here were fitted to the simple model shown in Figure 1. The experimental determination of reflectivity as a function of Q was compared and fitted to modelled reflectivity (Abelès, 1950) as a function of Q and an example plot is shown in Figure 2. To achieve the modelled fit, the following thin film parameters were varied; scattering length density, film thickness and roughness (of the air-film interface) as well as slight variations in background and scale factor. The roughness and scattering length density of the subphase were held constant at 4 Å and 9.45×10^{-6} Å^{-2} respectively. It was also assumed that there was no absorption by the X-rays.

In a previous related work (King et al., 2009) it was possible to calculate the surface coverage or amount of material at the air-water interface using the following equation:

$$\Gamma = \frac{\rho\delta}{b} \qquad (2)$$

where Γ is the surface coverage, ρ is the scattering length density of the film, δ is the film thickness, and b is the scattering length of the molecule. In the current study, b was unknown due to the origin of the samples, therefore the surface coverage at the air-water interface was taken to be proportional to ρδ.

For a reacting system, the relative surface coverage was considered, i.e. the product of the scattering length density and film thickness at time t, $\rho_t\delta_t$, relative to the product of the initial scattering length density and film thickness, $\rho_0\delta_0$.

$$\text{Relative surface coverage} = \frac{\rho_t \delta_t}{\rho_0 \delta_0} \tag{3}$$

For a small range of Q, scattering length density, thickness and roughness could in part be correlated and it could be difficult to fit independent unique values. However, the Q range available on I07 at the Diamond Light Source, allows uncorrelated unique values of scattering length density, thickness and roughness to generally be found.

4 Results and Discussion

The following section discusses the experimental X-ray reflectivity data and the associated data modelling for the oxidation of: atmospheric film material with gas phase ozone, atmospheric film material with the hydroxyl radical, sea-water film material with gas phase ozone and sea-water film material with the nitrate radical. The findings are then compared to relevant studies in the literature.

Throughout the following sections, the phrase, 'reflectivity profile' will be used to describe a plot of reflectivity of RQ^4 against Q such as the one shown in Figure 2. The solid red line in Figure 2 shows the excellent fit of the modelled reflectivity profile to the experimental reflectivity profile, which is plotted as black circles.

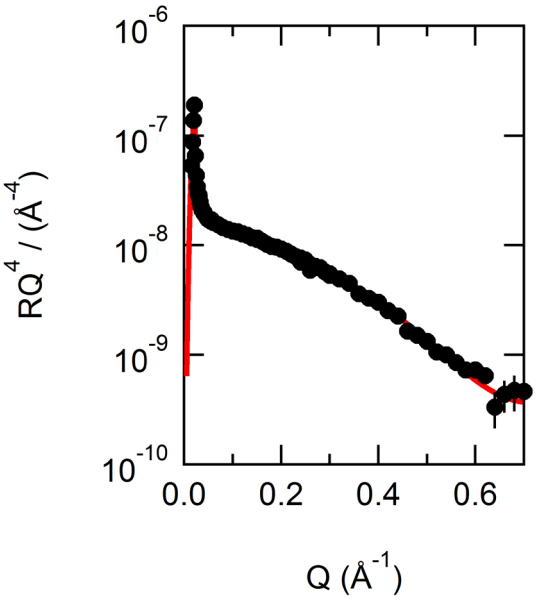

Figure 2-Example reflectivity profile, RQ^4 vs Q, for atmospheric film material during exposure to the hydroxyl radical. The modelled fit to the experimental data is shown as a solid red line, which is an excellent fit to the experimental data points (black circles).

4.1 Aerosol samples and gas-phase ozone

For the reaction of atmospheric film material with gas phase ozone, no change in the amount of material at the air-water interface was observed for atmospheric film material sampled with no denuder, an uncoated denuder or a coated denuder as shown in Figure 3. The modelled values show a constant amount of material at the air-water interface throughout the

experiment, suggesting that atmospheric film material may not be reactive to gas-phase ozone.

For the initial experiment conducted on atmospheric film material sampled without a denuder (blue triangles in Figure 3), a mixing ratio of ~0.1 ppm of gas-phase ozone was used. However, as there was no observed change in the surface coverage, the mixing ratio of gas-phase ozone was increased to ~1 ppm in an attempt to observe a change in the amount of material of the air-water interface. Increasing the mixing ratio did not cause a change in surface coverage, which supported the idea that atmospheric film material was unreactive to gas-phase ozone. The change in ozone mixing ratio is highlighted in Figure 3 by the green 'hourglass' symbols. The dashed line indicates the time that the ozoniser was switched on. The other two experiments (atmospheric film material sampled with a coated and uncoated denuder) plotted as red squares and black circles in Figure 3 were both conducted with a ~1 ppm mixing ratio of gas-phase ozone throughout the experiment and no change in surface coverage was observed.

The modelled atmospheric film thickness is also constant on exposure to ozone as shown in panel b) of Figure 3. The constant surface coverage and film thickness are interpreted to mean that there is no significant reaction between gas-phase ozone with the film material, which suggests that the atmospheric film material may not contain any readily oxidisable unsaturated bonds. If unsaturated bonds were present in the film, ozone would effectively cleave these bonds resulting in the production of smaller, more polar molecules which would either escape into the liquid subphase or into the gas-phase above the film (King et al., 2009, Gonzalez-Labrada et al., 2007, Voss et al., 2006, 2007). In doing so there would be a reduction in the amount of the material at the air-water interface and an associated decrease in film thickness (King et al., 2009). The general trend in constant surface coverage occurs regardless of the individual values fitted.

The uncertainty in the surface coverage is dominated by the estimated uncertainty in the film thickness. The accepted fit of RQ^4 vs Q is very sensitive to changes in the scattering length density but it is insensitive to changes in the film thickness. The value for the estimated uncertainty has therefore been determined as the deviation in the fit of RQ^4 vs Q from the accepted fit of RQ^4 vs Q to give an uncertainty of 50-70 % in the surface coverage. The uncertainty was estimated by varying both the scattering length density and film thickness in different ways in order to achieve the same modelled fit to the experimental data of RQ^4 vs Q.

The amount by which the variables can be changed that still results in an acceptable fit to the experimental data is 50-70 %.

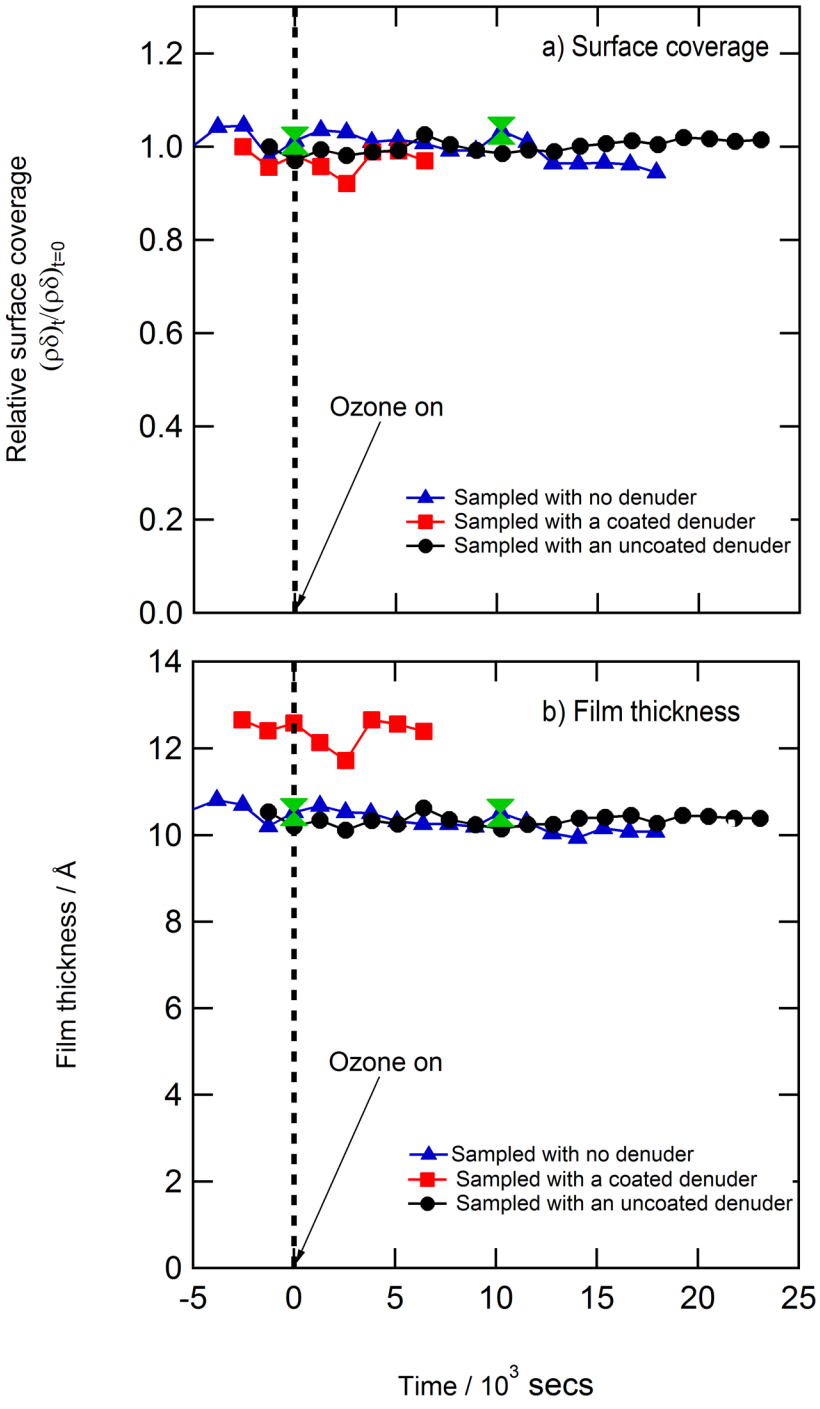

Figure 3. The upper panel, a), shows the relative amount of atmospheric film forming material at the air-water interface during exposure to gas phase ozone. The dashed black line indicates the time when gas phase ozone is admitted to the trough, prior to this there is only

molecular oxygen present. The three traces represent the three different types of aerosol sampling methodology, the red squares represent aerosol sampled with a coated denuder to remove ozone (Run 7 in Table 1), the black circles represent aerosol sampled with an uncoated denuder (Run 8 in Table 1) and the blue triangles represent aerosol sampled with no denuder (Run 1 in Table 1). For the red squares and black circles, the mixing ratio of gas phase ozone is ~1 ppm throughout the experiment, whereas for the initial experiment, marked by the blue triangles, the mixing ratio of gas phase ozone is initially ~ 0.1 ppm marked by the first green hourglass point on top of the blue triangles and is then increased to ~ 1 ppm marked by the second green hourglass point on top of the blue triangles. The lower panel, b), shows the fitted film thickness for the same three runs shown in panel a).

The modelled thickness for the atmospheric film material sampled with a coated denuder (red squares) is noticeably larger than those modelled for samples obtained without a denuder and an uncoated denuder. However, it is within the error possible for the determined film thickness and does not change drastically.

From the similar behaviour observed in Figure 3 for aerosol sampled with a coated and with an uncoated denuder it can be assumed that there is no difference between a coated and uncoated denuder. Thus, ambient atmospheric ozone pulled through the filter during aerosol sampling did not result in an artefact in this experiment, i.e. oxidation of all organic material before removal from the filter.

4.2 Aerosol samples and the hydroxyl radical

The data in Figure 3 was unexpected, therefore to confirm that the technique is sensitive to a reaction and loss of film material at the air-water interface, the experiment was repeated using a more reactive, less selective, aqueous based reactant, the hydroxyl radical (Mack and Bolton, 1999), which can abstract hydrogen as well as add to double bonds. Figure 4 shows the experimental reflectivity profile of atmospheric film material in the presence of the hydroxyl radical. The uppermost trace in Figure 4 represents the aqueous nitrate anion subphase with no surface film and the lowest trace represents the aqueous nitrate anion subphase with a thin film of atmospheric material. On exposure to UV radiation, the hydroxyl radical was produced and the reflectivity was observed to increase from the unreacted atmospheric film material on the nitrate anion subphase (lowest trace) with increasing time towards the nitrate anion subphase alone (highest trace). The change in the

reflectivity signal is indicative of a reaction between the atmospheric film material and the hydroxyl radical.

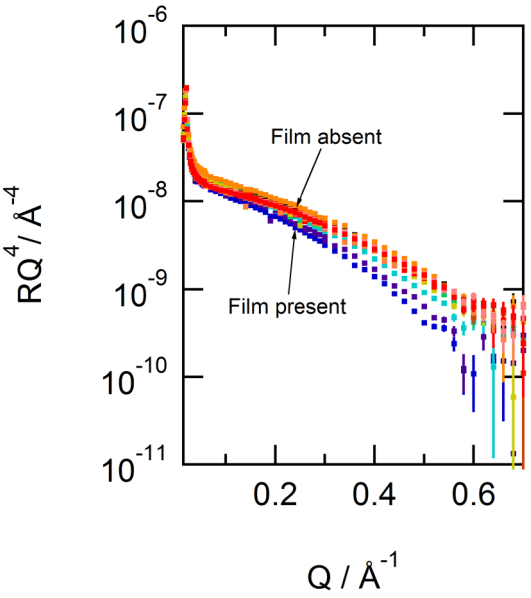

Figure 4. RQ^4 vs Q profile showing the change with time when atmospheric film material on a nitrate anion subphase is exposed to the hydroxyl radical. The blue squares represent the unreacted atmospheric film material at the air-aqueous solution interface. On exposure to UV radiation at ~254 nm, the reflectivity increases which is indicative of a reaction between the atmospheric film material and the hydroxyl radical.

Figure 5 shows the modelled surface coverage and thickness data for the reaction of the hydroxyl radical with atmospheric film material. In comparison to the lack of change in surface coverage observed in Figure 3 for reaction with gas-phase ozone, there is a clear decrease in the amount of material at the air-aqueous interface as well as a decrease in film thickness on exposure to the hydroxyl radical.

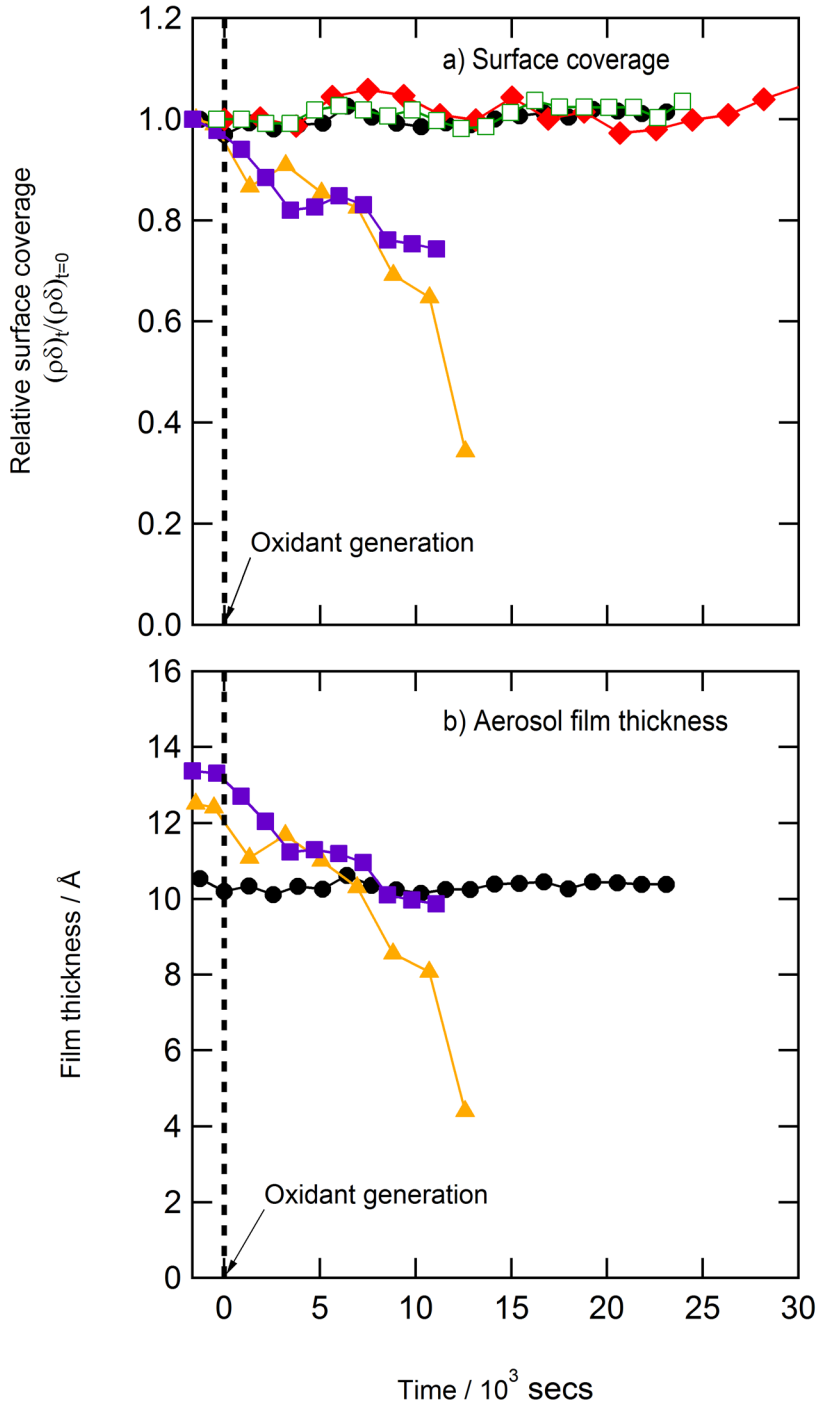

Figure 5. Panel a) shows the modelled relative surface coverage and panel b) shows the modelled film thickness. The purple squares and orange triangles in both the upper and lower panel represent atmospheric film material sampled with an uncoated denuder, (Run 12 in Table 1) and atmospheric film material sampled with a coated denuder, (Run 10 in Table 1) respectively, in the presence of the hydroxyl radical. The surface coverage decreases on exposure to the hydroxyl radical for both samples. The difference in reaction time is dictated

by the stability of the experiment. The black circles highlight the constant surface coverage observed when atmospheric film material (sampled with an uncoated denuder, Run 8) is exposed to gas-phase ozone. The dashed line represents the time when the oxidant is admitted to the trough environment, i.e. the time that the UV lamp or ozoniser is switched on. An oxygen blank is shown by the red diamonds (sampled with no denuder, Run 3, Table 1) in panel a) which represent atmospheric film material and oxygen. The hydroxyl radical is generated by photolysis of the aqueous subphase and Figure 5 shows that when hydroxyl is present there is an 'almost instant' decay in the amount of material at the air-aqueous interface. The associated blank for the UV radiation alone is shown by the unfilled squares (sampled with uncoated denuder, Run 11, Table 1) that represent atmospheric film material on water in the presence of UV radiation (~ 254 nm) alone i.e. no radical subphase present. The lower panel, b), shows film thickness for the same experimental runs shown in the upper panel a) excluding the two blanks. A clear decrease in the film thickness is observed on exposure to the hydroxyl radical whereas for comparison, the black circles show that there is no change in film thickness on exposure to gas-phase ozone.

A reaction between the atmospheric film material and the hydroxyl radical can be observed from the decrease in the relative surface coverage seen in Figure 5. The film thickness also decreases as shown in panel b) which potentially suggests a thinning mechanism. The proposed thinning mechanism is the reduction in the molecule length at the interface, i.e. subsequent consecutive reactions by the hydroxyl radical reduce the chain length of the surface active molecule by a small amount following each successful reaction. After repeated reactions, the surface active molecule is likely to be reduced to a small soluble or gaseous product and removed from the interface. However, a large part of the hydrocarbon chain will remain present at the air-water interface, which is why the surface coverage does not decrease completely to zero. The data in Figures 4 and 5 demonstrate a change in the surface active material at the air-water interface consistent with a reaction with the hydroxyl radical. The ability to monitor a reaction between a thin film of atmospheric material and the hydroxyl radical but not between a thin film of atmospheric material and gas-phase ozone suggests no observable reaction for ozone, rather than any experimental artefact.

As discussed in the method section, blank experiments were considered to eliminate the possibility that the change in surface coverage was due to film damage from the short wave (~ 254 nm) UV radiation required to generate the hydroxyl radical or from reaction with

molecular oxygen. The data for the two blank runs shown in Figure 5 with red diamonds and unfilled squares were conducted on atmospheric film material on a pure water subphase. The red diamonds represent an oxygen only blank and the unfilled squares represent a UV radiation (~254 nm) only blank. No change was observed in the surface coverage of the film for both blanks indicating that no reaction was induced by either molecular oxygen or UV radiation (~254 nm) alone.

4.3 Filter blanks

As described in the experimental section all the atmospheric aerosol samples were collected using quartz filters which were dissolved in chloroform with the aerosol sample. To demonstrate that the material being studied at the air-water interface was not introduced by the extraction process from filters, clean blank filters were dissolved in chloroform and added as a thin film at the air-water interface to observe any influence on the reflectivity profile. Three filter blanks were considered. Figure 6 shows the reflectivity of filter blanks compared to pure water. One of the filter blanks demonstrates no surface active film was generated by the extraction process. However, two of the filer blanks do give a small reflectivity signal equivalent to ~5 % of that measured for atmospheric film material.

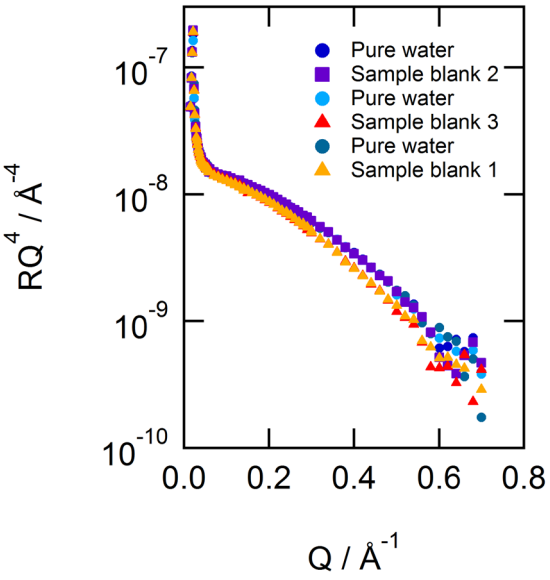

Figure 6. The reflectivity profiles for three different pure water subphases (circle markers) and three filter blanks (square and triangle markers) present at the air-water interface. Filter blank 2 as depicted by the squares overlies the reflectivity profile for the pure water subphase that it is present on. Whereas the reflectivity profiles for filter blanks 1 and 3 as depicted by

triangles do not directly overlie the reflectivity profiles for the pure water subphase that they are present on.

GC-MS analysis provided useful information on our atmospheric film material and filter blanks. All samples appeared to have weak concentrations and required derivatisation. Analysis of filter blank 1 was indistinguishable from the GC-MS analysis of the pure chloroform used in the film solution. Thus, the material shown in the filter blanks in Figure 6 is probably from contamination during cleaning the trough between experiments and may even be sample from an atmospheric filter from a previous run. In conclusion the filter blanks demonstrate that up to 5% of the atmospheric sample may be impurity.

GC-MS analysis of an atmospheric sample obtained with no denuder, identified the presence of 22-hydroxydocosanoic acid and stearic acid. However, the abundance of the stearic acid was particularly weak when compared to the signal arising from a stearic acid standard of 20 $\mu g\ ml^{-1}$ (approximately 1/5th of the standard abundance) as shown in Appendix A. It is proposed that unsaturated compounds may be present in the samples in such small concentrations compared to saturated compounds, that the unsaturated material could be below the detection limit of GC-MS. A low concentration of unsaturated coupounds could also mean that no significant reaction would be observed between atmospheric film material and gas-phase ozone which is in keeping with the modelled results in Figure 3. Another possible explanation for the lack of compounds observed by GC-MS is that the compounds could not be eluted from the GC-MS column or that the material giving rise to the surface pressure could not be resolved by GC-MS.

In conclusion, organic material extracted from real atmospheric aerosol samples can form stable surface active layers of ~ 13-25 $mN\ m^{-1}$ at the air-water interface. These atmospheric films appear to be unreactive to both ambient and large gas-phase ozone concentrations which could suggest the presence of little or no unsaturated material or the dominance of saturated material. The films are reactive to hydrogen abstraction as shown during reaction of the film with the hydroxyl radical. Pre-beamline work also showed that the isotherm of the material had no phase transition and the film did not break before 25 $mN\ m^{-1}$.

4.4 Sea water samples and gas-phase ozone and the nitrate radical

No change in surface coverage was observed for the reaction of sea-water film material and gas-phase ozone, as shown by the black circles in Figure 8 suggesting that sea-water material

is also unreactive to gas-phase ozone. As for the atmospheric film material, a more reactive radical reaction was performed, using the nitrate radical. The reason for the radical reaction is to ensure that the lack of reaction with gas-phase ozone was not an artefact of modelling, therefore the choice of the hydrogen abstracting radical was irrelevent. However, this will be verified in future experiments. Both the nitrate and hydroxyl radical are known to abstract hydrogen atoms and therefore have a different reaction mechanism to reactions with gas-phase ozone (Herrmannn et al., 1994, Herrmannn, 2003, Moise and Rudich, 2002).

The nitrate radical is a proposed cloudwater oxidant (Herrmannn et al., 1994) and is also generated by photolysis (of $S_2O_8^{2-}$ and rapid titration with NO_3^-) at longer wavelength (~360 nm) than generation of the hydroxyl radical (~254 nm). Previous work has demonstrated that 360 nm is less damaging to lipid films at the air-water interface than 254 nm. A change in reflectivity signal (Figure 7) and surface coverage (Figure 8) was observed for the reaction of the nitrate radical with a thin film of sea-water film material. The surface coverage of the sea-water film material decreases as shown by the blue squares in Figure 8, indicating that the film does react with the nitrate radical. A large decrease in surface coverage is not seen because the nitrate radical reacts selectively compared to the hydroxyl radical. A UV only blank experiment also demonstrated that the film did not degrade in the presence of 360 nm light.

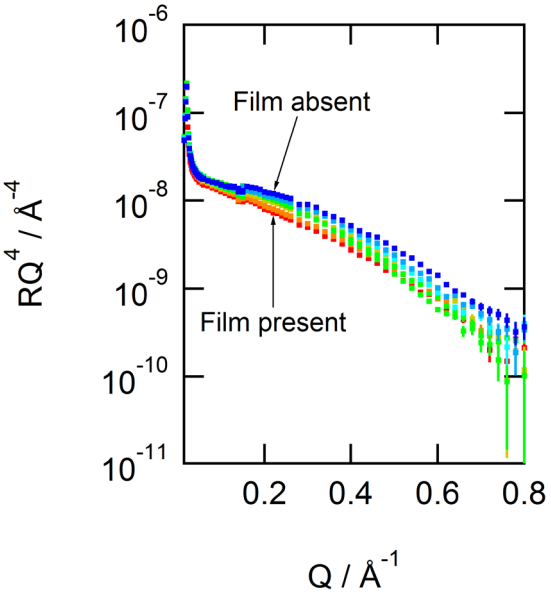

Figure 7. RQ^4 vs Q profile showing the change with time when sea-water film material is exposed to the nitrate radical. The red squares represent the unreacted sea-water film material

at the air-aqueous solution interface. On exposure to UV radiation at ~360 nm, the reflectivity signal increases (dark blue squares) which is indicative of a reaction between the sea-water film material and the nitrate radical.

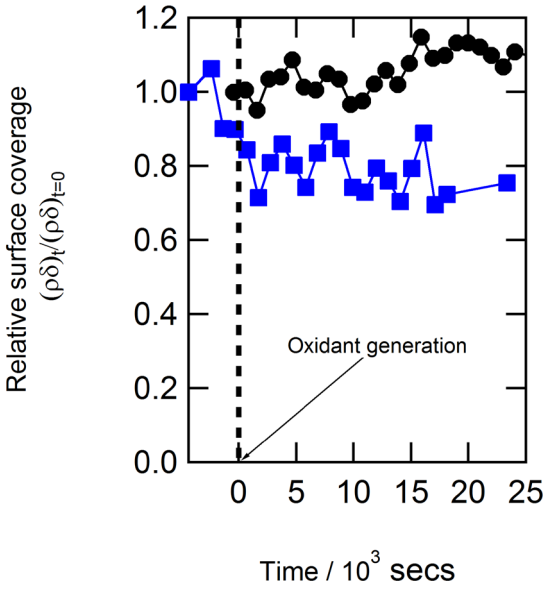

Figure 8. The blue squares (Run 3, Table 2 in the appendix) show a decrease in surface coverage for the reaction of the sea water film and the nitrate radical. The black circles (Run 5, Table 2 in the appendix) show no decrease in the surface coverage when the sea-water film material is exposed to gas phase ozone. The vertical dashed line indicates when the oxidants are generated, either aqueous nitrate anion or gas-phase ozone.

The uncertainty in the surface coverage is estimated to be between 50-70 %.

GC-MS and ESI-MS analysis indicated a lack of unsaturated material in the two sea-water samples as shown in Appendix A which is in keeping with the modelled lack of reaction between sea-water film material and gaseous ozone shown in Figure 8. A number of saturated compounds were identified in the sea-water samples using ESI-MS, notably the saturated fatty acids, stearic and palmitic acid were detected in both of the samples. Similaly to the atmospheric aerosol samples, it is also possible that there is much greater proportion of saturated material compared to unsaurated material in the sea-water.

In conclusion, organic material extracted from sea-water samples can form stable surface active layers of ~25mN m^{-1} at the air-water interface. As observed for the atmospheric film material, the sea-water films also appear to be unreactive to large gas-phase ozone concentrations suggesting the presence of little or no unsaturated material in sea-water

samples. However, the films are reactive to hydrogen abstraction as shown by the change in reflectivity (Figure 7) and surface coverage (Figure 8) during exposure of sea-water film material to the nitrate radical.

4.5 Comparison to relevant literature studies

Zhou et al., 2014 conducted studies into the heterogeneous oxidation of a thin film of linoleic acid, (a polyunsaturated fatty acid, PUFA) at the air-artificial sea water interface with gas phase ozone. Two experiments were performed in a glass boat, one on the heterogeneous oxidation of a thin film of linoleic acid at the air-artificial sea-water interface and a second on the heterogeneous oxidation of a real bulk sea surface microlayer sample (no added film). It is useful to compare the study by Zhou et al., 2014 to ours because it involves the heterogeneous oxidation of real sea-water material with gas-phase ozone.

Zhou et al. investigated the reaction mechanism and gas phase oxidation products resulting from the above reactions using proton transfer mass spectrometry (PTR-MS) and light emitting diode cavity enhanced differential absorption spectroscopy (LED-CE-DOAS). The sea surface microlayer samples were collected from Patricia Bay, Canada and the eastern equatorial Pacific Ocean. Volatile carbonyls were formed from the oxidation of a thin film of linoleic acid on artificial sea water, specifically, the reactive gas phase dicarbonyls; malondialehyde and glyoxal. It was therefore assumed that similar volatile carbonyl species would form from the oxidation of Zhou et al.'s real sea surface microlayer samples, assuming that polyunsaturated fatty acids such as linoleic acid are present in the sea-surface microlayer and indeed a variety of oxygenated VOCs were formed. Zhou et al., 2014 concluded that heterogeneous oxidation of sea-surface microlayer samples with gas-phase ozone may lead to VOC production but the identification of the reactants wasn't possible owing to the complex chemical composition of the sea-surface microlayer sample.

In the current X-ray reflectivity study, a constant surface coverage of both atmospheric and sea-water film material at the air-water interface on exposure to gas-phase ozone was observed. Combining this information with the GC-MS and ESI-MS analysis of the atmospheric and sea-water film material, which both did not show any unsaturated material, suggests that there is a very small proportion of unsaturated material in our samples. Zhou et al., 2014 stated that VOC's are believed to form from the oxidation of unsaturated materials such as polyunsaturated fatty acids, and VOCs were detected from the oxidation of their sea-

surface microlayer sample. A decrease in surface coverage was observed in the X-ray reflectivity study for the exposure of atmospheric film material to the hydroxyl radical and sea-water film material to the nitrate radical. From the decrease in coverage, it can be inferred that the material at the air-aqueous interface was oxidised and resulted in the formation of either a volatile or a soluble species which is consistent with the formation of gas-phase products as observed in Zhou et al.'s study.

In the current reflectivity study, there could be a low concentration of unsaturated material present in both our atmospheric and sea-water film material that could be below the analysis detection limit and may also be unresolvable on a GC-MS column. A low concentration of unsaturated material could explain why no reaction was observed with gas-phase ozone. It is therefore useful to determine the ratio of unsaturated material to saturated material detected in studies of other atmospheric samples.

4.5.1 Ratio of unsaturated to saturated material detected in other atmospheric sampling studies

There are numerous studies of organic aerosol in the atmosphere e.g. Saxena and Hildemann, 1996, Turpin et al., 2000, Hamilton et al., 2005 etc., and the following section will focus on pertinent studies that report the ratio of unsaturated to saturated organics in atmospheric aerosol. The results of the current X-ray reflectivity study could be consistent with atmospheric aerosol containing a small amount of unsaturated material and a large amount of saturated material that is able to form films at the air-water interface. Rogge et al., 1993, determined the concentration of organic compounds present in fine particulate matter sampled from ten sites in southern California over a year (1982) using GC-MS. Carbonaceous material constituted between 20-40% of fine particle mass and around two thirds of aerosol carbon was attributed to organic material (Gray et al., 1986). Figure 9 was adpated from Rogge et al., 1993 and summarises the percentage chemical composition of the mean annual fine particle concentration sampled in West Los Angeles in 1982. Of the organic material, 45-60% was elutable using GC-MS. It was then only possible to resolve 23-29 % of the elutable organics and from this, only 78-85% were identified as singular molecular entities. The proportion of n-alkenoic acids (unsaturated) detected was extremely low in comparison to n-alkanoic acids (saturated) as emphasised in the 'Resolvable organics' data in Figure 9, approximately ~2% n-alkenoic acids were identified compared to ~25% n-alkanoic acids. Oleic acid was the only n-alkenoic acid to be positively identified. The largest proportion of

compounds that were identifed were n-alkanoic acids and aliphatic dicarboxylic acids. In a previous study by Rogge et al., 1991, palmitoleic acid was detected from meat cooking emissions but was not detected in the 1993 study, and therefore it was suggested in the 1993 study that atmospheric reactions likely provided a sink for mono and poly unsaurated fatty acids. The low percentage of unsaturated fatty acids determined by Rogge et al., 1993, supports both the GC-MS, ESI-MS and the X-ray reflectivity results observed in the current study. No unsaturated material was observed in our GC-MS and ESI-MS analysis, which could indicate that the signal from our aerosol filters was dominated by saturated organics such as n-alkanoic acids or aliphatic dicarboxylic acids. Given that only ~50% of organic material was eluted in the study by Rogge et al., it is possible that ~ 50% of the organic material obtained in the current atmospheric aerosol samples remained on the filter paper and therefore was not eluted by GC-MS. A predominance of saturated material would also support the lack of reaction observed with gas-phase ozone.

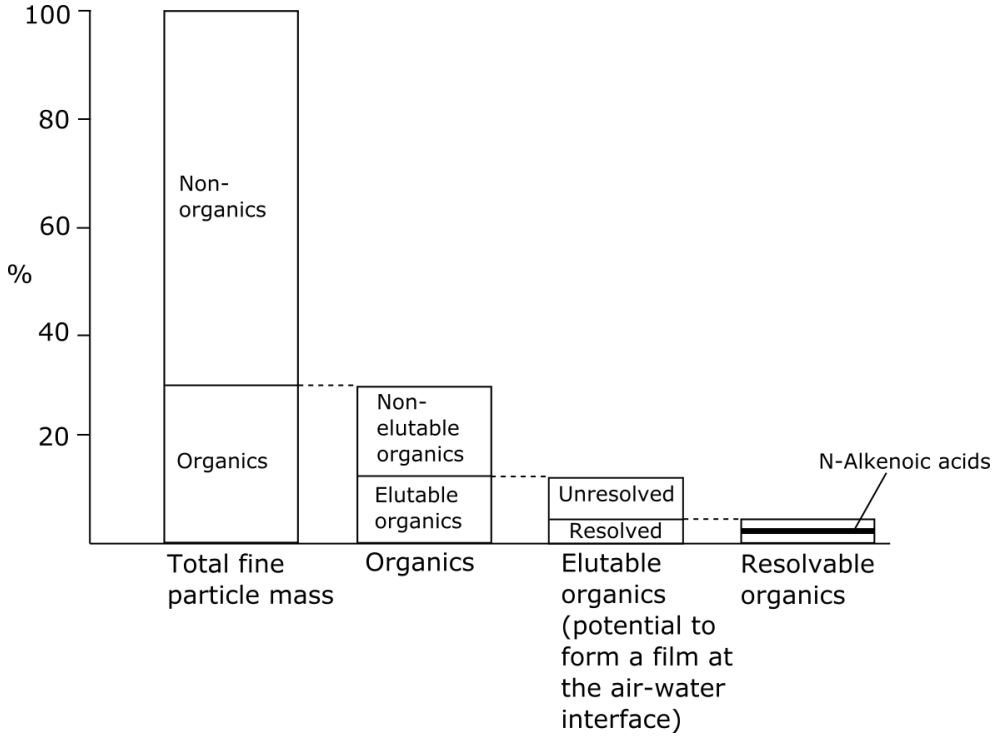

Figure 9. Adapted diagram from Rogge et al., 1993 showing the percentage chemical composition of material identified from a mean annual sample collected in West Los Angeles in 1982. The adapted diagram enphasises the small percentage of n-Alkenoic acids (~2 %) determined by GC-MS analysis compared to n-Alkanoic acids.

A number of studies on aerosol samples from different locations have also shown that unsaturated fatty acids are present in much lower concentrations than saturated fatty acids

(e.g. Kawamura and Gagosian, 1987, Simoneit and Mazurek, 1982, Abas and Simoneit, 1996, Mochida et al., 2002, Fang et al., 2002). It has been proposed that unsaturated fatty acids are not stable in the atmosphere and will either be rapidly oxidised (Kawamura and Gagosian, 1987, Simoneit and Mazurek, 1982) or decompose (Abas and Simoneit, 1996). Rapid oxidation by common oxidants such as gas-phase ozone, the hydroxyl radical or hydrogen peroxide is possible and large concentrations of ω-oxocarboxylic acids of hydrocarbon chain length 9 have been detected in marine samples (Kawamura and Gagosian, 1987). Kawamura and Gagosian, 1987 proposed that oleic acid is cleaved at C9 when oxidised and thus oleic acid is not detected in marine aerosols but many shorter saturated C9 chain acids are. Small concentrations of unsaturated fatty acids have been detected in aerosol samples collected over western USA (Simoneit and Mazurek, 1982) and their presence attributed to biogenesis close to the time of sample collection. Again, the small concentration is proposed to be due to the reactivity of unsaturated compounds to oxidation and enviromental decomposition. Abas and Simoneit, 1996, also found trace levels of unsaturated fatty acids in particulate samples obtained in Kuala Lumpur in Malaysia in the early 1990's, that they also attributed to biogenesis. Mochida et al., 2002 collected aerosols over the North Pacific from October 96-June 1997 and analysed them for fatty acids and determined a smaller concentration of unsaturated fatty acids compared to saturated fatty acids. With regards to polyunsaturated fatty acids, trace amounts were detected by Simoneit and Mazurek, 1982, in their study of aerosol samples collected over the rural and urban western USA but no polyunsaturated fatty acids were detected by Fang et al., 2002 in marine aerosols collected over 41 months over the western north pacific from April 1990-November 1993.

Gilardoni et al., 2007, used Fourier Transform Infra Red (FTIR) spectroscopy to determine the molar concentrations of functional groups present in submicron aerosol samples collected from four sampling locations during the International Consortium for Atmospheric Research on Transport and Transformation in the summer of 2004. Aerosol samples were collected on Teflon filters from two mainland sites in Nova Scotia, Canada, and in Maine, USA and samples were also collected by an aircraft over Ohio, USA and a research ship in the Gulf of Maine. Saturated and unsaturated material was found to dominate the organic mass and much larger masses were determined for saturated aliphatic C-C-H groups compared to unsaturated aliphatic C=C-H groups in samples from all locations. The ratio of unsaturated aliphatic C-C-H to saturated aliphatic C=C-H groups was 0.1 for the aerosol sampled by the aircraft over Ohio, whereas a ratio of 0.2 was obtained for the other three sampling locations which were

also all coastal locations. These ratios are similar to the concentration ratios of unsaturated to saturated C-H groups in water soluble organic carbon determined by Fuzzi et al., 2001 and Descari et al., 2000, using H-NMR spectroscopy. Gilardoni et al., 2007 postulated that the reason for the higher ratios of unsaturated compounds to saturated compounds at the coastal sites could have been due to a higher concentration of unsaturated material resulting from biogenic sources or a lower concentration of saturated material as a result of unprocessed primary combustion emissions. Gilardoni et al.'s 2007 findings of low concentrations of unsaturated compounds present in aerosol sampled from both inland and coastal locations support the current X-ray reflectivity results.

Given the available evidence in the above studies, it would appear that unsaturated materials are present in atmospheric samples in much lower concentrations compared to saturated materials and therefore films in the atmosphere are predominantly saturated. In the current study, organic film forming material is extracted from atmospheric aerosol and sea-water samples in chloroform. Therefore, only the amount of unsaturated material that can be extracted in chloroform can be estimated. Given the above literature studies it is estimated that the upper detection limit for unsaturated material that is extractable in chloroform in our samples is ~ 5 %.

4.5.2 Thin film studies

Previous studies have been conducted on the oxidation of thin films at the air-water interface (Eliason et al., 2003, 2004, Voss et al., 2006, 2007, Gonzalez-Labrada et al., 2006, 2007) and have typically followed the oxidation of a thin film using surface pressure measurements or spectroscopy. Particularly relevant studies on the oxidation of thin films at the air-water interface have been conducted using neutron reflectivity (King et al., 2009, Pfrang et al., 2014). Pfrang et al., used neutron reflectivity to follow the oxidation of a monolayer of methyl oleate at the air-water interface by gas-phase ozone and were able to determine a bimolecular rate constant that highlighted how a minor change in the molecular structure of a film (methyl oleate compared to oleic acid) strongly influences film reactivity. King et al., 2009 studied the gas-phase oxidation of a monolayer of deuterated oleic acid at the air-water interface with ozone using neutron reflectivity. Oleic acid was chosen as a proxy for unsaturated organic material found in the atmosphere. The surface coverage of the oleic acid at the air-water interface was modelled and a clear decrease was observed with time on exposure to gas-phase ozone. The study by King et al. 2009 shows that gas-phase ozone does

react with a monolayer of oleic acid at the air-water interface causing a decrease in surface coverage. A similar trend was expected on addition of gas-phase ozone to atmospheric and sea-water film material in the current X-ray reflectivity experiment but was not observed i.e. constant surface coverage on exposure to gas-phase ozone. More analysis is required in order to definitively determine whether unsaturated material is present in our sampled atmospheric film material. Atmospheric samples could also be collected for longer time periods in attempt to increase the amount of material extracted from the sample which may allow some unsaturated material to be detected by GC-MS or ESI-MS.

5 Conclusions

Stable films can be formed from material extracted from atmospheric aerosol and sea-water at the air-water interface. The X-ray reflectivity study of the heterogeneous oxidation of such thin films at the air-water interface demonstrates that the films are unreactive to gas-phase ozone and can be modelled as a constant amount of material at the air-water interface. The atmospheric and sea-water samples either do not contain unsaturated organic material, or contain unsaturated organic material in very low concentrations. It is likely that unsaturated material is present in very low concentrations in comparison to saturated material given the evidence in the literature (Kawamura and Gagosian, 1987, Simoneit and Mazurek, 1982, Abas and Simoneit, 1996, Mochida et al., 2002, Fang et al., 2002, Gilardoni et al., 2007). Therefore, oxidation by gas-phase ozone may not be an important atmospheric reaction and oleic acid could be a poor choice for a proxy for organic film forming material in the atmosphere. Ideally future studies should be conducted on aerosol samples collected at different stages in the aerosol lifetime to deduce which reactions are important at what stages. Future studies should also consider the oxidation of saturated compounds by radical reaction.

The X-ray reflectivity study of a thin film of material extracted from atmospheric aerosol with the hydroxyl radical and a thin film of material extracted from sea-water with the nitrate radical can both be modelled as a decreasing amount of material at the air-water interface. Therefore the film reacts and a film thinning mechanism is proposed, where radical attack of the hydrocarbon chain results in reduction in chain length of the surface active material at the air-water interface. However, due to the correlation of film thickness and scattering length density, more experiments at a higher Q range are necessary to confirm such a mechanism. The observed decrease in surface coverage on exposure of the thin films to radicals and the

constant surface coverage observed on exposure of the thin films to gas-phase ozone could also suggest that gas-phase oxidation by ozone is not important in the atmosphere.

In conclusion, X-ray reflectivity has been used to study the oxidation of thin films of material extracted from atmospheric aerosol and sea-water at the air-water interface. Results indicate that heterogeneous oxidation by gas-phase ozone may not be important in the atmosphere given the low concentration of unsaturated organics to saturated organics in sampled aerosol, whereas radical oxidation appears to be important and induces a thinning mechanism in the organic films. It is recommended that future studies consider aerosol samples collected at different stages in the aerosol lifetime to determine whether specific reactions such as gas-phase oxidation by ozone are important at particular stages. It has also been proposed that future proxy studies should also consider radical oxidation of saturated organics because oleic acid may not be the most atmospherically relevant proxy.

Acknowledgements

The authors wish to acknowledge Diamond beam time grants Si8744-1 and Si632-1. SHJ wishes to thank NERC for funding of grant NE/H019103/1 and the Research Complex at Harwell for use of their laboratories for sample preparation.

References

Andrews, E. and Larson, S. M.: Effect of Surfactant Layers on the Size Changes of Aerosol-Particles As a Function of Relative-Humidity, Environ. Sci. Technol., 27(5), 857–865, doi:10.1021/es00042a007, 1993.

Abas, M. R. Bin and Simoneit, B. R. T.: Composition of extractable organic matter of air particles from Malaysia: Initial study, Atmos. Environ., 30(15), 2779–2793, doi:10.1016/1352-2310(95)00336-3, 1996.

Abelès, F.: La théorie générale des couches minces, Le Journal de Physique et le Radium 11, 307-310, 1950.

Arnold, T., Nicklin, C., Rawle, J., Sutter, J., Bates, T., Nutter, B., McIntyre, G. and Burt, M.: Implementation of a beam deflection system for studies of liquid interfaces on beamline I07 at Diamond., J. Synchrotron Radiat., 19, 408–416, doi:10.1107/S0909049512009272, 2012.

Barnes, G. T. and Gentle, I.R.: Interfacial Science: An Introduction, Oxford University Press, 2005.

Blanchard, D. C.: Sea-to-Air Transport of Surface Active Material, Science, 146(13), 396–397, 1964.

Bubble-Film extraction fundamentals and application, Victor S. Gevod in Handbook of Surface and Colloid Chemistry, Third Edition Edited by Birdi, K.S., CRC Press, 585–630, 2008.

Decesari, S., Facchini, M. C., Fuzzi, S. and Tagliavini, E.: Characterization of water-soluble organic compounds in atmospheric aerosol: A new approach, J. Geophys. Res., 105(D1), 1481–1489, 2000.

Donaldson, D. J. and George, C.: Sea-Surface Chemistry and Its Impact on the Marine Boundary Layer., Environ. Sci. Technol., doi:10.1021/es301651m, 2012.

Draxler, R.R. and Rolph, G.D.: HYSPLIT (HYbrid Single-Particle Lagrangian Integrated Trajectory) Model access via NOAA ARL READY Website (http://ready.arl.noaa.gov/HYSPLIT.php). NOAA Air Resources Laboratory, Silver Spring, MD, 2015.

Ebben, C. J., Shrestha, M., Martinez, I. S., Corrigan, A. L., Frossard, A. A, Song, W. W., Worton, D. R., Petäjä, T., Williams, J., Russell, L. M., Kulmala, M., Goldstein, A. H., Artaxo, P., Martin, S. T., Thomson, R. J. and Geiger, F. M.: Organic constituents on the surfaces of aerosol particles from Southern Finland, Amazonia, and California studied by vibrational sum frequency generation., J. Phys. Chem. A, 116(32), 8271–8290, doi:10.1021/jp302631z, 2012.

Eliason, T. L., Aloisio, S., Donaldson, D. J., Cziczo, D. J. and Vaida, V.: Processing of unsaturated organic acid films and aerosols by ozone, Atmos. Environ., 37(16), 2207–2219, doi:10.1016/S1352-2310(03)00149-3, 2003.

Eliason, T. L., Gilman, J. B. and Vaida, V.: Oxidation of organic films relevant to atmospheric aerosols, Atmos. Environ., 38(9), 1367–1378, doi:10.1016/j.atmosenv.2003.11.025, 2004.

Ellison, G. B., Tuck, A. F. and Vaida, V.: Atmospheric processing of organic aerosols, J. Geophys. Res., 104, 11633–11641, 1999.

Falkovich, A.H., Schkolnik, G., Ganor, E. and Rudich, Y.: Adsorption of organic compounds pertinent to urban environments onto mineral dust particles, J. Geophys. Res., Atmos., 109, D02208, 2004.

Finlayson-Pitts, B. J.: Reactions at surfaces in the atmosphere: integration of experiments and theory as necessary (but not necessarily sufficient) for predicting the physical chemistry of aerosols, Phys. Chem. Chem. Phys., 11, 7760–7779, doi:10.1039/b916865f, 2009.

Fuzzi, S., Decesari, S., Facchini, M., Matta, E., Mircea, M. and Tagliavini, E.: A simplified model of the water soluble organic component of atmospheric aerosols, Geophys. Res. Lett., 28(21), 4079–4082, 2001.

Gilardoni, S., Russell, L. M., Sorooshian, A., Flagan, R. C., Seinfeld, J. H., Bates, T. S., Quinn, P. K., Allan, J. D., Williams, B., Goldstein, A. H., Onasch, T. B. and Worsnop, D. R.: Regional variation of organic functional groups in aerosol particles on four U . S . east coast platforms during the International Consortium for Atmospheric Research on Transport and Transformation 2004 campaign, J. Geophys. Res., 112(D10S27), 1–11, doi:10.1029/2006JD007737, 2007.

Gill, P. S., Gradel, T. E. and Weschler, C. J.: Organic Films on Atmospheric Aerosol Particles, Fog Droplets, Cloud Droplets, Raindrops and Snowflakes, Rev. Geophys. Sp. Phys., 21(4), 903–920, 1983.

González-Labrada, E., Schmidt, R. and DeWolf, C. E.: Real-time monitoring of the ozonolysis of unsaturated organic monolayers., Chem. Commun., 23, 2471–3, doi:10.1039/b603501a, 2006.

González-Labrada, E., Schmidt, R. and DeWolf, C. E.: Kinetic analysis of the ozone processing of an unsaturated organic monolayer as a model of an aerosol surface, Phys. Chem. Chem. Phys., 9(43), 5814, doi:10.1039/b707890k, 2007.

Gray, H. A, Cass, G. R., Huntzicker, J. J., Heyerdahl, E. K. and Rau, J. A: Characteristics of atmospheric organic and elemental carbon particle concentrations in Los Angeles., Environ. Sci. Technol., 20(6), 580–589, doi:10.1021/es00148a006, 1986.

Hamilton, J. F., Webb, P. J., Lewis, A. C. and Reviejo, M. M.: Quantifying small molecules in secondary organic aerosol formed during the photo-oxidation of toluene with hydroxyl radicals, Atmos. Environ., 39, 7263–7275, doi:10.1016/j.atmosenv.2005.09.006, 2005.

Helmig. D.: Ozone removal techniques in the sampling of atmospheric volatile organic trace gases, Atmos. Environ., 31(21), 3635-3651, 1997.

Herrmannn, H., Exner, M. and Zellner, R.: Reactivity trends in reactions of the nitrate radical (N03) and organic cloudwater constituents, Geochim. Cosmochim. Acta, 58(15), 3239–3244, 1994.

Herrmannn, H.: Kinetics of aqueous phase reactions relevant for atmospheric chemistry., Chem. Rev., 103(12), 4691–716, doi:10.1021/cr020658q, 2003.

IPCC, 2013: Climate Change 2013: The Physical Science Basis. Contribution of Working Group I to the Fifth Assessment Report of the Intergovernmental Panel on Climate Change [Stocker, T.F., D. Qin, G.-K. Plattner, M. Tignor, S.K. Allen, J. Boschung, A. Nauels, Y. Xia, V. Bex and P.M. Midgley (eds.)]. Cambridge University Press, Cambridge, United Kingdom and New York, NY, USA, 1535 pp, doi:10.1017/CBO9781107415324.

Kawamura, K. and Gagosian, R. B.: Implications of ω-oxocarboxylic acids in the remote marine atmosphere for photo-oxidation of unsaturated fatty acids, Nature, 325, 330–332, doi:10.1038/325330a0, 1987.

King, M. D., Rennie, A. R., Thompson, K. C., Fisher, F. N., Dong, C. C., Thomas, R. K., Pfrang, C. and Hughes, A. V.: Oxidation of oleic acid at the air–water interface and its potential effects on cloud critical supersaturations, Phys. Chem. Chem. Phys., 11(35), 7699, doi:10.1039/b906517b, 2009.

Koutrakis, P., Sioutas, C., Ferguson, S. T., Wolfson, J. M., Mulk, J. D. and Burton, R. M.: Development and evaluation of a glass honeycomb denuder/filter pack system to collect atmospheric gases and particles, Environ. Sci. Technol., 27(12), 2497–2501, doi:10.1021/es00048a029, 1993.

Lohmann, U. and Feichter, J.: Global indirect aerosol effects : a review, Atmos. Chem. Phys., 5, 715–737, 2005.

Mack, J. and Bolton, J. R.: Photochemistry of nitrite and nitrate in aqueous solution: a review, J. Photochem. Photobiol. A Chem., 128, 1–13, doi:10.1016/S1010-6030(99)00155-0, 1999.

Mason, B. J.: Bursting of Air Bubbles at the Surface of Sea Water, Nature, 174, 470–471, 1954.

Mochida, M.: Fatty acids in the marine atmosphere: Factors governing their concentrations and evaluation of organic films on sea-salt particles, J. Geophys. Res., 107(D17), 4325, doi:10.1029/2001JD001278, 2002.

Moise, T. and Rudich, Y.: Reactive Uptake of Ozone by Aerosol-Associated Unsaturated Fatty Acids: Kinetics, Mechanism, and Products, J. Phys. Chem. A, 106(27), 6469–6476, doi:10.1021/jp025597e, 2002.

Nelson, A.: Co-refinement of multiple-contrast neutron/X-ray reflectivity data using MOTOFIT, J. Appl. Crystallogr., 39(2), 273–276, doi:10.1107/S0021889806005073, 2006.

Pandis, S. N., Wexler, A. S. and Seinfeld, J. H.: Dynamics of Tropospheric Aerosols, J. Phys. Chem., 99(24), 9646–9659, doi:10.1021/j100024a003, 1995.

Pfrang, C., Sebastiani, F., Lucas, C. O. M., King, M. D., Hoare, I. D., Chang, D. and Campbell, R. A: Ozonolysis of methyl oleate monolayers at the air-water interface: oxidation kinetics, reaction products and atmospheric implications., Phys. Chem. Chem. Phys., 16(26), 13220–8, doi:10.1039/c4cp00775a, 2014.

Pöschl, U.: Atmospheric aerosols: composition, transformation, climate and health effects., Angew. Chem. Int. Ed. Engl., 44(46), 7520–40, doi:10.1002/anie.200501122, 2005.

Ramanathan, V., Crutzen, P. J., Kiehl, J. T. and Rosenfeld, D.: Aerosols, Climate, and the Hydrological Cycle, Science, 294, 2119–2125, 2001.

Rogge, W. F., Hildemann, L., Mazurek, M. A., Cass, G. R. and Simoneit, B.: Sources of fine organic aerosol. 1. Charbroilers and meat cooking operations, Environ. Sci. Technol., 25, 1112–1125, doi:10.1021/es00018a015, 1991.

Rogge, W. F., Mazurek, M. A., Hildemann, L. M., Cass, G. R. and Simoneit, B. R. T.: Quantification of urban organic aerosols at a molecular level: Identification, abundance and seasonal variation, Atmos. Environ. Part A. Gen. Top., 27(8), 1309–1330, doi:10.1016/0960-1686(93)90257-Y, 1993.

Rolph, G.D.: Real-time Environmental Applications and Display sYstem (READY) Website (http://ready.arl.noaa.gov). NOAA Air Resources Laboratory, Silver Spring, MD, 2015.

Rudich, Y.: Laboratory Perspectives on the Chemical Transformations of Organic Matter, Chem. Rev., 103(12), 5097–5124, 2003.

Saxena, P. and Hildemann, L. M.: Water-soluble organics in atmospheric particles: A critical review of the literature and application of thermodynamics to identify candidate compounds, J. Atmos. Chem., 24(1), 57–109, doi:10.1007/BF00053823, 1996.

Simoneit, B. R. T. and Mazurek, M. A.: Organic Matter of the Troposphere-II. Natural Background of biogenic lipid matter in aerosols over the rural western United States, Atmos. Environ., 16(9), 2139–2159, doi:10.1016/j.atmosenv.2007.10.056, 1982.

a) Tervahattu, H., Hartonen, K., Kerminen, V., Kupiainen, K., Koskentalo, T., Tuck, A. F. and Vaida, V.: New evidence of an organic layer on marine aerosols, J. Geophys. Res., 107(D7), doi:10.1029/2000JD000282, 2002.

b) Tervahattu, H., Juhanoja, J. and Kupiainen, K.: Identification of an organic coating on marine aerosol particles by TOF-SIMS, J. Geophys. Res., 107, 1–7, 2002.

Turpin, B. J., Saxena, P. and Andrews, E.: Measuring and simulating particulate organics in the atmosphere: Problems and prospects, Atmos. Environ., 34, 2983–3013, doi:10.1016/S1352-2310(99)00501-4, 2000.

Voss, L. F., Hadad, C. M. and Allen, H. C.: Competition between Atmospherically Relevant Fatty Acid Monolayers at the Air / Water Interface, J. Phys. Chem. B, 110(39), 19487–19490, 2006.

Voss, L. F., Bazerbashi, M. F., Beekman, C. P., Hadad, C. M. and Allen, H. C.: Oxidation of oleic acid at air/liquid interfaces, J. Geophys. Res., 112(D6), 1–9, doi:10.1029/2006JD007677, 2007.

Woodcock, A. H., Kientzler, C. F., Arons, A.B . and Blanchard, D. C.: Giant Condensation Nuclei from Bursting Bubbles, Nature, 172, 1144–1145, 1953.

Zhou, S., Gonzalez, L., Leithead, A., Finewax, Z., Thalman, R., Vlasenko, A., Vagle, S., Miller, L. A., Li, S.-M., Bureekul, S., Furutani, H., Uematsu, M., Volkamer, R. and Abbatt, J.: Formation of gas-phase carbonyls from heterogeneous oxidation of polyunsaturated fatty acids at the air–water interface and of the sea surface microlayer, Atmos. Chem. Phys., 14(3), 1371–1384, doi:10.5194/acp-14-1371-2014, 2014.

Table 1 details the X-ray reflectivity experiments performed on atmospheric film material and Table 2 details X-ray reflectivity experiments performed on sea-water film material at the air-water interface.

Table 1. Atmospheric film material experiment details.

Run Number	Sample	Aerosol collection time/ hours (time of year)	Experiment	Reaction observed	Provenance of aerosol (from back trajectories)
1	Aerosol filter	96 October 2013	Reaction with 0.1-1ppm O_3	No	EU, polluted
2	Filter blank	NA	Blank, pure O_2 1Lmin^{-1}	No	-
3	Aerosol Filter	96 October 2013	Blank, pure O_2 1Lmin^{-1}	No	EU, polluted
4	Filter blank	NA	Blank, pure O_2 1Lmin^{-1}	No	-
5	Aerosol with uncoated denuder	190 February 2014	Reaction with 1ppm O_3	No	Atlantic
6	Aerosol with coated denuder	217 February 2014	Reaction with 1ppm O_3	No	Atlantic
7	Aerosol with coated denuder	574 March 2014	Reaction with 1ppm O_3	No	EU, polluted and Atlantic
8	Aerosol with uncoated denuder	574 March 2014	Reaction with 1ppm O_3	No	EU, polluted and Atlantic
9	Aerosol Filter	140 October 2013	Test run for amount of material	No	EU, polluted
10	Aerosol coated denuder	217 February 2014	Reaction with OH radical	Yes	Atlantic
11	Aerosol with coated denuder	217 February 2014	Blank UV light only	No	Atlantic
12	Aerosol with uncoated denuder	190 February 2014	Reaction with OH radical	Yes	Atlantic

Table 2. Sea water film material experiment details

Run number	Sea-water sample amount	Experiment	Reaction observed
1	38µl	Reaction with ~0.1 ppm O_3 monochromater issues	No
2	43µl	Reaction with ~0.9 ppm O_3	No
3	42µl	Reaction with $NO_3^{\cdot}$ radical	Yes
4	42µl	Blank UV light only	No
5	43µl	Reaction with ~0.9 ppm O_3	No
6	41µl	Blank NO_3^- subphase and no light	No

Appendix A: GC-MS and ESI-MS Spectra

Atmospheric film material GC-MS spectra

GC-MS spectra of two different samples of aerosol film material as well as a filter blank. GC-MS spectra of a chloroform blank, n-alkanes and common fatty acids standards are also presented for comparison.

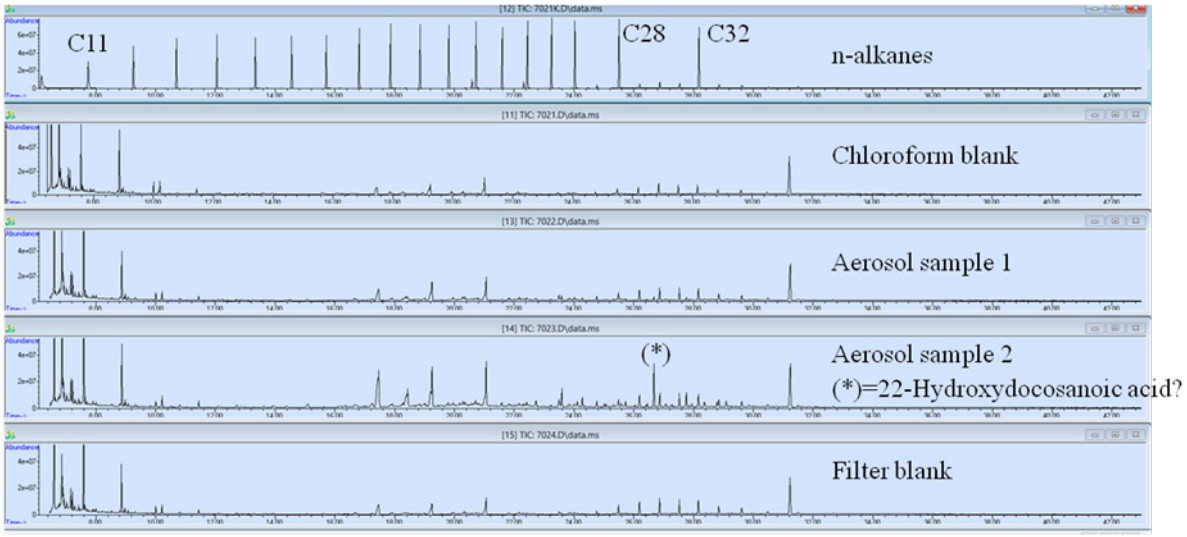

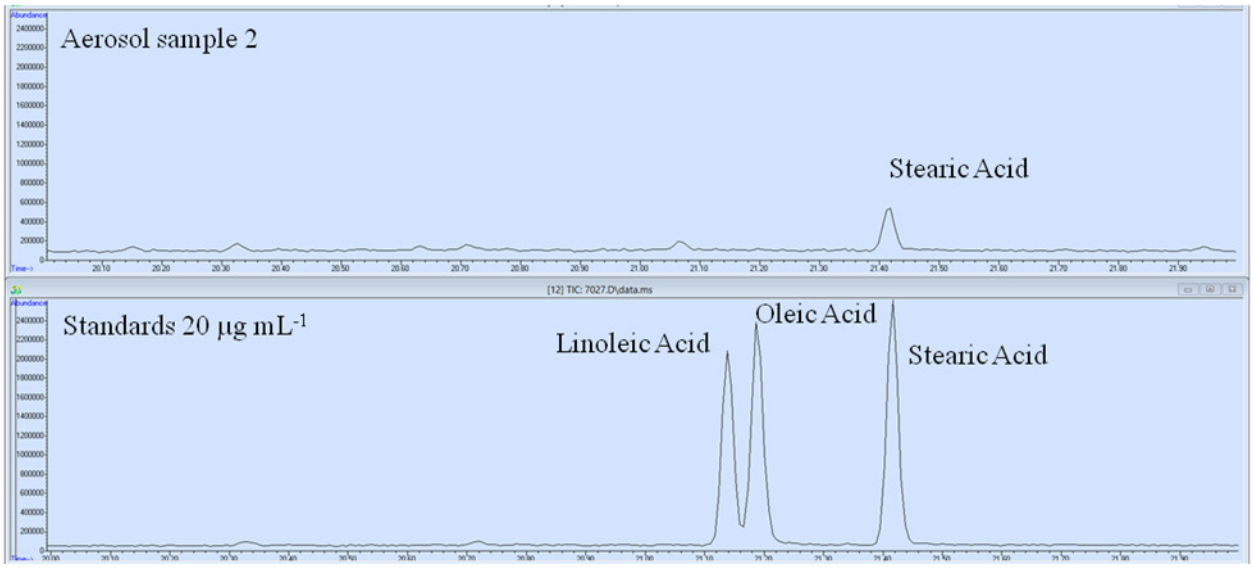

Sea-water film material GC-MS spectra

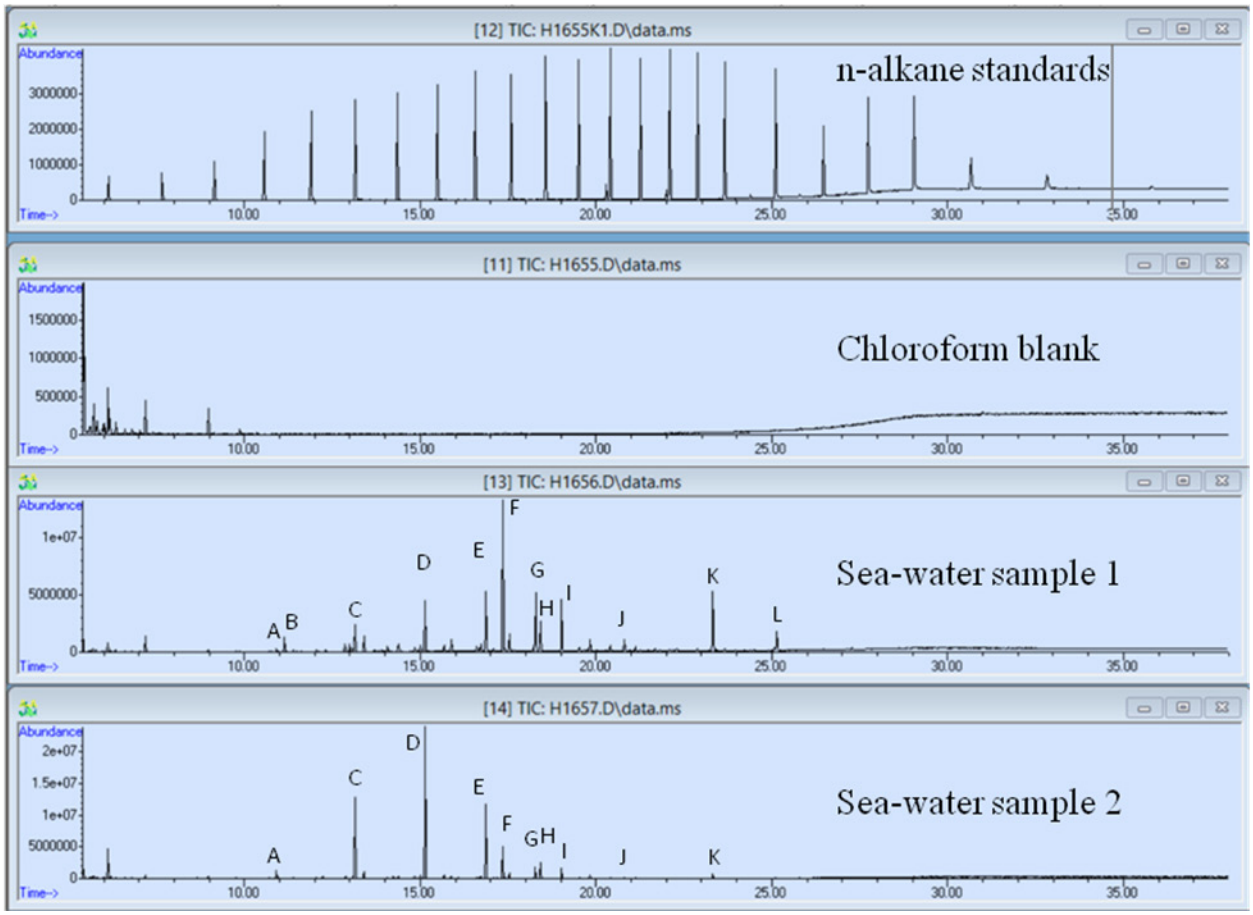

Possible peak identities:

A:2-(2-Butoxyethoxy)ethoxy

B:Dodecamethylcyclohexasiloxane

C:Tetradecamethylcycloheptasiloxane

D:Hexadecamethylcyclooctasiloxane

E: Octadecamethylcyclononasiloxane

F:Isobutyl phthalate

G:Dibutyl phthalate

H:Eicosamethylcyclodecasiloxane

I:Palmitic acid

J:Stearic acid

K:Bis[2-ethylhexsyl]phthalate

L:4,4'-Ethylenebis(2,6-di-tert-butylphenol)

Sea-water ESI-MS Spectra

Negative ions (acidic compounds) M-H

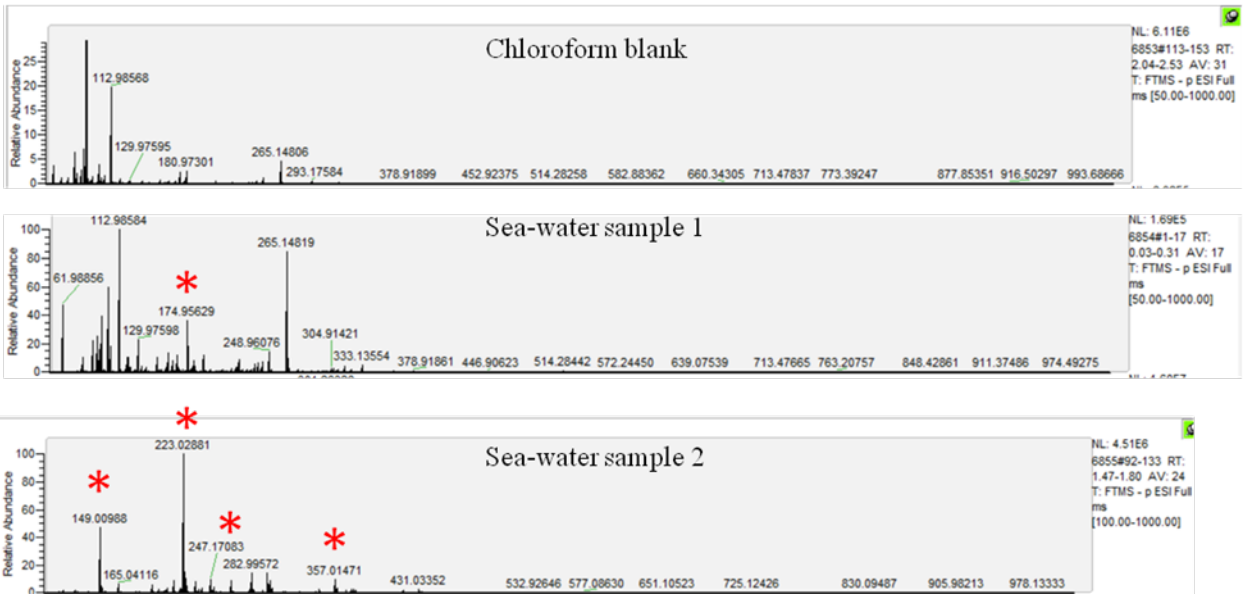

Possible identities of major peaks:

149.00968 $C_4H_6O_6$ 2,3 Dihydroxysuccinic acid (tartrate)

223.02881 $C_{10}H_8O_6$ Dehydrochorismic acid

247.17083 $C_{16}H_{24}O_2$ Phenyldecanoic acid

Positive ions (basic compounds) M+H or M+Na

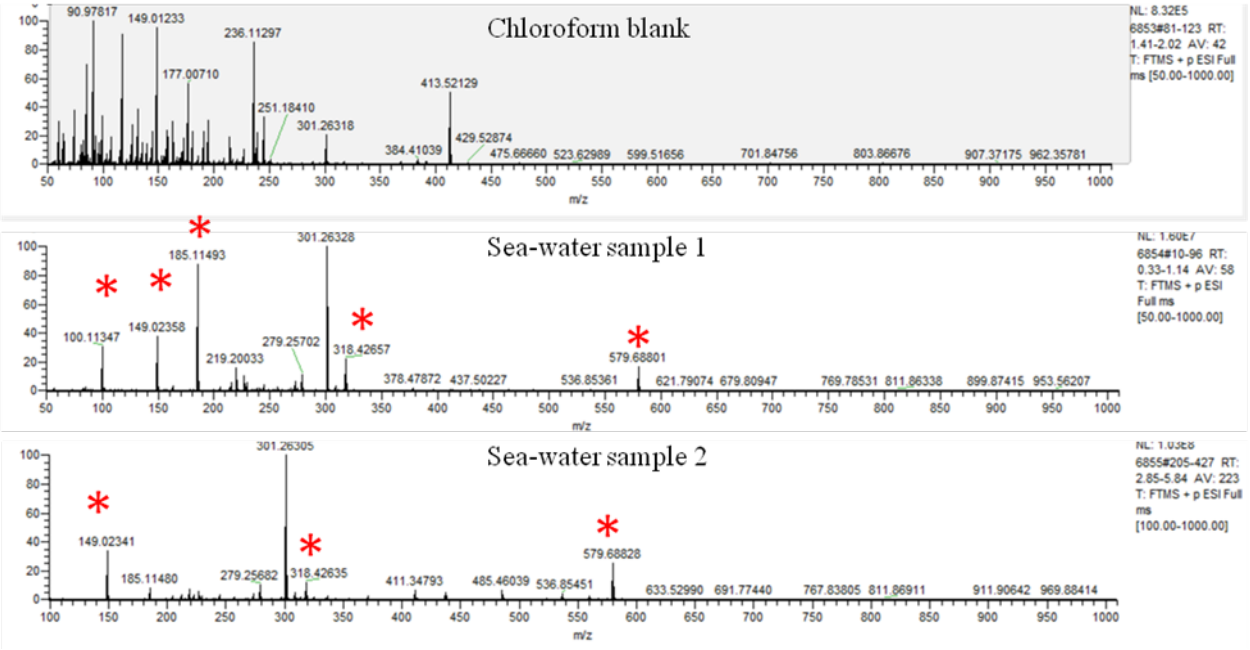

Possible identities of major peaks:

100.11347 $C_6H_{13}N$

149.02358 $C_6H_6O_3$ [+Na]

185.11483 $C_8H_{18}O_3$ [+Na]

579.68801 $C_{39}H_{78}O_2$

3. Summary and critical evaluation

3.1. Introduction

This thesis covers the study of thin films at the air-liquid and air-solid interfaces and their oxidation reactions using optical trapping and neutron and X-ray reflectometry. The majority of work covered in this thesis is motivated by evidence for the existence of core-shell aerosol in the atmosphere, e.g. Husar and Shu, 1975, Tervahattu et al., 2002, 2005, Russell et al., 2002. The aim of the work was to determine how the presence and oxidation of thin films at the surface of atmospheric aerosol affects aerosol optical and physical properties. The information obtained from these studies can subsequently be used by climate modellers to further understand how core-shell aerosol impacts on modern climate change. Related studies were also conducted on the oxidation of biologically relevant thin films at the air-water interface to assess the effect of the common air pollutant ozone on lung surfactant.

3.2. Characterisation of optically trapped core and core-shell aerosol

Optical trapping combined with white light Mie scattering was used to characterise uncoated polystyrene beads and silica beads coated in a thin film of oleic acid as proxies for atmospheric aerosol. A number of preliminary experiments were conducted that led to the work described in papers 1 and 2 which will be evaluated prior to summarising the results of papers 1 and 2 and discussing recommendations for future work.

3.2.1. Evaluation of preliminary optical trapping work

Prior to trapping and characterisation of solid aerosol, preliminary core-shell experiments were conducted on optically trapped liquid droplets of sodium chloride as a proxy for marine aerosol, which is one of the major sources of atmospheric aerosol (Boucher et al., 2013). Oleic acid delivered in methanol and dipalmitoyl-sn-glycero-3-phosphocholine (DPPC) delivered in methanol were both trialled as liquid coatings, where methanol was used to assist in nebulisation of the coating. Figure 1 shows the difference between a core sodium chloride Mie resonance spectrum (black trace) and a Mie resonance spectrum following nebulisation of oleic acid (red trace). The spectra were collected using a short acquisition time in order to monitor the changes in real time in the Mie resonance spectrum following the nebulisation of the oleic acid. The short acquisition time combined with the preliminary experimental set up used to conduct the experiments produced low intensity spectra with a significant amount of

noise as shown in Figure 1, which consequently resulted in a large amount of uncertainty in analysis of the spectra.

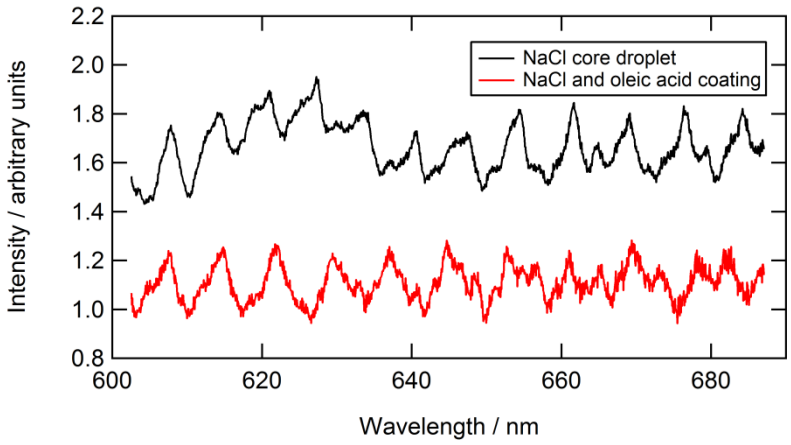

Figure 1. Comparison of the Mie resonance spectrum for an optically trapped sodium chloride droplet (black trace) to the subsequent Mie resonance spectrum of the same droplet following collisions with a number of oleic acid droplets (red trace).

As the core sodium chloride aerosol is a liquid, it was not clear whether the oleic acid had symmetrically coated the core sodium chloride droplet, or whether the oleic acid had mixed into the core aerosol droplet, making it difficult to determine the resultant morphology. Therefore liquid core-liquid shell systems were not pursued further and a more robust core-shell experiment was proposed: to coat a solid core aerosol with a liquid coating in order to maintain a distinction between the core aerosol and the coating material.

Polystyrene beads were selected as the solid core aerosol assuming that the surface of the beads was non-porous and characterised as described in paper 1. Preliminary experiments were conducted using a number of liquid coatings such as: dodecane; decane; squalene delivered in methanol; heptane and trans-5-decene. The coatings were selected so that they could be easily removed, owing either to their volatility (dodecane, decane and heptane) or their susceptibility to oxidation (squalene and trans-5-decene). Core-shell morphology was successfully judged by the ability to characterise the aerosol at different stages throughout the experiment i.e. the uncoated core polystyrene bead prior to coating, the polystyrene bead coated in a thin film and the core polystyrene bead following removal of the coating. Following nebulisation of the coating material, it was not clear whether the coating had spread to form a concentric coating on the surface of the polystyrene bead. Therefore attempts were made to remove the coating material in order to revert back to the initial uncoated polystyrene bead and its associated Mie spectrum. Despite the volatility of the solvents and the susceptibility of squalene and trans-5-decene to oxidation by gaseous ozone, it

was not possible to fully remove any of the potential coating materials in order to revert back to the uncoated polystyrene bead Mie spectrum.

Thus it was decided to coat core polystyrene beads with a material that should spread on the surface of the polystyrene bead and that can easily be removed. Oleic acid was selected as atmospherically relevant coating material (Fang et al., 2002, Mochida et al., 2002) that can be removed from the polystyrene surface on exposure to gaseous ozone. However, the core polystyrene bead was observed to react with gaseous ozone and the subsequent oxidation of a polystyrene bead coated in a thin film of oleic acid would result in both the oxidation of the core polystyrene bead and the oleic acid coating, meaning that it would not be possible to revert back to the original polystyrene bead following oxidation. Therefore silica beads were selected as a more atmospherically relevant proxy that were inert to gaseous ozone and studies were conducted to coat optically trapped silica beads in a thin film of oleic acid as described in paper 2.

3.2.2. Summary and evaluation of paper 1

Paper 1 describes the trapping of forty six polystyrene beads and the detailed characterisation of the size and wavelength dependent refractive index of ten beads using white light Mie spectroscopy. Mie theory was used to determine the radius of polystyrene beads to ± 0.4 nm and the wavelength dependent refractive index of the beads to ± 0.0005.

The optical trapping technique was evaluated in the methodology and will not be repeated here; however the data fitting process will be evaluated. For a single polystyrene bead, several iterative steps were employed to match the position of the calculated Mie resonances to the position of the experimental Mie resonances. For a specific bead radius, all three Cauchy coefficients were varied simultaneously in order to match the calculated Mie resonance positions to the experimental Mie resonance positions. The bead radius was then iterated and the Cauchy coefficients were simultaneously varied again to find the optimum fit of the calculated Mie resonances to the experimental Mie resonances at the new bead radius. The process was repeated to obtain a minimum in the fit as depicted in Figure 5, paper 1. An alternative to an iterative fitting procedure would have been to vary the bead radius *as well* as all three Cauchy coefficients simultaneously. However, the concurrent variation of bead radius *and* all three Cauchy parameters is computationally intensive and therefore impractical when analysing large amounts of experimental data. An iterative method was thus employed, making sure that the determined values of size and refractive index were

logical given the manufacturer's specified bead size and the available literature values for the refractive index of polystyrene beads. Excellent quality of fits were obtained between the calculated Mie resonance positions and the experimental Mie resonance positions for the ten polystyrene beads fitted in paper 1. Thus the use of an iterative fitting process was validated for the accurate determination of the size and wavelength dependent refractive index of polystyrene beads.

Future work should involve the characterisation of different types of atmospherically relevant solid aerosol to obtain a better insight into the light scattering properties of different types of aerosol.

3.2.3. Summary and evaluation of paper 2

Following validation of optical trapping and white light Mie scattering to precisely determine the optical properties of solid polystyrene aerosol, silica beads were optically trapped and coated with a thin film of oleic acid, as a proxy for mineral dust aerosol coated with an organic film in the atmosphere. Thirty five silica beads were optically trapped and seventeen beads were coated in a thin film of oleic acid, with three beads selected for detailed analysis. The coated beads were characterised using core-shell Mie theory, the core radius determined to ± 0. 5 nm and the core refractive index determined to ~± 0.0008. The oleic acid shell thickness was determined to ± 1 nm and the wavelength dependent refractive index of the coating was determined to ~± 0.0007.

The precision in the determination of the size of the core silica aerosol was lower than that reported for polystyrene beads because the Mie resonance spectrum for ~1.035 μm radius (manufacturer's specification) silica beads only contained four broad Mie resonances. More atmospherically relevant aerosol proxies are typically small in size and in the case of silica have a lower refractive index than the previously characterised polystyrene beads, resulting in fewer resonances in the silica Mie resonance spectrum. As discussed in the methodology section, a larger silica bead or a bead of a different chemical composition with a higher refractive index would have provided more resonances but would have been less atmospherically relevant and therefore ~1.035 μm radius (manufacturer's specification) silica beads were used.

To utilise the method described in paper 2 to fit a calculated core-shell spectrum to an experimentally obtained core-shell spectrum, it must be possible to optically trap a droplet of the coating material in order to determine its wavelength dependent refractive index prior to coating the core aerosol. If the coating material cannot be optically trapped, an alternative method of analysis would be to trap and characterise the core aerosol then subsequently coat the core aerosol and use core-shell Mie theory

to determine both the coating thickness and coating refractive index simultaneously. However, there is the possibility for larger error in the characterisation of the coating material from the simultaneous variation of both the coating thickness and the refractive index.

3.3. Coating effects on the Mie resonance spectrum

There is a limit when the coating reaches a certain thickness, where the backscattered Mie spectrum effectively becomes the same as an aerosol composed of only coating material, i.e. the MDR that forms at the surface of the trapped aerosol will not penetrate into the core. In the case of an oleic acid coating on a silica bead of radius 0.9559 μm, the backscattered Mie spectrum begins to resemble a droplet of solely oleic acid when the oleic acid coating is ≥ 300 nm in thickness as shown in Figure 2.

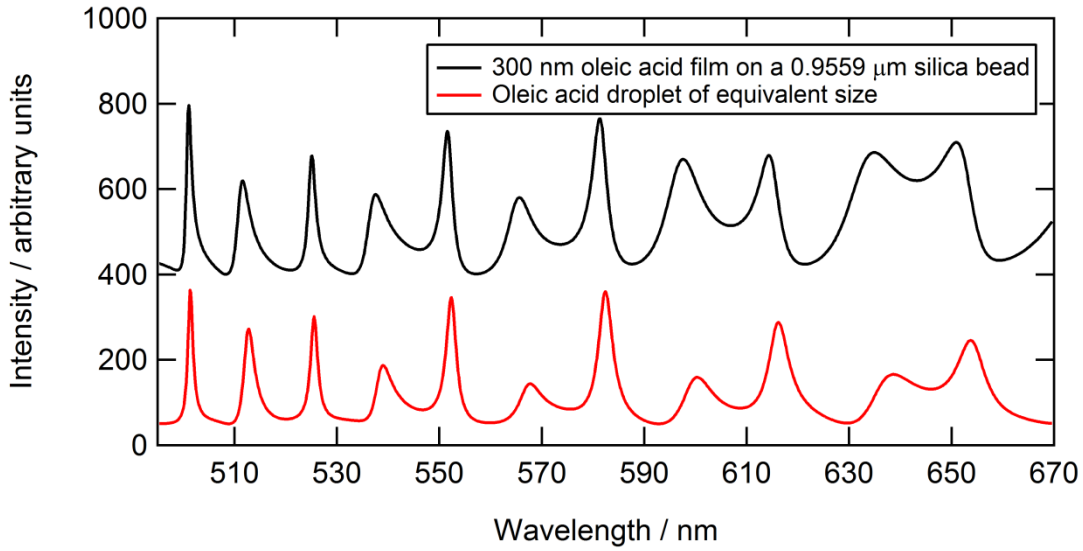

Figure 2. The calculated core-shell Mie resonance spectrum for a 300 nm thick oleic acid film on a 0.9559 μm radius core silica bead shown in black resembles the Mie resonance spectrum for a pure oleic acid droplet of equivalent size (1.2559 μm radius).

The oleic acid coatings studied in this thesis are achieved by the condensation of oleic acid vapour on to a trapped silica bead as described in paper 2. If the experimental flow rate of nitrogen gas (used to carry oleic acid vapour to the silica bead) and the temperature of the oleic acid reservoir are increased, it is possible for droplets of oleic acid to nucleate on Aitken nuclei present in the nitrogen gas stream. Droplets of oleic acid can collide with the optically trapped silica bead and form a much thicker coating. When a droplet of oleic acid collides with the optically trapped silica bead, a rapid change or jump in the position of the Mie resonances occurs. Assuming that the coating remains symmetrical around the core, core-shell Mie theory can still be used to

determine the coating thickness. However, a loss in spherical symmetry of the coating could also occur; it is possible that a small droplet of oleic acid could collide with the optically trapped silica bead and end up residing as a 'blob' of oleic acid on the surface of the optically trapped bead, distinct from the rest of the coating. A non-spherical coating cannot be analysed using core-shell Mie theory as it causes a reduction in intensity in Mie resonances and in some cases their complete disappearance. It is also possible for thicker films to result in the formation of a non-concentric coating where the core aerosol is displaced from the exact centre of the coating material. Such a phenomenon arises from the difference in densities between the core and shell which causes different optical forces to be experienced by the core and the shell (Kaiser et al., 1996). It is therefore important to be able to control the thickness of the film that is produced when coating an aerosol in order to distinguish between the core and the shell and to be able to analyse the coated aerosol using core-shell Mie theory.

3.4. Oxidation of oleic acid films on the surface of silica beads

Following characterisation of a thin oleic acid film on the surface of an optically trapped silica bead as described in paper 2, the nitrogen flow rate and oleic acid reservoir temperature were increased to form a thick coating on the surface of the silica bead. The thick oleic acid coating was subsequently oxidised by gaseous ozone and the reaction followed using Mie spectroscopy. As discussed in the preliminary work the core silica bead was inert to gaseous ozone and it was therefore expected that the oleic acid coating would be fully removed to leave behind the initial uncoated silica bead. On exposure to ozone, the Mie resonances were observed to shift in position indicating a decrease in film thickness followed by a rapid change in Mie resonance position which did not match the initial Mie resonance spectrum of the uncoated silica bead. It was therefore proposed that oxidation of a thick oleic acid coating resulted in the formation of oligomeric species that remained at the surface of the optically trapped silica bead. Owing to time constraints, this work was not pursued.

3.5. Future work

Future studies should involve the characterisation of other atmospherically relevant core-shell systems. It would be atmospherically relevant to focus on liquid coatings on core liquid aerosols, however as discussed in the preliminary work section there are a number of problems in attaining such a morphology. The core and shell material would have to be selected carefully to ensure no mixing of the coating with the core liquid aerosol. Another avenue for future work is the study of films consisting of more than one chemical because it is unlikely that a thin film on the surface of an atmospheric

aerosol will contain only one compound (Donaldson and Vaida, 2006). However, characterisation of the refractive index of mixed films may be problematic because refractive index mixing rules would have to be taken into account.

Following characterisation of static core-shell systems it is important to understand the effect of common atmospheric reactions such as oxidation of the coating material. Building on the initial oxidation of thick oleic acid films on the surface of silica beads, future studies should consider the oxidation of thin oleic acid films to observe whether it is possible to completely remove a thin film from the surface of a silica bead. Other studies could also consider the oxidation of mixed composition films as well as the effects of different oxidants. During oxidation of all core-shell aerosols, the film present at the surface of the aerosol will change in chemical composition and thickness meaning that the refractive index of the film will also change. Assuming that the core aerosol does not react with the oxidant and has been characterised prior to coating, only the thickness and refractive index of the coating will be unknown during oxidation of the core-shell aerosol. The chemical identification of the film during oxidation alongside the collected Mie resonance spectrum would greatly assist in the characterisation of an oxidised core-shell aerosol. Raman spectroscopy could be employed to determine the chemical constituents of the film during oxidation but the film would need to be quite thick in order to have enough material to a produce a strong Raman signal that could be detected. The change in film thickness could also be used to model the kinetics of the oxidation reaction. Determining the change in film thickness with time and determination of the associated reaction kinetics is an ideal way to compare optical trapping studies to neutron and X-ray reflectivity studies of the oxidation of monolayer films at the air-water interface as discussed in the next section.

3.6. Summary

To summarise, optical trapping was used because it is well suited to the study of laboratory generated aerosol as it is a non-contact technique that simulates the natural environment of the aerosol. The unique combination of optical trapping and white light Mie scattering have been used to accurately determine the size and wavelength dependent refractive index of solid aerosols and solid core-liquid shell aerosols for the first time using both Mie theory and core-shell Mie theory. Future work should concentrate on the characterisation of different atmospherically relevant systems and consider the oxidation of the core-shell aerosol.

3.7. Oxidation of monolayer films at the air-water interface

Neutron and X-ray reflectometry were used to study the oxidation of atmospherically and biologically relevant monolayer films at the air-water interface on a larger scale and using a different geometry compared to optically trapped aerosols. The amount of material at the air-water interface was followed over the course of the reaction for a number of chemically different films. Reaction mechanisms were proposed, film degradation kinetics modelled and assessments were made on the atmospheric and biological importance of such reactions.

3.7.1. Oxidation of a monolayer film of lung surfactant by gaseous ozone, Paper 3

Neutron reflectometry was used to study the oxidation of monolayer films of lipids at the air-water interface as a proxy for lung surfactant. Monolayer films of the lipid 1-palmitoyl-2-oleoyl-sn-glycero-3-phosphocholine, POPC were oxidised by gaseous ozone to study the affect of the air pollutant ozone on lung surfactant. During oxidation of the films, the amount of deuterated material at the air-water interface was observed to decrease and the surface pressure of the film was observed to rapidly increase then gradually decrease as shown in Figure 4 in paper 3. Selective deuteration confirmed that gaseous ozone reacts with the double bond on the oleoyl tail of the lipid cleaving it at the C9 position. The C9 portion of the oleoyl tail is then lost from the air-water interface either into the gaseous or aqueous phase and the remaining lipid undergoes a rearrangement at the air-water interface causing an increase in surface pressure. Neutron reflectometry is ideally suited for the study of such a reaction because of the mechanistic information gained from selective deuteration of the film at the air-water interface. Future work may consider chemical analysis alongside neutron reflectometry studies to obtain information on the rearrangement of the film at the air-water interface following oxidation. Techniques such as Fourier Transform Infrared Spectroscopy-Attenuated Total Reflectance (FTIR-ATR) and sum frequency generation (SFG) spectroscopy could be used to probe the structure and orientation of the monolayer film. FTIR-ATR involves directing an IR beam into a crystal which is in contact with the monolayer film. The IR beam is internally reflected and forms an evanescent wave which penetrates into the monolayer film; the energy from the evanescent wave is transferred back to the IR beam and finally output as an IR spectrum which can be analysed to obtain information on the chemical composition of the film. FTIR-ATR would have to be performed off the neutron beam line owing to the requirement of the crystal to contact the film; therefore SFG is preferable as it can be used in-situ. SFG

involves the combination of two pulsed laser beams (one in the visible and one in the IR) on the surface of the monolayer film resulting in light being emitted at the sum of the two incident frequencies (Bain, 1995). The intensity of the emitted light corresponds to the interaction of the frequency of the IR laser with vibrational modes of the molecules in the thin film. The frequency of the IR beam can therefore be scanned to provide a vibrational spectrum of the monolayer film; however the IR beam would have to be at a low intensity so as not to damage the film over the course of the oxidation reaction.

Further oxidation studies were conducted on mixed films of the lipid POPC and dipalmitoyl-sn-glycero-3-phosphocholine, DPPC as a proxy for lung surfactant at the air-water interface. Neutron reflectometry results highlighted a decrease in the amount of POPC at the air-water interface whilst the amount of DPPC remained constant, indicating that no other reactive species such as $^{\cdot}OH$ radicals were produced from the oxidation of POPC in the mixed film. Therefore oxidation of mixed lipid films by the air pollutant ozone is likely to only affect the unsaturated components present in lung surfactant causing a change in the organisation of material at the air-water interface and a consequent change in the associated physical properties of the film. Studies on a mixed lipid film are very relevant because lung surfactant exists as a mixture of lipids and proteins naturally. Future studies could consider the oxidation of mixed films using a different unsaturated lipid and DPPC to ascertain whether the reaction of gaseous ozone with a different unsaturated lipid releases any reactive species that would induce a change in the amount of DPPC at the air-water interface.

3.7.2. Oxidation of an atmospherically relevant film by aqueous phase radicals, Paper 4

In a separate study, neutron reflectivity was used to follow the oxidation of monolayer films of the lipid 1,2-distearoyl-*sn*-glycero-3-phosphocholine, DSPC, at the air-aqueous interface using the common aqueous atmospheric oxidants, $^{\cdot}OH$, $NO_3^{\cdot}$, $SO_4^{\cdot -}$. DSPC was studied as a proxy for organic detrital matter in the atmosphere. The amount of deuterated material at the air-water interface decreased on oxidation of the DSPC film and a multi-step degradation mechanism was proposed. The multi-step mechanism was applicable to each aqueous radical system and involved initial loss of a small deuterocarbon unit, followed by loss of a head group then finally loss of a tail from the lipid. The mechanism indicated that atmospheric films could be resistant to oxidation and that several steps may be required for complete removal of the film from the air-water interface. The multi-step degradation mechanism was kinetically modelled and fitted to the experimental decay in surface coverage to determine pseudo-first order

rate constants for each step of the mechanism. Radical steady-state concentrations were also determined by kinetic modelling and thus bimolecular rate constants were calculated for each step of the multi-step degradation mechanism for each experiment conducted. Results showed that monolayer films of DSPC at the air-water interface were susceptible to aqueous radical induced oxidation and the calculated bimolecular rate constants indicated that attack by the aqueous phase hydroxyl radical was faster than the aqueous phase sulfate radical. The lifetime of DSPC was calculated to be ~6 hours using a literature concentration for atmospheric aqueous hydroxyl radicals of 3.80×10^{-16} moldm^{-3}. It was concluded that the oxidation of lipid coatings are significantly important in the atmosphere because ~6 hours is enough time for a cloud or aerosol plume to be altered by the oxidation of any lipids that it may contain. However it may be difficult to detect lipid coatings in the atmosphere because of their ~6 hour lifetime which is relatively short compared to a typical aerosol lifetime of ~4 days. The film lifetime (i.e. surface active material present at the air-water interface including surface active reaction products) was also determined using the same atmospheric concentration of aqueous hydroxyl radicals, and a film half-life of ~2 days was calculated. The film lifetime was found to be critically dependent on the atmospheric aqueous radical concentration; a factor of ten difference in concentration i.e. 3.80×10^{-15} moldm^{-3} or 3.80×10^{-17} moldm^{-3} compared to 3.80×10^{-16} moldm^{-3} resulted in a much shorter or longer half-life of the film than a typical aerosol lifetime respectively. Therefore the value of the atmospheric aqueous radical concentration is critical to the atmospheric importance of aqueous radical induced oxidation of a thin film at the air-water interface of an aerosol. Using the concentration of aqueous hydroxyl radicals in the literature, a film half-life of two days is obtained and therefore oxidation of a lipid film by the aqueous hydroxyl radical is atmospherically important and should be studied further.

Critically evaluating the study, it is possible that another mechanism may exist to describe the aqueous induced radical oxidation of an unsaturated lipid at the air-water interface as both the number of steps in the mechanism and the weighting for each step were determined by trial and error to fit the multi-step mechanism to the decay in the amount of deuterated material at the air-water interface by eye. The determined rate constants from the fit of the mechanism to the experimental decay in the amount of deuterated material at the air-water interface impact on both the determined lifetime of DSPC and the overall film lifetime. If a different number of steps or weightings can also be used to model the degradation of deuterated material at the air-water interface then different rate constants may be determined which will affect both the DSPC and film lifetimes and ultimately impact on the atmospheric importance of the reaction. Future

work should therefore consider additional ways to validate the proposed multi-step mechanism.

One way to validate the mechanism would be to conduct a study on the aqueous radical induced oxidation of a similar fully deuterated saturated lipid such as DPPC to determine whether the same degradation model can be fitted to the decay in deuterated material at the air-water interface. If the same mechanism fits, it would suggest that the multi-step degradation mechanism can be used to describe aqueous phase radical induced oxidation of saturated lipid monolayers at the air-water interface. However, there is the fundamental question of whether DSPC is a representative proxy for atmospheric film forming material at the air-water interface. The aqueous induced radical oxidation of other atmospherically relevant film forming material such as oleic acid could also be studied and the degradation mechanism fitted to the experimental decay in surface coverage of a deuterated monolayer of oleic acid at the air-water interface. The assumption that aqueous phase radicals will react with a monolayer film of fully deuterated oleic acid is made. If the mechanism doesn't fit for the reaction of oleic acid then it can be concluded that there is no universal mechanism to describe the aqueous radical induced oxidation of monolayer films of both lipids and fatty acids at the air-water interface. Different degradation mechanisms may be required to describe the oxidation of chemically different monolayer films. Future work could therefore involve studying the radical induced oxidation of a number of monolayer films in order to determine the degradation kinetics for each monolayer film by varying the number of mechanistic steps and the individual weighting of each step.

Any other mechanistic information that could be obtained to help determine the chemical composition of the mechanistic steps would be ideal, such as in-situ chemical analysis of the film during oxidation. As previously mentioned, SFG could be combined with neutron reflectometry to obtain information on the chemical composition and organisation of material at the air-water interface. SFG has been previously used to study the organisation of monolayer lipid films at the air-water interface and the field has been reviewed by Sung et al., 2013. The next logical step in the study would be to repeat the neutron reflectometry experiment using a monolayer film of DSPC and conduct SFG spectroscopy simultaneously in attempt to validate the current multi-step degradation mechanism described in paper 4.

3.7.3. The effect of subphase viscosity and ionic strength on the oxidation of atmospherically relevant monolayer films, Paper 5

The effect of viscosity and ionic strength on the oxidation of monolayer films of oleic acid at the air-aqueous interface was also studied using neutron reflectometry. Monolayer films of oleic acid present on aqueous solutions of differing viscosities over the relative range 1-7.4 were oxidised using gaseous ozone and the rate of oxidation monitored as the rate of decrease in the amount of material at the air-aqueous interface. The rate of oxidation was found to be independent of the solution viscosity over the relative range 1-7.4. Therefore climate modellers can discount viscosity over the relative range 1-7.4 as well as the dissolution of ozone in the aqueous subphase from their aerosol models.

The independence of the oxidation of a monolayer of oleic acid by gaseous ozone to solution viscosity over the relative range 1-7.4 is only truly relevant if oleic acid is a realistic proxy for organic film forming material present at the air-water interface of aerosols. Future work could involve the study of mixed monolayers, because as mentioned in the evaluation of the core-shell paper, atmospheric film forming material is unlikely to consist of only one compound (Donaldson and Vaida, 2006). Studies could also be conducted using a different chemical to change the viscosity of the solution that also reacts with gaseous ozone meaning that there could be an interaction between the aqueous solution and the monolayer film during oxidation. However, interpretation of such an interaction may be complex, requiring additional analysis techniques such as Brewster Angle Microscopy (BAM) to gain further insight into changes in the orientation of the monolayer during oxidation. The definitive experiment would be to oxidise film forming material extracted from real atmospheric aerosol samples on solutions of differing viscosities but as discussed in paper 6, currently such films appear to be inert to gaseous ozone and the amount of material at the air-water interface cannot be followed using neutron reflectometry owing to the fact that the films cannot be deuterated. The alternative option would be to use X-ray reflectometry to follow the reaction but there would need to be a clear difference between the X-ray reflectivity signal of the viscous subphase and the monolayer film. If the signal from the monolayer film was not distinct then the data fitting would be very subjective.

3.7.4. Oxidation of atmospheric aerosol and sea water film forming material, Paper 6

Useful information can be obtained from studies of proxies of organic film forming material at the air-water interface such as oleic acid and DSPC, but it is also beneficial to study real atmospheric film forming material at the air-water interface if possible. Therefore film forming material was extracted from atmospheric aerosol and sea water samples and X-ray reflectivity was used to follow the amount of material at the air-water interface on exposure to gaseous ozone and the aqueous phase radicals $^{\cdot}OH$ and $NO_3^{\cdot}$. The samples were studied using X-ray reflectivity owing to the more intense signal that could be obtained over neutron reflectivity and also because the complex mixture of organics in real samples could not be deuterated to provide the required contrast to study such films using neutron reflectivity. Notably, the organics extracted from atmospheric aerosol and sea water samples both formed stable films at the air-water interface. No change in the amount of atmospheric aerosol or sea water film material at the air-water interface was observed on exposure to gaseous ozone, indicating that the films were inert to gaseous ozone. However, on exposure of atmospheric aerosol film material to aqueous phase hydroxyl radicals, and exposure of sea water film material to aqueous phase nitrate radicals a decrease in the amount of material at the air-water interface was observed indicating a reaction and thinning of the monolayer film. A lack of reaction with gaseous ozone but reaction with aqueous phase radials implied a possible lack of unsaturated material in the samples. Samples were analysed by GC-MS and ESI-MS and saturated compounds were found to be dominant. Combining the GC-MS and ESI-MS results with studies in the literature, it was proposed that the proportion of unsaturated material to saturated material present in the samples was very low and therefore no reaction was observed with gaseous ozone but the material reacted with aqueous phase radicals.

Unsaturated material is assumed to be present in high abundance in the atmosphere e.g. Gill et al., 1983, Russell et al., 2002 and Donaldson and Vaida, 2006, and several studies have been conducted on thin films of unsaturated compounds such as oleic acid for that reason, some examples are; Gonzalez-Labrada et al., 2006, 2007, King et al., 2004, 2009, Schwier et al., 2011, and Voss et al., 2007. Previous neutron reflectometry studies have shown that monolayer films of oleic acid and methyl oleate are susceptible to oxidation by gaseous ozone (King et al., 2009, Pfrang et al, 2014). It was therefore expected that real film forming material would react with gaseous ozone; however no change in the amount of material at the air-water interface was observed

on exposure of real film forming material to gaseous ozone and the proportion of unsaturated material to saturated material in the samples was deemed to be low.

As discussed in the section 2.7.3. ‘Sample collection methods’, the sampling and extraction processes used for atmospheric aerosol and sea water samples may have influenced the composition of material detected in the extracted organic material. Following alternative sample collection and extraction methods described in the aforementioned section, the X-ray reflectivity experiment could be repeated to determine whether the newly sampled monolayer films of either atmospheric aerosol or sea water film material react with gaseous ozone and if so which sampling and extraction method was used on the samples that reacted.

Future work should also involve studying the kinetics of aqueous phase radical induced oxidation of the film. The determination of a mechanism that describes the thinning mechanism observed when a monolayer of real film forming material is exposed to aqueous phase radicals is more important than the determination of a mechanism for the degradation of a proxy film such as the monolayer of DSPC described in paper 4. The shape of the modelled decay of real film forming material at the air-water interface in paper 6 suggests that the decay mechanism is exponential. However, future oxidation studies conducted on monolayer films of material that have been sampled and extracted in different ways may demonstrate a different shaped decay similar to the one observed in paper 4. Therefore, if a different decay mechanism is observed for the oxidation of monolayer films sampled using different methods, the initial step would be to try and fit the multi-step degradation mechanism described in paper 4 to the decay. It is likely that either the number of degradation steps or the weightings of the steps will require adjustment as atmospheric aerosol and sea water film material contain a mixture of compounds compared to a monolayer film of DSPC alone.

X-ray reflectivity of monolayer films at the air-water interface permits measurements to be made to a higher Q range, meaning that more information on the structure of the monolayer film can be obtained. The signal to background ratio is many orders of magnitude higher than in neutron reflectivity which means that studies can be conducted on samples that may not be possible using neutron reflectivity such as film forming material extracted from atmospheric aerosol and sea water samples.

3.8. Conclusions

The unique combination of optical trapping and white light Mie scattering was used to characterise laboratory generated aerosol to accurately determine aerosol size and wavelength dependent refractive index. Polystyrene beads were optically trapped in air as a proxy for solid aerosol and Mie theory was used to determine their size to ± 0.4 nm and their wavelength refractive index to ± 0.0005. Studies were also undertaken to generate and characterise core-shell aerosol. A number of preliminary experiments were performed on core sodium chloride droplets and core polystyrene beads using a number of potential liquid coatings. The findings of the preliminary work suggested that liquid coatings could mix with a liquid core and that a solid core may be more appropriate to generate core-shell morphology in the laboratory. Following trials with polystyrene beads, silica beads were successfully trapped and coated in a thin film of oleic acid as a proxy for mineral dust aerosol coated in an organic film. Core-shell Mie theory was used to determine the core silica size to ± 0.5 nm, the core wavelength dependent refractive index to ~± 0.0008 and the oleic acid coating thickness to ± 1 nm. More atmospherically relevant aerosols such as silica are typically small in size and have a low refractive index, meaning their Mie resonance spectrum will contain fewer peaks and therefore more uncertainty will be associated with the characterisation of more atmospherically relevant aerosol. Future work will include the characterisation of other atmospherically relevant systems as well as studies into the oxidation of coating. In order to characterise the thickness and refractive index of the coating during oxidation, the core aerosol must be inert to oxidation as determined in the preliminary experiments.

Neutron and X-ray reflectometry were used to study the oxidation of atmospherically and biologically relevant monolayer films at the air-water interface. Neutron reflectometry studies determined the mechanism of oxidation of biologically relevant lipid films by the pollutant gas ozone and found that only unsaturated lipids reacted when mixed films of saturated and unsaturated lipids were oxidised by gaseous ozone. A separate neutron reflectivity study showed that the rate of oxidation of a monolayer film of oleic acid was independent of the solution viscosity over the relative range 1-7.4 of the aqueous subphase, which means that the effect of viscosity over the relative range 1-7.4 can be discounted from climate models. Neutron reflectometry was also used to study the oxidation of a monolayer of DSPC induced by the aqueous phase radicals; $^{\cdot}OH$, $NO_3^{\cdot}$, $SO_4^{\cdot -}$. The oxidation reaction was found to proceed via a multi-step degradation mechanism and the lifetime of the film was found to critically depend on the atmospheric radical concentration. In addition to the oxidation of atmospherically relevant proxy films, X-ray reflectometry studies were also conducted

on monolayer films of organic material extracted from real atmospheric aerosol and sea water samples. The X-ray reflectivity experiments showed that real film forming material was inert to gaseous ozone but did react with the aqueous phase radicals $^{\cdot}OH$ and $NO_3^{\cdot}$. GC-MS and ESI-MS were subsequently conducted on the organic film forming material and saturated compounds were found to dominate both the atmospheric aerosol and sea water film forming material. Owing to the dominance of saturated material in the atmospheric aerosol and sea water samples it may be more relevant for future studies to focus on the radical induced oxidation of monolayer films of saturated material. Other avenues for future work will involve validation of the proposed degradation mechanism for a monolayer of DSPC under aqueous phase radical attack as well as the determination of the degradation mechanism for the aqueous phase radical induced oxidation of a monolayer of organic film forming material extracted from atmospheric aerosol and sea water samples.

In order to further connect the oxidation reactions studied using neutron and X-ray reflectometry to thin films on the surface of atmospheric aerosols, the same oxidation experiments could be conducted on optically trapped core-shell aerosols. The change in film thickness during oxidation can be followed using neutron or X-ray reflectometry and can also be determined during oxidation of a coating on a core-shell aerosol using core-shell Mie theory. Therefore the degradation mechanism of the film can be modelled to compare oxidation of monolayer films on a flat surface to more atmospherically relevant oxidation of monolayer films on a curved proxy aerosol surface.

In summary, optical trapping combined with white light Mie spectroscopy has shown that the formation of core-shell aerosol is physically possible and therefore core-shell morphology may exist in the atmosphere. Complementary neutron reflectometry studies have shown that the oxidation of thin films at the air-water interface are critically dependent on the atmospheric concentration of the oxidant and therefore may be important in the atmosphere. X-ray reflectometry studies and subsequent analytical findings have highlighted that unsaturated proxies may be a poor representation of organic film forming material in the atmosphere and that the aqueous radical induced oxidation of saturated organic proxies may be more atmospherically relevant.

3.9. Summary and evaluation references

Bain, C. D.: Sum-frequency Vibrational Spectroscopy of the Solid/Liquid Interface, J. Chem. Soc. Faraday Trans., 91(9), 1281–1296, 1995.

Donaldson, D. J. and Vaida, V.: The influence of organic films at the air-aqueous boundary on atmospheric processes., Chem. Rev., 106(4), 1445–61, 2006.

Fang, J., Kawamura, K., Ishimura, Y. and Matsumoto, K.: Carbon isotopic composition of fatty acids in the marine aerosols from the western North Pacific: implication for the source and atmospheric transport., Environ. Sci. Technol., 36(12), 2598–2604, 2002.

Garrett, W.D, and Duce, R. A.: Surface microlayer samplers in Air-sea interaction: instruments and methods, eds., Dobson, F, Hasse, L. and Davis, R., Plenum, New York, London, 1980.

Gill, P. S., Gradel, T. E. and Weschler, C. J.: Organic Films on Atmospheric Aerosol Particles, Fog Droplets, Cloud Droplets, Raindrops and Snowflakes, Rev. Geophys. Sp. Phys., 21(4), 903–920, 1983.

González-Labrada, E., Schmidt, R. and DeWolf, C. E.: Real-time monitoring of the ozonolysis of unsaturated organic monolayers., Chem. Commun., (23), 2471–3, 2006.

González-Labrada, E., Schmidt, R. and DeWolf, C. E.: Kinetic analysis of the ozone processing of an unsaturated organic monolayer as a model of an aerosol surface, Phys. Chem. Chem. Phys., 9(43), 5814, 2007.

Husar, R. and Shu, W.: Thermal analyses of the Los Angeles smog aerosol, J. Appl. Meteorol., 14, 1558–1565, 1975.

Kaiser, T., Roll, G. and Schweiger, G.: Investigation of coated droplets in an optical trap: Raman-scattering, elastic-light-scattering, and evaporation characteristics, Appl. Opt., 35(30), 5918–24, 1996.

King, M. D., Thompson, K. C. and Ward, A. D.: Laser Tweezers Raman Study of Optically Trapped Aerosol Droplets of Seawater and Oleic Acid Reacting with Ozone : Implications for Cloud-Droplet Properties, J. Am. Chem. Soc., 126(51), 16710–16711, 2004.

King, M. D., Rennie, A. R., Thompson, K. C., Fisher, F. N., Dong, C. C., Thomas, R. K., Pfrang, C. and Hughes, A. V.: Oxidation of oleic acid at the air–water interface and its potential effects on cloud critical supersaturations, Phys. Chem. Chem. Phys., 11(35), 7699, 2009.

Marty, J. C., Saliot, A., Buat-Ménard, P., Chesselet, R. and Hunter, K. a.: Relationship between the lipid compositions of marine aerosols, the sea surface microlayer, and subsurface water, J. Geophys. Res., 84(C9), 5707–5716, 1979.

Mochida, M.: Fatty acids in the marine atmosphere: Factors governing their concentrations and evaluation of organic films on sea-salt particles, J. Geophys. Res., 107(D17), 4325, 2002.

Pfrang, C., Sebastiani, F., Lucas, C. O. M., King, M. D., Hoare, I. D., Chang, D. and Campbell, R. a: Ozonolysis of methyl oleate monolayers at the air-water interface: oxidation kinetics, reaction products and atmospheric implications, Phys. Chem. Chem. Phys., 16(26), 13220–8, 2014.

Russell, L. M., Maria, S. F. and Myneni, S. C. B.: Mapping organic coatings on atmospheric particles, Geophys. Res. Lett., 29(16), 26–1–26–4, 2002.

Schwier, A. N., Sareen, N., Lathem, T. L., Nenes, A. and McNeill, V. F.: Ozone oxidation of oleic acid surface films decreases aerosol cloud condensation nuclei activity, J. Geophys. Res., 116(D16), 1–12, 2011.

Stocker, T.F., D. Qin, G.-K. Plattner, M. Tignor, S.K. Allen, J. Boschung, A. Nauels, Y. Xia, V. Bex and P.M. Midgley (eds.), IPCC, 2013: Climate Change 2013: The Physical Science Basis. Contribution of Working Group I to the Fifth Assessment Report of the Intergovernmental Panel on Climate Change Cambridge University Press, Cambridge, United Kingdom and New York, NY, USA, 1535 pp

Sung, W., Kim, D. and Shen, Y.: Sum-frequency vibrational spectroscopic studies of Langmuir monolayers, Curr. Appl. Phys., 13(4), 619–632, 2013.

Tervahattu, H., Hartonen, K., Kerminen, V., Kupiainen, K., Koskentalo, T., Tuck, A. F. and Vaida, V.: New evidence of an organic layer on marine aerosols, J. Geophys. Res., 107(D7), AAC 1-1-AAC 1-8, 2002.

Tervahattu, H., Juhanoja, J., Vaida, V., Tuck, A. F., Niemi, J. V., Kupiainen, K., Kulmala, M. and Vehkamaki, H.: Fatty acids on continental sulfate aerosol particles, J. Geophys. Res., 110(D6), 1–9, 2005.

Voss, L. F., Bazerbashi, M. F., Beekman, C. P., Hadad, C. M. and Allen, H. C.: Oxidation of oleic acid at air/liquid interfaces, J. Geophys. Res.,112(D6), 1–9, 2007.